Quantifying the damage of in-service rolling stock wheelsets using remote condition monitoring

By

Panukorn Krusuansombat

A thesis submitted to

The University of Birmingham

For the degree of

DOCTOR OF PHILOSOPHY

School of Metallurgy and Materials

College of Engineering and Physical Sciences

University of Birmingham

September 2022

Synopsis

The global railway network is set to continue to expand in terms of size, passenger numbers and freight tonnage in the coming decades. The occurrence of derailments can lead to major network disruption, significant financial losses, damage to infrastructure and rolling stock assets, environmental damage, and possibly fatalities and injuries. Defects in rolling stock wheelsets can potentially result in severe derailments if left to grow to a critical level. Rolling stock wheelsets are maintained using preventative maintenance techniques. Predictive maintenance solutions prevent unexpected failure, boost operational efficiency, and lower costs.

The railway industry has been looking into the development of advanced and effective condition monitoring with a low capital cost for the online and real-time assessment of the rolling stock wheels' structural integrity and subcomponents (wheels, bearings, brakes and suspension). Existing wayside measurement systems are based on different technologies, including hot boxes, acoustic arrays, wheel impact load detectors, etc. However, significant flaws, especially bearing failures, are challenging to identify. Hot boxes can only detect bad bearings after they overheat. This indicates that the bearing has failed and will be seized soon.

The combination of acoustic emission (AE) and vibration analysis has been used in this study to identify wheelset defects, particularly in wheels and axle bearings. Based on the new approach and thanks to the capability of early fault detection, predictive maintenance methods can be effectively applied whilst minimising the risk of catastrophic failure and reducing the level of disruption to an absolute minimum.

The present study looked into the quantitative evaluation of damage in axle bearings using an advanced customised vibroacoustic remote condition monitoring system developed at the University of Birmingham to improve the early fault detectability in in-service rolling stock wheelsets and improve maintenance planning. Laboratory tests using AE sensors and accelerometers were conducted to compare the sensitivity of each technique and evaluate the synergy in combining them. An experiment using the Amsler machine and bearing test rig proved that raw data and Fast Fourier transform (FFT) are inefficient for defect detection. More advanced signal processing techniques, including Kurtosis,

were also applied to find the ideal core frequency and bandwidth for a band-pass filter. Cepstral analysis determines the complex natural logarithm of data's Fourier transform, and the power spectrum's inverse Fourier transform. It helps identify the bearing defect's harmonics from vibration measurement.

High-frequency harmonics arising from wheel and axle bearing faults were proven to be detectable from the acquired AE signals. The trial at Bescot yard demonstrates wayside measurement using a compact data acquisition system. Kurtogram-based band-pass filters eliminate environmental and undesired vibrations. The filtered signal with a better signal-to-noise ratio has less noise than the original signal. Another real-world wayside measurement was conducted at the Cropredy site to demonstrate train and wheelset defect detection.

The experiments were held in the Long Marston test track under control conditions. They included onboard and wayside measurements where the AE sensors and accelerometers were placed in different positions. Spectral envelope analysis and EMD decomposition of AE onboard measurement indicated 2mm and 8mm roller fault according to bearing fundamental frequency. Unfortunately, vibration data from the same experiment did not show faults due to no amplitude modulation. Wayside measurements showed how RCM works on the railway network, which has environmental noise and a broken bearing with a 2mm roller flaw. The Wayside setup showed that the AE measurement detected the wheelset-bearing roller problem, but the vibration measurement did not. Vibration can identify wheel flats and severe axle-bearing failures. AE and vibration were assessed to detect lubricant-contaminated bearings using onboard measurement. Raw data and RMS of AE measurement showed the difference between damaged and healthy bearings. Unfortunately, vibration failed to identify the two bearing situations.

AE sensors can detect axle bearing defects while accelerometers can detect and quantify wheel tread defects. Unfortunately, accelerometers are much less sensitive to axle bearing failures unless the axle bearing defect has reached critical severity. Therefore, combining AE sensors and accelerometers is the best solution for quantifying the damage to in-service rolling stock wheelsets efficiently and effectively and minimising the likelihood of false alarms.The results from the present study show that the methodology discussed herewith has significant capabilities for the effective remote condition monitoring of rolling stock wheelsets with a low cost of implementation.

Acknowledgment

Firstly, I sincerely appreciate the precious support from my family and my lovely KNJ during this difficult time. I would also like to express my gratitude for their encouragement and motivation.

I owe a great deal of gratitude to my supervisor, Dr. Mayorkinos Papaelias, whose knowledge and experience have helped me tremendously throughout my study. He also suggested and guided me through every process of this research. Without his invaluable support, I would not complete this thesis.

This endeavour would not have been possible without my sponsorship from the Thai government's Ministry of Higher Education, Science, Research and Innovation. I truly appreciate their support for my living in the UK.

Special thanks to my co-supervisor, Dr Sakdirat Kaewunruen, for the opportunity of the oversea internship at EVOLEO technologies company in Porto, Portugal. I am also grateful to Dr Rodolfo Martins and his colleagues for providing a warm welcome and support throughout my stay in Porto.

I want to sincerely thank Dr. Patrick Vallely for setting up and providing the necessary facilities for the field studies at the Cropredy site and the Bescot yard.

Thanks should also go to Dr Sanaz Roshanmanesh, Dr Valter Jantara Junior, and Dr Farzad Hayati for the assistance and suggestions throughout this research.

Lastly, I'd like to mention the University of Birmingham's services and facilities, without which the accomplishment of this thesis was very challenging.

Publications

- P. Krusuansombat, M. Papaelias, S. Kaewunruen "*A review on remote condition monitoring and related signal processing for rolling stock wheelsets*". (Pending for submission)
- Giannouli, E., Papaelias, M., Amini, A., Huang, Z., Junior, V. L. J., Kerkyras, S. C., Krusuansombat, P., Márquez, F. P. G., Vallely, P. (2021). Detection and evaluation of rolling stock wheelset defects using acoustic emission. *Insight - Non-Destructive Testing and Condition Monitoring*, *63*(7), 403–408.

List of Contents

List of Figures

List of Tables

List of Abbreviations

AE	Acoustic Emission
AC	Alternating Current
ACFM	Alternating Current Field Measurement
Bw	Bandwidth
BS	British Standard
BPFI	Ball pass frequency inner race
BPFO	Ball pass frequency outer race
BSF	Ball spin frequency
CM	Condition Monitoring
CWT	Continuous Wavelet Transforms
DAQ	Data Acquisition System
dB	Decibel
DWT	Discrete Wavelet Transforms
ECA	Eddy Current Arrays
EMI	Electro-magnetic interference
EMD	Empirical Mode Decomposition
EEMD	Ensemble Empirical Mode Decomposition
EN	European Standards
Fc	Centre Frequency
FFT	Fast Fourier Transform
FBGs	Fibre Bragg Gratings
FEM	Finite Element Method
HFRT	High-frequency Resonance technique
HABDs	Hot Axle Box Detectors
HRC	Rockwell scale C
IMF	Intrinsic Mode Functions
ISO	International Organization for Standardization
MPI	Magnetic Particle Inspection

MTBF	Mean Time Between Failure
MTTR	Mean Time To Repair
MEMS	Micro-Electromechanical System
NDT	Non-Destructive Testing
RAMS	Reliability, Availability, Maintainability and Safety
RCM	Remote Condition Monitoring
RCF	Rolling Contact Fatigue
RMS	Root-Mean-Square
RTOF	Round Trip Time-of-Flight
RSSB	Rail Safety and Standards Board
STFT	Short-Time Fourier Transform
SNR	Signal-to-Noise Ratio
SAE	Society of Automotive Engineers
SK	Spectral Kurtosis
TSIs	Technical Specifications for Interoperability
TSK	Time Spectral Kurtosis
TAADs	Trackside Acoustic Array Detectors
UT	Ultrasonic inspection
WT	Wavelet Transform
WILDs	Wheel Impact Load Detector

Chapter 1: Introduction

1.1 Background and motivation

Railway operations face challenging requirements in various aspects, including high level of safety, increasing train speed, optimized passenger comfort, more capacity, higher availability and flexibility (Schmid, 2017). Whilst railway operations are dealing with these parameters to enhance competitiveness with reference to other modes of transport, they are also subject to stringent regulations and standardisation. For example, the Interoperability Directive and Technical Specifications for Interoperability (TSIs) which apply in the European Union state the essential requirements with respect to safety, availability and reliability, health, environmental protection, technical compatibility, accessibility (for people of reduced mobility) (Éric & Reinhard, 2020). At the first glance, rail vehicles are required to provide the highest level of reliability and availability with the highest degree of safety possible.

Within modern railway systems, there are many subsystems that are interfaced and integrated aimed at ensuring reliable, efficient and effective operations. Key subsystems include railway control, operations, rolling stock and infrastructure (Schmid, 2017). Accordingly, rolling stock and infrastructure need optimum interfacing, especially at the wheel-rail contact point. Rolling stock wheelsets are the key rolling stock components responsible for sustaining high operational axle loads, impact loads, vibrations and high travel speeds. In-service wheelsets are thus subject to various forms of degradation mechanisms including Rolling Contact Fatigue (RCF), impact, rail and wheel profile irregularities, severe dynamic loads and thermal effects due to friction.

Apart from the design aspects directly related to rolling stock operations, maintenance processes and procedures also have a key role in ensuring smooth operations and avoiding

unexpected faults to occur during the service. For example, effective and targeted condition monitoring (CM) can be used towards implementing condition-based or predictive maintenance processes and procedures successfully. Also, maintenance planning can be optimized, both in terms of human resources, equipment and spare parts. Since in the railway industry equipment should not be allowed to fail due to the disruption and the potential risks to life, goods and the environment associated with unexpected failures. Remote condition monitoring (RCM) can effectively mitigate these risks by generating useful data for the early identification of defects and thus, bringing down to an absolute minimum the likelihood of unexpected faults (Barke & Chiu, 2005a; Chong et al., 2010).

Since the author's home country is Thailand, it would be of great interest for State Railway of Thailand to develop a cost-effective, robust and reliable wheelset monitoring system that can be introduced to the local railway network as a means of improving reliability and safety of operations and optimising maintenance of existing and future rolling stock. Recently, Thailand's railway network introduced some limited capabilities on predictive maintenance for both infrastructure and rolling stock. This has also been the motivation for the author whom the Thai government is sponsoring towards achieving this objective. The implementation of wayside and onboard monitoring for the initiation and evolution of wheelset defects could support the further improvement and optimisation of railway systems and associated operations. Passengers and tonnage carried via rail has been increasing worldwide, and this has also been the case in Thailand where it is evident that this trend will continue until at least the end of this century. The State Railway of Thailand has provided information to the author regarding the current processes used for rolling stock wheelset inspection and data related to failures and modes observed in the field. The equipment used within this research should be reliable and compact in order to enable installation on any railway network service condition.

It is a necessary step toward putting the proposed method of monitoring the condition of wheelsets on the railway network in Thailand.

Efficient and reliable maintenance strategies are needed for optimum railway operations. Reliability, Availability, Maintainability and Safety (RAMS) needs to be maximized for both rolling stock and railway infrastructure. Reliability is a system or component's capacity to perform a function between maintenance intervals. The ability of the component to perform a defined function at a specified moment in time is related to its availability. Maintainability on the other hand is the ability of the component to be maintained and be restored to an acceptable condition allowing it to continue to perform its intended function or operation for a specified time. Safety is related to the ability of the system or component concerned to function or operate safely without the likelihood of failure that could expose passengers or the environments to harm (Hoskins, 2017). The applicability of RAMS is also relevant to failure rate, Mean Time between failure (MTBF) and Mean Time To Repair (MTTR) of a particular system or component. These parameters have a significant effect on maintenance strategies and procedures employed. Thus, a novel condition monitoring should support the RAMS approach. Early detection and identification of any defects of concern should significantly reduce MTTR and improve MTBF (D. J. Smith, 2017).

It is generally known that when defects are detected early in time, it will cost much less to maintain and repaid the problem whilst the likelihood of catastrophic failure is removed. When a defect affects the operation of the component, there is very little time left to perform the necessary maintenance before final failure becomes likely. Successful monitoring techniques may detect, identify, and quantify faults and their progression for effective maintenance planning. In this way RAMS can be optimised. Reducing failure rates and downtime are key requirements for decreasing operation expenditure of rolling stock and infrastructure assets. This should be coupled with the optimization of maintenance planning and processes. The

present thesis emphasises the importance of developing effective online condition monitoring to support the aforementioned capabilities towards enabling the optimization of railway operations.

Derailments can have serious accidents as they cause injury or even death of passengers onboard, or damage goods and harm the environment when freight trains are involved. Liu (X. Liu, 2017) discusses the railway accident causes reported by the Federal Railroad Administration. Accidents are categorised due to their cause into track failures, signalling failures, rolling stock failures, human errors, and miscellaneous causes (FRA (Federal Railroad Administration), 2011). The report summaries in satisfactory detail the mechanisms that can result in a railway accident. Certain studies by (Barkan et al., 2003; X. Liu et al., 2011) revealed that heavy-haul freight trains are more likely to derail due to larger impact loads to the track infrastructure. Overheating bearings and broken wheels caused by exposure to severe operating conditions can result in derailments. The frequency and severity of mainline accidents affecting hazardous materials transportation during 1992-2001 was studied by (Barkan et al., 2003). They categorised in more detail the causes of derailment based on the same principles as FRA. There were 50 cause groups in total considered. However, only a few of those were counted as they met the frequency and severity threshold required. Most of hazardous materials traffic relates to Class` I railroad mainline track, contributing to the study of derailment causes on class 1 heavy haul freight train used in the United States considered by (X. Liu et al., 2012). Figure 1-1 shows the statistics of severity and frequency of derailment of Class 1 freight train, by dividing them into four quadrants on the average of each axis. It could be clearly stated that bearing failures and broken wheels were found to be the top reason for rolling stock-related derailments.

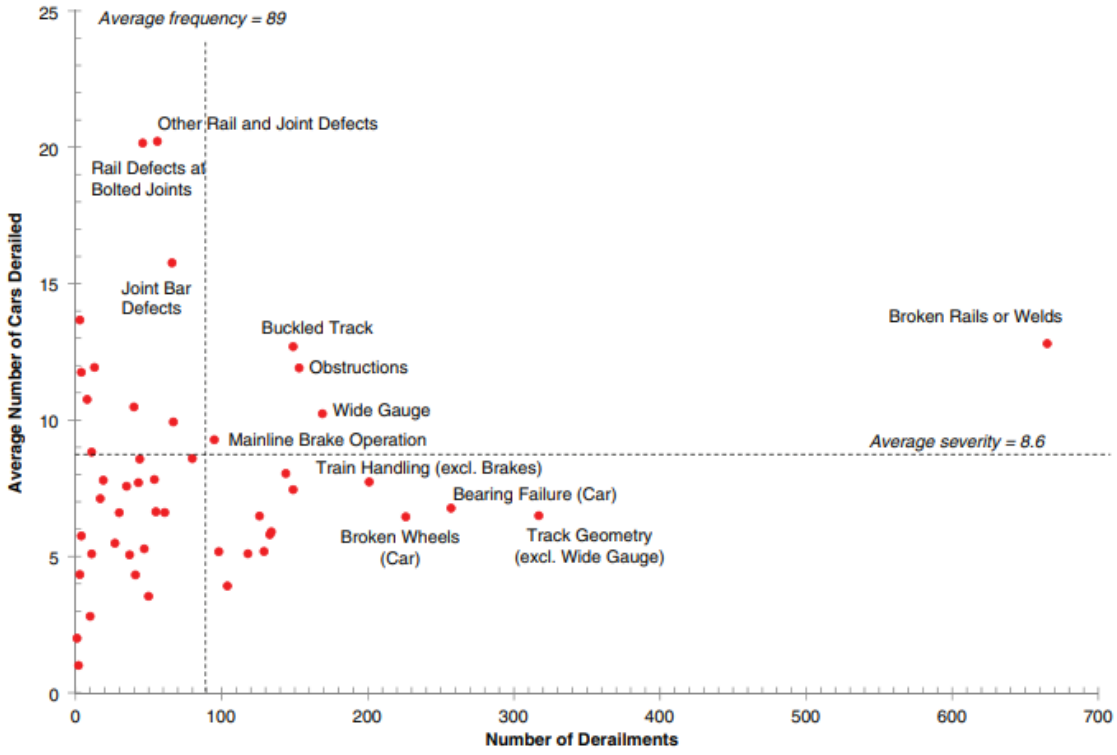

Figure 1-1: Severity as an average number of cars derailed and frequency of derailments classified by different causes of Class I main-line freight train, 2001-2010 (X. Liu et al., 2011).

The analysis performed by Liu (X. Liu, 2015) revealed a trend of temporal derailment rate per million train miles as displayed in Figure 1-2 based on their model evaluation using time parameter as a predictive variable. Liu studied the data of freight train derailments of four Class 1 railroads measured by million train miles from 2000 to 2012. The model used in the parameter estimation of their study focused on the temporal trend of train derailment rate. Obviously, the rate of freight train derailment by any cause has been decreasing in recent years.

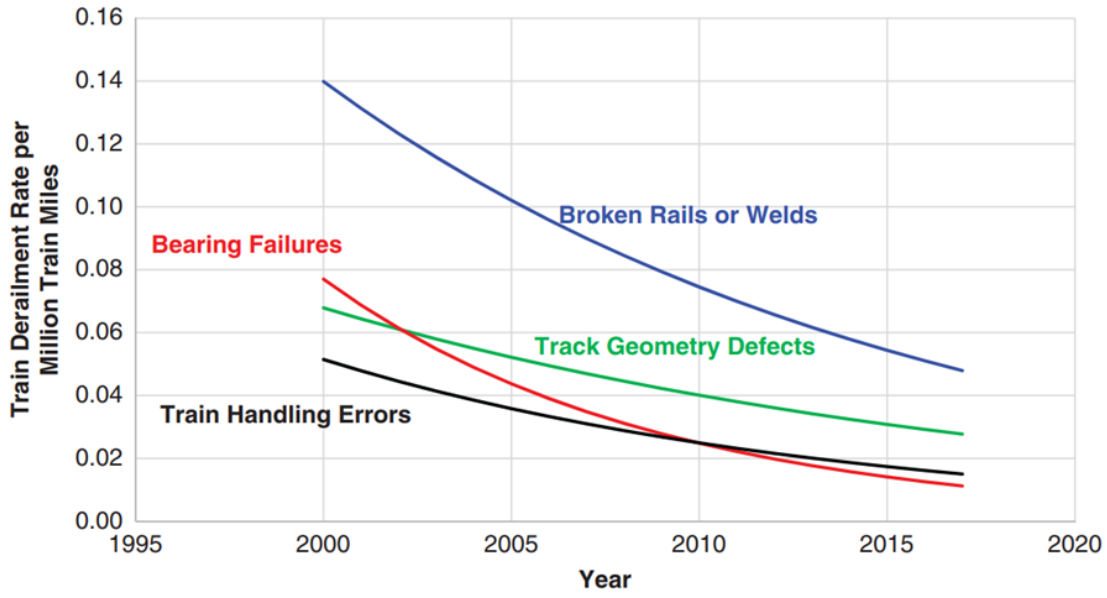

Figure 1-2: Statistical temporal analysis of freight train derailment rate per million train miles by causes (X. Liu, 2015).

Wheel irregularities can be classified into different types as discussed by Nielsen and Johansson (Nielsen & Johansson, 2000b). The main difference among wheel tread imperfections when considering the effect to the infrastructure is the frequency and level of impact loads on the wheel/rail interface. They concluded that the early detection of damage on wheels with timely replacement could reduce the costs of maintenance and result in a significant economic incentive for the railway industry.

The mechanisms resulting into faulty wheels causing train derailment have been considered (M. Papaelias et al., 2016a). Axle bearings need to withstand the weight of rolling stock and dynamic loads arising when they trains move at speed as the wheel rotates. Damaged wheels will lock up if the bearing seizes. As a result, only one wheel of the wheelset will carry on rotating causing the axle to perform a hacksaw motion. Eventually, the axle will fracture, since the extreme loads resulting by this abnormal motion are too high to be sustained, causing the train to derail. Whilst the wheel condition is very important for the wheel-rail interface interactions, axle bearings also handle the repetitive loads through their rotating elements.

Failure of the rotating elements of the bearing can result in final failure of the entire bearing and subsequent failure of the axle (Y. Li et al., 2018; Yi et al., 2018).

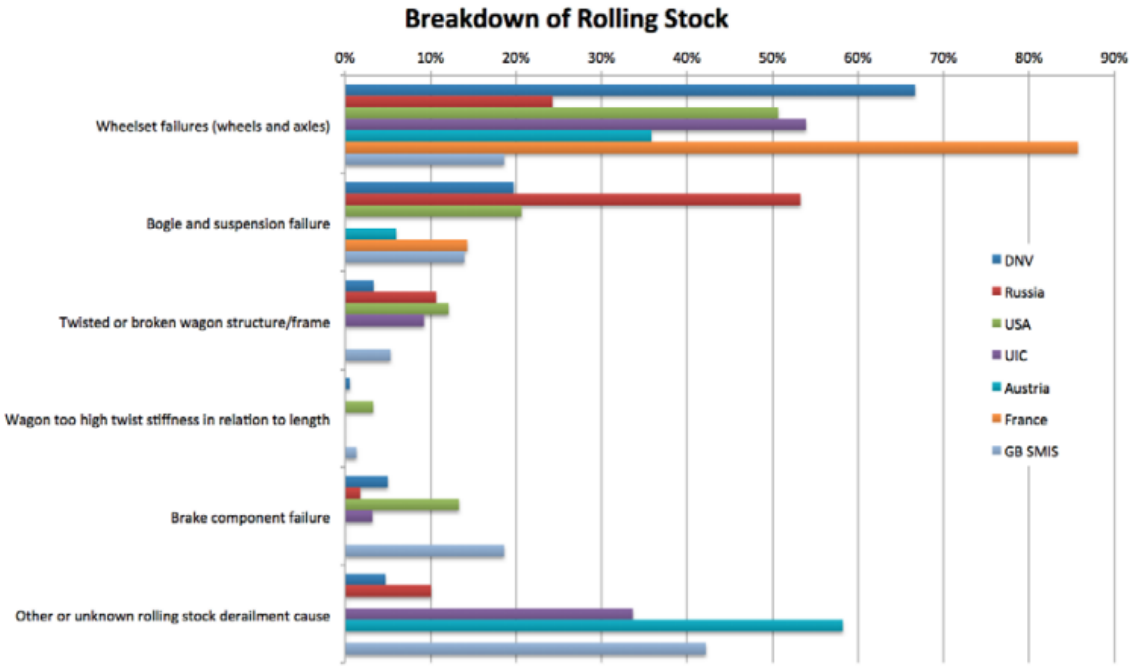

Figure 1-3: Breakdown causes of rolling stock resulting in freight derailments (Robinson et al., 2012).

The D-Rail project summarised in a database the freight train derailment incidents reported in recent years (Robinson et al., 2012). The causes of derailment associated with rolling stock are split into 6 categories. Figure 1-3 shows the percentages for each category classified for 7 regions across the world. Obviously, the main category which led to rolling stock derailment is related to wheelset failure. It relates to wheel and axle failure. Major factors related to freight derailment are high impact loads, high dynamic loads and thermomechanical effects.

Even though the causes of the derailment were generally associated with track failure and environment-related reasons, broken wheelsets. The wheelset failure was mainly found in freight wagons due to the severe loading condition and reduced running gear and braking

system maintenance. In addition, the degradation of the profile of the wheel treads and flanges were the main areas of the wheelset that required adequate maintenance.

Figure 1-4: The manufacturing defects of the wheel cause the derailment in Canada (Transportation Safety Board of Canada, 2015).

A wheel failure could result from various types of defects including cracking on the wheel surface. A derailment accident report from the Transportation Safety Board of Canada revealed that the reason for the freight train's derailment on 7 January 2014 was caused by shattered rims as seen in Figure 1-4 (Transportation Safety Board of Canada, 2015). The root cause was determined as a large porosity under the wheel surface which contributed to fatigue cracking. According to the investigation, the porosity formed during the casting of the wheel in 1991. However, the ultrasonic inspection (UT) during the manufacturing process and reprofiling did not detect the large porosity. Figure 3 displays how the left wheel of car CRDX 15109 caused the derailment when it finally failed from the crack initiating from the porosity. A missing part of the wheel caused the wheel to fracture and come off the rail causing the train to derail.

Another derailment of a freight train occurred on 28 August 2015 at Pangela, New South Wales (Australian Transport Safety Bureau, 2016). The Australian Transport Safety Bureau

concluded in their investigation report that the derailment was caused by a wheel failure which had been caused by multiple cracks in the rim area. These cracks had generally initiated due to the thermal change at the wheel surface during braking of the train.

Whereas the passenger trains generally are subject to more close maintenance, derailments associated with freight trains could create the likelihood of collision with a passenger train as in the Bromsgrove accident on 23 March 2020 (Rail Accident Investigation Branch, 2020). The locomotive derailed at the position close to the mainline just before the passenger train arrived.

The derailment accident of a grinding train near Dunkeld on 29/10/2018 was the direct result of a wheelset fault. The wheels of the trailing bogie started to slide, generating a large wheel flat on both sides of the wheelset and abnormal profiles on the flange area. This resulted in the wheel flange to climb over the switch and stock rails, causing the wheels to become trapped and cause high lateral forces that resulted in the rails becoming disconnected from the base. Again, a damaged flange developed and consequently climbed the crossover before the train derailed. To sum up, the other wheelset-related components should also be validated simultaneously (Rail Accident Investigation Branch, 2019a).

Another derailment was the result of a vertical split rim on the wheel of a Canadian freight train. This accident was also, investigated by the Transportation Safety Board of Canada. They mentioned various related factors and proposed the safety action necessary for implementing fault detection technologies to the existing monitoring systems. In addition, the criteria for fault detection on the wheel should be reviewed to provide better detectability and identification of faulty wheelsets (Rail transportation safety investigation report, 2018).

Wheelset flaws can cause degradation of the railway track infrastructure due to excessive impact loads after every single wheel revolution. Therefore, wheel/rail contact conditions could result into different mechanisms that can lead to wheel/rail failure. Furthermore, while each

wheel/rail system performs a different operation, they must be well-maintained. As a result, rolling stock and track engineers cannot allow a wheel or the rail to fail during the operation.

Non-destructive testing (NDT) was widely used for defect detection and evaluation in many applications, including marine, oil and gas, and piping systems, especially for detection and quantification of surface and internal cracks. Therefore, various techniques of NDT were applied in defect detection. However, the wheelset condition monitoring application has some limitations, including noise from the traction and braking system and infrastructure conditions. Thus, the acquired condition monitoring techniques should overcome these limitations first.

Acoustic Emission (AE) and vibration analysis have been proven to be useful examples for condition monitoring of railway wheelsets (M. Papaelias et al., 2014). One of the reasons to integrate those two techniques is the ability to classify and evaluate wheel and axle bearing defects by applying suitable signal analysis (M. Papaelias et al., 2014). AE was effectively used for the detection and evaluation of severity of roller defects on the bearing in a test freight wagon by (Amini, Entezami, & Papaelias, 2016a). Novel signal processing can further enhance the prospects of early defect detection and quantification.

The wheelsets rotate as the train moves along the railway track generating repetitive signals with respect to the rotational frequencies. The characteristic of each component's frequency in the wheelset varies with respect to the number of revolutions per minute. The recorded raw signals need to be analysed in the frequency domain in order to reveal the rotational information of the wheelset components of interest. Thus, for the purpose of fault detection, frequency-domain analysis is required to reveal the hidden information in the time-domain signals (Norton & Karczub, 2003a).

The methodology of signal processing for railway axle bearings or other rolling element bearings was studied using different algorithms. In order to come up with the optimum signal

processing methodology, the fundamental properties of the acquired raw data need to be considered (Norton & Karczub, 2003a).

1.2 Statement of problems

The main aim for an effective wheelset CM system is to provide effective predictive maintenance for rolling stock operators and avoid disruption and possible catastrophic derailments. In addition, CM can contribute towards improving RAMS of rolling stock assets whilst protecting railway infrastructure from collateral damage.

Although current CM systems for wheelsets can provide useful information that can be used for reliable operation and maintenance, only severe defects can be detected. In contrast, some already developed flaws could not be detected before the component starts to fail.

The helpful information of wheelsets during the in-service operation was not monitored and analysed, which reduces the efficiency of the maintenance system. Making a more structural focused CM system for wheelsets could help capture the defects in time and reduce the possibility of failure during the operation.

The present research introduces effective sensing techniques and robust signal processing to improve the early detection of wheelset defects. To achieve this, the author used acoustic emission and vibration to capture valuable information and quantify the levels of damages.

1.3 Aims and objectives

As mentioned earlier, derailments caused by wheelset failure were accounted as one of the significant problems which require early identification of failure to mitigate several accidents. However, due to the limitations of quantifying damage in a rolling stock wheelset, most railway networks still operate using old-fashioned monitoring systems. To be precise, there are reasons

including cost of investment, hassle related components and the employment of well-trained staff. As a result, it is challenging for every rail network to deploy adequate CM to eliminate the probability of derailments and service disruption caused by wheelset failures.

This thesis aimed to present an online CM of railway wheelset using the sensing techniques of AE and vibration for reliable and effective online CM of rolling stock wheelsets based on rolling stock and track information from onboard and wayside setups. The outcome and limitations of conventional and existing monitoring techniques are explained, giving an overview of how the railway industry deals with the wheelset maintenance approach. Wayside and onboard schemes are conducted via laboratory experiments and field trials to evaluate their benefits and drawbacks. AE and vibration are working together for the sensing techniques. Nonetheless, one could perform differently in terms of frequency range and parameters involved. Field results were gathered from Long Marston test track using dedicated test wagons. Wayside tests have been placed along with the Chiltern railway network at the Cropredy site. Data collected from all experiments were analysed using a range of signal processing techniques.

After studying and analysing fundamental knowledge of rolling stock wheelset CM, the presented work has been arranged into working procedures to achieve the following objectives:

- Understanding the rolling stock wheelsets, including materials, failures and general information of CM techniques. What are failures of the wheelset?
- Providing the inspection techniques and remote CM for wheelsets. How does each CM determine wheelset condition?
- Introduce the background of AE and vibration techniques. What are principles behind AE and vibration techniques?

- Perform the following experiments: laboratory-based of a motorised trolley with a single wheel, bearing test rig, onboard and wayside CM of wheelset. How to indicate wheelset condition?

- Using several signal analysis techniques to identify and quantify wheelset damages. How does different signal analysis improve wheelset data?

1.4 Thesis Structure

This thesis comprises seven chapters, including the introduction, conclusion and future work. They are listed and described below;

Chapter 1 – Introduction

In the first chapter, a brief description of the present railway system demands and their limitations on operating conditions are presented. RAMS which is the method of how to manage to maintenance is introduced. On top of that, the goal of RAMS is effectively related to an early detection of defects. Some derailment cases across the world which are related to wheelset problems are briefly stated in this chapter.

Chapter 2 - Rolling stock wheelsets, damages and condition monitoring techniques

Wheelset technical specifications and standards are presented as fundamental knowledge along with their materials and different types of damage mechanisms. The literature review on how each component in wheelset develops damage through in-service lifetime also provides an overview of wheelset microstructure. Moreover, various CM techniques for wheelsets are listed and reviewed, as long as track monitoring techniques which can indirectly provide information of the wheelset condition. Subsequently, the readers would understand the procedures and objectives of CM techniques for railway wheelset fault detection.

Chapter 3 - Inspection techniques and Remote condition monitoring for wheelsets

A review of existing NDT techniques is listed and described according to the popularity of the usage in railway systems worldwide. Although most of them are not novel approaches, they have been supporting wheelset inspection till the present. However, we cannot bear with in-depot assessment since railway systems are now operating under many challenging circumstances. As a result, various remote CM for wheelsets used by most of the railway networks are explained.

Chapter 4 - Acoustic Emission, vibration, and signal analysis

The fundamentals of Acoustic Emission and vibration analysis are reviewed and described with their application in CM approaches. Various signal processing techniques which could be used to identify the faults in the wheelset are also presented in this chapter.

Chapter 5 - Laboratory experiments

Laboratory-based experiments are described together with related instrument details. Rolling element test rig and motorised trolley with a single wheel are provided to demonstrate how the methodology of CM concept gain information for further analysis. The healthy and defective wheels and bearings are differentiated both in laboratory-based experiments and field trials. All test results are then analysed and discussed.

Chapter 6 - Field experiments

Onboard and wayside measurements demonstrated AE and vibration data retrieved from Bescot yard, Cropredy and Long Marston and Cropredy sites. The healthy and defective wheels and bearings are differentiated in aforementioned field trials. The data are analysed and discussed.

Chapter 2: Railway rolling stock wheelsets and faults

2.1 Wheelsets technical specification and standards

A wheelset is an integrated rolling stock mechanical system that consists of wheels, axle bearings and an axle. It is in charge of maintaining constant train motion. Wheelsets are attached to the bogie that supports the rolling stock superstructure. The wheelset is the most significant mechanical system of the assembly as it supports the train body's weight and loads. (Krusuansombat, 2018).

Wheelsets have no backup system to operate in the fail-safe mode. Thus, they must be safe, reliable, durable, and capable of operating over prolonged periods of time under challenging conditions. The key design basis for railway wheelsets has been unaltered throughout railway history with the exception of the use of monobloc wheels with better reliability. The entire weight of rolling stock bogie and superstructure is supported by the tapered bearings in the axlebox. The tapered bearings in the axleboxes are directly or through springs coupled to the running gear (The SKF Evolution Team, 2010a).

A trailing wheelset consists of an axle that rotates, two wheels that are attached to the axle through wheel seats cut into the axle, two external axleboxes, and rolling bearings installed on the axle journals. Figure 2-1 shows the wheelset for freight wagons which relies on the tyred wheel design although most freight and passenger rollingstock nowadays uses monobloc wheels. This old-fashioned design was introduced with the traditional tread-based braking system at the beginning of the rolling stock age (Bracciali, 2016a).

Figure 2-1: Wheelsets for rolling stocks (Bracciali, 2016a).

When locomotives were introduced back in the 1800s, wheelsets designs were not controlled by any standards. Various designs depend on their objectives and limitations with a range of usages. Since there are different specifications, each railway system relies on its standard or interoperable standards. A well-known example of the latter is technical specifications for interoperability (TSIs) which consider the provisions of a series of European Union Directives. However, each country might apply individual standards, which shall not neglect interoperability. For example, the United Kingdom has the Rail Safety and Standards Board (RSSB), which helps make the British railway safer and better with their research and standards. RSSB has GMRT2466 and RIS-2766-RST, which conform to several related standards, including Technical Specifications for Interoperability (TSIs), European Standards (EN), British Standard (BS), and International Organization for Standardization (ISO).

The wheel tread is the only part that interfaces with the rail head and comes into contact with the railway network infrastructure. Thus, the wheel tread profile needs to conform to the railhead profile. The principal requirements for wheelsets are distinguished between passenger and freight rolling stock. An example of a modern freight bogie is illustrated in Figure 2-2.

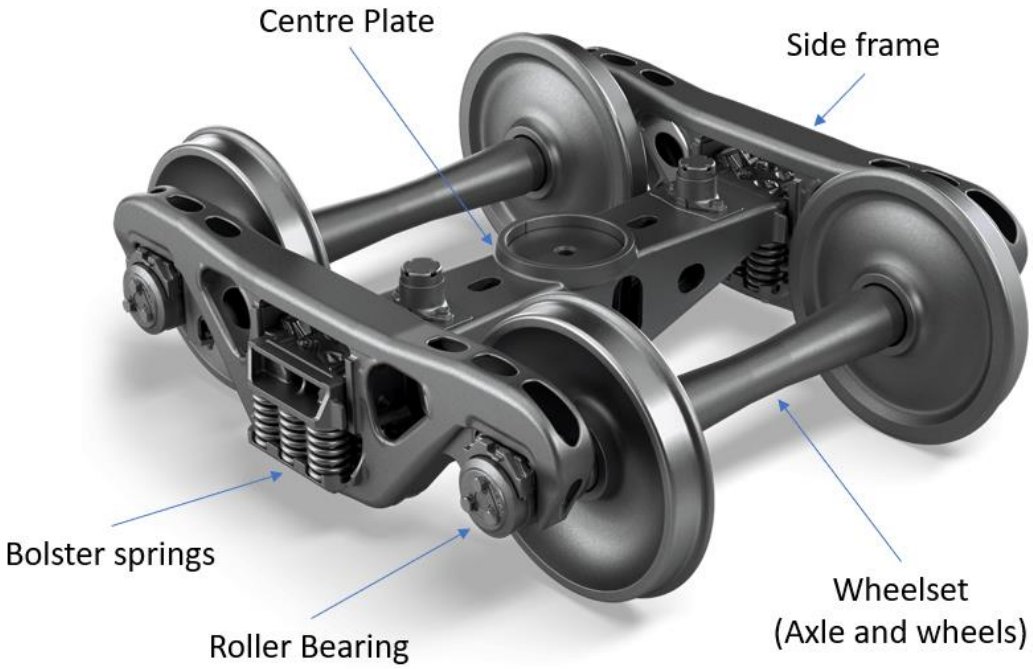

Figure 2-2: Freight bogie frame (Amsted Rail, 2019).

2.1.1 Wheel

In general, the wheel is not a complex structural component in railway rolling stock as it contains much fewer sub-components when compared with other parts. However, the manufacturing and materials used for wheels require a significant knowledge base based on several standards and regulations. Accordingly, it has limited alternative design options.

In general, wheels are classified into two main types by their appearance. A solid or monobloc wheel that is widely used in most railway vehicles and the tyred wheel or combined wheel contains wheel tyre, wheel centre, and Gibson ring. These are the two main railway wheel types. The latter was introduced since replacing a whole wheel was more expensive than reinstalling a steel tyre when the wheel has a worn surface. The tyre is made from a hoop of steel where it is later fitted around the steel wheel centre. Recently, tyred wheels have been mostly used for locomotive and freight wagons which tend to operate at lower speeds and result

in lower maintenance costs for freight wagon owners who operate with very tight margins of profit (Tedrail, 2015b).

The move from tyred wheels to monobloc wheels is nearly complete since the supply chain does depend on market and maintenance constraints. Advanced heat treatments allow the wheel to acquire compressive stresses in the rim that are useful against fatigue fracture propagation. Curved web geometry allows reduced residual stress wheels for tread-braked freight waggons (Bracciali, 2016a).

The structure of a solid wheel is illustrated in Figure 2-**3**, which comprises three main parts: the hub, wheel, and rim. At the bore surface, an axle is placed through the hub part. The web is in the middle between the hub and the rim. The tread and flange area of the rim is the interface between wheel and rail.

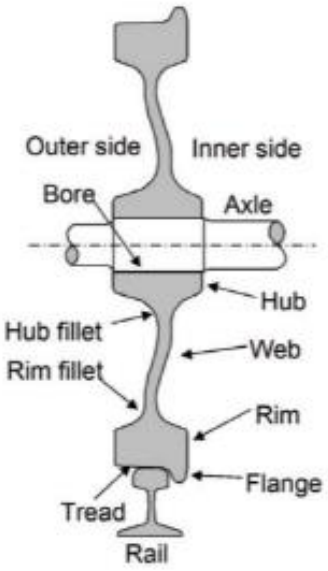

Figure 2-3: Cross-sectional of wheel and descriptions of each part (Okagata, 2013a).

The implementation of TSIs, mandated by a series of European Union Directives, has resulted in the reconsideration of all railway network standards described by Railway Group Standards in the United Kingdom. The primary standards for wheelsets are outlined in the Locomotive and Passenger Rolling Stock Regulations (Rail Safety and Standards Board, 2019).

The wheelset components can be assembled to the axle by shrink-fitting or press-fitting. Shrink-fitting requires the wheel to be heated at a temperature below 250°C. The EN 13260 standard controls interference between the wheel seat and hub (British Standards Institution, 2020a).

The wheel tread profile should conform to the EN 13715 standard, which states that there are three tread profiles of wheels including 1/40th, S1002, and EPS (GB P8) with 28 mm, 30 mm, and 32 mm. flange high, respectively. The standard allows a reverse slope (or a run-out taper) from 6.7 % to 15 %, with a nominal chamfer of 5 mm (British Standards Institution, 2020b). The latest EN 13715 standard was issued in 2020 to help achieve TSIs requirements. Any alternative wheelset design that does not meet the scope of the applicable TSI is required to conform to any European, British, American, or international standards. Where alternative approaches are necessary due to the characteristics of the particular wheelset, they are anticipated to be validated by technical arguments demonstrating that an equivalent standard of integrity with conventional wheelsets is attained (Rail Safety and Standards Board, 2019).

The two different manufacturing technologies, including casting and forging, are applied for railroad wheel production. Casting utilises the liquid of steel into a mould during the forming process, whereas forging uses an ingot of steel to be forged and shaped by the rolling process. In general, cast wheels provide better economic benefits than forged wheels due to their simpler process. However, in terms of properties, cast and forged wheels perform differently, which the latter is better in most mechanical aspects (Getmanova et al., 2017). However, it depends on operating conditions and limitations which would define the selection of those manufacturing types. The different cast and forged wheels standards are applied (Rail Safety and Standards Board, 2019).

Wheel tread profiles must either meet the TSI's conicity standards or comply with National Technical Rules. The wheel/rail interface features, vehicle suspensions, dynamics, and wheel/rail wear and maintenance always impact tread profile selections. The selection of a tread profile is determined by vehicle stability, suspension changes, vehicle load conditions, contact stress levels at the interface between wheel and rail, the profile's tendency to generate RCF, and track circuit actuation (Rail Safety and Standards Board, 2019).

2.1.2 Axle bearing

Rotating machines are generally seen in practically all industries. In every rotating machine, bearings are the most critical parts for proper operation between two related components, i.e., wheel and axle. Thus, bearings are technically required to operate within rotating equipment without failure (Khanam et al., 2014).

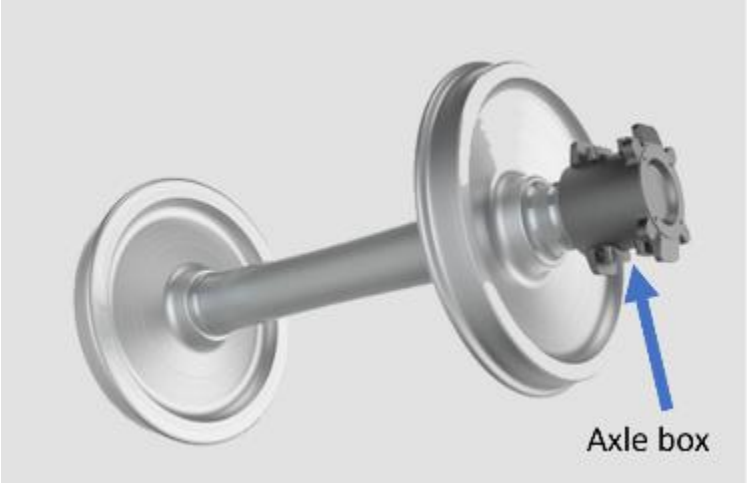

Figure 2-4: Axlebox at the end of the axle (PRC Rail Consulting Ltd., 2019).

As one of the key rotating machine components, a bearing retains the relative movement of two components to a predetermined rotational motion (Daniel et al., 2017). Since bearings are designed to reduce the friction between two rotating parts, they require the highest specification to meet reliability and standards. Therefore, each type of bearings is designed to work specifically for that relative rotating motion of the machine’s components.

Most industrial machinery use roller bearings. Bearings are crucial and critical mechanical components (Tandon & Choudhury, 1999a). Bearings are required to work on several challenging demands, including carrying the load accurately and reliably, whilst satisfying maximum noise levels allowed. Consequently, bearings have been a popular research subject with several improvements having been implemented in recent decades (SKF Group, 2017).

Rolling element bearings technically transmit forces between relative components of the machine. The selection of a proper bearing type and bearing profile relies on frictional resistance, the amount of load to carry, revolution or speed, and the mounting complexity (Jacobs & Plogmann, 2014).

Rolling stock moves along a pair of rails laid to guide the direction through the railway lines. The bearings carry the vehicle's weight and enable the smooth rotation of the wheelset. Axleboxes are designed to secure rolling stock bearings and are placed between the wheelset and the bogie frame. Figure 2-4 illustrates a typical rolling stock wheelset. All static and dynamic forces are supported by the axle bearings (SKF Group, 2011). Accordingly, axle bearings are an essential rotating part of rolling stock that connects the wheels and axle to the stationary parts of the vehicle (Brundisch, 2018).

The improvements in train bearings have been the subject of continuous development in tribological and lubricant research aimed at energy and lubrication savings whilst achieving the highest level of safety (SKF Group, 2011). Choosing the suitable bearings to fit the purpose of each application is key to the smooth operation without the occurrence of failures. In real-world conditions, various mechanisms can result in bearing damage which can eventually result in final failure. The changes in vehicle dynamics and vehicle use can trigger tribological mechanisms that can reduce the bearing operational lifetime (Entezami et al., 2020a). Excessive wear can arise due to high stresses and poor lubrication. Modern rolling stock

employ lubricated tapered roller bearings, instead of plain bearings used in the past that required higher amounts of maintenance and more frequent lubrication (Brundisch, 2018).

Bearing design, lubrication and their safe operation have been the subject of several tribological studies. These have led to the introduction of improved rolling stock bearings with better seals, lubrication, sensors, and rolling elements (The SKF Evolution Team, 2010b).

Oil-lubricated sliding bearings were initially employed in railway rolling stock before introducing grease. At that time, the oil loss during operation greatly damaged the tracks and environment, and inspection was often required to confirm the oil level and replenishment requirements. Therefore, grease has been employed as an alternative to allow bearings to operate maintenance-free. Over decades, the quantity of lubrication required was investigated to reduce costs and materials without further failure risks to the bearings. As a result, it was gradually decreased from 1700 to 700 g for open cylindrical roller bearings. However, another development significantly reduced the quantity to only 200-300 g of grease by launching a sealed cylindrical roller bearing unit (The SKF Evolution Team, 2010b).

Around the beginning of the twentieth century, rolling bearings have been developed to be used in the rail industry. They eventually substituted sliding bearings due to their smaller resistance to rotating motion and lower maintenance requirements. These axlebox bearing units can be designed as either tapered or cylindrical roller bearings. Both systems have distinct benefits and are utilised effectively in a wide range of railway vehicle applications (Bracciali, 2016b; The SKF Evolution Team, 2010b).

Figure 2-5: Tapered roller bearings with sub-components (The SKF Evolution Team, 2017)

Tapered roller bearings are widely used in rolling stock wheelsets (de Los Santos et al., 2017; C. Tarawneh et al., 2019; H. Wang et al., 1996). These comprise two rolling elements holding rings, generally called outer (cup) and inner (cone) rings. Figure 2-5 shows the components of the tapered roller. The main difference between those two rings is the rotation during the operation of the wheelset. The outer ring stands still to withstand the load at the top hemisphere, also known as "loaded zone, " while the bottom hemisphere carries no load, and is described as " unloaded zone. " The inner ring rotates concurrently with the wheel and axle. The press-fit couples it to the axle (de Los Santos et al., 2017; C. Tarawneh et al., 2019).

Tapered rollers are loaded during the operation when their weight is transmitted to the big rib of the inner ring. The rollers keep sliding in contact with the rib and are directed by it. The greater friction coefficient is provided by these bearings when compared with cylindrical bearings. With the help of recent advancements in surface roughness and contact geometry, the friction coefficient has been reduced (NSK, 2010).

The strong advantages of using tapered-roller bearings on freight trains include the almost low-friction rotation and the equally distributed heavy loads carried through the wheelset. Rolling elements or rollers are designed to transfer radial and axial loads across the outer and inner

rings, while the outer ring is attached to the bogie frame (Cuanang et al., 2020; C. Tarawneh et al., 2019).

Radial impact loads caused by rail crossings, switches, wheel flats, and dynamic radial loads caused by vehicle weight significantly affect axle bearings. They may also be subjected to axial stresses caused by lateral movement when trains travel on curved tracks. When all mentioned loads are combined, they create complex combinations, which directly load the axle bearings and can cause damage to initiate and propagate. Moreover, axle bearings must be built to provide simple disassembly and inspection as they are critical to the safety of operation (NSK, 2010).

Roller bearings produce fundamental frequencies when rollers travel over a surface abnormality on either the roller or the raceway. The bearing geometry including pitch and roller diameter, together with the corresponding speed of the two raceways, are responsible for defining fundamental frequencies. (Graney & Starry, 2012). These fundamental frequencies are extensively used for bearing diagnostics, revealed in further chapters.

2.1.3 Axles

Railway axles are essential components of railway rolling stock. Axles give driving torque to the wheels and maintain them aligned with each other and the vehicle body. Railroad axles are classified as freight wagon axles, coach axles, and locomotive axles (Tedrail, 2015a).

A railway axle is a solid beam component of a bogie that contributes the most to its overall design safety, with fatigue strength as the design driver. Some axle transmits driving torque to the wheels, while any axle should maintain wheel position concerning each other and support the vehicle body (Mistry & Johnson, 2020).

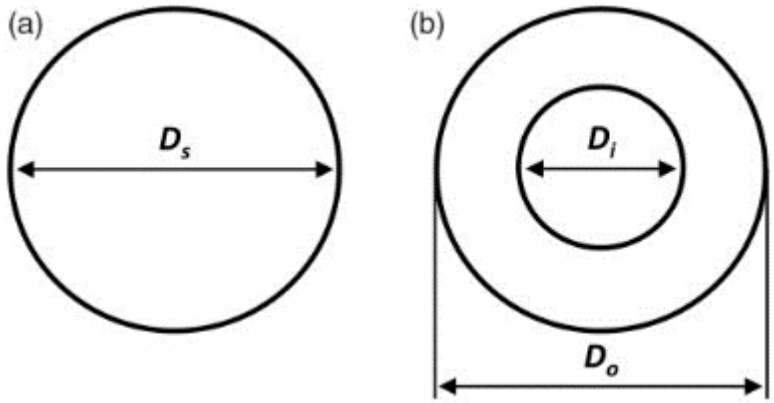

Figure 2-6: Cross-section of (a) solid and (b) hollow axle (Mistry & Johnson, 2020).

The axle is another important component in railway vehicles in terms of safety. However, it does not rely on a fail-safe design and thus, its safety and reliability is paramount for railway operations (Hirakawa et al., 1998).

Railway axles have been built and utilised for almost 200 years. The significantly higher speeds of the past decades bring complexity to the mechanical environment in which they are employed. For example, the derailment caused by a damaged axle can be catastrophic at speeds over 300 km/h (R. A. Smith & Hillmansen, 2004).

Historically, axles were solid at the cross-section. However, over the last thirty years, an increasing number of axles with an axial bore have been created, resulting in so-called hollow axles. This lightweight axle reduces the unsprung mass of rolling stock since the axle is lighter due to the lower amount of material used. As a result, the bending stress is also reduced. On top of that, the hollow axle allows more space for monitoring sensors to be placed inside, where the solid axle can only do after removing the axlebox (Bracciali, 2016b; Mistry & Johnson, 2020; R. A. Smith & Hillmansen, 2004). The comparison between two cross-sections of two different types of axles is displayed in Figure 2-6.

This complex designed wheelset comprised of inboard bearing journals and a hollowed-out axle requires careful inspection when assessing its sensitivity to fatigue (Hillmansen & Smith,

2004). The minimum fatigue limits for wheelset axles are different for both axle types. Since there is an axle bore effect on stress distribution (British Standards Institution, 2020a).

The European standards EN13103 for non-powered axles and EN13104 for powered axles explain how axles should be manufactured. In recent years, European regulations have mirrored rising rail car speed and safety needs. These standards define material utilised, how it was made, and service safety practises (Novosad et al., 2010).

Generally, modern axles are highly stressed safety-critical components that can be expensive in service due to the unreliability of practical techniques of crack detection and size, as well as a lack of relevant data to inform rational inspection intervals. As a result, there has been significant developments of small electronic devices used for service load monitoring in recent years. The key objective is to measure and quantify the actual loads subjected to railway axles (R. A. Smith & Hillmansen, 2004).

2.2 Metallurgy of wheelset components

2.2.1 Wheel material

Since the wheel is the most likely part of the wheelset to be worn out, the materials it is made of should be able to withstand wear and fatigue. During the operation, the wheel is rolling under normal and lateral loads, introducing high shear and contact stresses on the surface and the sub-surface structure. In addition, wheel slips in the contact patch could occur during operation. As a result, the thermomechanical loading needs to be taken into account. Thermomechanical and RCF and impact loads can lead to initiation and propagation of damage to both wheel and rail surfaces (Mädler & Bannasch, 2006). Generally, railway wheels are manufactured of steel grades with medium to high carbon levels, depending on the type of rolling stock on which they will be used.

For example, the AAR M-107 standard contains five-wheel classes, including Class L, A, B, C, and D, whose carbon content ranges from 0.47-0.77 in wt %. While the European standard, EN 13262, classifies the wheel materials into four classes (ER6, ER7, ER8, and ER9), with medium carbon content in the range of0.48 and 0.60 in wt % (Nikas, 2016; Okagata, 2013b). Table 2-1 summarises the steel grades carbon content and applicable hardness as per different standards used in Europe, North America and Japan respectively.

Table 2-1: Materials for wheels according to each standard.

Region	Specification	Steel grade	Carbon content (%)	Hardness HB
Europe	EN 13262 / UIC 812-3	ER6 / R6T	≦ 0.48	234-270 *
		ER7 / R7T	≦ 0.52	247-282*
		ER8 / R8T	≦ 0.56	258-296*
		ER9 / R9T	≦ 0.60	300-350*
North America	AAR M-107/M-208	Class L	≦ 0.47	197-277
		Class A	0.47-0.57	255-321
		Class B	0.57-0.67	302-341
		Class C	0.67-0.77	321-363
		Class D		341-415
Japan	JIS E 5402-1	SSW-QS	0.60-0.75	246-307
		SSW-QR		311-363
		SSW-QRH		295-347

Increasing hardness is an effective approach in reducing wear, however, this leads to increased considerations for RCF damage accumulation with operational time. The process involves adding alloying elements to the steel grade employed (most notably manganese and vanadium) and heat treatment, resulting in increased wear resistance and improved RCF resistance. Many engineers prefer to maximize rail life at the cost of wheel life (Nikas, 2016). However, the stronger rail may increase wheel deformation and accelerate the corrosion of wheel steel. To improve the safety and efficiency of high-speed trains, it is important to make the rails stronger and match the hardness of the steels in the rails and wheels (Shi et al., 2019).

The performance indicators for railway wheels include hardness, yield, and tensile strength. RCF damage is connected to yield stress and wear resistance to material hardness (Soares et al., 2016).

The mechanisms of wheel damage make necessary that wheel materials exhibit high resistance to wear. The steels employed typically have pearlitic structures which results in higher hardness. Pearlitic rails generally perform better than harder bainitic and martensitic rails even though they have lower hardness (Mädler & Bannasch, 2006).

The wheel material composition, manufacturing process used, and final microstructure determines the wear and RCF resistance for a particular range of dynamic loads. The wheel's damage mechanisms vary with tread depth and location. According to simulations by (Molyneux-Berry et al., 2014), The stress history at the wheel-rail contact affects hardness and microstructure. Increased wheel hardness can cause microstructural changes. At the surface level, the plastic flow and microstructural shear in conjunction with substantial radial stresses as a result of cursing, generating higher hardness.

Studies on the degradation of wheel and rail materials has seen extensive application of the twin-disc wear testing method (Lewis et al., 2010; Lewisa & Dwyer-Joyce, 2004). The study which compares R7T and R8T indicated that the latter provides better wear resistance without adding the wear rate of the wheel material (Lewisa & Dwyer-Joyce, 2004). Furthermore, according to the same wear testing method, R8T also performs better contact conditions than R7T during the transition to catastrophic wear levels (Lewis et al., 2010).

2.2.2 Axle bearings

The materials used for manufacturing the bearing components have significant effect on the performance and reliability of rolling bearings. Typical key parameters for the performance of the bearing rings and rolling elements include:

- Hardness and load bearing carrying capacity.
- Fatigue resistance under rolling contact circumstances.
- Cleanliness of the lubrication conditions.
- The dimensional accuracy of the components.

In comparison, other related factors for the cage include friction, strain, fictitious forces, chemical effects by lubrication, and other solutions used for the operation. In addition, the overall mitigation of roller bearings could be affected by corrosion, sudden loads, and elevated temperature. The tapered roller bearing, often used in railway rolling stock, comprises three basic elements: rollers, inner rings, and an outer ring. All elements are depicted in Figure 2-7.

Furthermore, the performance and reliability of rolling bearings can be degraded by the poor design of contact seals. Those integrated seals require the use of materials that provide strong resistance to oxidation, heat, and chemical substances. SKF suggested various materials for bearing rings, rolling components, cages, and seals to satisfy the demands of varied applications. In addition, specific coatings are recommended where adequate lubrication cannot be achieved or where an electric current flowing through the bearings must be avoided.

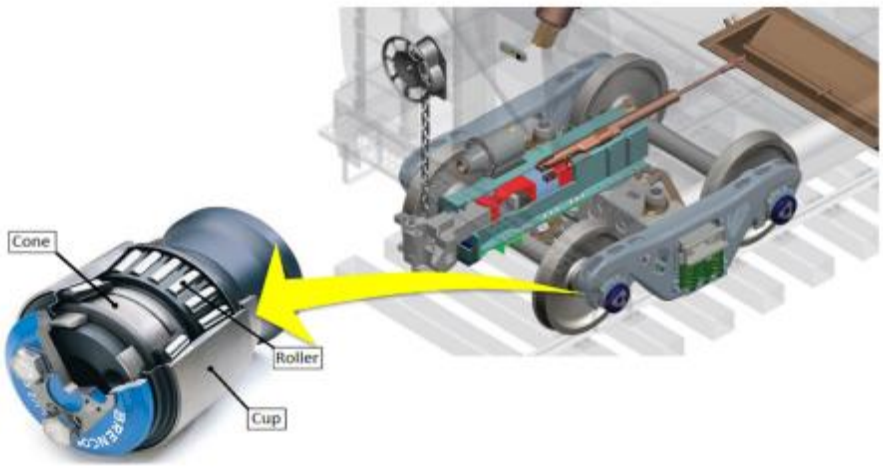

Figure 2-7: Tapered roller bearing applied for freight bogie (C. Tarawneh et al., 2021).

Rolling element bearing materials may be broken down into two primary types, according to industry standards: through-hardened and case-hardened materials. The first type is mostly used for ball bearings, while the latter is extensively used for roller bearings (NTN, 2020; SKF USA, 2018). However, induction-hardened steel is alternatively used for the raceway to reduce the effect of RCF while leaving the rest of the component untreated in order to retain structural strength and toughness (SKF USA, 2018).

A minimum hardness of 58 HRC is generally accepted for bearing components. Because of the lower hardness, the races are allowed to Brinell. Common bearing steels, such as 440C and SAE 52100, should not be used over 177 °C due to the hardness decrease with increasing temperature (Machine design, 2002).

In an effort to create steels appropriate for high-temperature bearings, through-hardened materials have attracted a significant level of interest. Hardness at high temperatures is achieved by using alloys containing varying quantities of molybdenum, tungsten, chromium, vanadium, aluminium, and silicon.

The main standard material for ball bearings is SAE 52100 steel, which is a high-carbon chromium steel grade with small additions of manganese and silicon. It is a hard and wear-resistant steel alloy (Machine design, 2002).

The main advantages of SAE 52100 include excellent hardness at 60-67 HRC and working at temperatures up to 120 °C. In addition, ball bearings and roller bearings which require high precision could also be made from this material (Otai Special Steel, 2021).

According to ISO 683-17:1998, the most common through-hardened bearing steel is carbon chromium steel, with typically 1 wt % C and 1.5 in wt % Cr. Carbon-chromium steel is one of the earliest and most widely investigated steel grades, owing to the ever-increasing demand for longer bearing service life. This rolling bearing steel's composition achieves the best possible

balance between production and application performance. This steel is often subjected to a martensitic or bainitic heat treatment, during which it is hardened to 58 to 65 HRC (SKF Group, 2018).

SKF has improved the cleanliness of the steel grades used for manufacturing bearing. Oxygen and non-metallic inclusions have been reduced in order to achieve better performance and longer operational lifetime (SKF Group, 2018).

Standard 100Cr6 describes the characteristics and special features of through-hardening rolling bearing steel. A higher-grade alloy would be preferable regarding the wall thickness of the components when considering the hardenability (Schaeffler Technologies, 2019).

Case-hardened materials or carburized materials are classified by the surface's thickness (more than 0.015 inches thick). The surface hardness of these materials varies from HRC 58 to 63 at room temperature, while the core hardness runs from 25 to 48 HRC. However, they are limited to a working temperature of less than 177 °C.

Case-hardening materials may have an advantage over through-hardening steels in situations involving high shock loads and severe vibrational stresses due to their soft, ductile inner core (Machine design, 2002; Schaeffler Technologies, 2019; SKF Group, 2018).

For increased ductility and toughness, steel can be carburised, or case hardened from the surface to the desired depth. In addition, case hardening increases hardness and toughness to the material's surface, making it appropriate for impact loads and more wear resistant. JIS SCM420 has a chemical composition approximately identical to AISI, SAE standard 4118, and German DIN standard 20CrMo4 or 25CrMo4. SKF and NTN claimed they use case hardened steel for roller bearings, specially tapered roller bearings commonly used in the railway wheelset (NTN, 2020; SKF Group, 2018).

JIS SUJ2 has a chemical composition approximately identical to AISI, SAE standard 52100, Europe DIN standard 100Cr6, and Chinese standard GCr15.

While the SUJ2 is commonly used, SUJ3 with increased hardening properties and a higher Mn content for large bearings is further developed for specific works. Finally, SUJ5 is SUJ3 with Mo added to improve hardening properties. It is utilised for oversized bearings or bearings with thick walls. Examples of the chemical composition of different bearing steel grades are summarised in Table 2-2.

Table 2-2: Chemical composition of widely used bearing steel as referring to different standards.

Standard	Grade	C	Mn	P	S	Si	Ni	Cr	Cu	Mo
ASTM A295	**SAE 52100**	0.93-1.05	0.25-0.45	0.025	0.015	0.15-0.35	0.25	1.35-1.60	0.3	0.1
DIN 17230	**100Cr6/1.3505**	0.90-1.05	0.25-0.45	0.03	0.025	0.15-0.35	0.3	1.35-1.65	0.3	–
JIS G4805	**SUJ2**	0.95-1.10	0.5	0.025	0.025	0.15-0.35	–	1.30-1.60	–	–
BS 970	**535A99/EN31**	0.95-1.10	0.40-0.70	–	–	0.10-0.35	–	1.20-1.60	–	–

Surface induction-hardening is used to selectively harden a component's raceway to limit RCF, leaving the remainder of the component unaffected to maintain structural strength (SKF Group, 2018).

Since vacuum-melted steels have a lower inclusion content than air-melted steels, they are more reliable and have a greater basic dynamic load rating. However, in terms of the cleanliness, no matter how far it has been improved, it is not always the case that the bearing life will also be extended. Generally, highly clean steels still include non-metallic inclusions, which can eventually lead to the initiation of fatigue cracks (Machine design, 2002; NTN, 2020).

Induction vacuum melting involves a cold charge being melted in an induction furnace and then poured into ingots under vacuum conditions. The disadvantages of this method include its high cost and fluctuations in quality due to refractory issues (machine design). In addition, induction hardening is generally applied to bearing raceway surfaces, thus, preferred over through hardening steel due to its reduced carbon content (NTN, 2020).

Consumable-electrode vacuum melting is a superior method of producing bearing steels. The product makes a more consistent high-quality steel than the induction-melting approach and provides various solidification conditions (Machine design, 2002; NTN, 2020).

Standard high-temperature bearings make use of silicon in the steel alloy to increase heat resistance at temperatures ranging from 150°C to 200°C. This means the bearing has an extended rolling fatigue life and is resistant to thermal expansion without any deformations. Bearings also make use of heat-resistant steels, which prevents melting and deformation even when subjected to high temperatures. High-speed molybdenum steel and high-speed tungsten steel are two steel grades commonly used (NTN, 2020).

A minor quantity of austenite can be found in the hard martensite matrix of conventional bearing steel microstructure. It is called retained austenite because there is no conversion into full martensite throughout the cooling step of the bearing steel quenching process. Instead, it transforms into a stable structure (martensite) due to application of stress resulting in dimensional change (NTN, 2020).

2.2.3 Axle material

European standards comprising EN 13261 Axles-product requirements and EN 13260 Wheelsets-product requirements define steel grades, mechanical properties, and fatigue properties.

European rail axles are manufactured by open die forging or rolling vacuum-degassed steel grades EA1N and EA4T. The surfaces are then machined for a concentric and balanced axle. Steel 30CrNiMo6, in accordance with DIN 10083 standard or comparable steels, are used for specific purposes such as high-speed trains (Novosad et al., 2010).

While EA1N is normalised carbon steel designed for general purposes, EA4T can provide better performance as it is a quenched and tempered low alloyed steel. The requirements in terms of the properties exhibited by these steel grades have been determined with reference to axle design set specifications. 30NiCrMoV12 steel is the high-strength steel that many high-speed and tilting trains in Italy utilise for railway axle manufacturing. Because of its mechanical properties and characteristics, unsprung mass and axle sizes can be reduced (Mancini et al., 2006).

The EN 14261: March2009 standard defines the fatigue limit of utilised steel grades, emphasizing the notch sensitivity coefficient q, which is required for calculating the safety parameter. Grade EA1N is widely used for non-powered railway axles with lower fatigue limit than EA4T. Table 2-3 summarises the chemical composition of axle material specified by different standards.

The first Japanese Shinkansen high-speed train applied major improvements in railway axle technology in 1964. Induction hardening is one of the methods used after the axle has been forged and finished to improve mechanical properties and performance. In this way, better axle fatigue strength and hardness combination can be achieved. The Shinkansen axle is made of 0.38 in wt % carbon as specified in S38C Japanese standard (Hirakawa et al., 1998).

Table 2-3: Chemical composition of axle material as referring to different standards (Mancini et al., 2006; Novosad et al., 2010; Tedrail, 2015a).

STANDARD	MATERIAL	CHEMICAL COMPOSITION									
		C	Mn	Si	P	S	Cr	Ni	Mo	Cu	V
EN13261	EA1N	≤0.40	≤ 1.20	≤ 0.50	≤0.02	≤0.02	≤0.30	≤0.30	≤ 0.08	≤ 0.30	≤ 0.06
	EA1T										
	EA4T	0.22-0.29	0.50-0.80	0.15-0.40	≤0.02	≤0.015	0.90-1.20	≤0.30	0.15-0.30	≤ 0.30	≤ 0.06
UIC811-1	A1(N)	≤0.37	≤ 1.12	≤ 0.46	≤0.04	≤0.04	≤0.30	≤0.30	≤ 0.05	≤ 0.30	≤ 0.05
	A1(T)										
	A2(T)	0.17-0.27	1-1.4	≤ 0.40	≤0.025	≤0.03	0.20-0.70	≤0.30	≤ 0.15	≤ 0.25	0.05-0.15
	A3N)	0.42-0.50	0.50-0.80	0.15-0.40	≤0.035	≤0.035	≤0.30	≤0.30	≤ 0.08	≤ 0.30	≤ 0.05
	A3(T)										
	A4(T)	0.22-0.29	0.50-0.80	0.15-0.40	≤0.035	≤0.035	0.90-1.20	≤0.30	0.15-0.30	≤ 0.30	≤ 0.05
	A5(T)	≤0.45	≤0.90	≤ 0.40	≤0.035	≤0.035	≤1.20	≤0.30	≤ 0.30	≤ 0.30	≤ 0.10
AAR M-101	Grade F	0.45-0.59	0.7-1	0.15-0.4	≤0.045	≤0.05	-	-	-	-	0.02-0.08
TB/T 2945	LZ50	0.47-0.57	0.6-0.9	0.17-0.40	≤ 0.03	≤ 0.03	≤ 0.30	≤0.30	-	≤ 0.25	-
JIS E 4502-1	SFA60A	-	-	-	≤0.035	≤0.04	-	-	-	-	-
JIS E 4502-1	SFA60B	-	-	-	≤0.045	≤0.045	-	-	-	-	-

The axle weight is one of the critical concerns when building a high-speed railway. Lightweight axles have been based on hollow axle designs. However, that could be further improved by using advanced composite materials for the hollow axle. The benefits of reducing axle weight also expand to reducing unsprung mass leading to lower loads. In addition, the lighter system would generally be more friendly to the wheel-rail interface. The result contributes to less track and infrastructure damage (Mistry & Johnson, 2020).

2.3 Wheelset damage

2.3.1 Wheel damage

Wheels on trains easily break or wear out. Increases in axle loads and running speeds lead to more severe damage accumulation. Wheels must be turned after a specific mileage has been covered in service to remove flaws and return them to the appropriate profile. The wheels must

be replaced after multiple repetitions of turning once their diameter has reached the minimum length permitted. Wheel maintenance maintains the safety of railway operation and reduces the effects of RCF. However, it also reduces the lifetime of wheels (Zhu et al., 2019).

The evolution of wheel tread damage from the study of wheelset monitoring using four strain gauges attached to the axle, as shown in Figure 2-8, illustrates the development of RCF clusters which are out-of-roundness wheel damages during almost half a year from left to right. Figure 2-8 (a) shows some minor cracks on the side of the wheel tread. Figure 2-8 (b) depicts the formation of the growth of RCF flaws on the tread between January and March. Lastly, Figure 2-8 (c) shows how some RCF clusters growing into bigger defects in May 2019. The data obtained from the measurements of out-of-roundness wheels were used as input in simulations to evaluate contact forces between wheel and rail and bending stresses. In addition, the evolution of RCF damage in wheels was investigated (Maglio et al., 2022).

Figure 2-8: The progression of wheel tread damage of wheel over five months, taken in (a) January (b) March, and (c) May 2019 (Maglio et al., 2022).

The contact patch between the wheel and the rail is generally 1 cm2 in size, but it varies as the track section changes along the curve. Hertzian analysis is employed for calculating wheel-rail contact geometry and stress. Contact mechanics describes how the elastic-plastic deformation affects the wheel-rail interface with different contact stress levels. Traction forces at the wheel-rail interface result in increased contact stresses due to the rolling and sliding motion of a wheel. Accordingly, the formation of plastically deformed zone is caused under the surface, where RCF may initiate and propagate subsequently.

Depending on their properties, environmental conditions, and compositions, different steel grades can exhibit different wear patterns. Some particular examples include friction modifiers and enhancers, including sands and leaves at the wheel-rail contact. There are two types of wheel-rail interaction that are of interest: sliding and rolling (Lewis & Olofsson, 2009a).

Surface and subsurface failures are the two types of rail and wheel fatigue failures. Surface-initiated fatigue, which occurs in both rails and wheels, is induced by the plastic flow. The plastic flow will develop cracks due to the surface material's ratcheting and/or low-cycle fatigue. When cracks started, they usually grew to a depth of 5 mm or less in the wheel material. The final fracture is introduced as the fractures grow on the wheel tread. (Lewis & Olofsson, 2009a).

As increasing operational speed is now spreading over the modern railways, care must be taken to guarantee the safety and dependability of different subsystems and elements of rolling stock. Rail wheels are essential parts. Residual stress in the wheels occurs as a consequence of thermal load during braking. Braking-induced residual stress as a result of the test condition's heat load is one of the major challenges. If feasible, it is preferable in traffic to create less residual stresses and decrease remaining residual tensions in the wheels (Strážovec et al., 2019).

The wheel failure modes could be classified into several categories; however, not all are present at the same probability. The analysis of wheel failure modes was conducted to estimate the probabilistic models for each major failure mode, including wheel flat, loosened tyre, scaled wheel, and tyre wear (Spiroiu & Nicolescu, 2018).

2.3.1.1 Wheel flat

Unintentional sliding on the rail causes a railway wheel flat. The sliding and sudden cooling when the wheel begins rolling might develop brittle martensite around the flat.(Jergéus, 1998).

During the braking operation, railway wheels could get stuck and eventually perform sliding rather than rolling on the rail. At this point, wheel flats can possibly be generated which consequently produce the biggest and most prevalent dynamic stresses on tracks. The excessively high impact loading on the track caused by wheel flats defined by the defect's size and form, axle weight, and train speed (Remennikov & Kaewunruen, 2008).

It is well-known as the most typical local surface damage. Wheel flats result into wheel-rail impact and cause vibration throughout the entire vehicle-track system (Y. Li et al., 2016). Due to the excessive impact loads arising, wheel flats can be precursors of damage in rails as well as axle bearings.

With reference to the full-scale field study of creating wheel flats by (Jergéus et al., 1999), a numerical model which is able to predict the wheel flat development was introduced. The model was based on wheel flat samples which have been metallographically analysed. The effect of distributions of martensite and heat-affected material was determined. The results showed that the flat growth rate is strong at the beginning of sliding but slows as sliding continues. Cracks were detected in the martensite to develop into the safe zone of material below the martensite.

If a wheel flat is identified early, when both size and severity are modest, turning the wheel can remove it. However, minor wheel flats can generate a significant impact even if the rail vehicle moves slowly (Iwnicki, 2006).

The wheel slips along the rail, which might be caused by a defective, frozen, or poorly maintained brake or by weather (rain, snow, leaves, etc.) (Brizuela et al., 2011a).

The dynamic impact load, which depends on factors like the width of the wheel flat and the speed of the train, is much greater than the static load (R. Gao et al., 2019).

A numerical analysis describes how wheel flats affect the dynamic behaviour of the ballasted and concrete slab track. Their results revealed that the presence of a wheel flat with a 2mm depth based on the vehicle speed of more than 25 km/h would introduce a disconnection between the wheel and the rail (Vale, 2021).

Wheel flats are generally classified into two types considering their profile and the time when they are stimulated. The first type is the recently formed wheel flat, which produces sharp edges at the time of flat creation. While the second type, which is called the rounded wheel flat, immediately develops from the first one as a consequence of wear and plastic deformation.

The maximum impact force is substantially determined by the depth of the wheel flat, as is the occurrence of loss of contact. Maximum impact forces also vary significantly between recently produced and rounded wheel flats. (Pieringer et al., 2014).

As wheel flats generate impact loads, the rail could be damaged or even broken by a critical head check crack. The study on the influence of flattened wheels with various temperatures, wheel flat lengths, and crack sizes on risks for rail breaks is presented by (Sandström & Ekberg, 2009).

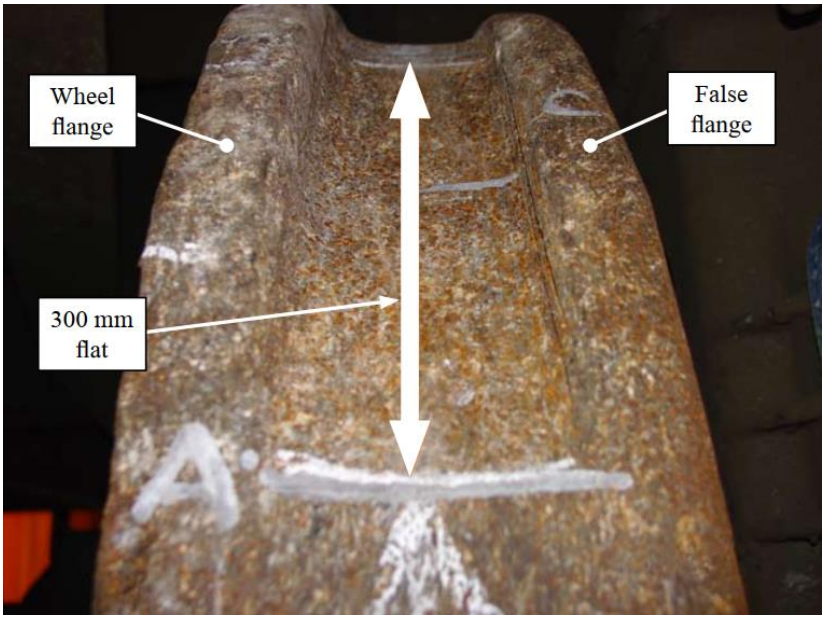

Figure 2-9: Wheel flat and false flange on the right leading wheel of freight wagon (Rail Accident Investigation Branch, 2006).

An example of freight train derailments caused by wheel flats occurred on 18 October 2005 at Hatherley Near Cheltenham Spa, United Kingdom. The Rail Accident Investigation Branch report revealed that the wheel flat was caused by the immediately applied handbrake. The large flat measured 300 mm in length and deep false flanges on the leading wheelset of the freight wagon are displayed in Figure 2-9.

2.3.1.2 Cracks

Rolling contact or thermomechanical fatigue are the most common causes of cracks in a wheel. Several rolling stocks classes, particularly freight trains, have brake blocks designed to generate a lot of friction to stop the train in place.

However, the temperature will naturally rise according to friction during the braking process, and high-stress levels will be present. Thermomechanical fatigue, high stresses and extreme temperature can generate the propagation of fractures on the wheel tread surface. Manufacturing issues cause most cracks that arise in the wheel's mass in the microstructure of

the steel applied for the wheels. Hydrogen molecules form microstructure holes. These pores function as stress raisers, allowing fractures to grow and spread swiftly before breaking (Amini, 2016).

2.3.1.3 Shelling

Micro-cracks, which are caused by high strains in the wheel/rail interface area due to high axle loads and creep forces, are a major contributor to wheel shelling (Dukkipati & Dong, 1999a). Wheel shelling is a piece of wheel tread that generally be larger than 5 mm in size. Shelling cracks often form at a sharp angle to the surface (Moyar & Stone, 1991).

2.3.1.4 Spalling

Researchers claim that increased train speed promotes spalling because it causes wheel and rail wear and RCF (W. Wang et al., 2013; Zakharov & Goryacheva, 2005). Contact stress, thermal stress, axle load, friction, and material of wheel and rail are all related to the occurrence of wheel spalling (W. J. Wang et al., 2008).

When a wheel slides on the rail while braking, this is a thermomechanical problem. Large amounts of frictional energy are created instantly, allowing the temperature of the wheel surface to extend over the austenization limit. After heating by the wheel slide is generated, rapid cooling is introduced and initiates the development of martensite, which fractures further during wheel/rail loading cycles (Zakharov & Goryacheva, 2005).

2.3.1.5 False Flange

In general, false flanges coincidently occur with wheel flats as the wheelset is sliding along the track under lowered adhesion conditions. When the leading wheelset started to slide, generating the wheel flats. During the train's journey, the wheel treads are starting to have wear on the

flange area and causing damages on the outside edges called ‘false flange.’ (Rail Accident Investigation Branch, 2019b).

2.3.1.6 Periodic wheel defects

Railway wheels become non-circular or develop the growth of out-of-round due to wear, and periodic wear patterns appear on their circumferences; this is called polygonisation (Meywerk, 1999). Torsional vibrations of wheelset axles and lateral dynamic vibrations of the complete wheelset create creepages that cause corrugation wheel wear (Brommundt, 1997).

Polygonal or corrugated wear could be spotted on the wheels of locomotives, freight trains, metro trains, and high-speed trains (Tao et al., 2020).

The two most common periodic wheel flaws are wheel polygonisation and wheel corrugation. Wheel polygonisation, in general, has a periodic irregularity around the circumference situated on a constant wheel radius. The main difference between polygonisation and corrugation is the irregularity's wavelength and amplitude. The wavelength of the polygonisation varies from 14 cm to the diameter of one wheel, and the amplitude is around 1 mm. Wheel corrugation is more common on block-braked wheelsets. This flaw has a 30–60 mm wavelength and an amplitude of fewer than 10 microns (Nielsen & Johansson, 2000a).

Publications categorise the evolution of wheel polygonisation or corrugation into three fields: (1) initial wheel defects, (2) natural vibration of the vehicle–track system, and (3) thermoelastic instability (Tao et al., 2020). Corrugation and polygonalization create high-frequency wheel-rail contact forces, vibrations, and noise (Nielsen et al., 2003).

2.3.2 Axle bearing damage

Many studies concluded that the damage on bearings for any rotating machines is important since they can result in downtime and failure. Axle bearings are the most critical component in

rolling stock (H. Wang et al., 1996). Some aspects of freight trains were described as why axle bearings are generally easily damaged. Due to the large weight and high speeds of railcars, bearing failure can cause journal burn-off (Cuanang et al., 2020). Apparently, the cost of damage could result in millions of dollars, as referred to (H. Wang et al., 1996). At the operational speed, which may vary depending on the service, the higher speed is generally known to push axle bearings to the limit and make them the most subjective to severe failure leading to hot axle problems (Cuanang et al., 2020).

The quantity of vibration and noise produced by bearings is consistent, regardless of the presence or absence of a problem. Faults cause significant vibration and noise changes. Therefore, a system that can detect bearing defects early is necessary (Amini, 2016).

There are several mechanisms of bearing failure that occur during bearing operation. The most likely is wear, caused by the loss of a lubricant film between the rolling components and raceways (Gohar, 2001). In the existence of holes and cavities under contacting surfaces, subsurface stresses can cause inelastic surface deformation (excess stresses/fatigue spalling). (H. Liu et al., 2019). Usually, modest surface wear from fatigue causes fracture and cracking on bearings (Amini, 2016).

Changes in the carbon content of steel will result in microstructure changes and potentially affect the mechanical properties. High carbon concentration correlates with high hardness, strength, and abrasion resistance. On the other hand, high carbon content is correlated with poor plasticity and toughness. The study on microstructural and microhardness concluded that the microporosity and pores underneath the subsurface region are the main causes of crack initiation and propagation. Roller misalignment concentrates tension on the tiny end of the roller, which suffers extra damage as a result. Crack growth mode is stimulated because of the

changes in fracture angle, which finally causes the roller to suffer different levels of fatigue damage (Guo et al., 2018).

Rolling element axle bearings affect the dynamic behaviour of wheelsets and cause vibration and noise in rolling stock subsystems. In addition, bearing defects can occur during usage or manufacturing (Rafsanjani et al., 2009).

There are several types of axle bearing failure modes classified by root causes as referred to the report by (SKF Group, 2012), which include;

- Wear: Two different types of wear include abrasive and adhesive wear. Variations in the speeds of the contact surface are the cause of wear. Differences in speeds can be caused by a number of factors, including kinematic slip, acceleration, and deceleration. Abrasive wear is caused by lubricating abrasives. These might be external or internal contaminants. Abrasive wear typically results in dull surfaces. Surface adhesive wear often occurs, resulting in rolling element slipping (SKF Group, 2012).

- Fatigue failure: Fatigue is always one of the roots of many component failures, which for rolling element bearing is especially called “Rolling Contact Fatigue (RCF).” Contact fatigue at the surface is made prone to contact Hertzian contact stresses (Jacobs & Plogmann, 2014). The bearing's rolling and sliding operations are combined and generate these stresses. Contact fatigue will expand in microstructural relocation, which then causes changes in maintained austenite, residual stress, and morphology of martensite. Finally, contact fatigue stimulates crack initiation and crack propagation (Grabulov, 2010). Even in fairly well-lubricated rolling bearings (with a substantial lubrication coating), RCF still develops. Eventually, RCF could differ from abrasive and adhesive wear. Otherwise, RCF can just be presented by degraded lubrication conditions. RCF is eventually represented by metallic particles breaking off the surface of the raceways or rolling components (Jacobs & Plogmann,

2014). Figure 2-10 illustrates (a) wear changed the contour of the raceway (b) fatigue damage of bearing rollers and (c) surface-initiated spalls in roller bearings.

Fatigue failure can also be classified into subsurface initiated fatigue and surface-initiated fatigue (Upadhyay et al., 2013). The first involves local plastic deformation, which causes fundamental fatigue. Structural changes occur, leading to some strain localisation (Olver, 2005). In contrast, the second has resulted from the inadequate lubrication properties, i.e., contamination and low viscosity. The contamination at the lubrication way as a direct result of ceramic or metallic particles produces markings on the raceway. It makes a microspall that initially becomes a shiny surface but breaks up the surface.

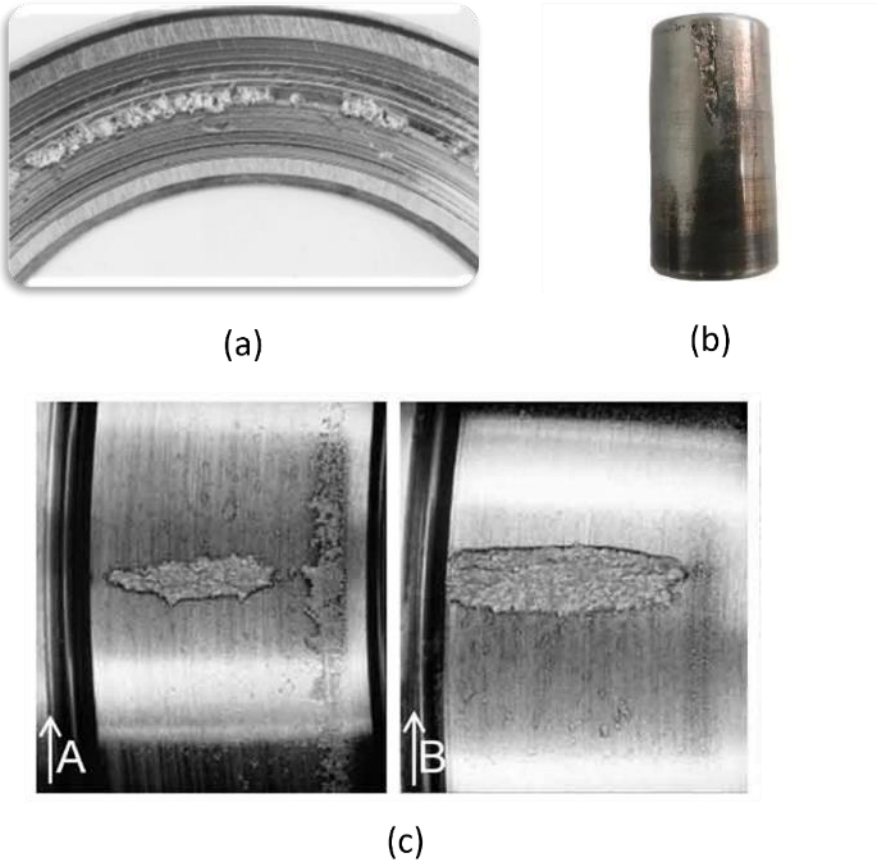

Figure 2-10: Bearing defects: (a) Wear changed the contour of the raceway (b) Fatigue damage of bearing rollers (c) Surface-initiated spalls in roller bearings (SKF Group, 2012).

• Corrosion: Tribological failures are generally related to lubricant's chemical composition (Jacobs & Plogmann, 2014). For instance, some bearing components are damaged because of lubricant degradation caused by corrosion. Therefore, maintenance prevents failure against tribological failures from failing is always better than periodic inspection (Scott, 1973). A tribological contact model predicts higher near-surface sliding friction. RCF effectively causes grey discoloration (Gegner, 2011).

(SKF Group, 2012) classified corrosion damage of bearings into two types: moisture corrosion and fretting corrosion. According to its name, moisture corrosion is caused by corrosive substances and high humidity. The effect of moisture corrosion quickly damages bearings. While fretting corrosion is caused by small but mighty movements between two surfaces subjected to cyclic loads during the operation. The poor fitting of the housing area between the bearing bore and shaft could cause a gap where some air can access through unsealed surfaces, and corrosion can now start to progress. The study from (Engineering Manager Schaeffler UK, 2008) revealed the result of black erosion, which was developed after water penetrates the bearings when they are stored. A number of the rollers also developed black corrosion marks, which corresponded to the vibration at the cage rotational frequency. There is corrosion-resistant bearing steel that can deal with the corrosion from moisture and other sources. Key parameters of the bearing chemical substances include carbon content and chromium content. To archive the high wear and fatigue resistance, both carbon and chromium content are added (Jacobs & Plogmann, 2014).

• Excessive load: One of the improper usage conditions harms axle bearings. Rolling element bearings that are radially loaded and geometrically accurate are still capable of producing vibration. The excessive load could be caused by a faulty installation which contributes to either radial or axial directions (S. Kulkarni & Wadkar, 2012).

• Misalignment: Another severe operating condition studied in high-speed roller bearings is misalignment. It was revealed that misalignment could cause the sudden failure of the roller bearings when it exceeds a critical point (Savaskan & Veinot, 1987). An example's numerical results from (Andréason, 1973) show that even little misalignment considerably impacts load distribution, resulting in lower bearing rated life. The load distribution on tapered roller bearings is essential to bearing life. It is possible that the bearing's life will be shortened as a result of poor load distribution by misalignment. Misalignment is caused by unequal weight distribution on the roller. While the roller's purposefully built crowning may handle minor misalignment, it cannot avoid harm when the misalignment is severe. As a result of the cup and cone's inability to balance the misalignment, high-stress concentration occurred at the roller tip, resulting in early bearing failure (Gurumoorthy & Ghosh, 2013).

• False Brinelling: When machinery and aggregates are subjected to vibration, this type of damage is widely recognized. False brinelling can also happen with load vibrations or tiny rotating oscillations. This failure is distinguished by ripple markings corresponding to the rolling part's spacing. False brinelling results from a lack of lubrication induced by squeezing it out of the contact (Jacobs & Plogmann, 2014).

• Other failure modes include electrical erosion, fractures, and cracks. Through rolling bearings, variable frequency inverters may generate high-frequency voltage and current. When rolling bearings are subjected to passing of electric current, both the lubricant and the rolling bearing are impacted (Jacobs & Plogmann, 2014). Fractures (or cracks) occur when the ultimate tensile strength is overcome, fractures (or cracks) occur. Fractures causes can be divided into three including; the excessive tensile strength of the material caused by local impact or overstressing, Bending, which causes the fatigue strength to be surpassed, and Thermal cracking when two surfaces are rubbing up against each other (SKF Group, 2012). Different types of corrosion defects on axle bearing are illustrated in Figure 2-11.

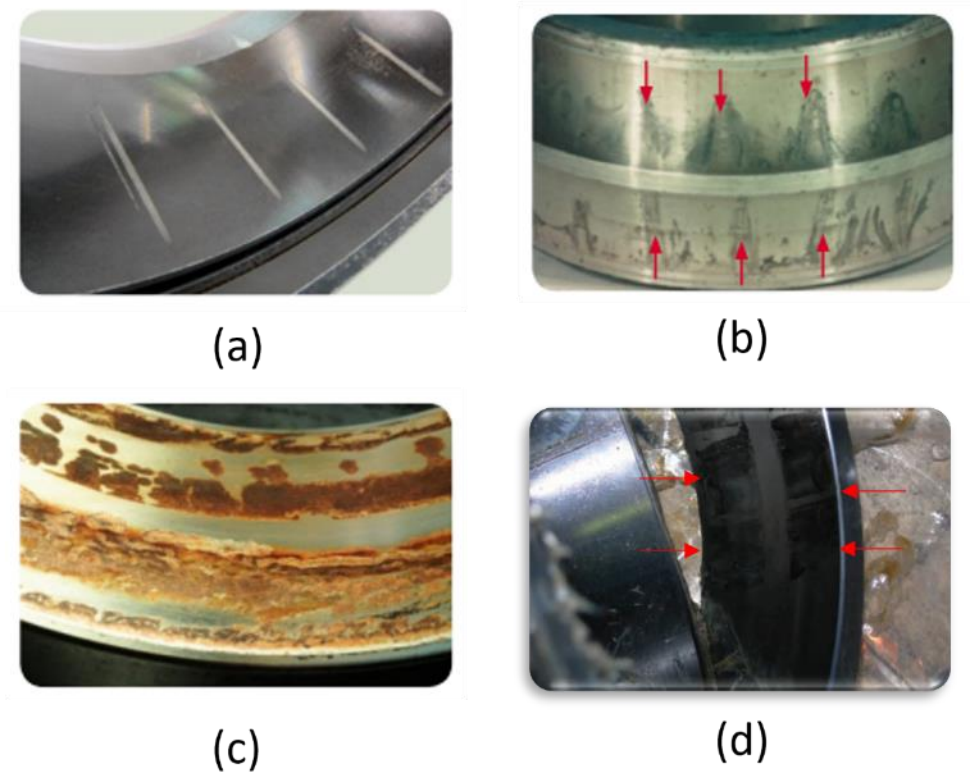

Figure 2-11: (a) False Brinelling (b) Moisture corrosion (c) Fretting corrosion (d) Black corrosion (SKF Group, 2012).

2.3.3 Axle damages

As described earlier, the railway wheelsets are subject to cyclic loading. The risk of fatigue failure happens after a considerable duration of related loads. Like the wheel and axle bearing, the axle must be securely removed from the service before it fails catastrophically and result in serious derailment (Náhlík et al., 2017).

Due to fatigue life issues, the design of the axle has been studied extensively, along with calculations and testing as followed by specific standards. Due to high-speed trains and growing safety demands, these techniques are regularly updated, improving service safety (Novosad et al., 2010).

Railway axles are built to last for a long in-service lifetime. However, there are recorded incidents of their failure caused by faults that occur during operation and act as a source of formation and growth of cracks to critical size (Yasniy et al., 2013).

Since axle steels have a relatively low ultimate tensile stress and a high ductility, fatigue fracture is often brittle. (Bracciali, 2016b) mentioned that this is why the axle gets bent based on modest nominal loads with mild stress concentration. Figure 2-12.

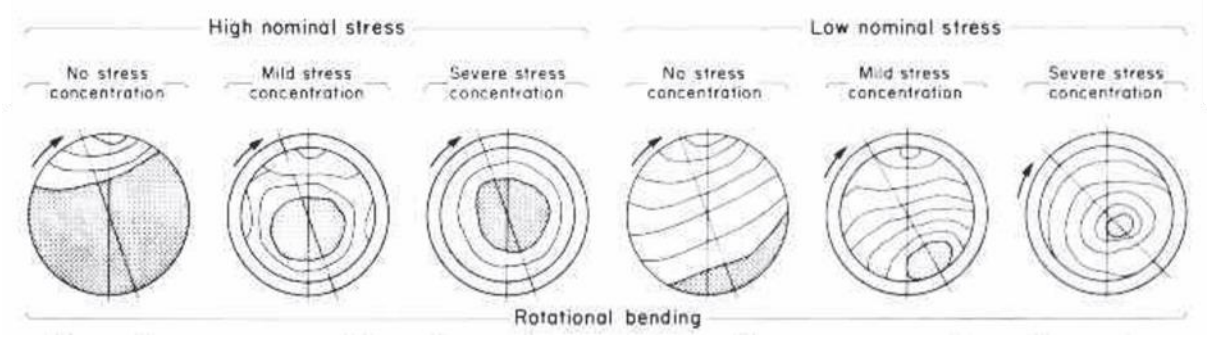

Figure 2-12: Possible marks on the axle surfaces under a range of stress consitions (Bracciali, 2016b).

The axle damage at the journal area could be logically linked with the failure of rolling element bearings. The impact of interference fit and journal bending on failures of axle bearings was addressed by (Chang et al., 2020). It should be noted that greater interference fits diminish journal strength owing to increased contact pressure. In bearing design and application, journal bending should also be addressed. As can be observed, journal bending can have a negative impact on the lubrication state (Chang et al., 2020).

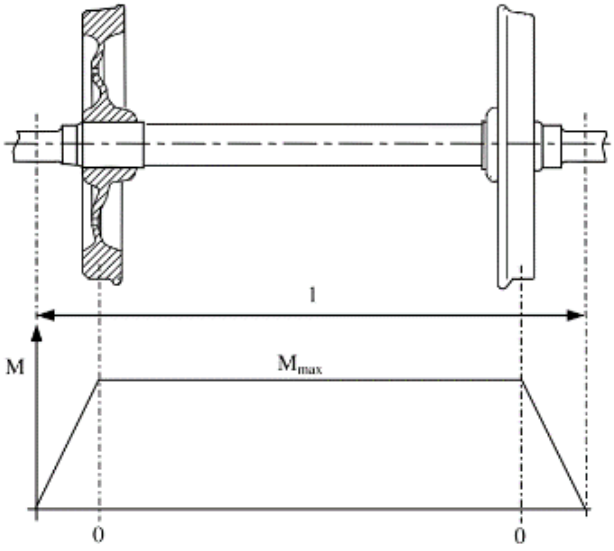

Figure 2-13: Bending moment on the axle (Gerdun et al., 2007).

(Gerdun et al., 2007) discovered fatigue cracks in the bearings' inner rings. The dynamic strength is effectively lowered after a long period. As a result, the rings expanded, and the axle began to slide between them. In addition, the bearing proceeded to heat up due to the friction. Broken rings and restricted rolling also caused damage to the cages.

According to Figure 2-13, the bending moment develops from the bearing to the wheel. It reaches its highest value and remains constant along the axis until it approaches zero at the other bearing. When the bending moment is the smallest or zero, the axle will be broken precisely in the bearing area.

Figure 2-14: The missing piece of the axle due to the deformation along the circumference (Gerdun et al., 2007).

The axle's fractured section is shown in Figure 2-14, where it has deformed along its circumference due to sliding. The ultimate shearing fracture occurred in the centre, where concentric patterns may be seen (Gerdun et al., 2007).

Bending and press-fit loading are the two primary loading sources in the vital area. Press-fit loading remains constant throughout the servicing time (for a given location). However, due to dynamic forces, bending loads is shifting (impact of a ride to the curved track, over switches, and crossings. The elastic material standard of EA4T (EN) steel was considered in their analysis. This study demonstrated that the influence of the railway wheel's press-fit loading should be considered when estimating the residual fatigue lifespan of railway axles (Náhlík et al., 2017).

For axles with external journals, the EN 13103-1 standard is presently used in Europe. The method stated in the standard is meant to keep axles from getting cracks. Cracks can also form when damage and/or corrosion pits develop. Rail roughness variations affect axle strains, which can overcome wheel out-of-roundness degeneration and generate RCF clusters (Maglio et al., 2022).

2.4 Summary

Wheelset components and their functions have been presented in this chapter. Bearing types which are widely used for railway wheelsets have been reviewed. The metallurgy of wheelset components was described, including their universal standards. Moreover, the standards and requirements of each wheelset component have been discussed. Wheelset damage has been listed together with some examples of common sub-component damage. Lastly, the causes and effects of each damage type have been introduced.

Chapter 3: Inspection techniques and condition monitoring techniques for wheelsets

3.1 Non-destructive testing for wheelsets

Wheelset inspection still relies on conventional inspection techniques, some of which have been developed many decades ago. Even though there have been significant advances in electronics and automation of the inspection of process, the fundamentals of the inspection processes used remain effectively the same. The most commonly employed inspection techniques are mainly based on visual, electromagnetic and ultrasonic methods. More recently, a wide range of automated inspection systems has been commissioned by rolling stock operators for inspecting wheelsets more efficiently, reliably and quickly. Visual inspection is included as a rapid qualitative evaluation method, but for more in-depth and quantitative inspection other techniques are required, particularly Ultrasonic Testing (UT). UT in particular, apart from cracks can also be used to identify manufacturing defects, such as large inclusions, during quality control of new wheelsets (Amini, 2016a).

Removal of the wheelsets from the bogie is required during routine maintenance in order to carry out detailed inspection. However, it is more convenient if the inspection can take place directly when the wheel is still attached to the bogie. CM should be capable of monitoring wheelsets while they are in service without the need to remove them from the bogie. In addition, automated tools, including lasers and high-resolution cameras, can help visual inspection for the evaluation of the wheel profile and tread surface condition according to the requirements set by operational railway standards for different types of rolling stock.

Effective inspection can decisively contribute towards an efficient maintenance strategy in order to minimise the chance of catastrophic failure and possible derailment. Advanced NDT techniques and a well-managed maintenance plan can be useful for ensuring safe rolling stock operations. Maintenance can be optimised through the use of effective CM of wheelsets. Next, the different NDT procedures currently utilised by the industry for the examination of rail wheelsets will be examined.

3.1.1 Visual Inspection

Visual inspection is generally a simple approach for evaluating the surface condition of the wheel, bearings, and axle. The use of specially designed measuring tools helps identify parameters of interests as defined in the relevant standard. For example, wheel inspection may use a steel measuring gauge to evaluate a number of important parameters, such as flange width, flange height, flange angle, rim thickness, and tread profile (Laing O'Rourke, 2020a).

According to the inspection standard, visual inspection can also be used for the evaluation of tapered roller bearings. The axle end cap should be the first location to be inspected as there could be missing parts, i.e., lubrication plugs, cap screws, and set screws in the axle boxes. These parts are related to the tightness of the bearings. The end cap should be inspected for damage or wear caused by a misplaced adapter. It is necessary to inspect axle boxes or package units for loose backing rings and excessive wear on the boxes, adaptors, or mating faces on the side frames. Any seals might be missing or broken, and excessive grease surrounding a seal could indicate damage. (Laing O'Rourke, 2020b). Figure 3-1 shows the gauge used for the wheel inspection.

Figure 3-1: Steel wheel measuring gauge (Laing O'Rourke, 2020b).

Laser equipment could help reduce the time required for the completion of the visual inspection process. According to Figure 3-2 (de Almeida Costa et al., 2020), a Portuguese train operating company replaced a manually measuring gauge device in 2017. The result shows the reduction in measuring time from 90 minutes to 20 minutes for multiple measurements of 16 wheelsets. There are also more benefits of using laser equipment in cost savings and improved measuring precision, since it can effectively reduce human errors.

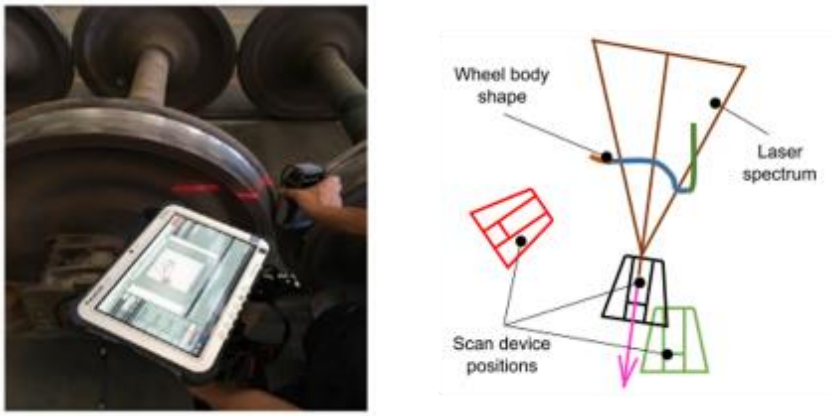

Figure 3-2: Laser equipment (de Almeida Costa et al., 2020).

A number of factors can have an impact on measurements. For example, they may be affected by how each railway operator utilises the measuring instrument, the device's calibration, and the location of the wheelset. Ideally, various inspection instruments should produce comparable results when measuring the same wheel many times.

It is generally known that any measurements in engineering always involves some level of error. However, the American Society of Mechanical Engineers (ASME) introduced a methodology to control the measurement uncertainty. The concept relies on several parameters, including precision index, bias error, combining errors, parameter uncertainty, and result uncertainty (Abernethy et al., 1985).

Visual inspection is limited to rolling stock temporarily removed from service during planned maintenance. These measurements also require trained personnel according to level 1 and 2 inspection standards even when automated tools are employed during the inspection. The early detection of cracks and flaws is unlikely to be feasible using visual inspection alone. However, visual inspection can successfully detect a number of other defects, including possible surface cracking.

3.1.2 Ultrasonic

Various ultrasonic techniques for the inspection of rolling stock vehicles and their wheelset have been used for more than 50 years. Ultrasonic techniques are currently widely employed as one of the primary methods of non-destructive evaluation of wheelsets, particularly the wheel and the axle. Figure 3-3 shows it principles. (Pohl et al., 2004) employed an ultrasonic multi-probe arrangement to minimise the effect of the mode conversion and other possible sources of noise in the ultrasonic signal. It is essential to utilise shear waves with polarisation in the disc plane. Shear wave probes with a pitch and catch design have shown to be promising for tangential crack detection (Pohl et al., 2004).

In single ultrasonic probes, interference arising from wave mode conversion can be an issue since such probes use polarised shear waves parallel to the wheel plane. The probe locations at the wheel rim must be carefully set to enable satisfactory level of detectability of possible cracks within the different areas of the wheel disc region (Wüstenberg et al., 2001). The fact

that the waves must pass over disc sections of varying thicknesses adds to the level of complexity of the UT process. Thus, careful manipulation of the probe positions is required.

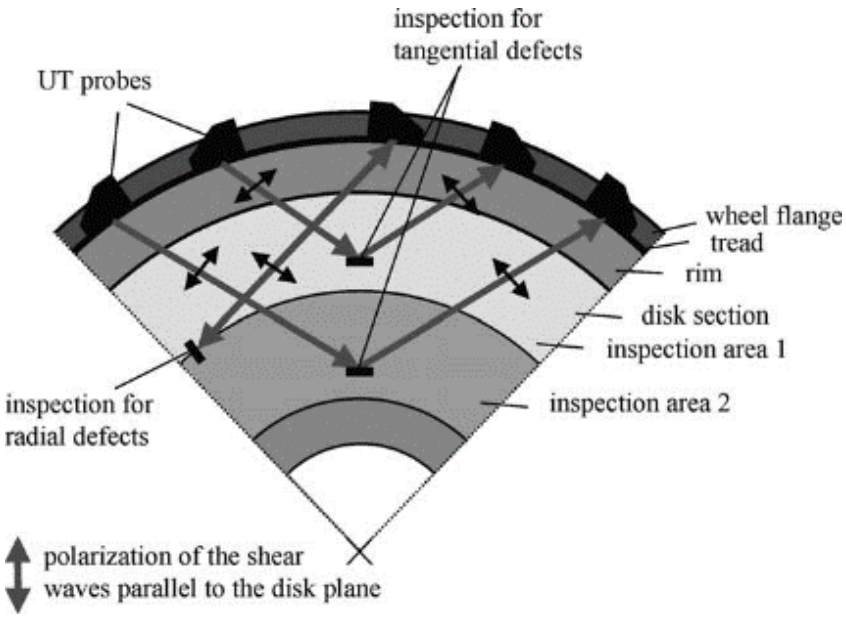

Figure 3-3: A section of wheel disk with the ultrasonic inspection concept (Pohl et al., 2004).

It should be noted that some of the wheels are equipped with brake discs as shown in Figure 3-4, making access for other NDT inspections impossible, such as magnetic particle testing or eddy current scanning (Wüstenberg et al., 2001).

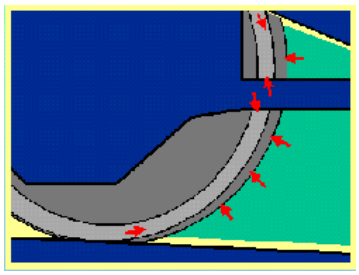

Figure 3-4: possible area on wheel disc where ultrasonic probes can be installed (Wüstenberg et al., 2001).

Duringon-site inspection, operational problems can be addressed at least to some extent by using non-contact ultrasonic methods. Such techniques include laser ultrasonics, which makes use of a pulsed laser in order to generate ultrasonic waves in the material using thermal effects and various ultrasonic wave detectors including conventional piezoelectric sensors (Montinaro et al., 2019).

As it has been already mentioned earlier conventional ultrasonic techniques are the most often employed methods of wheel and axle inspection. However, more recent developments in ultrasonic phased array technology have allowed a switch towards their use instead over conventional single UT probes. The use of ultrasonic phased arrays can increase the probability of detection of defects as well as make the overall inspection easier and more accurate. However, it requires more expensive equipment and appropriately probe design and operational frequency. Phased array probes, like the conventional UT probes, can be manipulated during the inspection process either manually or automatically using robotic arms. Ultrasonic inspection methods require removing the train's wheelset, which is time-consuming and costly. Effective ultrasonic inspection requires surface preparation and a couplant, such as water-based gel, to guarantee good ultrasonic wave transmission between the probe and the examined component (Montinaro et al., 2019).

Ultrasonic phased array operation from the inner wheel rim may examine the tread and chamfer region. It is a way for compensating for the probe’s wide beam coverage, whilst allowing for high efficiency, and consistency of the inspection quality (Peng et al., 2014).

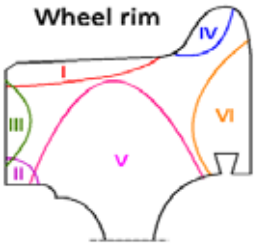

Figure 3-5: Side view of the wheel rim shows each inspection area (Peng et al., 2012).

The wheel rim is separated into six regions, as shown in Figure 3-5. Each part of the wheel rim is evaluated using an ultrasonic beam emitted from a position on the surface of the wheel tread and inner side of the rim. Most ultrasonic wheel inspection methods analyse circumferential flaws with longitudinal waves. The large-angle transverse wave is used to test spalling defects in the tread. The limited number of probes always results in an ultrasonic beam blind region, and the spalling defect exacerbates coupling and obstructs transmission. Figure 3-6 shows the phased array probe on the wheel rim (Peng et al., 2012).

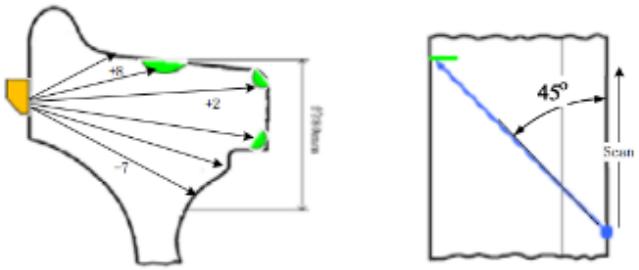

Figure 3-6: Phased array lateral probe inspection the wheel rim (Peng et al., 2012).

When using ultrasonic phased arrays for railway axle inspection, the optimisation of the phased array probes used for the inspection of the various axle geometries specified was performed using a computer model for directivity calculations. The space between the wheel and the brake is quite small. As a result, the accessibility of phased array probes is restricted. Furthermore, some axles feature surface contours curved around the circumferential and axial direction. This

condition must be considered while optimising phased array probes. As a result, the restricted accessibility between the wheel and the brake disc requires flexible sound field adaption. Phased array techniques effectively allow the inspection of the whole circumference with a single line scan as shown in Figure 3-7 (Erhard et al., 2003).

A new technique known as Full Matrix Capture has been developed for ultrasonic phased array inspection (Peng et al., 2014). The FMC is an ultrasonic data acquisition method where progressively a single element transmits and all elements in the array receive to collect the entire time-domain signals for each transmit and receive element pair. Figure 3-8 shows the principle of wheel ultrasonic phased array evaluation.

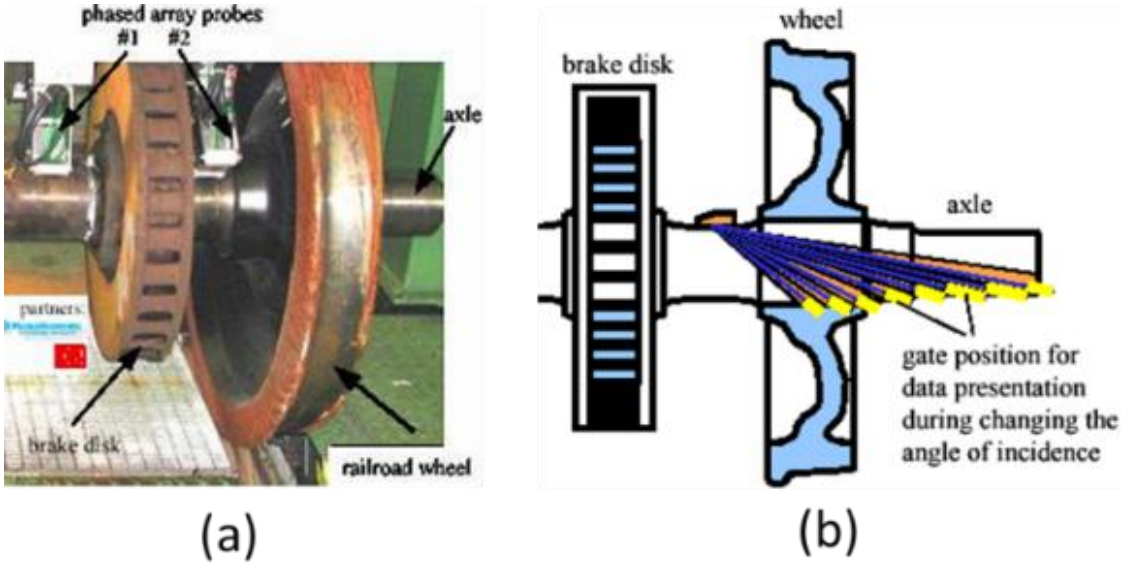

Figure 3-7: (a) The setup of phased array probes at the railway axle (b) Schematic diagram of gate position at different angles for data output (Erhard et al., 2003).

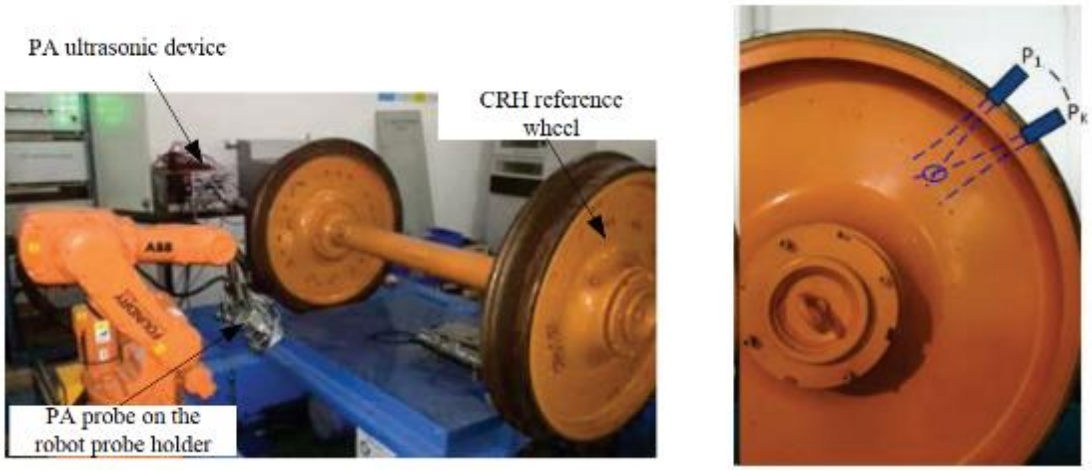

Figure 3-8: The CRH reference wheel with the ultrasonic testing system (Peng et al., 2014).

An ultrasonic phased array system developed by GE Inspection Technologies has been utilised to minimise total axle inspection time. One phased array unit with fourteen active elements is mounted on each side of the axle body for ultrasonic examination as displayed in Figure 3-9 (Kappes et al., 2007).

Some drawbacks of using phased array technology for wheelset inspection were identified by (Cavuto et al., 2018). These include problematic adaption to varied wheel profiles, a constraint restricting their incorporation into the system for monitoring the wheelset while the train is moving, the measurement setup's complexity, and the need to use contact probes.

Many researchers tried to tackle the issues mentioned earlier. Laser ultrasonic techniques have been employed by utilising high-power laser sources and air-coupled receiving probes, providing entirely non-contact approaches that are versatile in installation and setup. As illustrated in Figure 3-10, the laser ultrasonic system was placed with the laser source and receiving probe on opposing sides of the wheel.

Figure 3-9: Probe system carriers for wheel and axle inspection by GE company (Kappes et al., 2007).

Optimising laser energy permits laser ultrasonic testing on the complete wheels. The probe generates the ultrasonic wave through thermal ablation. An air-coupled detection probe is responsible for receiving the emitted signal and identify any defects and their position and severity (Cavuto et al., 2018).

Laser ultrasonics uses an air-coupled ultrasonic probe to detect high-energy pulsed laser ultrasonic waves. Consequently, the measurement process is fully non-contact, including ultrasonic wave transmission and detection, allowing for a significant reduction in testing setup time and more flexibility. It provides a substantial advantage over conventional NDT technologies currently used for rolling stock component diagnostics, such as contact phased array approaches (Cavuto et al., 2016). However, what cannot be ignored is the potential of surface damage to the component being tested due to thermal effects arising from the laser pulses used to generate the ultrasonic signals. Due to a decreased signal-to-noise ratio (SNR), minor flaws may not be seen.

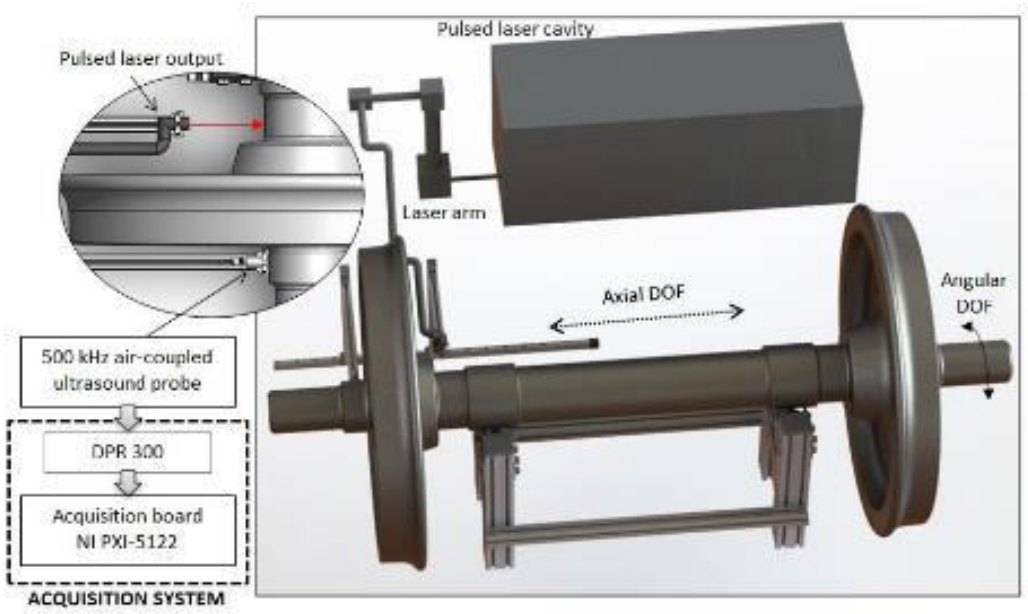

Figure 3-10: The experimental setup of Laser ultrasonic testing (Cavuto et al., 2018).

To generate guided mode acoustic signals, contactless laser ultrasonic waves are described as an effective procedure (Kenderian, Cerniglia, Boro Djordjevic, et al., 2005; Montinaro et al., 2019). Remote ultrasonic wheel defect inspection uses a simple laser emitter and receiving probe (Montinaro et al., 2019). Single laser pulse forms Rayleigh wave on rail wheel tread. By aligning the laser beam, the Rayleigh wave travels around the wheel's surface in opposing directions. Unless a detector is placed at the same level as the emitting point, two arrivals matching each wave's travel route can be seen at any test point on the wheel surface. Transmitted and diffracted waves are more complex than reflected waves, especially when considering Rayleigh wave propagation and wheel design (Kenderian, Cerniglia, Djordjevic, et al., 2005). Laser-ultrasonic inspection takes longer measuring time than phased array and is more expensive to run. (Montinaro et al., 2019).

The laser-ultrasonic technology is also employed to identify defects in a painted railway axle with simulated flaws that match fatigue fractures. This approach has the benefit of not requiring wheelset disassembly, especially in low-speed mode, such as when utilising an underfloor lathe. Thus, the axle's out-of-service period is reduced. In this situation, instead of using a

conventional or rotational UT probe, this approach can be based on the reflection mode on the collar. However, for certain defects that are located under the axle journal (i.e. under the bearing seat) detection is not feasible. Therefore, transmission signal is needed at the end of axle. (Montinaro et al., 2020).

Combining laser generation with air-coupled ultrasound detection allows the method to be entirely non-contact and can operate remotely. Ultrasound detection by laser demands reflective, flat, and smooth surfaces. At the same time, air-coupled ultrasonic generation is ineffective for detecting internal faults in metals due to reflections of the ultrasonic waves at the surface of the test piece. Therefore, hybrid non-contact ultrasonic techniques have been introduced in industrial environments (Kenderian, Cerniglia, Djordjevic, et al., 2005). Figure 3-11 shows the equipment setup for shattered rim cracks inspection of rail wheels. According to Snell's law, there must be an air gap between the detector and the wheel's surface, which the detector is designed to receive the longitudinal bulk wave rather than the Rayleigh surface wave. The concept can prove that cracks from the shattered rim and thermal fatigue can be detected along the wheel tread.

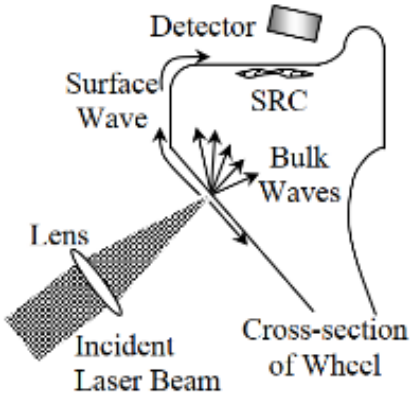

Figure 3-11: Schematic diagram of the rim cracks (Kenderian, Cerniglia, Djordjevic, et al., 2005).

3.1.3 Eddy Current Testing

Eddy current technology has gained popularity as a dependable, quick, and practical way for evaluating complicated shapes and huge production quantities, especially for surface axle CM. A cylindrical or cubic coil carrying current is positioned near the test item in a conventional eddy current test. A coil delivered alternating current (AC) generates a magnetic field that interacts with the test piece and creates eddy currents (Janousek et al., 2008).

This technique aims to identify the defects by measuring the change in impedance between the probe coil and the axle. Metallurgical changes, like as fractures, enhance eddy current phase and amplitude (Hashizume et al., 1992).

Eddy Current Arrays (ECA) have been introduced for detecting surface and sub-surface cracks over an area quicker and more reliably. It is based on the same concept as Eddy Current Testing but with several coils intentionally configured in the same probe assembly.

The implementation of ECA technology for axle surface inspection is explored in the paper by (Lanzagorta et al., 2018). Based on their work, the isotropic flexible Eddy Current pattern has been designed to lower the lift-off effect and provide high SNR. Furthermore, they finally get the system performed on the actual railway axle with simulated cracks on a different area. Accordingly, ECA was able to identify cracks with a range of sizes, orientations, and locations. Figure 3-12 shows (a) the axle specimen with artificially induced cracks on a different area and (b) the measurement of the probe.

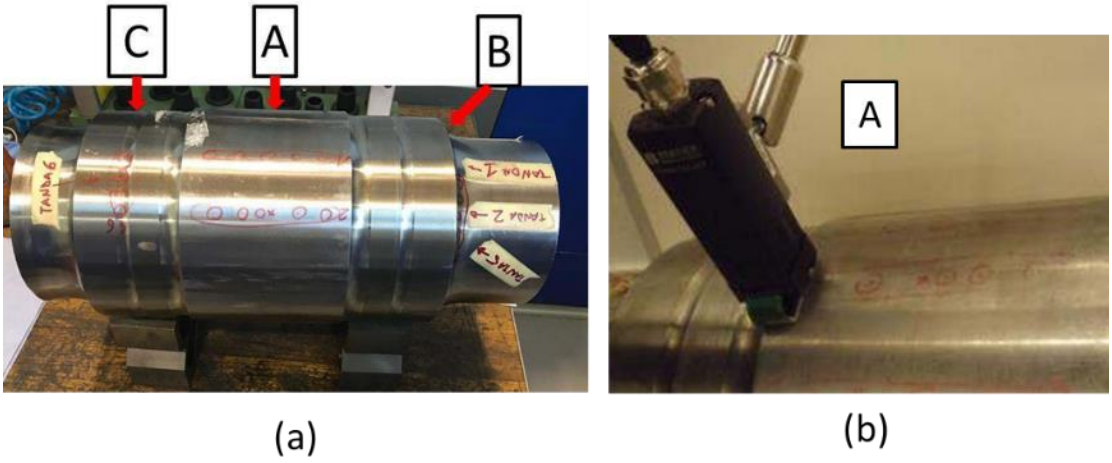

Figure 3-12: (a) Axle specimen with artificially induced cracks on a different area (b) The measurement of the probe (Lanzagorta et al., 2018).

There are also other possible useful applications of eddy current techniques, including measuring the wheel's properties. Two eddy current sensors in conjunction with a laser displacement transducer were presented as a method for dynamically measuring the diameters of train wheels (Y. Gao et al., 2014). Figure 3-13 illustrates the setup for dynamically monitoring the train wheel.

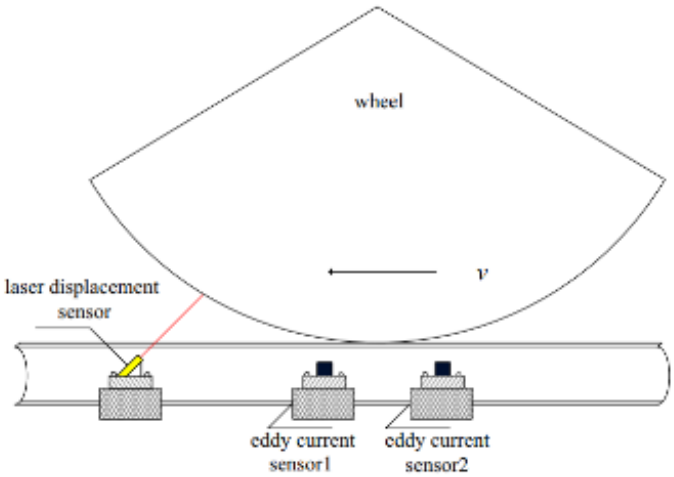

Figure 3-13: The integration of one laser displacement transducer and two eddy current sensors (Y. Gao et al., 2014).

Another study that relies on the same concept and improves the measurement accuracy has been reported by (Zheng et al., 2019). This study claimed that the wear of the wheel tread and rail top would potentially reduce the accuracy. They developed a simple solution based on three one-dimensional lasers to address this issue.

3.1.4 Alternating Current Field Measurement

Alternating Current Field Measurement (ACFM) detects and measures surface fractures via electromagnetic examination. It needs no elimination of surface coating. However, the first time ACFM was used in the rail sector was to examine axles. ACFM outperformed Magnetic Particle Inspection (MPI) and an improved eddy current approach in many experiments (Topp & Smith, 2005).

The concept produces an alternating current to flow in the thin skin of the test piece near the surface. If no faults are found, the electrical current will remain unchanged by providing a remote uniform current into an area of the component under test. When there is a fracture, the uniform current is disrupted.

After that, the fractures allow the alternating current flow through the end of the surfaces (Topp & Smith, 2005).

ACFM can be utilised for axles and rail inspection based on a special probe and multiple field sensors. When inspecting the vehicle's axle, an array probe is usually employed. These are more complex probes with several sensors to check a considerably larger area than standard probes. As the probe travels, each sensor is sampled and an encoder registers the distance (Topp & Smith, 2005).

The axle part under the Earth Return Brush (ERB) on an in-service power axle proved problematic to inspect using standard approaches. Limited access and contaminated fluids on

an in-service box made MPI inappropriate. The ultrasonic examination was also not possible due to axle geometry. A tailored ACFM array probe was built to test the axle under the brush while it was still attached to the train (Topp & Smith, 2005).

The improvement of ACFM in providing an accurate defect sizing was presented by (Nicholson et al., 2013). The inspection system applied a micro-pencil probe to obtain experimental ACFM measurements of manufactured and actual RCF faults. This endeavour intends to size all RCF fracture types in rails and wheels. Within the probe, two magnetic field sensors measure the Bx and Bz signals (the x and z elements of the magnetic field, respectively), which are then utilised as input in the ACFM software for defect sizing. The sensor is operated by a robotic arm and works with a laser distance sensor as shown in Figure 3-14. If the fracture shape is known, the suggested model may be used to forecast the size of the crack.

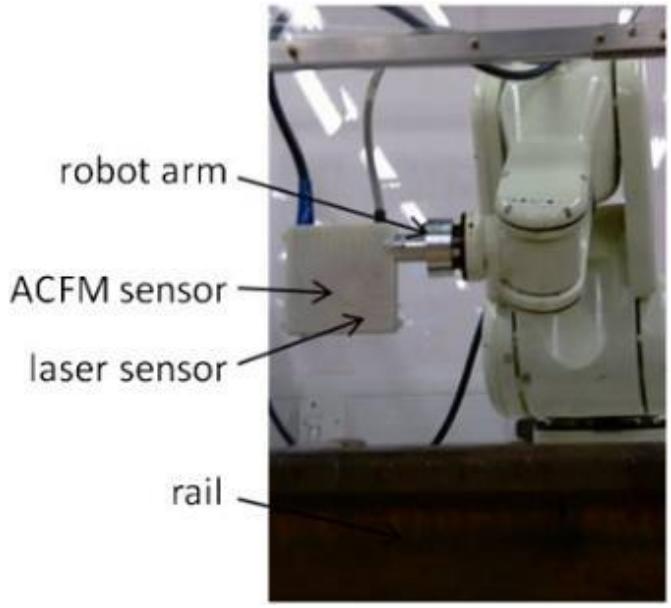

Figure 3-14: The robotic arm model FS02N from Kawasaki holding ACFM sensor and laser distance sensor (Nicholson et al., 2013).

Because of signal interactions, quantifying cracks within closely spaced clusters is more challenging than quantifying isolated single cracks. It is useful to have knowledge of the

number and spacing between cracks before ACFM is deployed for quantification purposes rather than detection. It is also important to provide a strategy for reliably determining the background signal intensity in cases where prior defect identification has not been performed.

A portable ACFM system approved for UK rail inspection at walking speed is available. Because RCF fractures have a more complicated geometry than ordinary fatigue cracks, the size technique must be modified. The uniform current field and associated magnetic field interactions with angled RCF cracks as seen in Figure 3-15 is required to be considered, using three sensing coils, so apart from x and z directions, the y direction has also to be taken into account. A finite element method (FEM) model was employed that has previously been verified using experimental data for isolated rail RCF cracks (Nicholson & Davis, 2012). The implications of sensor lift-off variation and non-optimal probe angle, both important in developing automated monitoring systems, have been simulated and analysed.

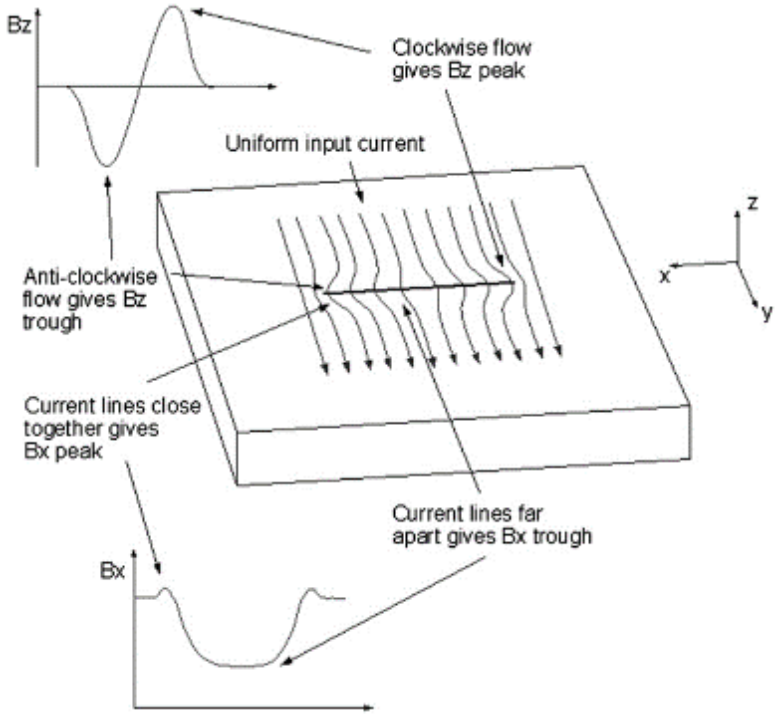

Figure 3-15: Schematic diagram of ACFM measurements (Lugg & Topp, 2006).

The crack pocket length may then be estimated using theoretical modelling of various fracture sizes and forms, assuming the crack is semi-elliptical in shape.

ACFM techniques can be implemented to detect and quantify RCF cracks in rails while simulating real-world conditions (M. P. Papaelias et al., 2008). This study examines low-speed (0.1 m/s) testing on fractured rail surfaces. The spinning rail rig, seen in Figure 3-16, is unique in the world and allows for the evaluation of several NDT methods in a laboratory setting with actual-world circumstances. The University of Birmingham has built a 3.6 m-diameter rotating rail rig capable of 1 to 50 mph. The result revealed that The ACFM system effectively identified all artificially created defects. Based on their findings on artificial crack size trends, differences in anticipated crack diameters are connected to machining errors' excessive crack mouth opening at rail faults' surface.

Figure 3-16: The spinning rail rig at the University of Birmingham (M. P. Papaelias et al., 2008).

The characterisation of wheel RCF defects using ACFM was proposed to provide the better detection of various crack lengths and depths (Juna, 2017). Range of artificial cracks on different high-speed railway wheel samples was applied to study the response of ACFM. The result summarised that the ACFM technique working at lower is more versatile than higher frequencies at detecting and sizing cracks in rolling stock wheels. Additionally, the average background signal running at a higher frequency is much lower than for the ACFM system running at a lower frequency. When dealing with electromagnetic NDT, they mentioned that generating a magnetic field in at least two directions is critical. During the inspection operation, the probe lift-off is a critical aspect that must be managed, as other researchers have already pointed out.

3.2 Condition Monitoring techniques for wheelsets

Railway systems require higher safety and reliability levels due to their critical nature. Recent research has focused on structural health monitoring and early wheelset fault diagnosis. (M. Papaelias et al., 2016b). If wheelset problems aren't detected earlier, railway operations risk catastrophic damage to rolling stock and infrastructure, namely derailment (Bladon et al., 2004). The rail industry has made significant efforts to enhance train maintenance by employing online CM techniques to avoid unexpected train breakdowns and accidents (Vale et al., 2016).

3.2.1 Wayside measurements

The integration of available technologies would be an excellent approach for trackside or wayside CM of rolling stock. For example, Consolidated Rail Corporation in Philadelphia introduced automated wayside inspection using ultrasonic technology (Steets & Tse, 1998). Based on the advancement of electronics in terms of complexity, there were several incidents in building efficient wayside systems to reduce the requirement for visual inspection of freight

train’s components. The automated failure detection of freight car components, included the possible identification of defective bearings, dragging brake, and wheel defects. The integration of different wayside devices could minimise the number of derailments and accompanying damage.

For decades, researchers have been working hard to develop effective roadside monitoring systems. First, however, it is necessary to determine the best deployment locations for such monitoring systems. Since the monitoring system’s cost is relatively high, the maximum benefit from the wayside measurements must be provided.

One study of cost-effective installation of wayside defect detection was conducted by (Ouyang et al., 2009) to optimise the system’s performance. Their models were based on Lagrangian relaxation, which assists in calculating the highest total expected inspection benefits while maintaining within budget restrictions. The model's practical application was verified with railcars running on the United States' train network. The outcome proved that the model can effectively help planning the application of wayside measurements.

The ultrasonic technique has been one of the most widely techniques for non-destructive inspection in the railways and rolling stock for decades. For example, a wayside detection system of cracks in railroad wheels was studied by (Hackenberger & Lonsdale, 1998). They first implemented in-service detection of internal wheel failures using ultrasonic probes that did not require direct contact with the wheel. A high-frequency vibration was introduced through the wheel sample in this study. It benefited from the reflections, which may occur if some cracks are present within the wheel. They concluded that more severe faults or those formed at different wheels locations necessitate more investigation to obtain an adequate level of detectability.

Another approach that can improve the wheel monitoring efficiency was introduced by analysing the kinematic of the echo. Several studies which proved the concept of echo were further presented. The first study by (Brizuela et al., 2009) mentioned using a dynamic ultrasonic approach. They attempted to push the boundaries of ultrasonic technology, which was previously limited to offline wheel monitoring. The presented approach also measured trains travelling at moderate speeds, and the entire monitoring process took only a few seconds. Using echoes formed by the transducer's transmission at the wheel-rail interface. In contrast to prior research, the transducer was positioned on the monitoring rail. They also investigated the identification of wheel flats using an improved wheel tracking algorithm that employs hardware implementation and detects interaction echo movement (Brizuela, Ibañez, & Fritsch, 2010). During the transmission of ultrasonic waves, echoes were collected and utilised for additional signal processing. To quantify wheel flat sizes, they measured Round Trip Time-of-Flight (RTOF) of ultrasonic pulse from transducer to rolling point during motion. When the measurement wheel travels across a regular circular region (without a flat spot), the RTOF of pulses will remain unaltered.

Works have been carried out in another study that integrated the Doppler effect for wheel flat detection (Brizuela, Ibañez, Nevado, et al., 2010). The proposed approach involved shifting the frequency and phase of the rail-wheel contact. The received signal will indicate a frequency shift matching the prescribed speed while the wheel moves along the measurement rail at a constant speed. The difference between emitted and received frequencies indicates wheel defects. The working principles of this approach are illustrated in Figure 3-17.

A year later, they adopted the propagation of ultrasonic pulses (Rayleigh waves) over a measuring rail for wheel-flat identification (Brizuela et al., 2011b). A wheel's rolling surface causes an acoustic wave called the Rayleigh wave to circulate around it. Calculating the distance in the RTOF between ultrasonic pulses and the rail-wheel intersect point determines

the wheel flat's x- and y-axes. Figure 3-18 illustrates the measuring setup for calculating the RTOF. They inserted a transducer at the end of the monitoring rail to induce Rayleigh waves and an echo at the wheel-rail contact point. Normal wheels have a 1 to 1 speed-to-train-speed ratio. The ratio is changed, however, if there are flat areas on the wheels; as a result, the speed of the train and the wheels are not in sync.

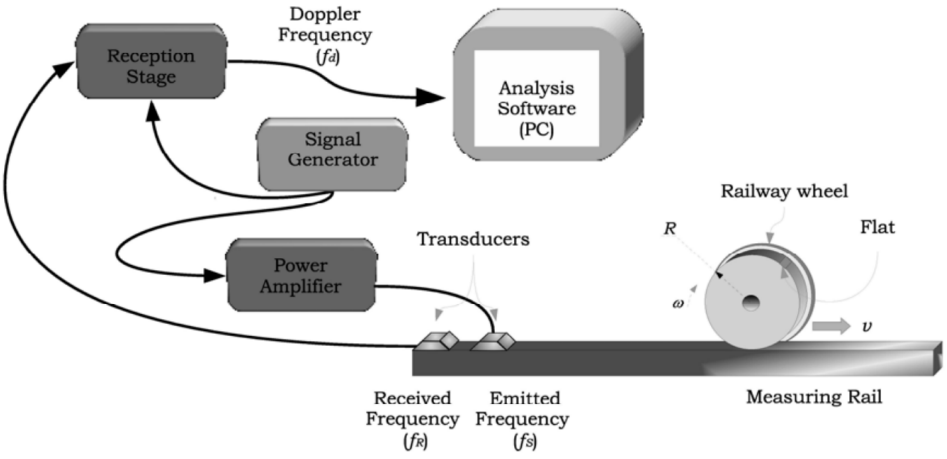

Figure 3-17: Using Doppler effect for wheel flat detection based on ultrasonic transducers. (Brizuela, Ibañez, Nevado, et al., 2010).

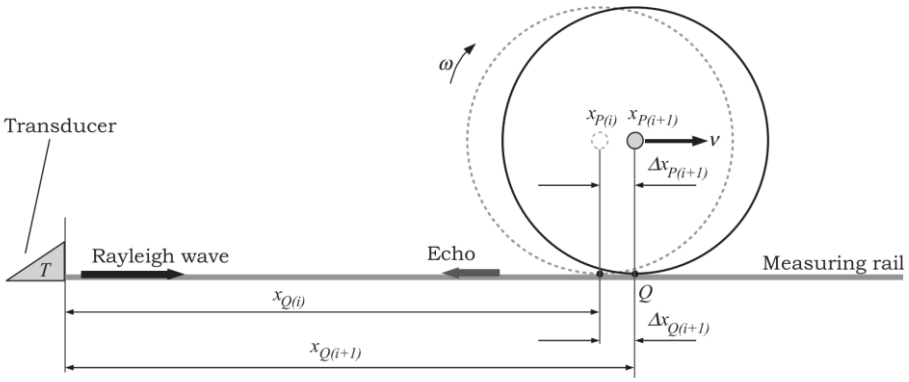

Figure 3-18: Using Rayleigh wave on measuring rail for wheel-flat detection (Brizuela et al., 2011b).

Weight-in-motion and wheel-rail interaction can be used for CM of railway wheel. The responses between rail and wheel would generate valuable information for the wayside measuring system. Strain gauges are also available for this matter since they can provide signals for further analysis. However, field measurements with real-world conditions have always been a better way to pr ove the concept of novel wayside monitoring systems. Thus, the research carried out in Portugal by (Meixedo et al., 2015) set up an online remote CM for wheel flat detection. They also suggested that the enormous loads created by frequent wheel flats might cause significant vibrations that extend throughout the railway system. The project monitored the network's weight transported by rolling stock wheelsets based on a wayside monitoring approach.

The straight track sections on a ground level were chosen because of the cancellation of external stresses from the curved track sections. The detection of wheel flats was based on a periodic change in strain. As a result, the monitoring results contains the acceleration and the direction of the train, as well as the quantity of axles. The monitoring system combined the use of accelerometers and strain gauges. The designed system is a competitive, flexible, and resilient wayside device capable of detecting wheel impacts and weighing a moving train. Figure 3-19 depicts the installation of all sensors along the measurement rails.

Figure 3-19: The actual site containing accelerometers and strain gauges (Meixedo et al., 2015).

A few years later, the study of wheel CM based on strain gauges was further improved via modern signal processing. The proposed method used envelope spectrum analysis and track irregularity. It noted the flat spot's location and severity (Mosleh et al., 2021).

Since Fast Fourier Transform (FFT) has been used as a fundamental signal processing for wheelset monitoring for decades, however, it was revealed by many studies that it fails to capture defect-related signals in some environments. For instance, it could not distinguish high-frequency elements from the disturbance in the output signals. Therefore, the envelope spectrum can also be applied to the monitoring system of high-speed train operation. This study highlighted the use of envelope spectrum as a signal analysis for wheel flat detection with normal track conditions. Figure 3-20 shows 12 recorded rail shear pressures and a roadside equipment to detect rail shear.

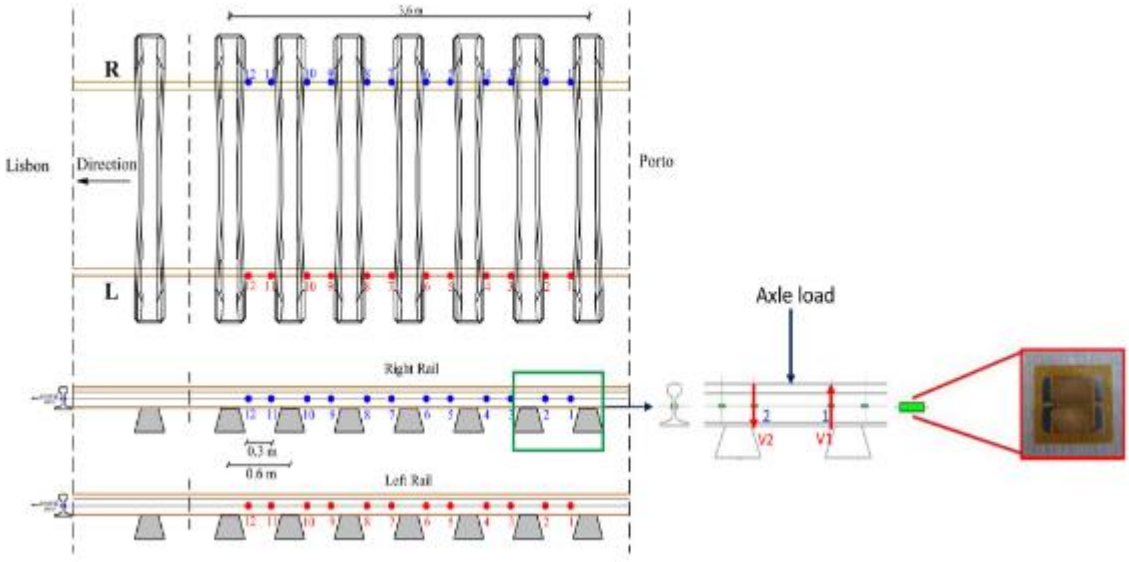

Figure 3-20: Strain gauges positions on the measuring rails (Mosleh et al., 2021).

The temperature measurement devices put on the wayside are selective equipment for monitoring the axle bearing health. Infra-red sensors or a set of beam systems were utilised in some studies in order to create an alarm system. Further details will be discussed in section 3.3.

Fibre Bragg Gratings (FBGs) are photo-imprinted in the core of optical fibres using a UV laser. They reflect wavelengths approaching the Bragg wavelength as bandpass filters. Due to their narrow-band amplitude spectra, they are well-suited for wavelength-multiplexing transmission over a single optical cable. Due to the temperature sensitive property, Bragg wavelength amplitude spectrum shifts linearly and reversibly. (Kouroussis et al., 2016).

Field tests were carried out with FBGs sensors affixed to the rail's foot, where the most suitable area for the sensor is in the middle of a sleeper bay (Kouroussis et al., 2015). The sensor experiences a maximum Bragg wavelength change when a train wheel passes. As a result, a high acquisition rate is needed.

(Kouroussis et al., 2016) showed that the dominant frequency technique can improve a commonly used FBG interrogation method based on wavelength–amplitude conversion for railway monitoring.

FBGs were deployed for wheel flat detection on the Madrid-Barcelona high-speed line in Spain (Filograno et al., 2013). These FBG sensors were placed at different allocated positions between sleepers on the rails in each space. As shown in Figure 3-21, there are three sequential sections between sleepers. Each side of the rails contains eleven FBG sensors. Each sensor measures different parameters, which later are combined as a trace of rolling stock. As refer to the first section in Figure 3-21; one sensor which is placed on the rail foot measures bending.; another two sensors are also installed on the rail web concerning the middle line of 45 degrees in order to deal with shear stress; the last one was just applied to confirm the temperature difference in the rail which revealed that the change is not significant as the temperature development was prolonged.

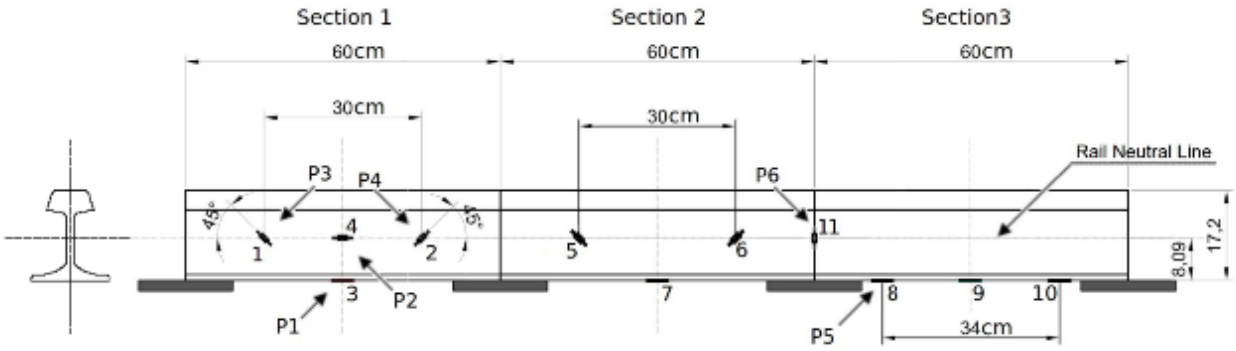

Figure 3-21: The setup of strain gauges on the measuring rail (Filograno et al., 2013).

The second section applied the same concept as the first without using the temperature measurement. In the third section, vertical and bending sensors are added to each sleeper. Figure 3-22 shows the actual area of strain gauges at the installation point.

An output signal from the train with a healthy wheel (as seen in Figure 3-23 (a)) illustrates no indication of peaks after using high-pass filter (as seen in Figure 3-23 (b)). On the other hand, an output signal from the train with a defective wheel (as seen in Figure 3-24 (a)) is not efficient enough to indicate the wheel defect. As a result, a high-pass filter has been used in Figure 3-24 (b) to reveal the fault.

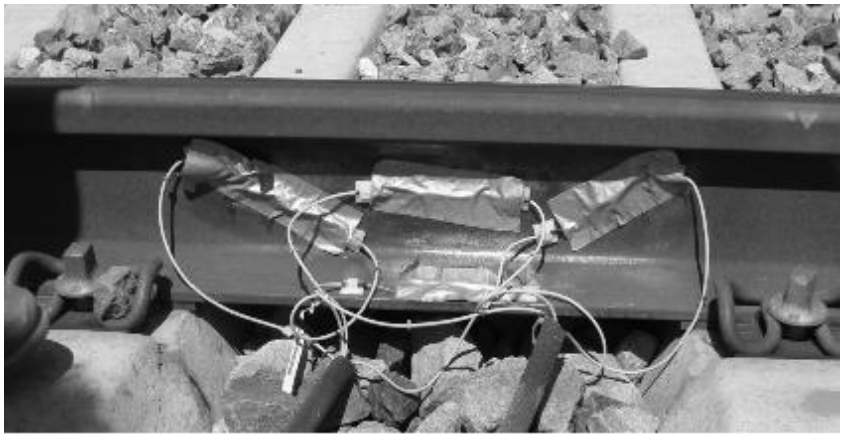

Figure 3-22: The actual condition of section 1 in Figure20 (Filograno et al., 2013).

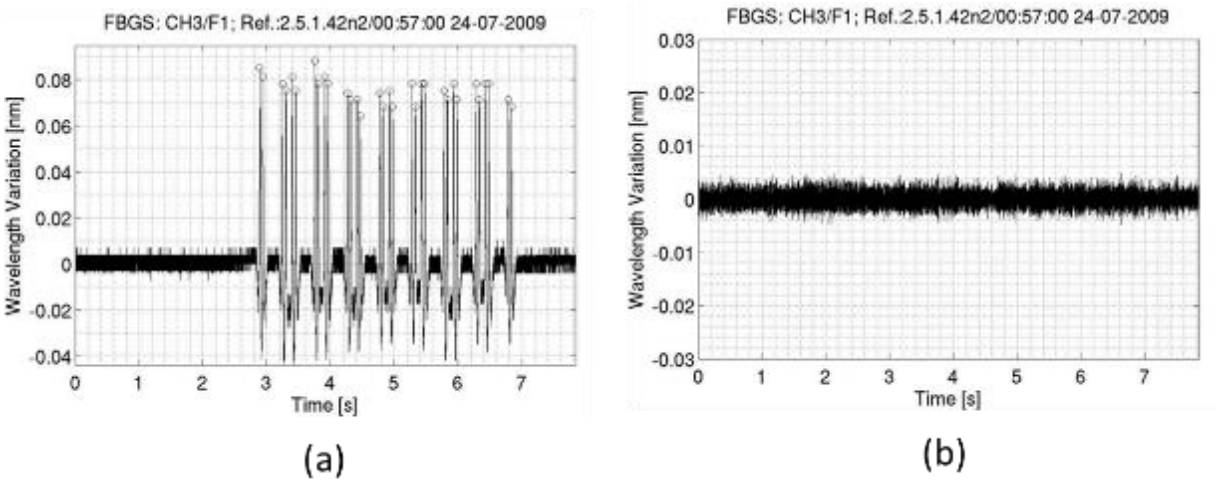

Figure 3-23: Signal from a healthy train (a) a trace of wavelength from sensor P5 of an S-103 SIEMENS VELARO at 49 m/s (b) high-pass filtered signal (Filograno et al., 2013).

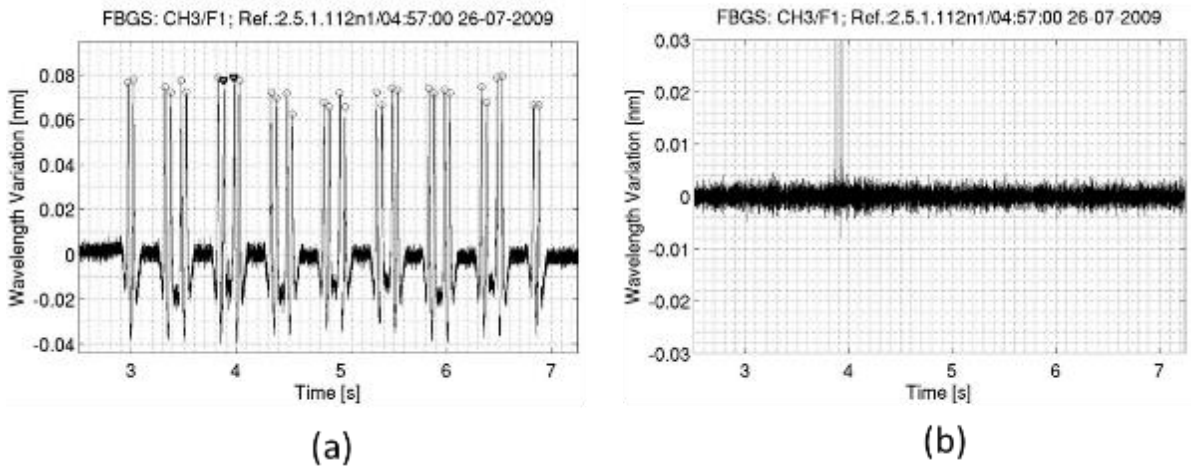

Figure 3-24: Signal from a train with a defect in a wheel (a) a trace of wavelength from sensor P5 of an S-103 SIEMENS VELARO at 49 m/s (b) high-pass filtered signal (Filograno et al., 2013).

Using a high-pass filter and FFT helped the study reveal how the output signals exceed the threshold when there is an obvious out-of-roundness or a flat spot in the wheel. However, a fibre-optic solution to this problem is unquestionably near-ideal since noise issues are avoided. Furthermore, the detection of damaged wheels is substantially more dependable than traditional technology, which is heavily influenced by electromagnetic noise.

FBGs have also been used to assess wheel and rail characteristics, but their effectiveness is readily undermined in electromagnetic interference (EMI) train environments. However, the sensing fibre was applied to mitigate the EMI problem since it is all-dielectric (Anderson, 2006). Another real-time wheel defect detecting system using FBGs by (Wei et al., 2011) also proposed a solution to bypass the EMI effect. The sensors measure how the rail bends when a wheel moves along it. The frequency component that reveals interaction quality is extracted and processed to detect passing wheel faults. This system's sensors and connecting fibres are EMI-resistant. This characteristic is especially beneficial to the current electrified rail network since the sensor network is resilient to EMI. Figure 3-25 depicts the sensor installation arrangement. FBGs 1 and 2 measure the north-direction track, while FBGs 3 and 4 measure the south-direction track. A pair of sensors are placed so that an axle's two wheels pass through them simultaneously. The system measures in-service wheel condition real-time.

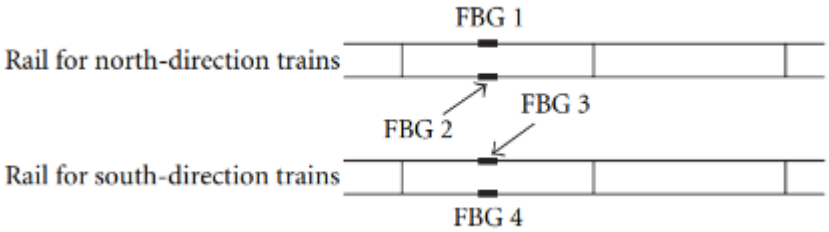

Figure 3-25: The installation layout of FBGs (Wei et al., 2011).

Since the use of FBGs for wheel defect detection of High-Speed railways was rarely conducted, the study by (X. Liu et al., 2018) examined the problem of wheel defects in high-speed trains based on online wheel CM. A FBG-based online monitoring system detects local wheel flaws and polygonisation. Figure 3-26 illustrates the field test setup in which FBGs are densely deployed at 0.15 m intervals to obtain dependable monitoring results with high fidelity. The suggested methods can identify wheels with local defects and estimate the depth of the defect.

The recommended detection method's local defect and polygonisation detection capability was evaluated by driving test trains with damaged wheels through an instrumented rail section.

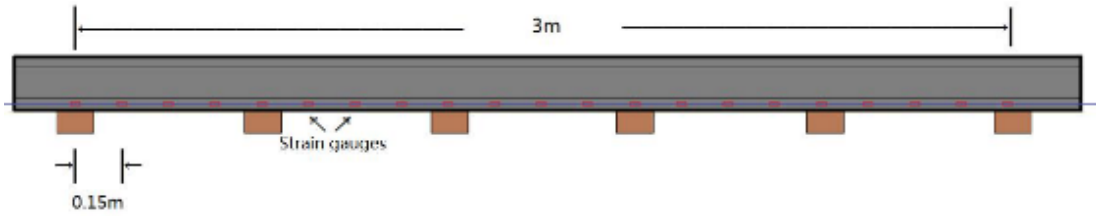

Figure 3-26: FBG sensors installed on the rail by (X. Liu et al., 2018).

Most FBG-based trackside signalling systems don't use train speed. Some disadvantages of FBG-based trackside signalling systems include the harmful effect of EMI, as mentioned earlier. Thus, the FBG-based accelerometers are better to be placed on the sleepers (Yüksel et al., 2018). They created a unique signal demodulation approach for extracting valuable information from somewhat noisy traces recorded by fibre optic accelerometers (owing to the sensor head's extremely high sensitivity).

Figure 3-27 shows a commercial-grade accelerometer attached to the sleeper. The overall configuration of the monitoring equipment installed in this experiment is illustrated in Figure 3-28. FBG accelerometers on the sleeper and rails, optical couplers, a fibre optic hub, and a shielded feeder wire join the sensor network to the interrogator (Yüksel et al., 2018).

Figure 3-27: The accelerometer installed on the sleeper (Yüksel et al., 2018).

Another recent study uses the FBG as an optical sensor for monitoring wheel flat, which (Sharan et al., 2021) proposed. According to the output from strain measurements installed on the railway track, the results revealed that the noisy signals might come from the trains with defective wheels. Figure 3-29 shows how a faulty wheel causes an inconsistent strain impulse on the track. In contrast, good wheel strain signals are regular and even.

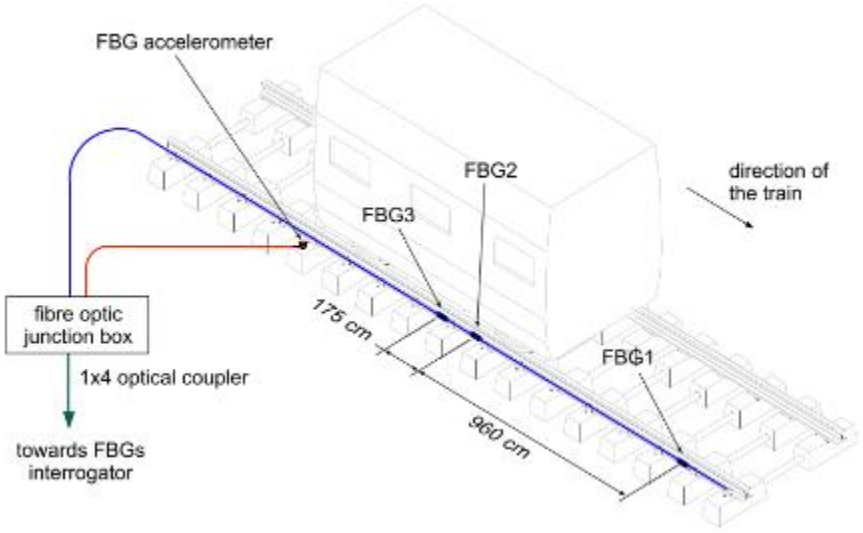

Figure 3-28: The layout of the FBGs sensors at Mons–Liège (Yüksel et al., 2018).

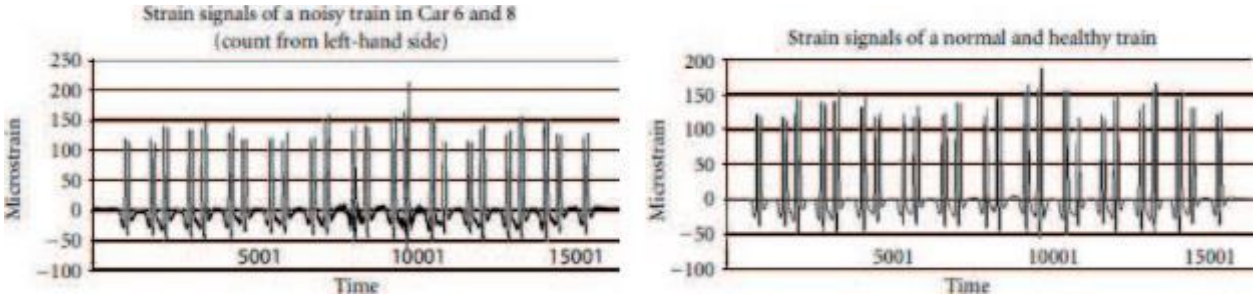

Figure 3-29: Strain signals from (a) noisy signals (b) normal signals (Sharan et al., 2021).

The flat wheel's output signals would be processed using filters to reduce noise and acquire data. Results help us examine wheel and rail parameters and monitor wheel condition. This analysis revealed that strain monitoring data, which optical sensor FBG can understand, can determine a train's speed, gross train weight, axle weights, and axle spacing in real time.

FBG systems can be further developed to provide the wheel's weight and their defective status in real-time and in normal operation, as a wayside system (Iele et al., 2016). Furthermore, the interrogator system was utilised to detect the light reflected by all FBGs mounted along the rail. The train's Bragg wavelength trend is a tiny and durable interrogator for FBG sensors. Furthermore, the wheel flat detection feature was also added to the system, which is conducted by applying a High Pass Filtering to the raw signal gained from each FBG sensor on the rail foot. Each sensor is used to monitor an area of the rolling surface of each wheel, with a length equal to the sensor's range of effect. As a result, the output signals (as seen in Figure 3-30) from the signal processing provide a normalised waveform for each wheel, comprising a sequence of five so-called vibrational levels (one for each portion of circumference monitored by the single FBG sensor).

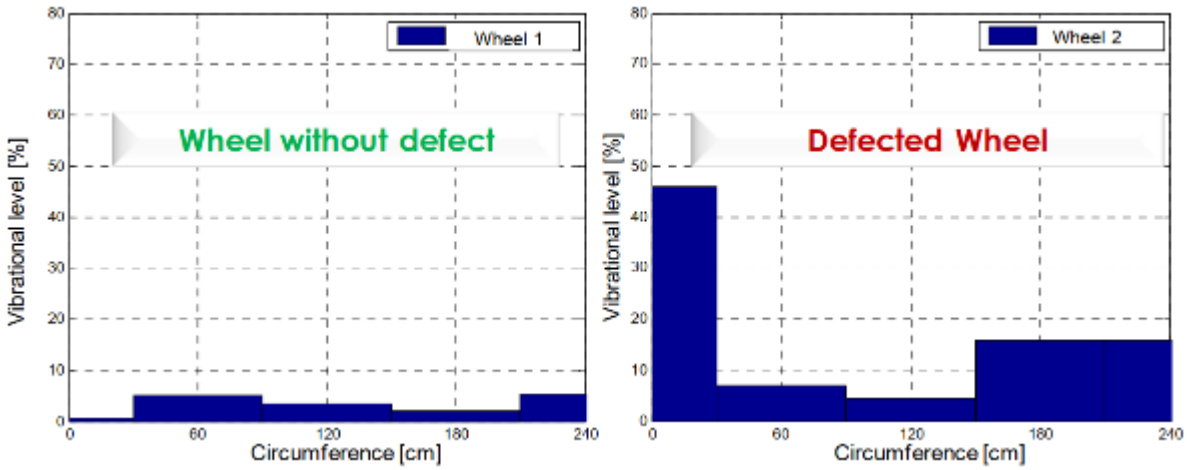

Figure 3-30: The post-processed output of vibrational levels retrieved from (a) healthy wheel and (b) defected wheel (Iele et al., 2016).

In the 1990s, acoustic data was another possible technique that was introduced for wayside wheelset CM, especially for evaluating the condition of axle bearings (Cline et al., 1998). A group of microphones was laid on the trackside to detect defective axle bearings during normal service operation. Time-based and spectral data were chosen. The main benefit of wayside

measurements over onboard measurements is the ability to detect and assess more than hundreds of axle bearings daily.

Recently, there have been several pieces of research related to the application of microphones and recording devices for the early detection of defective bearings (Entezami et al., 2014). The application of modified acoustic array system for the wayside monitoring proved that it can be used to monitor an axle box on a straight track of nine metres. However, the system picked up some background noises from the environment. Another study (Zhang et al., 2018) provided a solution by combining ISVD with resonance-based signal sparse decomposition (RSSD). Some field trails have been done to prove a model of the acoustic monitoring device, which aim at reducing the number of sensors installed in each railcar. Thus, the consistency of the output data was improved (Bondarenko et al., 2019). However, the acoustic monitoring does require the substantial configuration to compete with other novel techniques.

3.2.2 Onboard measurements

Onboard fault detection systems might increase railway operational efficiencies as the railway demands more efficient operation. Real-time CM lowers inefficient maintenance tasks. Real-time rolling stock diagnostics boost availability and safety (Bernal et al., 2018).

For many years, a wide range of sensing techniques for railway wheelset onboard CM has been introduced. Generally, each method would be designed to be used specifically for each purpose. To be precise, each wheelset component would require individual sensing techniques as the parameters involved might not be related.

The wheel profile wear would be a fundamental parameter that requires practical measurement tools. Onboard CM notifies operators about deteriorating wheel flange thickness. A non-expensive inductive displacement sensor is used to assess wheel flange thickness. Therefore, the presented system can monitor both the dynamic and static of a train. It offers superior

accuracy and precision at a lower cost than conventional multi-camera systems along railway lines and onboard laser-based systems (Turabimana & Nkundineza, 2020).

The onboard system used for CM of derailment coefficient was studied by (Matsumoto & Tanimoto, 2018). Generally, the derailment coefficient is calculated by Lateral force (L) divided by Vertical force (V). It might be monitored via a trackside system as many commercial railway lines do. As the authors want to maintain the idea of wheel-rail friction management, they opted to employ an onboard spraying friction modifier system. A group of strain-gauges on the wheel plate detect vertical and lateral force. This concept enables monitoring failures generated on the rails and the wheels by determining the force acting between them.

Several available techniques for wheel-rail contact force are being investigated for the derailment mechanism study. After Nadal's formula was developed, many researchers have explored the derailment mechanism. However, the complexities of the derailment process have not been well investigated, although it is commonly acknowledged that abrupt changes in contact forces mainly cause the derailment. The effective evaluation of contact forces during rolling stock operation is seriously required, especially for the current railway systems, which rely on much higher speed than the age when the wheel and rails were invented (Ren & Chen, 2019).

The measurement of wheel-rail contact force is also employed in many academic research experiments. These include polygonised wheel wear and rail corrugation, as long as vibration between vehicles and infrastructures. The wheel's periodic stresses on the wheel web and axle can be evaluated using the Wheatstone bridge circuit when the wheel runs over the rail. For example, the study by (J. Wang et al., 2021) mentioned double bridge signals with 90-degree phase delays in rotating coordinates. This method can utilise strain gages to provide constant contact forces in a global coordinate system. Under multiple direction contact stresses, the

instrumented wheelset demands high SNR bridge outputs and minimal bridge coupling effects. As illustrated in Figure 3-31, the holes drilled in the wheel web are the best places to produce the maximum vertical load sensitivity and the minimum cross-sensitivity to lateral loads (J. Wang et al., 2021). Figure 3-32 shows the wireless signal transfer system on the wheelset.

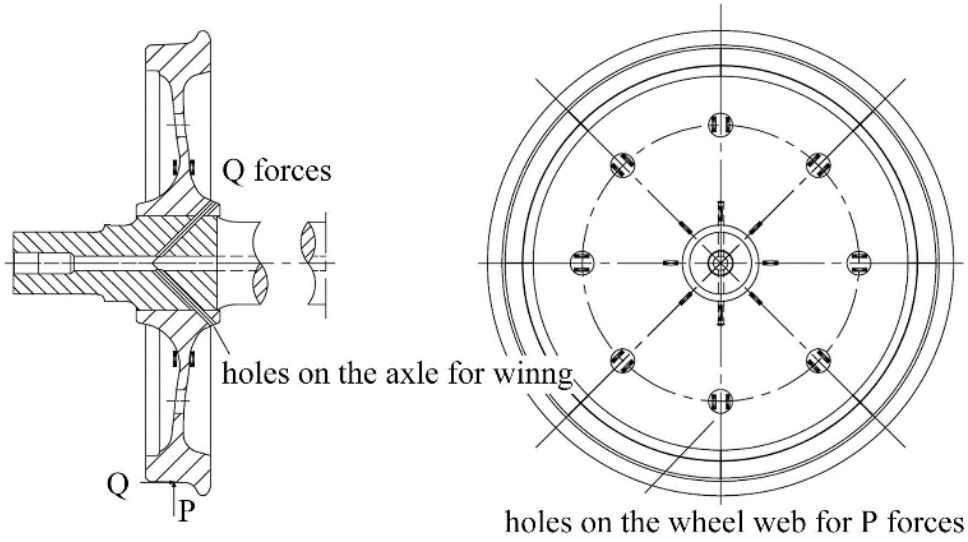

Figure 3-31: Conventional instrumented wheelset with drilled holes for wiring (J. Wang et al., 2021).

Figure 3-32: Specially designed auxiliary brackets for wireless signal transfer system (J. Wang et al., 2021).

EN 14363 specifies online reference procedures for measuring wheel-rail contact forces and axle stresses to demonstrate vehicle safety. The related parameters include the (Y/Q) max (or Nadal's coefficient), the guiding forces Ymax, and the maximum vertical force Qmax (Jin, 2020). Figure 3-33 demonstrates (a) an antenna unit and (b) instrumented wheelset of the high speed train

The following strategies are primarily used to increase signal quality and minimise noise. Using full bridges of strain gauges, the shortest cable layouts by optimisation of the connecting path on the wheelset, the usage of twisted-pair wires with anti-electromagnetic tinfoil, the high insulating resistance between strain gauge and wheelset measuring bridges and the signal amplification on the wheelset.

Figure 3-33: The wheels mounted under high-speed train model CRH6 in China (a) antenna unit (b) instrumented wheelset (Jin, 2020).

While there are various ways to place the railway wheel's strain gauges that correspond with the objective of each measurement, low accuracy is the primary point that could be the fundamental problem that might be seen in most of the available positions of the strain-gauges. The main point of the strategy presented by (Gomez et al., 2011) is the elimination of harmonics of the output signals.

FBGs are also available for onboard monitoring of online wheel defect detection. Strain data of the wheelset were retrieved by FBGs attached on the bogies of a high-speed operating train. The monitoring model is based on 52 FBG strain sensors. In addition, they also added FBG temperature sensors, accelerometers (tri-axial), and noise. Both FBG strain and temperature sensors are connected to the data logger with the monitoring system by optical fibre cables. This study finally identified two different cases of wheel defects (Y. W. Wang et al., 2020).

The flange contact has been one of the parameters interested by researchers. Onboard monitoring based on mounting a single stationary transducer on a railway wheel was introduced to provide information on the flange contact. However, the methodology was conducted between two specimens from the wheel and rail samples. The ultrasonic pulse from the transducer is transmitted and reflected between two materials. A gel-based couplant was used to connect the transducer to the flat surface of the wheel specimen. This study's main objective was to consider how possible an application of a wheel-mounted ultrasonic sensor can be utilised to detect flange contact. It is possible to determine whether flange contact occurs and estimate the normal and lateral loads. The authors mentioned that using this concept for the field measurements would require more study on the position of sensing equipment. Moreover, the predicted correlation between pulse rate and the dynamic nature of flange contact should also be provided (Lewis et al., 2008).

There are several other onboard CM systems for the wheelset based on acceleration. These will break the limitation of previously mentioned studies by better signal quality and data analysis. However, examples of CM approaches using accelerometers will be listed in Chapter 4.

3.3 Existing Remote condition monitoring for wheelsets

Many studies have investigated available technologies for Remote CM (RCM) purposes to provide significant benefits over traditional inspection processes. RCM would generally help

railway operators gain more efficiency in their maintenance aspects. Consequently, RCM techniques might potentially be a useful tool for boosting rolling stock RAMS. RCM can assist railways plan condition- or prediction-based maintenance programs, enhance resources, and boost rolling stock availability.

3.3.1 Hot Axle Box Detectors (HABDs)

Heat detection of the wheelset is another approach for CM. Hot Axle Box Detectors (HABDs) have been introduced to the railway system since the 1960s as a wayside health monitoring system for rolling stock axle bearings. Infrared sensors on the rails detect axle bearing issues. Infrared sensors point towards the direction of bearings, which measure the temperature of the bearings and compare with the standard values. Detected bearings will trigger a warning system to communicate with the train driver or the related staff that the bearings can be removed to stop the possibility of a derailment (Karunakaran & Snyder, 2007; Sneed & Smith, 1998).

However, the accuracy of HABDs may need to be evaluated further since the heat from the surrounding environment could cause errors in the measurements. Several laboratory and field trials were undertaken to improve HABD performance.

The association between temperature profiles and bearing defects was studied by measuring spalls on exterior (cup) and inner (cone) rings (C. M. Tarawneh et al., 2016). The severity of the defect dramatically influences the likelihood of successfully capturing a damaged bearing. Bearings with major defects are far more likely to be noticed than bearings with minor defects. But bearings with problems on the inner and outer rings can sometimes work at normal temperatures. Thus, many damaged bearings might be undetected, which can cause serious problems. Current bearing CM systems are insufficient since they rely primarily on temperature data, which does not appear to provide clear differentiation between defective and healthy bearings.

Correlations between temperatures under varied loading circumstances, operating speeds, and bearing conditions have been examined (Mealer et al., 2017). They employed a single-bearing dynamic test setup that resembles the roadside detection system. Then they compared the infrared sensor temperature to thermocouple and bayonet sensors on the bearing cup. The results retrieved from the infrared temperature sensor installed in HABDs revealed that the most concerning aspect of the overall error is the dynamic response of the sensor. Furthermore, the infrared sensor inaccuracy is also affected by the scanned region where the infrared temperature sensor gets its data. The results of this investigation imply that attempting to improve the wayside HABD measurements by programming correctly would be a callous effort.

Furthermore, the infrared sensors have an issue when recording higher normal bearing temperatures than faulty ones, and some underestimating temperatures were detected on the field test (C. Tarawneh et al., 2018). They also found that the inboard raceway monitoring location is the most effective position where better precision and accuracy could be provided.

3.3.2 Wheel Impact Load Detectors (WILDs)

Wheel Impact Load Detector (WILDs) comprises a group of strain gages implemented for the structural health monitoring system. By using WILDs, the monitoring system is based on the wheel impact data that provides the actual status of the wheels. The threshold has been set to identify defective wheels in passing rolling stocks which all data will be reported to the monitoring system (Partington, 1993).

However, two additional criteria include the wheels operating with a high dynamic impact increased over a small amount of time and the wheels running with a normal impact increased within a short time (Stratman et al., 2007). Figure 3-34 determines (a) displays strain gauges on the neutral axis of the rail web, whereas (b) illustrates the field condition.

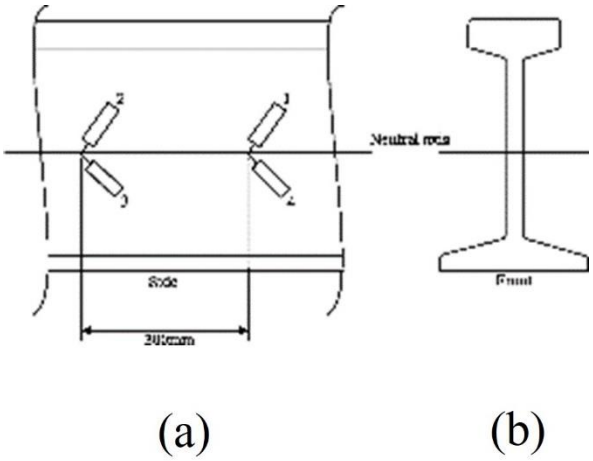

Figure 3-34: The setup of strain gage (Stratman et al., 2007).

The study of impact load characteristics caused by wheel flats and shells was conducted by using a FEM to validate the actual data from the field, they can investigate two wheels caused by defective wheel treads. WILD was also stimulated by using FE model which is further used for measuring dynamic force generated by the net shear strain difference. FE model analysis showed that net shear strain differential dynamic force equals wheel-rail contact force. Axle load, speed, and rail-pad stiffness affect wheel flat (Dukkipati & Dong, 1999b).

The study by (X.-Z. Liu & Ni, 2017) proposes a trackside WILD based on FBGs and a data-based wheel local fault detection approach for high-speed trains. The suggested detection approach was validated using an 8-car EMU fitted with wheelsets with simulated local faults as the test train. This proposed concept illustrates wayside CM for a large number of wheel detections. Furthermore, the system may support numerous FBG layouts and remote monitoring by utilising fibre optic sensing techniques. This online CM performance revealed that the suggested process, which includes the WILD system and the outlier analysis algorithm, has high accuracy in detecting local wheel defects.

WILD statistics may underestimate actual loading levels since the sites are designed with premium components to eliminate load fluctuation caused by inconsistencies in track geometry and support conditions (van Dyk et al., 2013). Therefore, the related infrastructure must be appropriately selected, and several factors may be required in establishing the design wheel load for the track system (van Dyk et al., 2017).

3.3.3 Wheel Profile Monitoring

Wheel Profile Detectors check wheel tread as rolling stock passes. The utilisation of digital image acquisition and processing provides the information which will later be compared with the standard profile. In addition, the difference between the exact and intended profile is recorded. Thus, the manual inspection of the wheel profile can be removed while reducing the human procedures (Barke & Chiu, 2005b).

Lasers are the illumination sources, while an image of the wheel profile is provided by a digital camera, as shown in Figure 3-35. However, the collected profile is distorted due to the camera's angle, along with the laser concerning the wheel. As a result, output images must be transformed into three-dimensional coordinates to compare each profile to a specification.

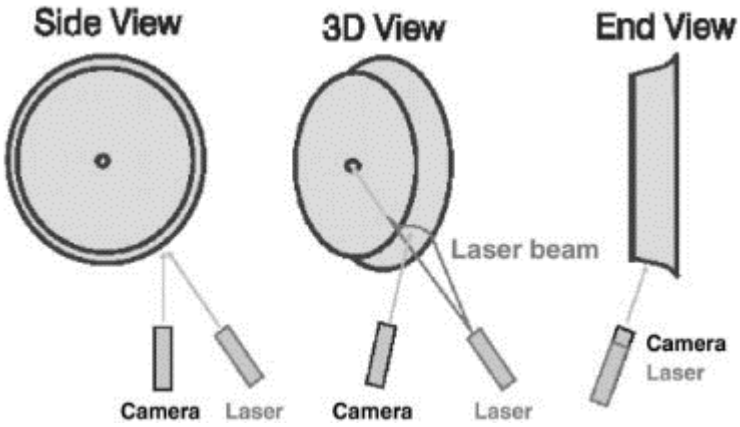

Figure 3-35: The arrangement of laser probe and digital camera of the wheel profile monitoring (Barke & Chiu, 2005b).

3.3.4 Trackside Acoustic Array Detectors

The arrays of high-quality microphones were applied to gain the audible noises generated from the axle bearing of in-service rolling stock (Amini, 2016). Trackside Acoustic Array Detectors (TAADs) could be named differently depending on the registered commercial name. Since the 1990s, TAAD has been used to identify defective roller bearings on railways (Cline et al., 1998).

Wayside acoustic detection requires a complex setup of electrical equipment and hardware, including a single or a group of microphone arrays, cables, data acquisition, and processing systems. Defective bearings frequently have higher signal amplitudes at rotating frequencies than healthy bearings. According to the study, defective bearings emit demodulated spectral frequency peaks that depend on speed, load, and size (Cline et al., 1998).

Even though TAADs provide positive aspects for the defect detection system, the efficiency of their principles is still not perfect. Thus, HABDs should also be available as another wayside system to detect axle bearing faults (Amini, 2016a; J. Wang et al., 2014). Furthermore, it was stated that Trackside Acoustic Detection System (TADS®), another commercial name for TAADs, is also working together with HABDs in the field (C. M. Tarawneh et al., 2016).

Another issue related to the utilisation of TAADs was mentioned by (Amini, 2016a). The installation of the site requires ample space for the housing structure. Therefore, this application could cause a problem when installed in tracks with a third conductor rail present.

Three problems related to TAADs were outlined, including demodulation of acoustic data, Doppler effect, and reduced defect frequency (J. Wang et al., 2014). Therefore, they proposed a new synthetic-detection technique to mitigate these issues. Modeling and experiments suggest that the recommended strategy can improve TAAD detection performance.

3.4 Summary

Visual, electromagnetic, and ultrasonic inspection techniques which are commonly used for rolling stock wheelset condition monitoring, were presented. While in-service condition monitoring helps reduce maintenance work, it is not widely used. Phased array ultrasonic eddy current testing and alternating current field measurements, limited to predictive maintenance usage, were also described. Moreover, it was noted that available wayside and onboard condition monitoring techniques are low, cost-effective, complex, and insufficient. Such techniques were presented with their advantages and drawbacks. The output data should provide additional information regarding wheelset components to obtain predictive maintenance. Therefore, multiple generated defects inside the wheelset at an early stage are required to be revealed. Finally, the newly developed condition monitoring system using advanced techniques is the key to solving the problem.

Chapter 4: Acoustic Emission, vibration, and signal analysis

4.1 Principles and application on rolling element bearings

Rotating machines during operation with time may be subject to vibrations which sometimes can be a sign of degradation and can give rise to serious concern regarding structural integrity. Vibrations are normally associated to the progressive degradation of individual components or groups of components depending on their severity. In general, vibrations are related to a component's oscillatory motion around a resting point, which is referred to as the equilibrium position. Thus, by monitoring vibration signals acquired from rotating operating machines it is possible to ascertain the health of the individual components and the root cause of the vibrations. Normally, to identify the exact component or components suffering from degradation using vibration measurements, it is also necessary to have knowledge of the kinematics of the system. Thus, the rotational frequency of each component within a rotating machine can provide useful information related to the heath condition of the machine. Vibration analysis has been employed for decades to detect faults and incipient failures, allowing maintenance engineers to carry out corrective, condition-based or predictive maintenance actions before catastrophic failure occurs (Tandon & Choudhury, 1999b).

Rolling stock wheelsets are rotating components which have a critical function since they can lead to derailment if they fail. Wheelsets are also the part that interfaces with the railway infrastructure under different loading conditions and challenging operational environment. While the rolling stock is moving, the wheelset is subject to forced vibrations. This type of mechanical phenomenon happens when an object vibrates due to external excitation, such as a hammer strike. This results in vibrations to be excited over a range of frequencies. The techniques related to signal analysis will effectively reveal the vibration spectrum allowing the detection of faults that may affect different rotating machine components.

Vibration analysis is typically carried out using industrial accelerometers which are based on piezoelectric crystals. However, recent developments in electronics have allowed the gradually increasing use of micro-electromechanical system (MEMS) accelerometers in the place of conventional piezoelectric industrial accelerometers at least in some industrial applications. This is because MEMS accelerometers' response sensitivity has been increased, and their working frequency range has been expanded to encompass higher frequencies, boosting their utility. Moreover, their low power consumption allows more versatile applications to be realised, which are not as straightforward or easy with conventional piezoelectric accelerometers. Accelerometers have been widely used for fault detection in different types of rotating machinery for decades. One of the important requirements for any type of sensor, is to provide a satisfactory SNR to enhance sensitivity as well as facilitate further signal processing. Many studies have confirmed the usefulness of vibration analysis for assessing the structural health of rotating machines either continuously or intermittently (Amini, 2016b; Amini et al., 2017; Entezami et al., 2020b; M. Papaelias et al., 2016c).

Acoustic emission (AE) is another structural health monitoring approach that detects audible and inaudible noise during component rotation and elastic waves released by the components.

Both vibration analysis and AE testing require the application of effective signal analysis. This chapter presents the operational principles of these techniques and their application in the industry. Moreover, a comparison has been performed to reveal the advantages and disadvantages of each of the technique which in reality are not competing each other but are complementary to each other when used in combination. The range of available signal analysis methods will be reviewed with a focus on their use for analysing vibration and AE signals associated with railway wheelset monitoring.

4.1.1 Acoustic emission

Modern AE testing due to its passive nature, has been considered to be a distinct NDT technique in comparison with other methods. The potential of using AE for the investigation of healthy and damaged specimens made from N50A beryllium and 7075 aluminium was revealed (H. L. Dunegan et al., 1968). According to their conclusions, the characteristics of the AE signals recorded from flawed specimens were related to much higher stress intensity than those from unflawed specimens. However, they discovered some drawbacks during the use of AE with the most important being the generation of noise in the frequency range selected for detecting the useful AE signals and the quality of the AE sensors (H. Dunegan & Harris, 1969).

Acoustic emissions are elastic stress waves created in deformed and loaded material. When a crack propagates, the energy is released as a stress wave. The AE sensors installed on the test piece detect the generated AE signals (Roger, 1979a). The elastic waves result in the oscillating movement of molecules underneath and at the surface of the material being monitored. A substance deforms elastically when exposed to temperature or stress. Stress waves cause surface displacements in the measured material, which may be detected by piezoelectric AE sensors (Pao et al., 1979; Pollock, 1969).

AE was originally considered for use in static applications. During that time, AE was widely used to detect crack growth in various materials and became a powerful tool for structural integrity surveillance and the fundamental study of fracture mechanisms as well as for monitoring crack growth under cyclic loading environments. The use of AE required further developments since it was limited to specific work and laboratory experiments, even though the use of AE phenomenon in solids is a valuable tool for both structural integrity monitoring and fundamental research into material failure causes, especially for pressure vessels, wire ropes or cables (Hutton, 1970).

AE was developed for fracture monitoring of statically loaded materials, later dynamically loaded structures, including spinning machinery. Early detection of faults was found to be feasible with AE because piezoelectric sensors offer higher sensitivity than other methods used previously. This is critical for any CM solution since the ultimate aim is to provide trustworthy data that can be analysed to optimize maintenance schedule and avoid unexpected failures. (Mba & Rao, 2006).

One of the initial low-speed studies on AE focused on defect detection in roller bearings (Roger, 1979b). They suggested that an online assessment of the signals arising from the mechanical noise, vibration, and heat, normally related to defects, could be used to effectively assess damage severity. The analysis carried out would permit the identification of faults of concern helping prevent unexpected downtime by allowing the timely planning of maintenance. AE and vibration analysis were used on anti-friction bearings in offshore slewing cranes. They also applied different signal processing techniques, finding that the kurtosis value can be utilised to characterise the output signal with respect to the presence of spalling damage. Due to the high sensitivity, damage in the bearing's race and rollers may be detected.

AE signals are often high frequency and therefore, they can attenuate rapidly. Therefore, AE sensors should be placed at suitable locations to optimise the detection capability of possible faults in components of interest. Nonetheless, mounting the AE sensor on a non-rotating machine component is frequently feasible, since the signals will be transmitted through the structure even if the AE sensor has not been mounted directly on the component being monitored, such as a bearing or gear (Catlin, 1983).

Before AE, vibration techniques were widely used to check the condition of rotating machines. However, subsequent tests proved the capability of AE and its usefulness for monitoring rotating components. A comparison between AE and vibration monitoring of rolling element

bearings was presented (Hawman & Galinaitis, 1988). The vibration data failed to reveal useful information on several small outer race defects. Even it was retrieved from improved vibration monitoring, adding multiple sensors, and adaptive noise cancelling techniques. On the other hand, AE can demonstrate the capacity of AE monitoring to detect small defects. It was noted that the available signal analysis techniques at that time were limited in terms of the utilisation of AE signals. The main concern was the background noise that affected the output data. Compared with the background noises, the low-frequency vibrations associated with tiny race defects provided insignificant energy to the system. However, stress wave emissions over 100 kHz can offer a clear indication of the problem, providing an earlier and more reliable signal of bearing deterioration.

The ability to classify the defect of rolling element bearings was mentioned in the research as AE can effectively deal with high noise environments during the monitoring approach. Another important aspect was the high SNR that played an important role in any utilisation of defect detection using signals from the selected sensors (Hawman & Galinaitis, 1988).

During the 2000s, various researchers developed and extended the use of AE to a wide range of NDT for industrial sectors as the AE phenomenon can reveal useful structural health information. For example, a review of AE applications indicated that AE is a passive and receptive technique, different from other NDT techniques (Vallen, 2002a). On the other hand, AE sensors are used to find surface flaws caused by stress waves that are stronger than normal and are emitted from the source of interest. Stress waves are subsequently transformed into electric signals that may be seen after digitisation via the piezoelectric effect.

Since the 1980s, the use of AE has been extended to monitor dynamic approaches especially rotating machines. However, many research studies usually saw the limitation of the operational speed of rotating bearings. One of the first examples was applying AE transducer

S1000BM, calibrated to work under high frequency up to 1 MHz to respond to the high-frequency displacement of the surface being monitored (J. D. Smith, 1982). The result revealed that the AE sensor might not deal with relatively high background noises when running bearing at low speeds. However, it can work with medium speeds better than acceleration signals. He also mentioned a common problem with acceleration and acoustic emission: the isolation of defect pulses from artificial pulses. Every time a ball inside the bearing faces the defect, there was a response from the AE transducer during the speed of once-per-revolution of the bearing. The development of the ae transducer was needed to cope with better defect detection.

A few years later, an experiment by (McFadden & Smith, 1984a) showed that the non-uniform frequency response profiles of an AE transducer would make it harder to monitor vibrations of bearings at high speeds. Based on the results of studies that included both axial strain and base bending, base bending contributes significantly to the amplitude of the signal produced. The AE transducer responded to the bending generated by the bearing housing's local distortion as each ball passed. As a result, the signals might reveal only low-frequency noise that might affect the detection of small defects. Because of the AE transducer's exceptional sensitivity to base bending, small defects in bearings may be detected at extremely low rotational speeds. While at normal speeds, most of the base bending signal is masked, and some noise consequently occurs.

According to AE signals of rolling element bearings during the experiment, bursts are generated from the set of defects on the roller and raceway interfaces. Different defects on the inner race, outer race, and roller would produce different burst frequencies. The AE sensor will transfer the helpful information that will be further used for feature extraction. Furthermore, this application can introduce online monitoring for bearing that does not require a hassle system and human operation, making the monitoring behave like an automatic detection system. (C. J. Li & Li, 1995) tried out an experiment setup that comprises a data acquisition

package, which provides an Analog-to-digital conversion of the input signal, where software algorithms were applied under control by a supervisor application. According to his study, the data acquisition package contains an AE transducer, an amplifier, a band pass filter, and an Analog-to-digital converter. Later, other researchers will find all these components in most of the AE setups.

As the frequency bandwidth of AE measurement ranges from 100 kHz to 1 MHz, the vibrations of defects that occur in a bearing material by phase transformations and other mechanisms will be discovered. (Miettinen & Pataniitty, 1999) mentioned that AE measurement effectively detects defects in low-speed bearings. Before testing, the test bearing had been organically damaged on its outer race during regular industrial usage. The flaw was detected using the AE time signal and the slowest AE pulse count approach.

Because the voltage levels in AE measurements are relatively low, the impact of environmental interference on the measurement must be considered. Environmental interferences can be triggered by other sources than the rotation of the bearing. Likewise, the higher rotating speed might generate background noise, making it difficult to determine the cycle time of the fault frequency (Miettinen & Pataniitty, 1999).

The pattern of the AE is influenced by factors such as the size and form of the fault on the rolling surface. When the rolling element passes across the fault, it generates an emission burst cluster. In this circumstance, selecting the appropriate time for the pulse count approach is challenging, and the different emission clusters are likely distorted together. As a result, the measurements were also carried out using low-frequency measuring techniques. In their study, the rotational speed limit at which the defect could still be reliably detected using those approaches was between 10 and 20 rpm. (Miettinen & Pataniitty, 1999).

(He et al., 2011) researched AE bursts for complete ceramic bearing defect detection and diagnosis. They experienced the effectiveness of their experiment based on bearings with five different conditions: healthy bearing, inner race defect, outer race defect, cage damage, and ball defect. The test relied on full ceramic bearings coupled with the motor shaft controlled at 600rpm. The AE signals were retrieved at a 5 MHz sampling rate and collected in a total number of 400 AE bursts. The AE burst data was collected using two wide bands (WD) type AE sensors and a PCI-2 data collecting board. AE sensors were attached to the bearing housing with special adhesive. Bearing seeded fault tests were performed on a modified bearing test rig, as shown in Figure 4-1. However, the system used in this experiment still requires other related devices for a better quality of output signals, for example, a pre-amplifier. Further analysis based on the extraction of three AE features using an empirical mode decomposition (EMD) revealed that the greatest condition indicator combination is the group average of Root-Mean-Square (RMS) and the group standard deviation of RMS, which provide the classification accuracy of 93%. In contrast, the group average of kurtosis individually performed the lowest classification error among three AE features (RMS, peak value, and kurtosis).

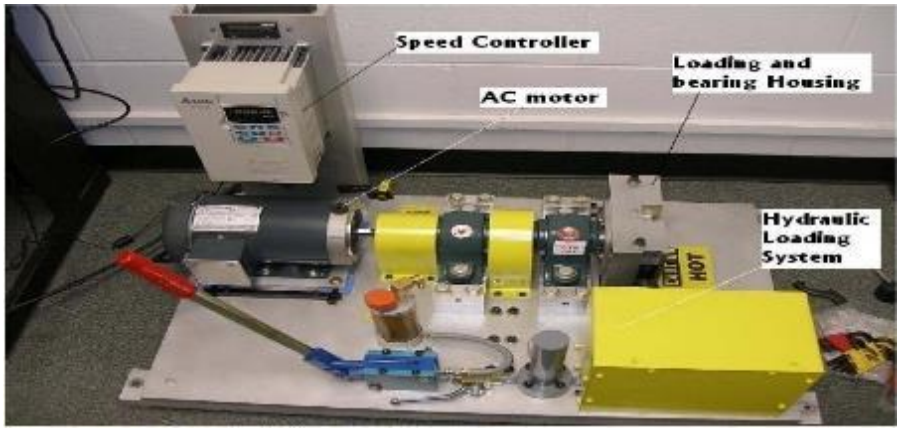

Figure 4-1: The ceramic bearing test rig (He et al., 2011).

In most circumstances, the frequency bandwidth in conventional AE measurements is 20 kHz to 1 MHz. However, it is more helpful to focus on 100-500 kHz. AE signals generally develop quickly and unpredictably, not observed in ultrasonic or vibration testing. To begin the process of evaluating AE signals, it is necessary to first differentiate them from passing waves. The voltage threshold has been set up to reveal AE signals apart from signals that go above the voltage level. The amount of background noise determines these threshold values (Grosse & Ohtsu, 2008).

Figure 4-2 is a typical example of an AE signal. The parameters that can predict fracture or crack development have been identified. The following are the signal parameters that are often utilised for analysis;

- Duration: A waveform's time interval between the AE signal reaching the first threshold and the last AE signal beginning to fall below the threshold.
- Rise: A waveform's time between the AE signal exceeding the initial threshold to the AE signal reaching its maximum amplitude.
- Amplitude: The amplitude is connected to a system feature that can indicate detectability based on a voltage threshold.
- Hit: When a signal first passes a certain threshold, the system begins to collect data for the analysis. A hit describes a waveform of the mentioned interval is a waveform of that interval when AE activity and other characteristics are detected. For example, there is one hit, as seen in Figure 1.
- Count: The amount of times the signal's amplitude surpasses the threshold. Figure 1 demonstrates that a hit has nine counts.

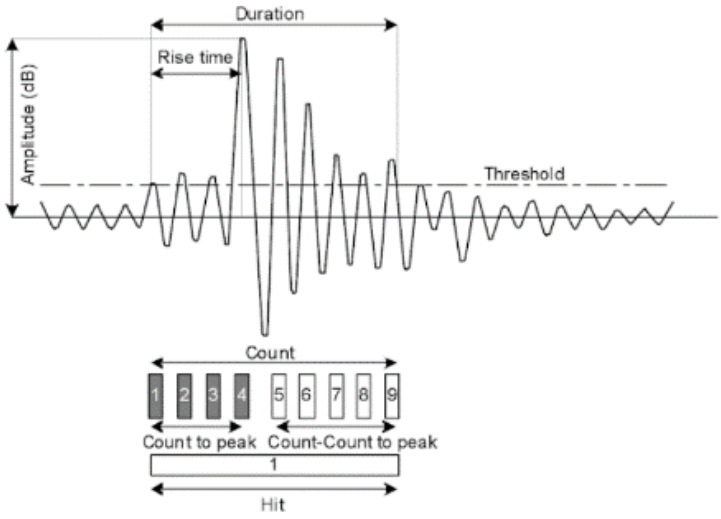

Figure 4-2 Typical AE signal with related parameters (Grosse & Ohtsu, 2008).

One of the important terms that influence acoustic emission activity is the Kaiser effect. The Kaiser effect states that if certain stress is given to material and it causes acoustic emission, more emission will not be produced in the material until the predetermined amount of stress is exceeded, even if the load is entirely withdrawn and then reapplied (Miller, 1987). As a result, the kaiser effect stimulate the crack propagation and growth. It can also impact the AE activity induced by a bearing flaw when a rolling element passes across the fault and creates stress in the material.

Different factors from the signal can be derived to determine an AE source's relevance and interpret the AE signal. Signal waveform is defined by source qualities, signal path, sensor features, and measurement system. The parameters retrieved from the signal are determined by the kind of signal (Miettinen & Pataniitty, 1999).

Advantages of AE include:

- Low-cost operation as it was utilised

AE offers a low-cost monitoring solution for machines with few sensors. It is a solid procedure that has been standardised, where the proper analysis is provided (Amini, 2016b).

- Fast Installation

The installation of AE sensors is quick and simple, requiring just minor surface preparation. Since the AE transducer requires only a simple magnetic coupling using simple adhesives, for example, Araldite. The mixture of base and solvent can be mixed up and ready for measurements within a few minutes (Amini, 2016b).

- High sensitivity

AE generally has higher sensitivity than other sensing techniques, especially conventional vibration analysis. Thus, it helps AE measurements tackle an early detection of functional defects (Amini, 2016b).

- High SNR

AE has a greater SNR than vibration analysis for gear pitting detection. (Singh et al., 1996). Since AE can effectively detect the bearing defects on slow-speed operation using the pulse count method, increased rotation speed would generate higher AE signal resolution. Therefore, a better SNR would be available (Miettinen & Pataniitty, 1999). This enables the efficient application of generic time-domain signal processing methods (Amini, 2016b).

However, Disadvantages of AE were mentioned in several studies which contain:

- Weakened signals along with distances

Distance and interfaces degrade output signals. AE sensors should be placed as close to the predicted emission source as practicable (Amini, 2016b).

- Source variations

More than one source simultaneously would trigger the output resulting in the noise as an unwanted signal in the data (Miller, 1987).

- Special signal analysis

The use of exclusively designed signal analysis is required to identify defects from AE signals (Miller, 1987).

- Sensitive to non-repetitive signals

AE sensors made from sensitive piezoelectric sensors generally give rise to irregularities in the collected signals. As the high SNR is provided, AE signals can have an impact on the measurement in both positive and negative ways (Holroyd, 2009)

4.1.2 Vibration

The vibration technique has been utilised to monitor rotating machines before AE technology. However, when those machines operate for many cycles, enough to generate some changes in components, especially bearings, vibration caused by faulty bearings would change the characteristics of rotating elements according to related causes. As a result, the bearing's distinctive features suit vibration monitoring and other monitoring approaches (Malla & Panigrahi, 2019).

Rolling components and a bearing surface imperfection create an impact force, which then transfers to other locations, such as the inner race, outer race, balls, and cage of the rolling element bearing (Malla & Panigrahi, 2019).

A review of vibration and acoustic measurement methods for the detection of defects in rolling element bearings was presented by (Tandon & Choudhury, 1999b). Only widely used measurement method for equipment CM can discover 90% of machine problems by analysing vibration signals.

Rolling element bearing defects are due to several causes, as stated in chapter 2. Consequently, rolling defects are categorised into distributed and localised defects (Nerella et al., 2017).

Changes in rolling element and raceway contact force intensified distributed faults. Vibrations caused by extensive flaws must be investigated for bearing quality inspection and CM (Patidar & Mandloi, 2015).

The vibration level is significantly affected by impact energy, recording location, and bearing construction. Distributed faults increase the rolling component and raceway contact force, creating vibration (P. Gupta & Pradhan, 2017). The vibration response of the bearings was generally analysed in the frequency domain. Since sparse defect frequencies match with local defect frequencies, it is quite difficult to distinguish from frequency itself whether a peak is local or spread (Nerella et al., 2017).

In order to stimulate localized defects, there are two approaches that researchers widely use. The first method is to operate the bearing unit until the defect is shown while monitoring the changes in the vibration output signal (Kim, 1984). Adding an artificial fracture to a bearing and evaluating its vibration response is selective (Tandon & Nakra, 1992a).

A remarkable growth in contact stresses causes pulses of short duration because of the interaction between the element's local defect and its mating surface. These pulses generate vibration, which may be measured (Sunnersjö, 1978).

Bearing vibration signals are separate. Fault, non-uniform loads, flexural bearing modes, machinery-driven vibrations, and noise are sources of those signals (Y.-F. Wang & Kootsookos, 1998).

Bearing vibration monitoring consists of three major stages. The first stage is data collection, which involves capturing raw vibration signals. The second stage is feature extraction, which involves using the right vibration signal processing techniques to pull out relevant features. Generally, the problematic bearing's vibration signal can be assessed in time, frequency, or

both. Last, system maintenance is chosen based on extracted features. (P. Gupta & Pradhan, 2017).

The illustration of the test rig studied by (Saruhan et al., 2014) for vibration analysis of defects from ball bearings is shown in Figure 4-3. A three-phase AC induction motor is coupled with a variable speed control device to incorporate multiple speeds. The mounting housings are outfitted with two bearings. The normal and defective bearings are inserted in the inboard bearing housing. In addition, the normal state bearing is fitted in the outboard bearing housing. The use of four 608A11 accelerometers was distributed vertically and horizontally with a 100 mV/g sensitivity and a frequency range from 0.5 to 10 kHz.

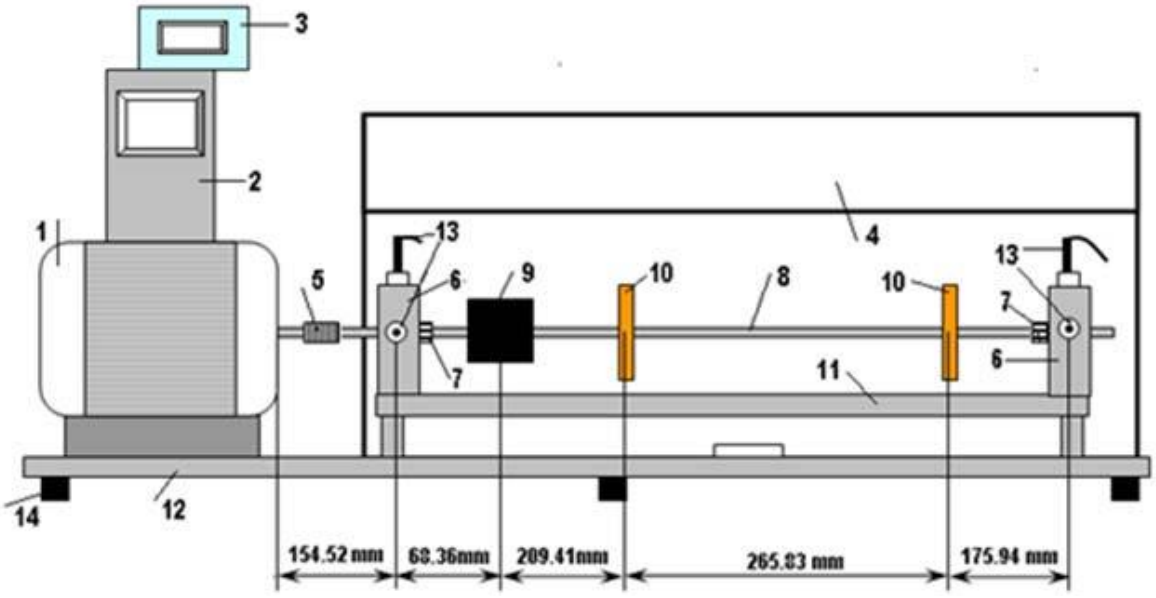

Figure 4-3: Bearing test rig (Shiroishi et al., 1997a).

Another bearing defect detection of seven damage levels of a tapered roller bearing using a Wilcoxon 625T high-frequency accelerometer to gain vibration signals and a Physical Acoustic Corporation type R04 AE sensor to acquire high-frequency stress waves was presented by (Shiroishi et al., 1997a). This is one of the primitive comparisons between accelerometer and AE sensor for defect detection of roller bearing. The defect-related frequencies were

determined at 1200 rpm and used for signal analysis using high-frequency resonance technique (HFRT) and an adaptive line enhancer (ALE).

According to the study, a programable filter was used to mitigate aliasing. In addition, low-pass filters were also applied to improve accelerometer and AE data acquisition. Compared with other bearing test rigs, the common component is the hydraulic loading cylinder to generate the desired loading conditions for the experiment. Also, the data acquisition (DAQ1200) was applied to transfer both output data from the accelerometer and AE sensors to the computer (PC). As a result, the demodulated AE signal produced by the processor (ALM8) was comparable to a raw signal modified using the HFRT technique. Figure 4-4 displays the setup of presented experiment.

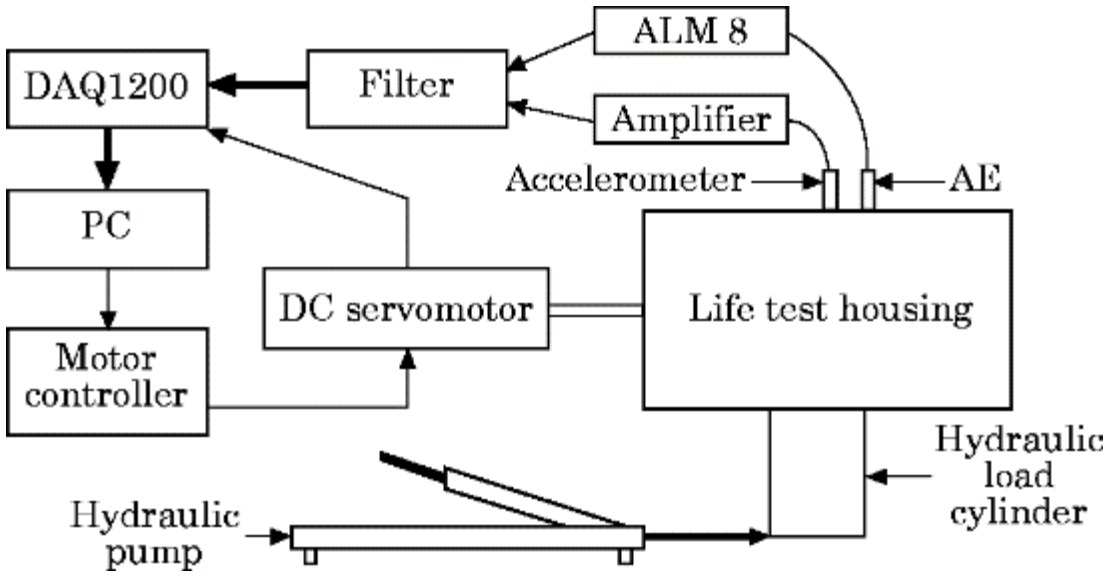

Figure 4-4 The experiment setup for AE and accelerometer monitoring (Shiroishi et al., 1997a).

The outer raceway fault has the shortest vibration transmission path to the transducer. The study by (McFadden & Smith, 1984c) discovered that the spectrum data collected for the ball defect, particularly in the absence of a loader, does not indicate harmonics of the defective frequencies. As a result, the ball defect has less frequency harmonics. The defect may not

always be in touch with the races due to a free spin in either direction. While the presence of an outer raceway defect was observed by the corresponded harmonics or ball pass frequencies.

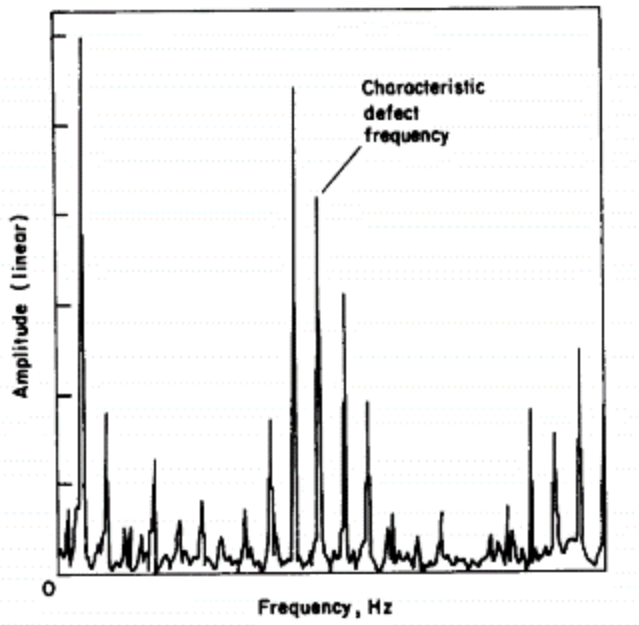

Figure 4-5 Envelope Spectrum of bearing with inner race defect (McFadden & Smith, 1984c).

The envelope spectrum was selected as the approach to provide the frequency spectrum, as illustrated in Figure 4-5. Each spectrum clearly shows the specific defect frequency (McFadden & Smith, 1984b). A model for evaluating a rolling element bearing's demodulated vibration under continuous radial load with an inner race fault has been devised. Vibration model is created by combining bearing load distribution and transfer function amplitude at rolling element passage frequency. Finally, the model can predict the spectrum's frequencies and further amplitudes of the bearing components.

According to a review of CM of rolling element bearings by (Malla & Panigrahi, 2019), the widely used vibration analysis procedure starts with the proper location for installing sensors. It does require the appropriate cleaning of that assigned area. Then, accelerometers should be correctly connected with ports on the data acquisition. Also, the direction of each axis (axial

and radial) should be carefully selected to provide useful data. Furthermore, the other related equipment, including the FFT analyser and amplifier, would provide better demodulated signals in the time and frequency domains. Lastly, the results from the software will be the input of the diagnosis to identify the sources of the defects in each piece of equipment. As a result, bearing load distribution and transfer function amplitude at rolling element passage frequency create vibration model.

Roller bearings for the railway were combined with the automatic computer systems, enabling the diagnostics ability and condition prediction using a single vibration measurement. The study by (Azovtsev & Barkov, 1970) revealed the comparison between diagnostics of different conditions of locomotives, including the static lifted locomotives, the static locomotives placed on a special stand, the moving locomotives with the roller defects, the moving locomotives with the deviations in wheel circularity, and the moving locomotives on the track with gaps between rails. They recommended two techniques to monitor rolling element bearings in locomotives. The first is to provide locomotives with roller stands equipped with diagnostic computer systems to ensure the rotation of wheels from an external drive. This will secure wheel rotation during the measurements. The second is to employ specialised equipment to measure roller bearing noise from passing trains to solve the modulation of the signal problem.

The study of rolling stock bearing CM systems for a wagon used to transport sugar cane was presented by (Lamari, 2008). The problems related to preventive maintenance include reducing the downtime and impacts on safe operation. The system relies on the narrow-gauge track network. Although the smaller system compared with the normal freight and passenger train, the design concept of the presented vibration system for bearing CM could be well adapted to the existing railway system. Figure 4-6 shows the accelerometers attached to each wheelset in the wagon, where both of them are placed on the wheel rotators, using either a hydraulic or electrical drive. As the wheels revolved at a predetermined pace, accelerometers situated on

the loaded side of the bearing housings would capture vibration data for each bearing simultaneously. The appropriate installation of the accelerometer must be provided, as the output data would not contain useful information. Also, the moving wagon's speed must be monitored to work with the vibration frequencies. He mentioned the main benefit of using a vibration system instead of the others would be the portable module to be adjusted for different sites, enable the tracking of bearing problems, and provide significant earlier warning of bearing failures. However, a considerable amount of research and development is required to thoroughly understand its efficiency and functionality.

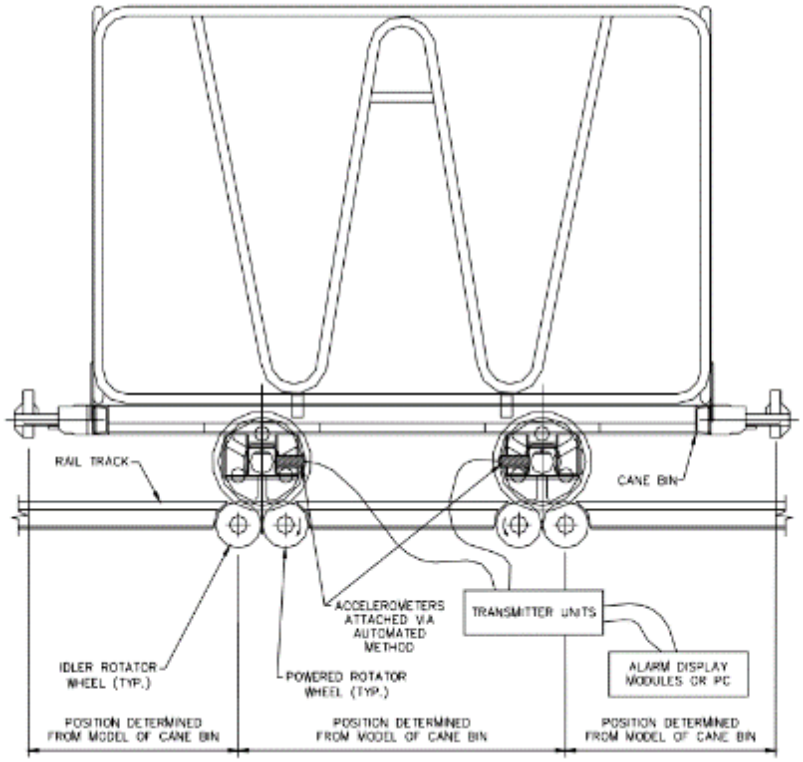

Figure 4-6 Concept design of the sugar cane wagon coupled with the monitoring system (Lamari, 2008).

The vibration analysis of bearing CM will be successful if the essential parameters, including loading conditions, operational speed, and time information, are provided. Moreover, the bearing dimensions are also needed for further calculations of fundamental frequencies.

Advantages of vibration include:

- Well-known approach
- Portable system
- Fundamental signal analysis

Despite many advantages of vibration analysis, there are some limitations that other techniques would mitigate based on a similar system.

- The ability to predict the developing faults

4.2 Application of acoustic emission and vibration techniques

Several case studies are using AE and vibration analysis for inspection techniques. As mentioned earlier, most of them are related to rotating machines, especially bearings. However, several implementations of a more advanced system, including gears, wind turbines, rotors, and shafts.

4.2.1 Rotating machines

The use of vibration analysis for the gear fault diagnostics based on fundamental statistical features was studied by (Lebold et al., 2000). Since many feature vectors were previously reviewed, they mentioned that the details from those references were not clarified in the pre-processing process. The feature extraction techniques for detecting gear failures were divided into five main groups upon their pre-processing preferences. The groups include raw, time-synchronous averaged, residual, difference, and band-pass mesh signals. Each one contributes the advantage over the signal analysis for gear fault detection.

Early detection of gear fault using acoustic emission by (Raad et al., 2004) has proved the use of AE could be competitive with the widely used vibration technique. The experiment was

based on a test rig using a gearbox unit comprising two single-stage gear units. Each unit relies on different spur gears with a number of 20 teeth and 40/40 teeth, respectively. At a speed of 1000 rpm, the output data analysis was acquired by calculating the kurtosis value of each tooth. After the threshold has been assigned, the kurtosis amplitude can reveal an early detection of gear defects before the spalling fault appears. However, the generated burst that is the detection indicator is not powerful enough to remain visible after the failure has occurred. Furthermore, they also compared AE signals with vibration signals on the spectral analysis as refer to the early identification of gear faults. The final results revealed that using AE in conjunction with vibration would be more effective as AE contributes to wider frequency band on spectral analysis and reveal harmonics related to the faults on the spectral envelope analysis, as displayed in Figure 4-7.

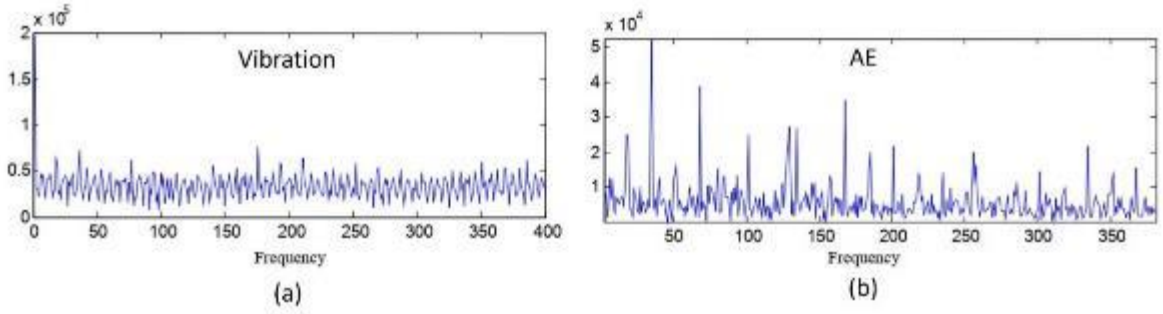

Figure 4-7 The squared envelope of (a) vibration signal and (b) AE signal of the gear teeth (Raad et al., 2004).

Artificially induced gear cracks were used to monitor a lab-scale, single-stage gearbox used in rotating machinery and power drivetrains. Numerous hours of testing were carried out, and several measurements were made utilising acoustic emission and vibration monitoring. The study by (Loutas et al., 2009) aimed to extract parameters–and features and evaluate their diagnostic behaviour to find the most promising and appropriate for future health monitoring systems. Time, frequency, and discrete wave transform parameters were chosen. AE and

vibration techniques highlighted the significant changes in gearbox operation based on the transition in parameter values. Figure 4-8 shows three AE sensors and two vibration sensors on a single-stage gearbox testing bench. The diagnostic results using novel and conventional proved the potential application of both monitoring techniques for CM of a single-stage gearbox.

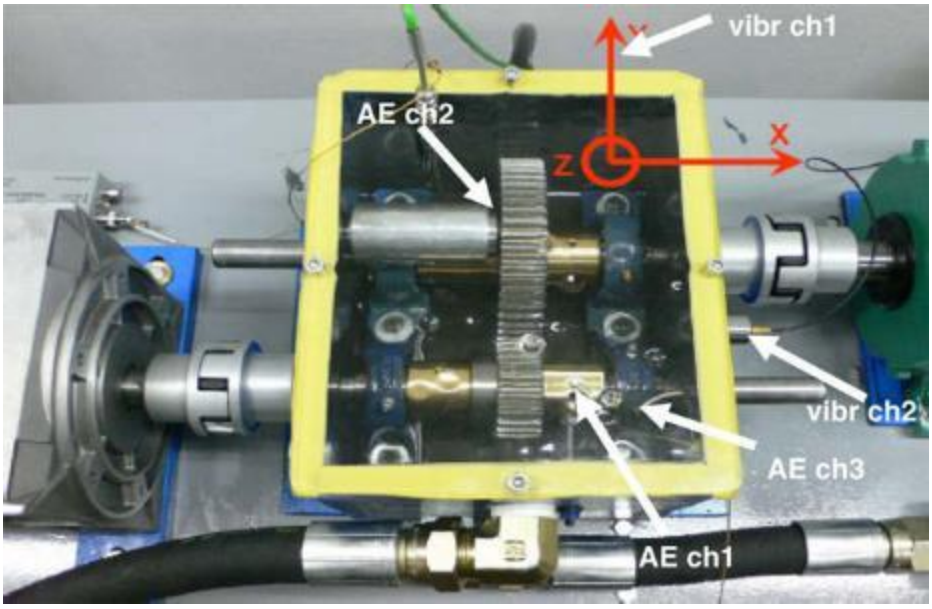

Figure 4-8 Experiment setup for gears testing with AE and vibration sensors (Loutas et al., 2009).

AE was used to monitor wind turbine blades during static and fatigue testing in the 1990s (Shiroishi et al., 1997b; Sutherland et al., 1994). They utilised AE for routine blade inspection by developing specially modified testing. The first experiment stated that AE could be effectively used for primary blade failure detection. AE can notice the build-up of hot spots on the structure when the load exceeds the threshold before the wind turbine blade fails. Even though no significant signal analysis was provided, they concluded that AE events were useful for potential failure verification. The experiment relied on time-of-flight measurements of AE events to determine the velocity of the acoustic wave, which will be used to examine accurate source location. Two AE sensors were mounted at different positions, one close to the source

and another placed 50 cm away. The generated AE signal was stimulated by pencil lead breaking on the surface of the turbine blade (Sutherland et al., 1994). However, since the Fiberglass reinforced plastic is a typical material used to fabricate large wind turbine blades, the application of AE would be different from the general methods applied with metallic structures. Cracks in the link between two elements of the structure, such as a joint between a spar and the skin, and rips in the skin or a spar are the two major failure modes in a wind turbine blade. AE has been highly successful in detecting all of these failure causes and, in certain cases, identifying them based on amplitude analysis of AE signals. Unfortunately, the significant acoustic attenuation in FRP limits amplitude analysis unless the origin of the individual signals can be determined and adjustments for distances travelled added to the signal amplitudes (Beattie, 1997).

(Joosse et al., 2002) also mentioned that AE could identify and characterise damage processes in wind turbine blades, particularly with non-audible signals produced by damage propagation at low loads. Their analysis was based on the blade certification procedure and laboratory static and fatigue blade testing to failure. Experiments demonstrated NDT using AE on a set of small blades.

Pattern recognition software and/or strain-based filtering are required for the assessment. Furthermore, detecting large amplitude and high energy events appears to be extremely relevant in failure prediction, supporting the expectation that field monitoring is possible.

Vibration and AE analyses were used to create a new wind turbine gearbox and generator state monitoring system with automated alarms (Soua et al., 2013). Wind speed and turbine power generate vibration and AE signal. AE signals are required to identify shaft and gearbox irregularities.

The vibration technique was implemented for a non-destructive evaluation of the integrity of structures, predominantly for structural doubly tapered bars and automotive camshafts (Adams et al., 1978). Constant vibration response determines damage detection method. To be precise, they measured the natural frequencies up to three modes of damage levels, including undamaged conditions. Their concept relies on additional flexibility of the rotor together with the stiffness using receptance analysis techniques. As a result, the change in the natural frequency is noticed where the damage location would also be identified. Also, the magnitude of the additional flexibility is constant for every mode.

Vibration analysis can employ motor current signature fault analysis (MCSA). With the existence of the interbar current, the core vibrations are generated in the axial direction. Thus, the multivariable supervision systems presented by (Concari et al., 2008) allow online monitoring of induction motors. The sensor uses polysilicon springs to sustain the system over the silicon wafer and withstand acceleration forces. Figure 4-9 shows the components of the vibration signal acquisition setup which includes preamplification and amplification to improve the signal condition. To be concluded, a custom-built sensor was capable of detecting machine vibrations caused by broken bars and those caused by interbar currents.

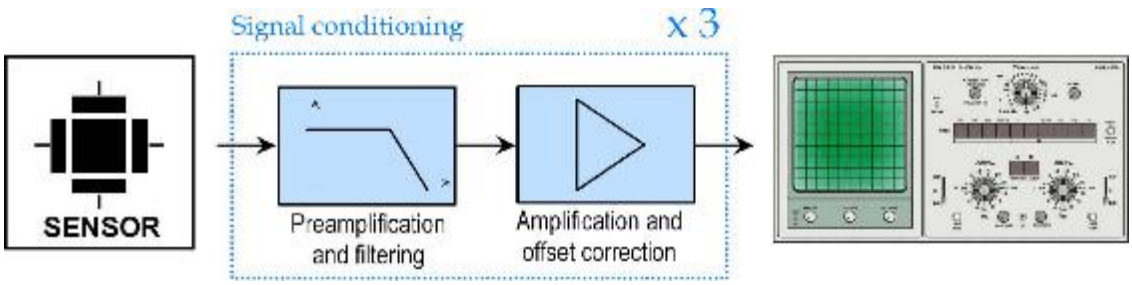

Figure 4-9 Vibration signal acquisition setup (Concari et al., 2008).

4.2.2 Railway uses

The study of AE's rail-wheel interaction is based on laboratory conditions using rail-mounted sensors with featured rail defects. The remarkable result proved that AE signals could reveal

the minor surface defects, which reoccur at a distance according to the wheel circumference. Furthermore, the amplitude of the 'background' AE recorded from the typical rail–wheel interface has been determined to be speed-sensitive (Entezami et al., 2016). Defects and misalignment between rail and wheels could impact the AE by the normal interaction. Therefore, the magnitude analysis, including Peak and Kurtosis events, was chosen to inspect the defect-AE correlation. This technique might be used to measure the cumulative intensity of the rail–wheel interaction, leading to novel rail monitoring devices (Thakkar et al., 2010).

A laboratory-based experiment utilised acoustic emission for wheel flat detection on a scaled-down test rig comprising a single wheel running on a full-circle track profile was later presented (Thakkar et al., 2012). The study used simulated wheel faults to create online wheel flat detection approaches utilising rail-mounted AE sensors as illustrated in Figure 4-10.

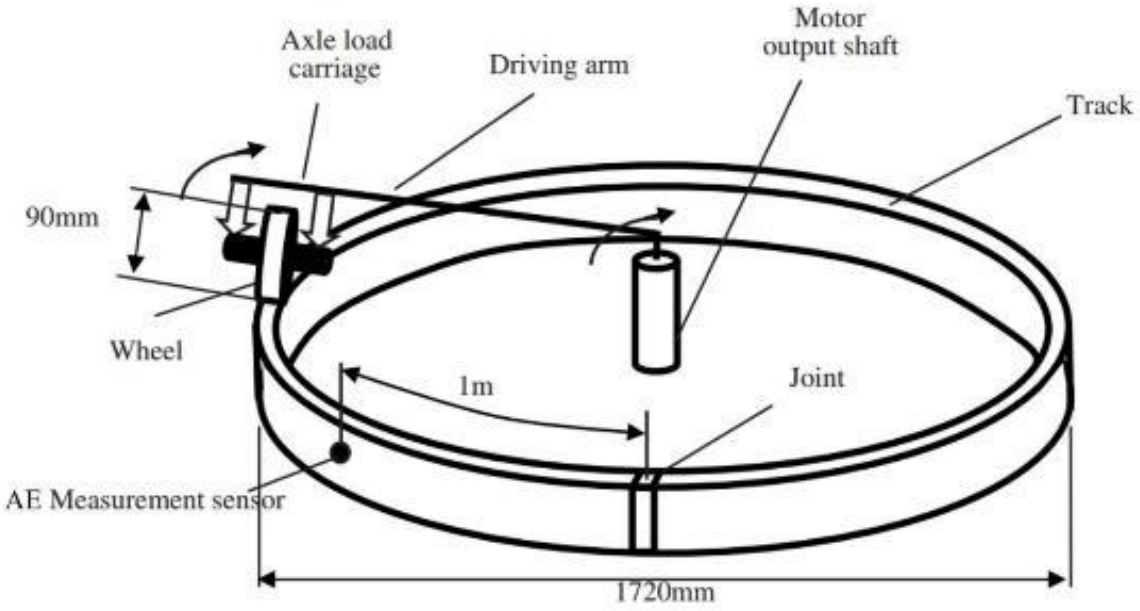

Figure 4-10 A full-circle track profile designed for wheel flat experiments (Thakkar et al., 2012).

As a result, wheel defect signals can be retrieved from a raw signal accommodating track defects and other noises by introducing a moving source model and suitable frequency filtering. The associated AE time series are dominant, containing a fundamental frequency equal to the rotating frequency of the wheel. The amount, size, and circumferential distribution of the wheel flats and the axle load affected the harmonic waveform, while the wheel's rotating speed determined the fundamental frequency. It is stated that, with proper calibration and modification, the provided technique might be utilised to identify wheel faults in railway wheel CM utilising track-mounted or wheel-mounted sensors.

Another research by (Anastasopoulos et al., 2010) revealed the potential for railway wheelsets' wayside CM, which is generally related to flat surfaces. Different AE sensors were installed on the tracks as the railcars or trams passed at varying speeds. They applied a multi-dimensional analysis, integrating Time-Driven Data, Hit Driven Data, and extended waveform streams recorded concurrently. RMS offered a smooth profile of the output signal, enabling the analysis of time-domain data, including inspecting the time interval between the axles and bogies as they travel through each sensor. However, combined analysis of AE DSP software and pattern recognition using specialist software is necessary to realise the full potential of all accessible data in the time and frequency domains. Wheel flat detection was successfully introduced with a low operating speed. Unfortunately, the location of defects requires further improvements.

After the analysis of the AE, the signal has been conducted through magnitude parameters on the time domain. The combined analysis of retrieved AE data based on the time and frequency domain finally introduces a more effective approach to generating high accuracy defect detection. (Bollas et al., 2013) conducted AE measurements of passing trains containing wagons with healthy wheels and artificially flattened wheels, with a range of speeds and directions. They installed two PAC R15i and two R30a sensors on the trackside, that the wheel with induced circumferential flat defect would roll on. Once a Fourier transform is performed

immediately to the processed RMS signals, it produces a frequency spectrum full of random harmonics. In an effort to eliminate the undesired harmonics, the discrete derivate of the RMS signal is generated and loaded into the program, where it is further processed using a pitch identification method.

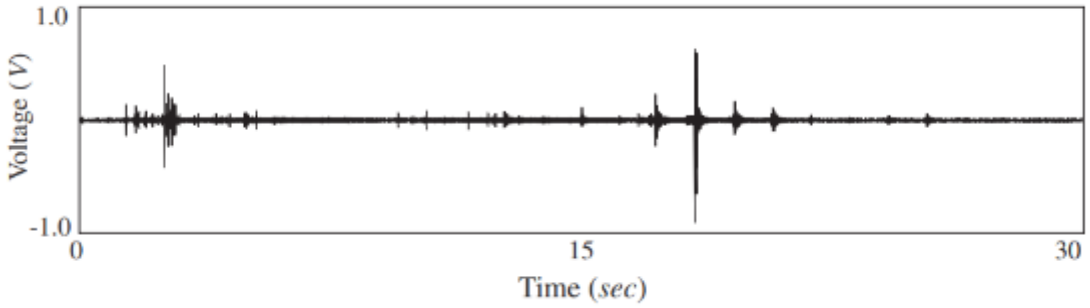

Figure 4-11 Raw signal of AE waveform gained from the R30a sensor installed on the track (Bollas et al., 2013).

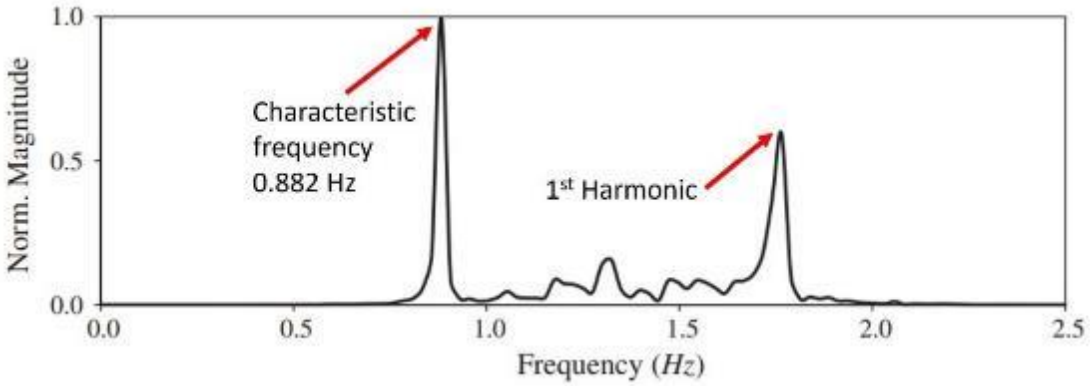

Figure 4-12 The first peak and its harmonic corresponding to the fundamental frequency of the defect with five mph train velocity (Bollas et al., 2013).

The authors mentioned that the information about the fundamental rotational frequency retrieved from the raw data is difficult to reveal. This is because the sensor's frequency bandwidth is much greater (hundredths of kHz). Raw signal from the AE sensor retrieved from sampling rate of 2 MHz illustrates signal in time domain as displayed in Figure 4-11. Moreover,

a band pass filter (10th order Bessel) was implemented in conjunction with FFT for the whole raw data to improve the AE waveform on the frequency domain. At the speed of 5 mph, the calculated frequency is 0.85 Hz, while the final normalized data display two peaks of 0.882 and its first harmonic as seen in Figure 4-12. With the development of the novel signal processing containing several steps based on the nature of the signal, the largest peak corresponding to the fundamental frequency can finally be identified.

AE and vibration techniques have been combined for onboard monitoring of railway axle bearings (Amini et al., 2017). The parameters, including rotating speeds and defect sizes, were investigated. Time-domain analysis, including peak-to-peak values, RMS, crest factor, and kurtosis, provided useful information for bearing defect detection. It was noted that the impacts from wheel defects would generate more energy as the rotating speed rises. AE data finally reveal a higher amplitude of larger defect size, where vibration signals failed. However, this study also noted that time-domain analysis has limitations in identifying defect sizes. In addition, noises from the environment affect magnitude values based on time-domain analysis, which requires sophisticated signal analysis to mitigate and reveal obvious information for wheel defect detection.

Previously, they had tried a couple of laboratory and field trials, providing an overview of a simple yet useful procedure for bearing defect detection, which relies on a modified onboard AE CM system (Amini, Entezami, & Papaelias, 2016b). They conducted the frequency domain analysis to study how harmonics of defective bearings develop over the spectrum, where FFT was the key to the analysis.

However, FFT was unable to discover the type of defect, and the spectral envelope analysis was further implemented for this purpose. The fundamental frequency was calculated as referring to the rotating speed. The spectral envelope analysis picked up a series of harmonics

starting from the defect frequency of 16.99 Hz. The correlation between the reported data by the manufacturer and the actual value was made, as a result of speed offset during the test.

Figure 4-13 proved that using spectral envelope analysis in conjunction with FFT can reveal the characteristic frequencies and harmonics, where the bearing's kinematics can be detected. These are required for the analysis of defect detection. On-board axle bearing issues can be identified using spectral envelope analysis. The result from modified bearing test rig proved that spectral envelope analysis is able to differentiate the healthy and defective bearings based on characteristic frequencies. Even though field tests could obtain the same results, the surrounding noises would challenge the analysis. It is also proved that AE can only identify the defect's presence in the moderately damaged bearing because of the poor SNR.

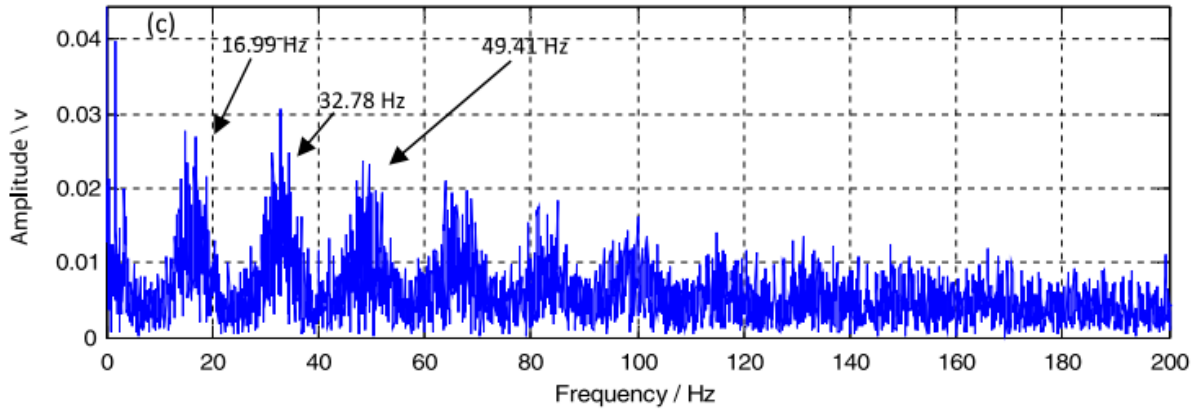

Figure 4-13 Measurement of onboard AE on a bearing with a major roller defect (Amini, Entezami, Huang, et al., 2016).

In terms of wayside CM approaches, another study by (Amini, Entezami, Huang, et al., 2016) established that Time-spectral Kurtosis (TSK) is ideal for wheelset defect diagnosis location because it can attenuate surrounding sounds and the amount of uncertainties in the result, resulting in Figure 4-14. This study found it difficult to discover damaged bearings and non-Gaussian sounds online. AE rail sensors and a trackside data gathering module modify rail network wayside monitoring. A range of roller defect size including 2 mm, 4 mm, and 8 mm

were implemented on the same side of the freight wagon. The field trials were run at 48 km/h on a straight track. Sampling frequency, wheel diameter, distance between wheelsets, and record time interval were employed to determine the time difference between peaks to find the bearing problem. AE measurements produce high-amplitude waves in output data, limiting the capacity to identify flaws. Frequency domain analysis helps ease this limitation in standard signal processing procedures. Moving RMS and moving kurtosis can identify axle bearing difficulties, but they cannot perform well when there's a poor SNR. Noising from the braking system will stimulate the signal and increase the RMS value and the kurtosis, which mislead the defect detection. This study underlined the usefulness of TSK for signal analysis of railway bearing faults, which uses time and frequency domains and kurtosis values for each frequency band.

Based on their health status, axle box acceleration sensors can provide useful information on wheel vibrations generated by the wheel and rail conditions. The research by (Baasch et al., 2021) utilises the cepstral analysis for wheel CM data processing. The cepstrum is suitable for detecting and separating periodic signals from the rest of the signal. The train speed is the key input since the vibration signal is generated by periodic changes concerning the rotating frequency of the wheel. The spatial domain cepstral analysis is the inverse of the wavenumber.

As such, a peak show how often the axle bearing accelerometer signal changes. The peak represents the wheel's circumference and can be used to measure its diameter. In the case of vibration technique, CM of wheel surface defects can potentially use the data from axle bearing accelerometer.

The information of velocity and location from onboard vibration measurement was proved to be useful as the correlation between the speed dependent and independent vibrations by (Heirich et al., 2013). The readings of a vertically placed acceleration sensor onboard a rail

vehicle reveal that certain frequencies have a horizontal vehicle speed dependency. Using a vertical and translative acceleration sensor, a vehicle parametric model of wheel size and distance would be obtained. An investigation identifies the principal vibration sources of a train in motion, which are classified as speed dependent or independent. Since the vibrations are generated by various sources and the vehicle response, the complex output could result in a variety of frequencies, magnitudes, and orientations. They demonstrated a method for monitoring absolute location, absolute speed, and wheel diameter based on vehicle vibrations. A matched filter, which was derived from wheel speed and consequently corelated with vibration signal in spatial domain, was acquired to provide the localization.

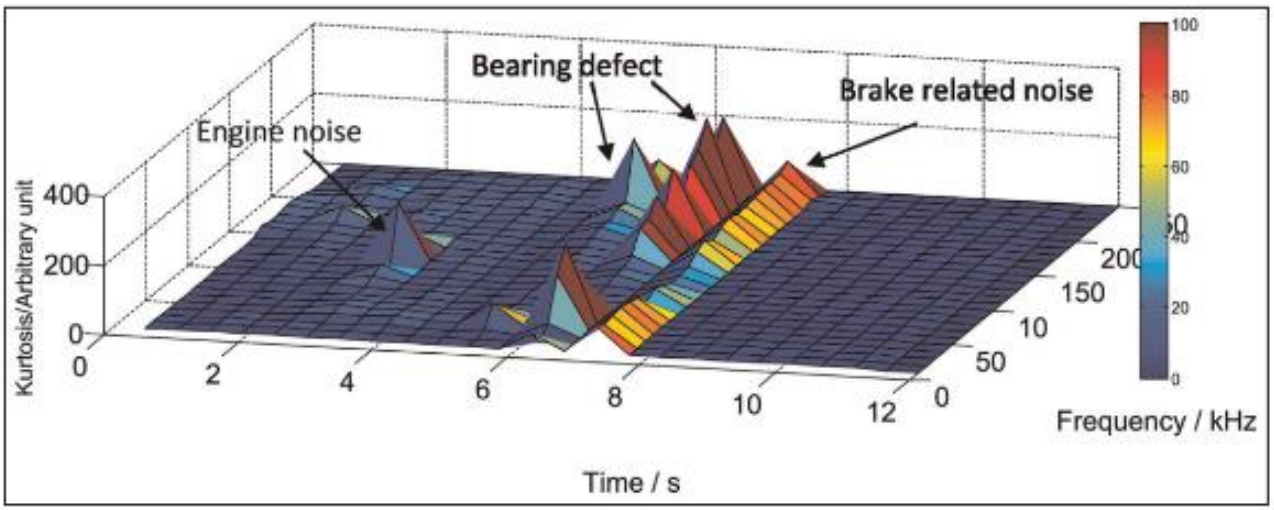

Figure 4-14 Time Spectral Kurtosis diagram of AE signal from wayside measurement with roller bearing defect (Amini, Entezami, Huang, et al., 2016).

4.3 Comparison between Acoustic emission and vibration

Many researchers compared AE with vibration techniques to detect the defect in rotating machines. However, several aspects of the efficiency and performance of both techniques depend on each experiment's preference. Therefore, each statement will not be suitable for

every experiment. However, it is useful to realise the difference between the two methods, and one could not replace another.

4.3.1 Higher Frequency

AE transducers measure crack-generated stress waves. Like accelerometers, AE transducers have inertia loadings on a piezoelectric crystal, which is amplified. The difference between AE sensors and accelerometers is that the crystal's self-inertia is the only loading in AE sensors. Since the vibration patterns are intricate, several crystal resonances reach up to frequencies of 2 MHz (McFadden & Smith, 1984a).

The use of vibration for early-stage defect detection of rolling bearing at extremely low rotational speed is limited since the impact produces relatively little energy. The fault may be hard to spot in frequency but evident in time domain (Miettinen & Pataniitty, 1999).

Due to the signal's high-frequency components, AE monitoring presents unique challenges. According to the obvious attenuation of stress waves caused by material losses and component interfaces, the position of the AE sensor is far more critical than the placement of the accelerometer.

AE transducers that are commercially available regularly exhibit a less uniform amplitude response as a function of frequency than accelerometers. In addition, the data acquisition and processing system must be configured to handle the high-frequency signal of AE preference.

Fewer transducers are generally required for AE system when compared with conventional accelerometers. AE is created on a microscopic scale, making it more sensitive than other CM methods and allowing for the discovery of flaws at an earlier stage. AE is immune to mechanical noise and structural resonances typically under 20 kHz since it detects high-frequency elastic waves (Loutas et al., 2009).

4.3.2 Signal-to-noise ratio

Wideband AE signal stimulation from bearing flaws yields stress waves exceeding 100 Hz. Thus, AE signals potentially provide a higher signal-to-noise ratio than which gained by the standard low-frequency vibration monitoring. As a result, bearing problems can be recognized early (Sturm & Uhlemann, 1985).

4.3.3 Defect Detectability

In terms of defect detection ability, a comparison of AE and vibration measurement techniques was mentioned in the study by (Tandon & Nakra, 1992b). After examining several available parameters, the inner race fault of deep grove ball bearings is better discovered by observing AE ringdown counts, envelope acceleration, and AE peak amplitude. Envelope acceleration and AE peak amplitude better identified outer race faults. The best way to detect ball defects is by measuring AE peak amplitude. It identifies tiny ball faults better than any other method.

A tapered roller bearing assembled as a mix of Timken LM490209 cup and LM490238 cone was chosen for the condition diagnostics using AE and vibration measurements (Shiroishi et al., 1997b). The speed of 1200 rpm was the based rotational speed in their experiment. The accelerometer was more sensitive than the acoustic emission sensor at this speed. Once the AE did discover a defect, it was prominent, with the peak ratio rising by order of magnitude. Furthermore, by comparing the capabilities of the accelerometer and the AE sensor, the accelerometer detected outer defects more accurately than the AE sensor. When the inner defect detection was placed, the AE sensor was insensitive to all tests. The emissions generated by the AE sensor were not strong enough to be detected. Inner race defect-generated AE signals must travel further and over more interfaces than other faults. Additionally, signal strength may be reduced if the AE wave's path to the sensor is not straight. They also concluded that the accelerometer detected all types on par with the AE sensor.

4.3.4 Defect size identification

On the other hand, the defect size could be more challenging for early detection. AE can detect an earlier defect, while the vibration technique rarely reveals the possibility. Moreover, (Al-Ghamdi et al., 2004) stated that it might also indicate defect size, allowing the user to monitor the pace of bearing deterioration.

The ability of the AE technique to predict the defect size on bearings was later studied by (Al-Dossary et al., 2006, 2009; Al-Ghamd & Mba, 2006). They established a link between AE burst duration and bearing defect length, allowing the user to determine bearing degeneration without vibration investigation.

Raw AE data may not show a system or component's true condition. Preprocessing AE signals before analysis is generally required (Amini, 2016b).

Table 4-1 Comparison between AE and vibration methods.

Feature	AE	Vibration
Frequency range	20kHz - 2MHz	5Hz - 10 kHz
Signal-to-noise ratio	High	Average
Defect Detectability	More efficient at high-level noise environments	Needs the certain level of severity
Defect size Identification	Preprocessing and signal analysis can make it feasible	Hardy reveal

4.4 Signal analysis of vibration and acoustic emission in rotating machines

Both vibration and AE need signal analysis to detect and diagnose faults in spinning equipment. Signal magnitude, time-domain analysis, frequency domain analysis, and time-frequency analysis are widely used signal analysis techniques. However, further available techniques were gradually presented in several novel research related to the improved CM of rotating

machines. Each technique has its benefits and drawbacks, so one cannot replace another. In general, signal magnitude and time-domain analysis are easy to perform as they require inexpensive and simple instruments, whereas others need exceptional understanding and more complex instruments. The experiment should make an appropriate decision as a more robust technique would provide better-detailed information about the output data. More than one technique is generally applied to each analysis since there could be many parameters, and each technique does not suit all. Therefore, specialist techniques efficiently identify noise sources in heavily noise-contained environments (Norton & Karczub, 2003b).

The analysis of a rolling bearing would require related equations for signal analysis. There are several sub-components inside, including rolling elements, cage, outer and inner race. They generally contact others, which will generate a complicated vibration signal. A collision between a defect on the bearing surface and another area generates an impact. As a result, a series of mechanical hits may exist in a bearing signal due to the fault passing through the load zone (Tandon & Choudhury, 1999b).

Certain frequencies may be relevant due to the geometry of the bearing depending on the type of fault. The equations below determine the characteristic frequencies of a bearing. (Norton & Karczub, 2003b).

Fundamental Train (Cage) Frequency, FTF, represents damage to the cage

$$f_{FTF} = \left\{\frac{f_s}{2}\right\}\left\{1 - \frac{d}{D}cos\ \emptyset\right\} \qquad (4\text{-}1)$$

Ball Spin Frequency, BSF, represents damage to the rolling element

$$f_{BSF} = \left\{\frac{D}{d}\right\}\left\{\frac{f_s}{2}\right\}\left\{1 - \frac{d^2}{D^2}\cos^2 \emptyset\right\} \qquad (4\text{-}2)$$

Ball Passing Frequency Outer Race, BPFO, represents damage to the outer race

$$f_{BPFO} = n\left\{\frac{f_s}{2}\right\}\left\{1 - \frac{d}{D}cos\ \emptyset\right\} \qquad (4\text{-}3)$$

Ball Passing Frequency Inner Race, BPFI, represents damage to the inner race

$$f_{BPFI} = n\left\{\frac{f_s}{2}\right\}\left\{1 + \frac{d}{D}cos\ \emptyset\right\} \qquad (4\text{-}4)$$

where $\boldsymbol{f_s}$ determines the shaft rotation speed in Hz, d determines the ball or roller diameter in metres, D determines the mean roller race diameter in metres, ∅ determines the contact angle in radian, and n determines the number of rollers.

According to the above calculations, bearing's fundamental parameters related to the bearing health based on specific speed can be explained. Also, each component would generate a different envelope signal based on individual fundamental frequency, as shown in Figure 4-15.

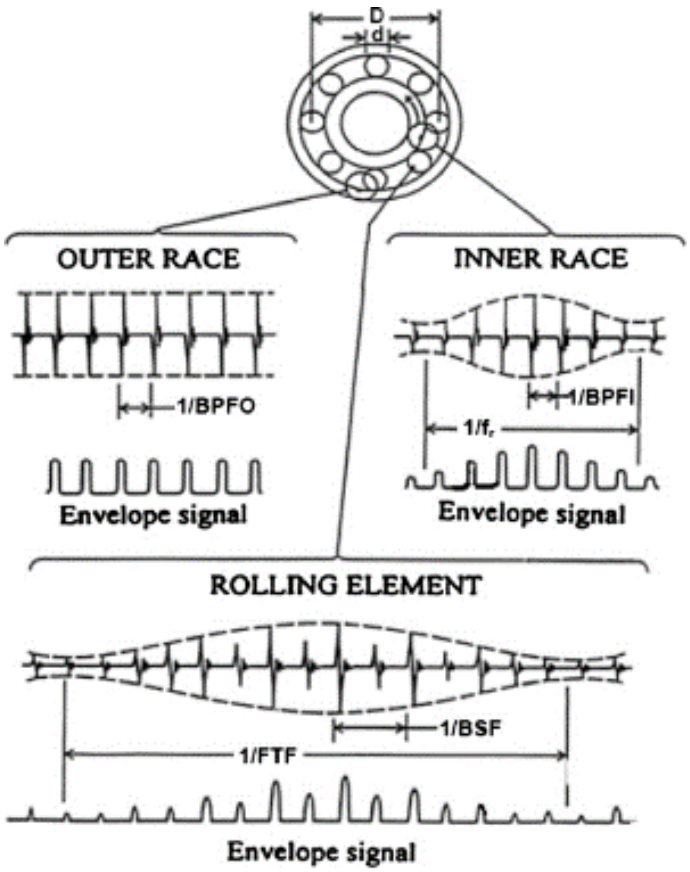

Figure 4-15 Typical and envelope signals from rolling element bearing local defects (Randall & Antoni, 2011).

Those frequencies are evaluated depending on the non-slip operation of rolling components. However, the experiment in the actual condition would see some errors by a few percentages of specific characteristic frequencies as some slips do occur (Randall, 2004). To process AE signals, fairly typical diagnostic methods such as an HFRT methodology that comprises demodulation and FFT were utilised. As a result, an enhanced bearing diagnostic method would significantly increase detectability.

4.4.1 Time domain analysis with signal magnitudes

Magnitude analysis is sometimes the simplest technique to analyse the output signal. The mean value, RMS, skewness, and kurtosis are statistical magnitude moments of the signal with varying levels. Historically, a maintenance engineer may be concerned with merely the overall magnitude of a signal at times. Prior studies on the performance of a certain piece of machinery frequently give adequate criteria to allow the definition of "OK" and "NG" levels. Many researchers have utilised RMS to indicate problems in time-domain analysis.

A basic example is the acceptable overall dynamic stress level and the related vibrational velocity at a crucial spot-on rotating machinery. Due to impacts and noise, the allowable peak and RMS sound level are used. It is also extremely typical for RMS. The peak vibration levels are continually measured at various points on an airliner. In many cases, simple analytic equipment for determining the total magnitude of the signals is all that is necessary (Norton & Karczub, 2003b).

For signal magnitude analysis, the distribution of peaks or extrema of discrete events has been studied. As a result, statistical information regarding the distribution's skewness is necessary. The mean value of a distribution is its first statistical moment, while the mean-square value is its second statistical moment. The third statistical moment of a distribution is its skewness,

while kurtosis is the fourth statistical moment. The last two parameters could also be called probability density moments. Examples of magnitude analysis are listed below;

Peak-to-Peak value

$$\frac{1}{2} = [\max(x_i) - \min(x_i)] \qquad (4\text{-}5)$$

Root mean square (RMS)

The fundamental time-domain approach computes RMS values. The RMS value of a signal is a factor of time data that measures the amount of energy contained in the signal. RMS is calculated using the equation below (Lebold et al., 2000).

$$RMS = \sqrt{\frac{\sum_{i=1}^{N}(x_i)^2}{N}} \qquad (4\text{-}6)$$

Given N is the number of data.

However, moving RMS is generally used for the signal analysis of rotating machines. It is an approach to calculating RMS values of a designated size of the windowed signal, regarding the speed of the monitored object. The raw data may be analysed using moving RMS to determine the major peaks of interest in the retrieved signal (Amini, 2016b).

Crest factor

Because the RMS may not disclose changes in the early phases of rotating machine failures, the crest factor could make a better signal magnitude for the analysis. Crest factor is the ratio of Peak value to RMS (Lebold et al., 2000). A crest factor near unity is produced by zero modulation and mild sinusoidal modulation of the resonance, while a higher crest factor would indicate the modulation by machine faults (McFadden & Smith, 1984c). The crest factor's equation is as follows:

$$Crest\ Factor = \frac{Peak\ Value}{RMS} \qquad (4\text{-}7)$$

Skewness

As its name suggests, skewness denotes the degree to which the probability density curve is skewed. By means of the standard deviation, the third moments or the skewness are typically non-dimensional (Roger, 1979b). Skewness could be given as below.

$$skewness = \frac{1}{N}\frac{\sum_{i=1}^{N}(x_i - \overline{x})^3}{\sigma^3} \qquad (4\text{-}8)$$

Skewness measures the data's probability function symmetry. It is a symmetric function at the mean when skewness is zero. The positive skewness would display the long tail to the right-hand side (high values), where the outliers are more than the mean value. On the other hand, the negative skewness would illustrate the long tail to the left-hand side (small values), where the outliers are less than the mean value (Norton & Karczub, 2003b). Figure 4-16 illustrates those variations of skewness distributions.

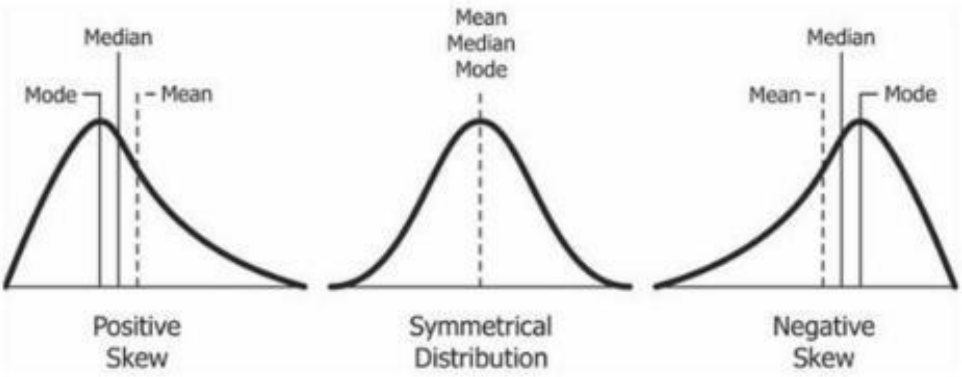

Figure 4-16 A common link between mean and median in a skewed unimodal distribution (Alatefi et al., 2019).

Kurtosis

Since the 1970s, Kurtosis has been used for a very long time as a parameter that may be used to determine how severe machine flaws are, including rolling element bearing (Dyer & Stewart,

1978). One of the examples is the CM of anti-friction bearings, as stated in section 4.1 (Roger, 1979b).

Kurtosis is sensitive to spikes vibration signals; therefore it can be used to evaluate bearings. It resists loading and shaft speed. The kurtosis of the data reveals its peakiness. It is the fourth moment based on the standard deviation (Roger, 1979b). Kurtosis could be given as below.

$$kurtosis = \frac{1}{N}\frac{\sum_{i=1}^{N}(x_i-\overline{x})^4}{\sigma^4} \qquad (4\text{-}9)$$

The kurtosis value for an amplitude distribution with a Gaussian distribution is 3 (typical of random amplitude noise created by a new bearing). Its value ranges between 3 and around 20 for an irregular signal, typical of a slightly damaged bearing. Early and advanced damage situations can be determined by evaluating the frequency dependence of kurtosis.

Using AE signals to study damaged shafts indicated that kurtosis and skewness readings can be used to assess fracture size (Pimentel-Junior et al., 2016).

4.4.2 Frequency domain analysis

A convenient way to use involves determining frequency-related factors like resonances and defect harmonics, which may be matched to bearing faults after they have been identified. Frequency domain analysis may enhance bearing flaw detection over time-domain analysis. In frequency domain analysis, FFT is the first frequency technique employed.

Another powerful tool for spectral analysis which was used to be very popular in last decades is Cepstral analysis (Norton and Karczub, 2003). The inverse Fourier transform of the logarithm of autospectrum is the core of the derivation of the power cepstrum $C_{pxx}(\tau)$ which can be calculated by:

$$C_{pxx}(\tau) = F^{-1}\{\log_{10} G_{XX}(\omega)\} \qquad (4\text{-}10)$$

Where $G_{XX}(\omega)$ is a single-sided energy spectral density. τ is the independent variable in the dimensions of time separation similarly to the auto-correlation function and is defined as quefrency. It is a parameter measured in seconds and is the corresponded term of frequency interval in the standard frequency spectrum.

Instead of the inverse Fourier transform, the power cepstrum can be calculated as the square of the forward Fourier modulus s shown below:

$$C_{pxx}(\tau) = |F\{\log_{10} G_{XX}(\omega)\}|^2 \qquad (4\text{-}11)$$

In terms of application, the power cepstrum can sometimes provide the identification of harmonics as refer to the vibration signal of rotating machine while the normal spectral analysis is unable to. The reason behind this is that the power cepstrum bypasses the transmission path and unconditionally reveal the fault related items on the quefrequency domain. The reason for this is that the power cepstrum skips the transmission route, revealing all fault-related items in the quefrequency domain unconditionally (Konstantin-Hansen & Herlufsen, 2010). However, It might conceal information carrying a spectral content summary, reducing the usable elements in the frequency domain. It is worth mentioning that the power cepstrum as a cepstral analysis must be used in comparison with spectral analysis.

4.4.3 Short-time Fourier transform (STFT)

Short-time Fourier transform (STFT) determines signal frequency and phase. STFT is determined by splitting a time-varying signal into equal-length segments and then using Fourier transform (Sejdić et al., 2009). A fundamental yet powerful approach as it can be further developed and used in many advanced signal processing technique (Malla & Panigrahi, 2019).

In continuous-time case, the STFT multiplies a function using a window function, noting that the window function must be non-zero. The Fourier transform is then used to generate a signal's two-dimensional representation (time and frequency domains). This can be expressed as:

$$STFT\{x(t)\}(\tau,\omega) \equiv X(\tau,\omega) = \int_{-\infty}^{\infty} x(t)\ w(t-\tau)e^{-i\omega t}dt \qquad (4\text{-}12)$$

Where $x(t)$ is the input signal and $w(t)$ is the window function, with a complex function describing the phase and magnitude over time and frequency domains, $x(t)w(t-\tau)$. $X(\tau,\omega)$ is the Fourier transform of $x(t)w(t-\tau)$. A Hann window or Gaussian window is used for the window function. STFT ($X(\tau,\omega)$) is also known as windowed Fourier transform or time-dependent Fourier transform since its function is the Fourier transform function multiplied by the window function.

In discrete-time, data is transformed in frames (typically overlapping to decrease artifacts at the border). The Fourier output of each frame is added to a matrix containing magnitude and phase for each time and frequency point. For example, to compute discrete-time STFT $X(m,\omega)$, the mathematical expression is below:

$$\{x(n)\}(m,\omega) \equiv X(m,\omega) = \sum_{n=-\infty}^{\infty} x(n)w(n-m)e^{-j\omega n} \quad (4\text{-}13)$$

Instead of τ, m is discrete where ω is continuous, with signal $x(n)$ and window function $w(n)$. Both values are discrete and quantized since the FFT is extensively utilised.

The spectrogram represents the function of Power Spectral Density is the magnitude of squared of the STFT, as below:

$$\{x(t)\}(\tau,\omega) \equiv |X(\tau,\omega)|^2 \qquad (4\text{-}14)$$

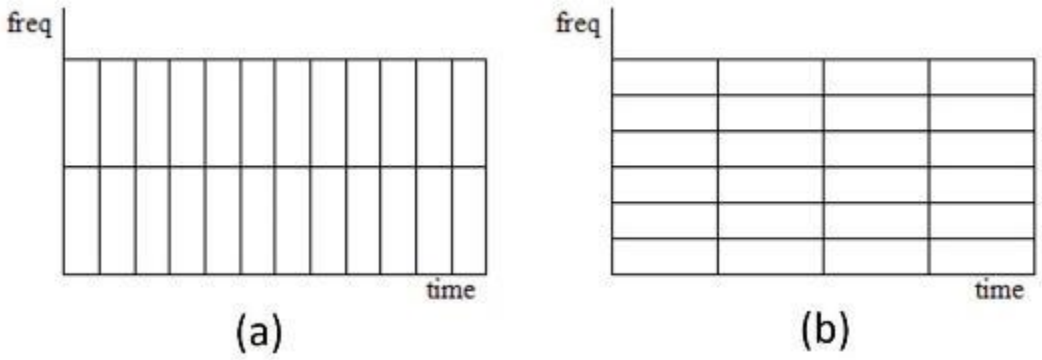

Figure 4-17 A comparison between (a) wideband spectrogram and (b) narrowband spectrogram (Sejdić, E., Djurović and Jiang, 2009).

STFT can be considered a varying window size of a two-dimensional domain between time and frequency. Thus, the trade-off when modifying the time window is related to frequency resolution. Either way, increasing the frequency resolution by increasing the number of samples in a window or decreasing the sampling rate will make a larger window size and consequently reduce the time resolution. This is called a narrowband spectrogram, as illustrated in Figure 4-17 (b). On the other hand, an increase in time resolution by shortening the window will decrease the frequency resolution, as shown in Figure 4-17 (a). The best window size would provide the balance between a great signal resolution and an appropriate computation time based on the system. Thus, it is a main disadvantage of the STFT that it is a fixed resolution.

4.4.4 Spectral Kurtosis, Time Spectral Kurtosis, and Kurtogram

Spectral kurtosis (SK) may determine which frequency bands contain a signal with the greatest impulses. The frame Fourier output is added to a matrix including magnitude and phase for each time and frequency point. However, it used to be called a frequency domain, Kurtosis, first introduced in the marine application (Dwyer, 1983).

SK captures transients and their frequency domain placements. It was based on the real part of STFT and measured a signal's impulsiveness as frequency (Antoni, 2006). Figure 4-18 demonstrates a computation of SK, which comprises time and frequency in the same diagram. First, the STFT is formed by overlapping a small-time frame with the record. The input signal is then separated into bands of different frequencies, and SK is computed. Next, the spectra for each window position are shown in a 3-D graphic with time and frequency on opposing axes. Lastly, SK is worked out for each frequency line. (Sawalhi & Randall, 2004).

For many decades, SK has been a robust approach for identifying and extracting signals related to problems in rotating mechanical systems. SK can find features or conditional indications for defect detection and categorization on its own. SK may provide critical inputs such as ideal bandwidth as pre-processing for other tools such as spectral envelope analysis.

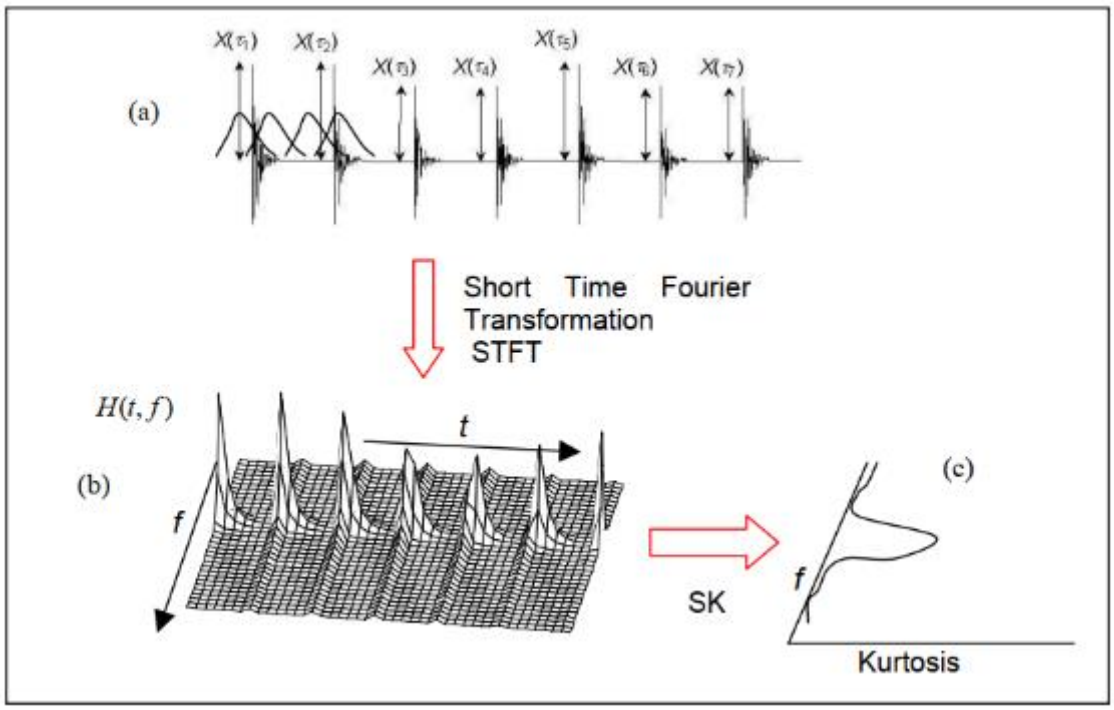

Figure 4-18 Computation of SK for an artificial bearing fault signal (Sawalhi & Randall, 2004).

Time Spectral Kurtosis

By adding the time axes to SK, the Time Spectral Kurtosis (TSK) is able to demonstrate signal in 3 axes: time, frequency, and kurtosis amplitude. Consequently, The TSK approach can detect transients in the frequency and time domains. The TSK technique can detect rolling element bearing faults that cause quick impulses (Chen et al., 2014).

However, false detections might arise while processing signals gathered from in-service train wheel-bearings. Random impulses can create these inaccuracies, lowering TSK's overall capability to identify bearing defects. As a result, TSK is scarcely employed, despite its suitability for defect detection (Antoni & Randall, 2006). It requires improved clarity in the definition and a clear understanding of the procedures.

Kurtogram

The kurtogram is the utilisation of the kurtosis in various window frequency bandwidths, which was presented for detecting and classifying non-stationarities in a signal. The demonstration of an effectively powerful method of using the SK as a pre-treatment to spectral envelope analysis based on only two parameters. Kurtosis is calculated for several window lengths and frequencies. The main objective is finding the central frequency and the filter's bandwidth, which enlarges some criteria on the filtered signal (Antoni & Randall, 2006).

A short window will provide high SK values, and, as a result, this would be preferable for most cases (de la Rosa et al., 2008). Conversely, a too-short window will result in an SK with a low kurtosis value, obscuring certain information. An improvement on the time-consuming characteristic of the kurtogram has been improved by (Antoni, 2007) to resolve the issue.

Kurtogram could be used for making a band-pass filter which will improve the SNR of the output, consequently keeping the impulse-like profile of the signal (Antoni, 2007).

Both SK and the kurtogram are introduced as they could help choose the best suitable frequency band for demodulation of spectral envelope analysis (Randall & Antoni, 2011).

4.4.5 High-Frequency Resonance Technique (HFRT) / Spectral envelope analysis

The high-frequency resonance technique (HFRT) was developed in the research of bearing diagnostics in helicopter gearboxes by the US army (Darlow et al., 1974). It is also known as spectral envelope analysis, which will be described together.

An assessment of vibration monitoring of rolling element bearings using the high-frequency resonance method (HFRT) noted that the technology's use was restricted until the envelope spectrum could be thoroughly understood (McFadden & Smith, 1984c).

HFRT generally improves the signal processing approach's input signal by using a defect signal's substantial amplitude in the region of high-frequency system resonance. Within the elimination of low-frequency mechanical noise, it produces a demodulated signal with a high defect to SNR.

HFRT mainly comprises three steps. First, an original signal displayed in Figure 4-19 (a) is band-passed around a specific high-frequency band and the centre at a selected resonant frequency of the signal, generating a cleaner signal in Figure 4-19 (b). Then, a half-wave rectifier will demodulate the band-passed signal, resulting in Figure 4-19 (c). Lastly, it is filtered by low-pass filtering to remove high-frequency elements and retain the low-frequency information related to rotating machine defects, as seen in Figure 4-19 (d). However, only HFRT based on these steps would not be effective for the noise-contaminated signal, which is generally happened. Some improvement could be seen as an Adaptive Line Enhancer is implemented after the HFRT process. An example demonstrates the diagram of signal processing for bearing condition diagnostics can be seen in Figure 4-20 (Shiroishi et al., 1997b).

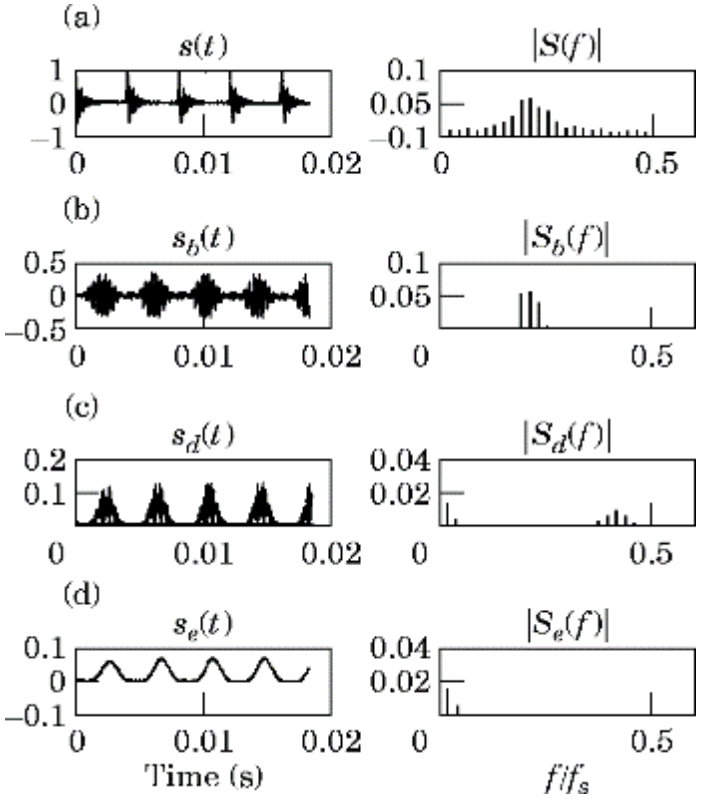

Figure 4-19 The process of high-frequency resonance technique (Shiroishi et al., 1997b).

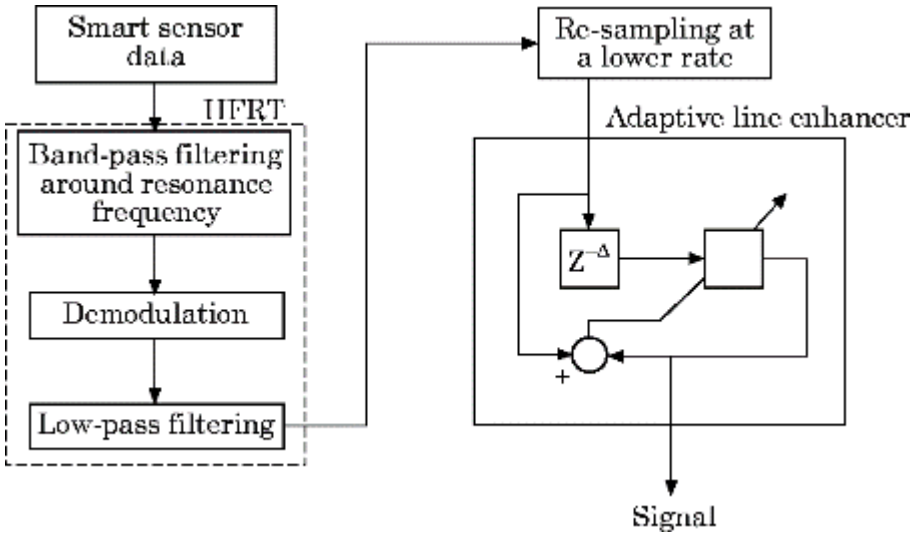

Figure 4-20 Signal processing diagram (Shiroishi et al., 1997b).

Many research after the 1980s mentioned HFRT as spectral envelope analysis as well known. Fortunately, there were additional techniques applied for the modulation process.

Since the effect of background noise on the detection of damage in a machine is always presented during the spectral inspection, the spectral envelope analysis is introduced to signal to process. It was specified as the benchmark technique for bearing diagnostics as the raw signal spectrum frequently offers minimal diagnostic information concerning bearing defects. First, spectral envelope analysis is performed by performing a signal band-pass filter in a high-frequency band where structural resonances amplify fault impulses. Spectral envelope analysis using a Hilbert transform or similar technique identifies impact events (Entezami et al., 2020b). After that, the amplitude is demodulated to create the needed diagnostic information regarding the repetition frequency and modulation by the specific frequency where the fault travels through the reference point (Randall & Antoni, 2011).

The Hilbert transform is the most widely used technique adopted in bearing diagnosis. As shown in equation (1), the Hilbert transform of a signal represents phase-shifting Fourier components on its frequency spectrum by $\pm\pi/2$ (Kannan et al., 2019).

$$\hat{x}(t) = \frac{1}{\pi}\int_{-\infty}^{+\infty} \frac{x\tau}{t-\tau} d\tau \qquad (4\text{-}15)$$

All steps related to envelop analysis are illustrated in Figure 4-21, which includes the illustration of the demodulation step. Like HFRT, spectral envelope analysis could start with the fast-Fourier transformation of a signal using the Hanning window function to modify the signal into the frequency domain. Subsequently, a band-pass filter eliminates high-frequency random noise and strong low-frequency components, maintaining just high-frequency vibrations (Tyagi & Panigrahi, 2017). At this point, SK and kurtogram could help find the appropriate value for filtering the signal, as stated in the previous topic. Next, the inverse FFT returns the signal to the time domain, where the envelope is analysed using a phase shift conditional instruction. Finally, the FFT has been applied again to the envelope signal to emphasise the fault frequencies on spectrum analysis (Bonnardot et al., 2004).

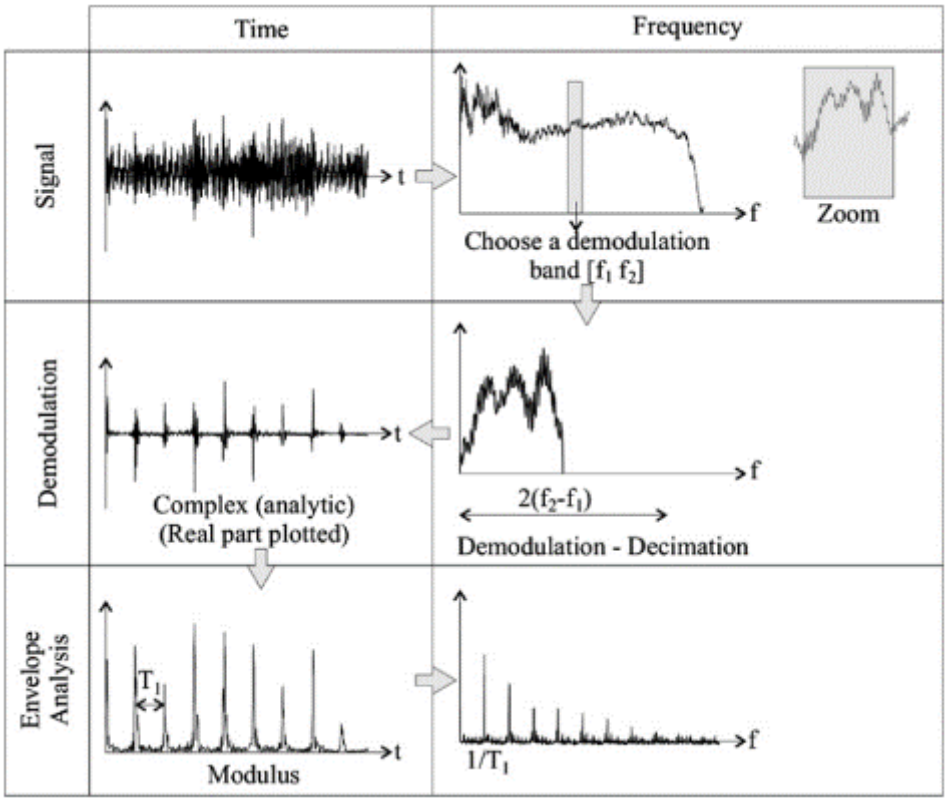

Figure 4-21 The detailed approach of the Envelope Technique (Alegranzi et al., 2012).

4.4.6 Wavelet transform

Wavelet transform (WT) reveals non-stationary signal analysis' intrinsic information when time domain and frequency domain analyses cannot. Since there are various limitations in the signal analysis of rotating machines, researchers are always keen to develop such competitive techniques for specific usages and conditions. WT analysis is one of the pre-processing techniques designed to extract the significant properties of the original dataset, such as discontinuities, trends, and breakdown points (Rajaee & Shahabi, 2016). WT is a variable window technology that highlights rotating machine signals' frequency and low-frequency components using time intervals. WT data may be decomposed into approximation and detail coefficients on a multiscale. (Bendjama et al., 2012). WT typically works in conjunction with other signalling processes to reveal the defective frequency bands.

WT was firstly introduced by Morlet in 1978. A mother wavelet is introduced for the decomposition of the original signal into a family of functions in terms of time and frequency. The basis functions for wavelet analysis are formed by dilation and translation of a prototype function or a mother wavelet $\psi_{i,j}$. There are two types of wavelet transforms which contain Continuous wavelet transforms (CWT) and discrete wavelet transforms (DWT) (P. G. Kulkarni & Sahasrabudhe, 2013). The wavelet transform performs the decomposition following an equation below

$$\psi_{j,k}(x) = 2^{\frac{1}{2}} \psi_{j,k}(2^j x - k) \qquad (4\text{-}16)$$

This function is generated from a mother wavelet $\psi\ (x)$ which is dilated by j and translated by k. The mother wavelet is needed to conform to the following condition (K. K. Gupta & Gupta, 2007)

$$\int \psi(x)dx = 0 \qquad (4\text{-}17)$$

The discrete wavelet function of a signal $f(x)$ is computed by

$$c_{j,k} = \int_{-\infty}^{\infty} f(x)\ \psi_{j,k}^{*}(x)dx \qquad (4\text{-}18)$$

$$f(x) = \sum c_{j,k}\psi_{j,k}(x) \qquad (4\text{-}19)$$

Where, $\psi_{j,k}^{*}$ and $c_{j,k}$ are the convoluted conjugate of the mother wavelet and the approximate coefficient, respectively.

To compute the mother wavelet $\psi(x)$, the scaling function $\varphi(x)$ is introduced as equation (4-20)

$$\varphi(x) = \sqrt{2}\sum h_0(n)\varphi(2x - n) \qquad (4\text{-}20)$$

$$h_1(n) = (-1)^n h_0(1 - n) \qquad (4\text{-}21)$$

$$\psi(x) = \sqrt{2}\sum h_1(n)\psi(2x - n) \quad (4\text{-}22)$$

where $h_0(n)$ plays a significant role in DWT and is computed corresponding to wavelet bases with varying features.

Despite being one of the mathematical functions that break signals into a range of frequency components, WT is different from STFT since each part is examined with a resolution proportional to its size.

As a result, they are appropriate for analysing physical circumstances characterised by abrupt spikes and discontinuities in the signal. The WT can de-noise a distorted bearing vibration signal. The decomposition parameters employed, and the wavelet threshold was chosen to define de-noising efficiency.

Wavelet analysis is more accurate and faster than classical time-frequency analysis for railroad wheel flat identification. The experimental results provide a strong statistical foundation for accurate diagnostic forecasts in the 10-100 km/h range. High-level wavelet decomposition monitors axle transit before quantifying train speed and constructing a masking figure for flat wheel identification (Belotti et al., 2003).

The quantitative estimation procedure of wheel-flat damage detection using discrete WT was later presented by (Belotti et al., 2006). According to their previous study, the masking Figure 4-22 was introduced as a validated axle pass-by signal. DWT of rail acceleration can help identify axle position on a six-axle locomotive and four four-axle carriages. The bogie's energy value is compared to an experimentally optimised threshold to determine its condition.

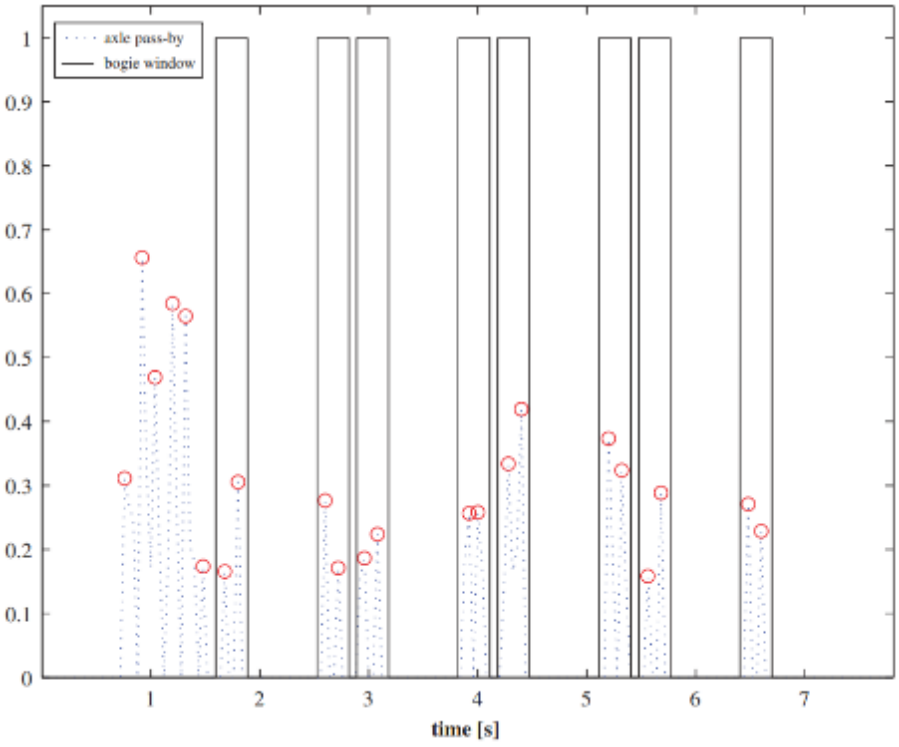

Figure 4-22 Bogie-mask window from axle pass-by signal generated by DWT (Belotti et al., 2006).

An effective technique was suggested to be the combination of local Fourier analysis and wavelet analysis. This approach helps identify and localise transients and unknown waveforms in the time domain.

The widely used WT expanded the application to CM rolling element bearings. (Hemmati et al., 2016) looked into the best band-pass filter by using wavelet packet transform and envelope detection with an analysis focusing on enhancing kurtosis and Shannon entropy. Apparently, the presented methodology reveals bearing characteristics frequencies from AE signals, which are generally obscured by background noise from mechanical vibrations of rotating components. Moreover, the Hilbert transform can offer defect information for signal envelope analysis. Time-frequency domain methods that employ the WT aim to decompose the vibration signal rather than demodulate it. The WT is typically used as a filter for signal processing, and

its functional parameters can be adjusted using a genetic or similar optimization process (Alegranzi et al., 2012).

Daubechies wavelet is chosen as one of the mother wavelets for the discrete wavelet transform. The wavelet toolbox in Matlab provides the analysis using one-dimensional wavelet decomposition. It allows the decomposition of the original signal into approximation and detail coefficients. The results may differ as the approximation order is altered.

4.4.7 Empirical Mode Decomposition (EMD)

Rotating machines generally produce non-linear and non-stationary signals, which typically require district and sophisticated signal processing techniques. Any complex data collection may be broken down into a small set of "intrinsic mode functions (IMFs)" that are amenable to Hilbert transformations with the use of a "empirical mode decomposition" technique. It stands out among other decomposition techniques because it relies on an adaptive basis system, which uses the local characteristic time scale of the data than spurious harmonics (N. E. Huang et al., 1998). To be precise, the EMD does not work on the frequency space as other techniques. Instead, the decomposition makes the inherent basis that the data should contain numerous coexisting simple oscillatory modes of considerably different frequencies, one overlaid on the other, at any given time (N. E. Huang & Wu, 2008).

The original signal $x(t)$ is decomposed into a series of IMFs $\sum_{i=1}^{n} c_i(t)$ and the residual $r_n(t)$ as displayed in equation (7) below;

$$x(t) = \sum_{i=1}^{n} c_i(t) + r_n(t) \qquad (4\text{-}23)$$

Where $c_i(t)$ is the i -th empirical mode, $i \geq 1$

To compute EMD, it starts with the rules of each empirical mode or IMF_i are required to meet as follows: (1) The quantity of extrema and zero crossovers must be equal or differ by no more

than one crossover. (2) The mean of local maximum and minimum envelopes is 0 for any data point. With the description of an IMF, any function may be decomposed using a sifting process. It is an algorithm for extracting IMFs from the initial signal $x(t)$. The sifting procedure must be performed as many times as necessary to ensure that the extracted signal meets the criteria of an IMF.

$c_i(t)$ is the order i-th empirical mode, while $r_n(t)$ is the last residue when the total empirical modes are retrieved. Each empirical mode $c_i(t)$ is also called IMF_i. The steps with IMF criteria consideration and sifting process are listed and displayed in Figure 4-23 (Dybała & Zimroz, 2012; Lei et al., 2013). The process of determining IMFs from the original signal is summarised here:

Start the EMD process of signal $x(t)$ by given $r_0(t) = x(t)$ and $i = 1$

Extract the order $i - th$ IMF

Given $h_{i(k-1)} = r_{i-1}$ and counting $k = 1$

Identify local maxima and minima of $h_{i(k-1)}$

Compute the cubic spline of each to get the upper and lower envelops

Get the local mean envelope $m_{i(k-1)}$ between those two lines

Compute $h_{ik} = h_{i(k-1)} - m_{i(k-1)}$

Investigate the IMF contribution of h_{ik} and given $c_i = h_{ik}$Otherwise, repeat the above steps starting from process III. Continue with $k = k + 1$

In case h_{ik} is an IMF, compute the residue from $r_{i+1} = r_i - c_i$. Investigate the number of local extrema, if r_{i+1} contains more than one extremum, then repeat step II. continue with $i = i + 1$

In case r_{i+1} is the residue of the original signal, end the process. Finalise all IMFs and the final residue $r_n(t)$ is provided.

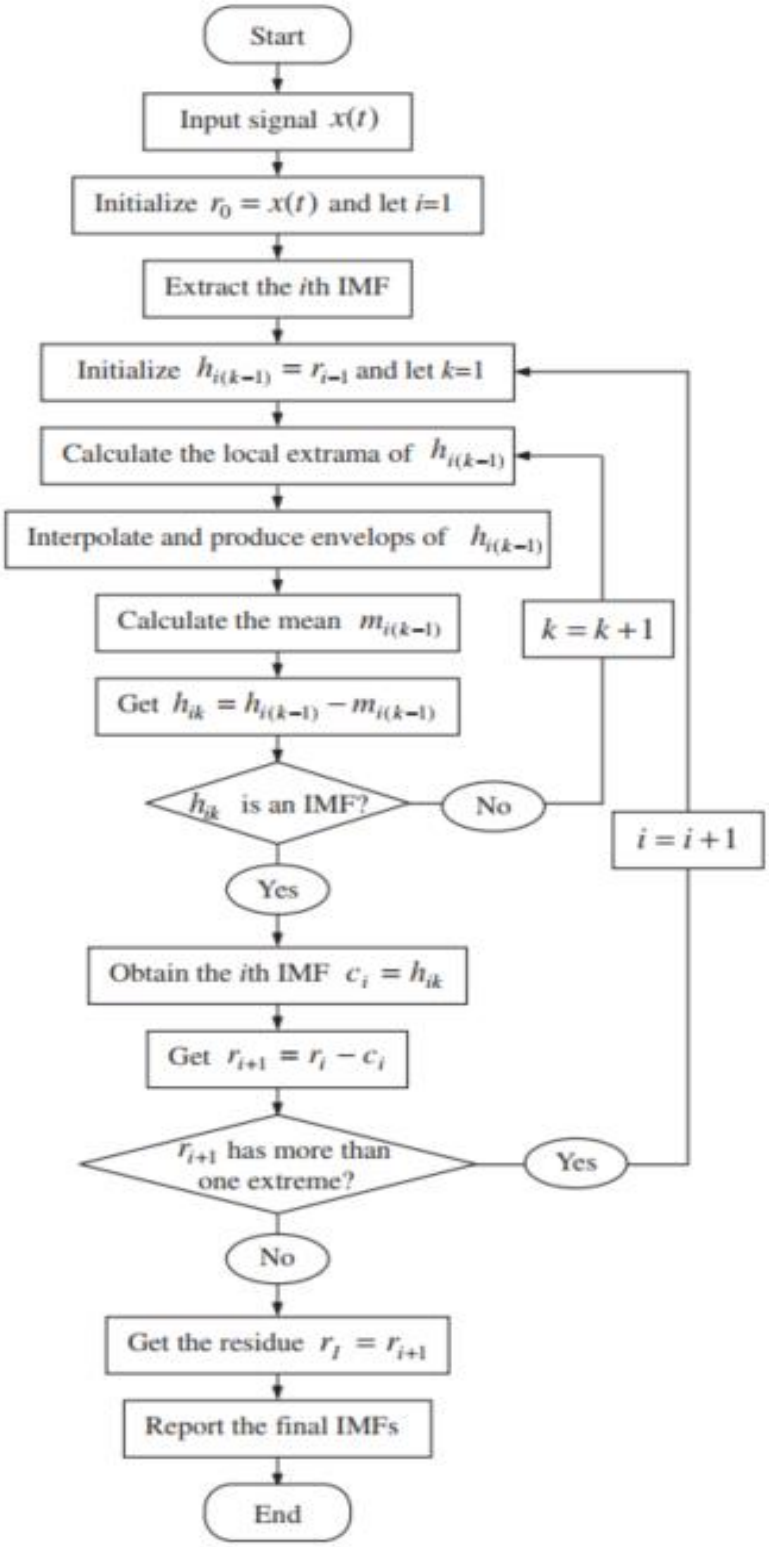

Figure 4-23 Flow chart of EMD process (Lei et al., 2013).

However, the common problem with the EMD process is the mode mixing, while a single IMF contains widely disparate scales in different IMFs. IMFs are twisted and fail to exhibit fault features when EMD is chosen to diagnose rotating machine defects (Lei et al., 2009). To solve mode mixing, an upgraded Ensemble Empirical Mode Decomposition (EEMD) was implemented (Wu & Huang, 2009). The EEMD adds finite white noise to the signal to solve mode mixing. EEMD repeats the EMD decomposition for each attempt but with various noises, yielding the means of related IMFs as the best IMF option. In addition, multiple decompositions averaging is introduced, using the white Gaussian noise to clean the local interference of active abnormal events (K. Wang et al., 2020).

A comparison between vibration measurement and acoustic technique for ball bearing fault detection was conducted using EMD to derive the non-stationary characteristics related to defects (Hiremath & Reddy, 2014). Artificial damages on inner and outer race were applied to bearing samples in addition to a good condition bearing. The major finding is that the effective EMD can provide successive estimations of defects in accordance with information from IMFs.

Wavelet packet decomposition and Hilbert-Huang transform (EMD) proved effective for spindle bearing CM. (Law et al., 2012) tried the mentioned technique on AE signals to reveal the related frequencies which were generated from the simulations through the correlation between the temperature response and the magnitude of AE. When compared with acceleration signal, AE enable the more efficient CM of spindle bearings.

At the final glance, there is none ready-to-use solution for either acceleration and AE signal to be practical and useful for the actual CM. Each setup of equipment and measuring environment would require specially designed technique to study the characteristic frequencies of rotating machines and their elements.

4.5 Summary

Principles and applications of AE and vibration techniques together with their strengths and weaknesses have been described in this chapter. AE are formed as the elastic waves propagated in deformed and loaded materials. The energy is released as a stress wave when the crack is inside or on the surface of a material. Studies of AE on early bearing defect detection were presented. AE can finally reveal some bearing defects that vibration could not deal with.

On the other hand, the vibration technique, primarily used for condition monitoring of rotating machines, works on the mechanical event that reveals an oscillatory movement of the sample. Examples of improved vibration techniques used for bearing defect detection were discussed. Railway uses of AE and vibration techniques have also been discussed, with important information provided for this study.

In addition, both AE and vibration techniques used for bearing CM will be successful if the essential parameters, including loading conditions, operational speed, and time information, are provided. Moreover, the bearing dimensions are also needed for further calculations of fundamental frequencies.

A comparison between AE and vibration technique has been reviewed. AE provides early detection through higher sensitivity and signal-to-noise ratio. Moreover, it is generally compact and versatile when the installation is taken on the field test. However, vibration techniques require less advanced signal processing techniques to provide fundamental condition monitoring data. According to other studies in this chapter, using AE with vibration techniques will be more efficient as each can provide different advantages and disadvantages.

Furthermore, available signal processing analysis on AE and vibration data from rotating machines were discussed. These include Time domain analysis with signal magnitudes, RMS, Crest factor, Skewness, and Kurtosis. Frequency domain analysis, Short-time Fourier

transform (STFT), Spectral Kurtosis, Time Spectral Kurtosis, Kurtogram, High-Frequency Resonance Technique (HFRT) / spectral envelope analysis, wavelet transform and Empirical Mode Decomposition (EMD).

Chapter 5: Laboratory experiments

5.1 Instruments

A series of lab experiments were undertaken to evaluate and calibrate the CM system utilising vibration signals and AE measurements. The concept of this chapter would contribute to the demonstration of compact system and inexpensive equipment related to further applications in field trials. Results from this chapter would illustrate an overview of generated signals from both sensing techniques, leading to the fundamental knowledge for data analysis. The information of each component within the measuring system will be provided together with the limitations when applied in the real-world conditions. Since harmonics related to the rotating elements are easily masked by surrounding noises, specifically designed signal processing techniques are required for defect identification process.

5.1.1 Acoustic emission sensors

The experiment uses a short transient AE event generated by elastic energy release. Similar to an earthquake when the flaw acts as the epicentre, the elastic waves propagate in all directions. Figure 5-1 illustrates how AE sensors retrieve propagating sound from the source, i.e., a defect on the surface.

The elastic waves propagate in a concentric profile around the source which can be effectively detected by one of the AE sensors despite the large surface area where those small sensors are placed.

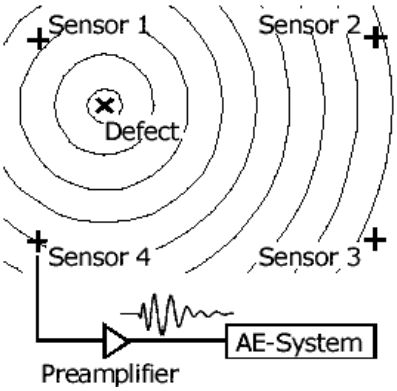

Figure 5-1 The propagation of elastic waves through AE sensors (Vallen, 2002b).

There are related parameters which contribute to the maximum detection of AE sensor, i.e., the material properties, the shape and geometry of the measured object, and the surrounding environments. AE sensors can detect elastic waves at several metres on flat and cylindrical metal surfaces. Thus, AE can be in place where other techniques might not be able to measure the attenuating signals on the specific areas (Vallen, 2002b).

The main components of the AE measurement include:

1. Test sample with load applied – generating mechanical tensions

2. Source initiation – releasing elastic energy

3. Wave transmission – between the source and sensor

4. AE sensors – converting mechanical contents into electrical AE signals

5. Acquisition unit - obtaining an electronic data collection from an electrical AE signal

6. Display unit – plotting output signals on the specific application

7. Signal processing model – evaluating the signals according to specifically designed techniques

5.1.2 The concept behind AE sensors

As mentioned earlier, Piezo-electric sensors were chosen as the most suitable sensor for AE measurements. The main reason involves the robustness of Piezo-electric sensors is significantly higher than other conventional sensors, they also provide more sensitive manner.

The frequency range between 100 and 300 kHz is used to examine metal samples' integrity. Accordingly, the resonance of the AE sensor should be about 150 kHz with the wide coverage of sensitivity. The sensor's spatial range is also indirectly determined by the resonance frequency. The sensitivity of piezoelectric sensors can be as high as 1000V/mm.(Vallen, 2002b).

Theoretically, high frequencies are easily weakened with a short detection distance. Frequencies below 100 kHz would also generate by background noise from further distance. There are electrical and mechanical noises which normally present on the output signal (Vallen, 2002b).

The AE sensors have a wide range of application depending on the sensitivity, resonant type, operating temperature range, and working environments. Moreover, there are general purpose and specific types of AE sensors available according to the project preferences and budget. Some operating situations demand a specific type of AE, however a general-purpose AE sensor may suffice at the first assessment (Vallen-Systeme GmbH, 2011).

Standard commercial acoustic emission sensors use a single Lead Zirconate Titanate piezoelectric crystal (PZT). Theoretically, high-frequency elastic waves can cause the piezoelectric crystals to be elastically deformed. Deformation creates tiny electric impulses that may be amplified and digitised. Figure 5-2 illustrates the enclosed AE sensor’s internal components.

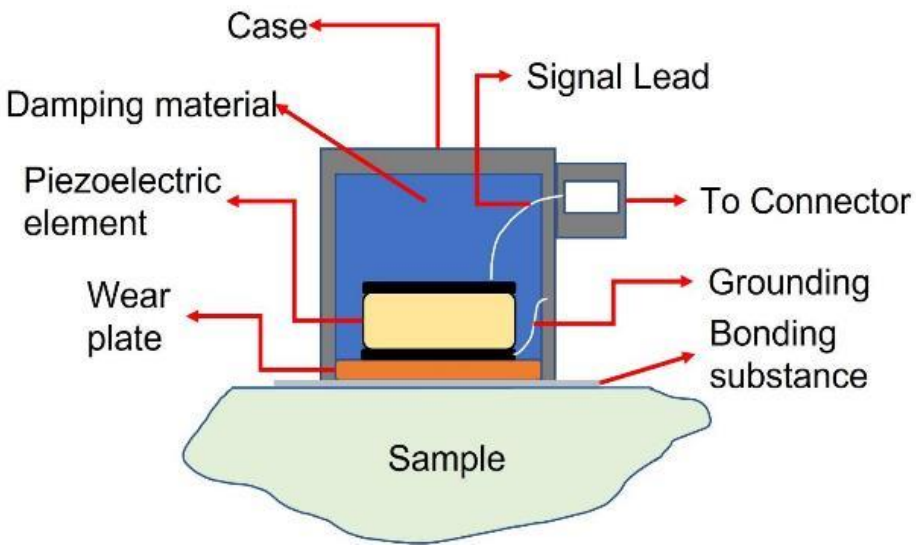

Figure 5-2: The structure of AE sensor.

Wear-resistant plate made of Al_2O_3 is located at the bottom end of the AE sensor as the encloser protecting the whole sensor. With the very high stiffness of the wear-resistant plate, it allows the transmission of elastic waves from the structure being monitored through the Piezo element inside, which is linked to the connector. The wear plate is very essential ensuring waveforms from the sample are captured without any dampening effects that might lead to incorrect analysis findings.

There are two main types of AE sensors as refer to their operational preferences: including wideband or differential sensors, and narrowband or resonant sensors. It should be noted that the selection of AE sensor type must be one of the essential steps before taking the measurements as the AE sensor not only detect the waveforms but also reduce noise from the environment, which can pollute the signal and make signal processing more difficult. Each type of AE sensor will also sense the different range of the frequency response. The wideband type generally acts a widely flat-frequency response curve. Narrowband piezoelectric crystals are more sensitive at certain frequencies, called resonant frequencies. As a result, the piezoelectric

crystal's responsiveness is amplified at resonance frequencies. To reduce mechanical noise below 100 kHz, narrowband is better to wideband (Z. Huang, 2017).

In this study, AE sensor model R50α resonant type (narrowband) manufactured by Physical Acoustics Corporation (MISTRAS) was chosen. The sensor's body is made of solid stainless-steel rod, making it exceptionally durable and dependable. The ceramic base, along with a 30-degree chamfer profile of the sensor's body, generates the isolation from the structure during the experiment to reassure a low noise operation. The operating frequency range of 150-700 kHz is provided as refer to the official product sheet data. The R50α has the operating temperature range from -65 to 175 ºC. It weighs 32 grams and comes with tiny dimensions of 19 mm wide and 22.4 mm in height. This is perfect for tight space with limited access for huge connection of wires and related equipment. The application of this sensor can also take place in noisy environment of various industries such as welding monitoring.

As illustrated in Figure 5-3, The main resonant frequencies of R50α are at 170 kHz, 220 kHz, and 350 kHz (red graph). The compatible preamplifier type are 0/2/4 and 2/4/6, where each digit describes following logarithmic decibels (dB) 0dB, 20dB, 40dB, and 60dB. In this study, R50 resonant sensors from Physical Acoustics Corporation (MISTRAS) were adopted. The R50 resonant sensor operates at a frequency range of 100 to 700 kHz. The principal resonance frequencies are 170, 220, and 350 kHz (MISTRAS, 2011b).

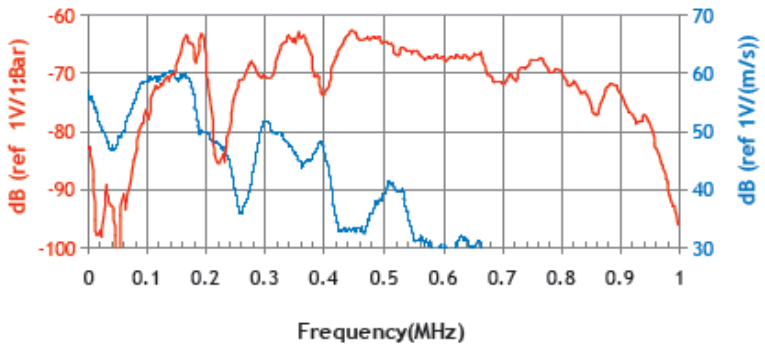

Figure 5-3: Frequency response of an R50α (PAC, 2011).

5.1.3 AE measurement system

The equipment list applied for AE measurements contains various components. Fortunately, AE system is adaptive and available for customization. Therefore, specifically designed system includes a series of useful elements that contribute to the signal delivery until it is ready to be displayed on the application. The related components comprise of:

AE sensor – It is attached to the sample via a magnetic holding device. While the connector of AE sensor is linked to a preamplifier. Figure 5-4 illustrates the AE sensor model R50α from Physical Acoustics Corporation (Ltd) or PAC UK which is now MISTRAS.

Figure 5-4: AE sensor R50α (MISTRAS, 2011b).

Pre-amplifier & main amplifier – Since the voltage transmitted by AE sensors are normally of low amplitude, which requires the amplification unit. The most widely used amplitude gains is between 0dB and 60dB based on the source preferences (Ferrando & Mulier, 2015; Ferrando Chacon, 2015). Gain is the output's amplitude divided by the input's amplitude. It's usually measured in logarithmic decibels (dB). Pre-amplifiers are placed near sensors to amplify their electric impulses. It works with the main amplifier to generate a sufficient amount of signals. Before the data capture card digitises the signal, both amplifiers raise its strength. Preamplifier can be included or connected individually.

In this study, the separate type of pre-amplifier (2/4/6) is chosen to provide the connection between the AE sensors and the main amplifier. Figure 5-5 displays the pre-amplifier from PAC with 20/40/60dB gain. Therefore, the gain settings include 20dB, 40dB, and 60dB. The

selection can be made by the toggle switch at the side of its body. Parameters related to the adjustment of gain comprise of load condition and speed. Trials of gain setting would provide the output amplitude it is too low or too high when compared with the optimal value, which will make the analysis possible. DC power is supplied to the pre-amplifier by the main amplifier.

Figure 5-5: Pre-amplifier from PAC with 20/40/60dB gain (MISTRAS, 2011a).

The main amplifier from Physical Acoustics Corporation (MISTRAS) model AE2A is chosen as it is a low noise, high-performance and wide bandwidth systems for AE sensors. It is displayed in Figure 5-6. The bandwidth of PAC AE2A ranges from 3 kHz – MHz while it is capable of internal gain between 0 and 61dB in 3dB steps.

Figure 5-6: Amplifier from PAC model AE2A (PAC, 2004).

Adhesive substances – The adhesive substances are based on the type of AE sensor installation. The type of application includes Glue type (for piping inspections), Magnetic hold-downs (for ferrous samples), Waveguides (high temperature applications)

Magnetic hold-downs were selected for experiments in this study as all samples are ferrous substances. However, the wayside measurement on cast manganese crossings used the glue type via Araldite adhesive instead of magnetic hold-downs. Rapid and easy setting epoxy provides the sufficient strength to the coupling between AE sensor and the monitoring samples. It should be noted that applying light pressure to the contact until set via a tape between 20 minutes and 2 hours allows the full strength. Figure 5-7 displays Araldite A0002 Rapid Epoxy.

Figure 5-7: Araldite A0002 Rapid Epoxy (Lawson H.I.S. Ltd, 2022).

Data acquisition (DAQ) – While there are various choices of the DAQ unit, it is worth to mention that the signal types, number of channels, desired sample rate, resolution, and accuracy of signal collection from the device all contribute to determining which DAQ equipment to choose. The DAQ unit sits between the data logging computer and the main amplifier.

There are two DAQ units providing a series of data in this study. The first is Agilent (Keysight) U2531A which extract the AE and vibration signals acquired during the experiments. Figure 5-8 shows the actual DAQ unit used in this study. This was connected to the computer via Universal Serial Bus (USB) cable. When operated in single-channel mode, it can acquire data at the sampling rate up to 2 MS/s (per each channel) with 12-bit resolution according to the

technical data sheet from Keysight. It also allows simultaneous sampling of data per each channel through dedicated Analog-to-digital.

Figure 5-8: DAQ U2531A (KEYSIGHT Technology, 2019).

Another DAQ unit comes in a small form factor from National Instruments (NI) model NI-9223 as shown in Figure 5-9. The connection was made through the USB type encloser which also provide the LED status of the DAQ unit. The maximum sampling rate is 1 MS/s (per each channel) with 16-bit resolution according to the technical data sheet from NI. ADCs are embedded inside the DAQ unit to provide the capability on measuring the impact and best wave testing. Each channel's input signals are buffered, conditioned, and sampled by an ADC. An independent signal path for each channel in conjunction with separated ADC enable the simultaneous measurement for all channels.

Figure 5-9: DAQ NI 9223 (NATIONAL INSTRUMENTS, 2016).

DAQ units share similar specifications that would not lead to issues on the measuring data. To be precise, it depends on the setting on the parameters rather than the hardware differences.

However, the combination of AE sensors and accelerometers requires two separate DAQ units since each could only be used to log the same output signals. As a result, two DAQ units are needed for AE and vibration measurements, each DAQ for recording data from up to four channels. Two DAQ devices may operate at different sampling rates to accommodate acoustic emission and vibration measurements.

Computer (PC) – Acoustic emission and acceleration signals were digitised with a PC, monitor, and other peripherals. A customised data logger created by MATLAB is applied for the data logging and storage. These output data in specified file type (.cdf or. daq) will consequently pay tribute to the data analysis.

With its compact size and versatility in usage, a small-form-factor computer unit developed by Intel was introduced in some experiments as a selective for a giant and heavy industrial-grade PC. It is also called the Next Unit of Computing (NUC) which is fully customisable for the specific usage and budget. It also provides useful connections, including HDMI for the display, USB ports for mice and keyboard adapters, and high-speed USB for DAQ or data storage. In addition, Bluetooth and Wi-Fi connections are built-in for extended wireless capabilities during the experiment condition.

Combining the sensing equipment with a small but mighty NUC would unlock the limitation on the field trials. The only significant size of equipment is only the display monitor, not a conventional industrial-grade PC.

The process chain of AE signal acquisition is illustrated in Figure 5-10. The process starts with the generated mechanical stress within the test object, which is normally created by applying external forces. The material behaviour which is influenced by material properties generates

the excitation of AE signal by releasing of elastic energy, e.g., crack initiation. Elastic energy produces the propagation of wave through the material which is able to be detected and converted into the AE signal by the AE sensors. The AE measurement system consequently processes the AE signal using data acquisition unit.

5.1.4 Accelerometers

The industrial grade piezoelectric accelerometers model Wilcoxon 712F which is integrated with BNC cable were introduced as the sensing element for vibration data in this study. Wilcoxon 712F accelerometer works within a frequency range of 9 Hz to 15 kHz. The main reason to choose the industrial grade accelerometer because it is capable to operate under the challenging operational conditions in the field trails. It features a linear frequency response with a nominal sensitivity of 100 mV/g. The accelerometers are powered by a 12-channel power supply from Vibrametrics with an output voltage of 18 VDC. Moreover, the resonance frequency of this accelerometer is higher than 45kHz, which is over the measuring frequency range. A vibration calibrator oscillating at 159.2 Hz was utilised to calibrate the accelerometers used in the testing. To calibrate the accelerometer, the device using built-in magnets is provided with the installation of the sensor.

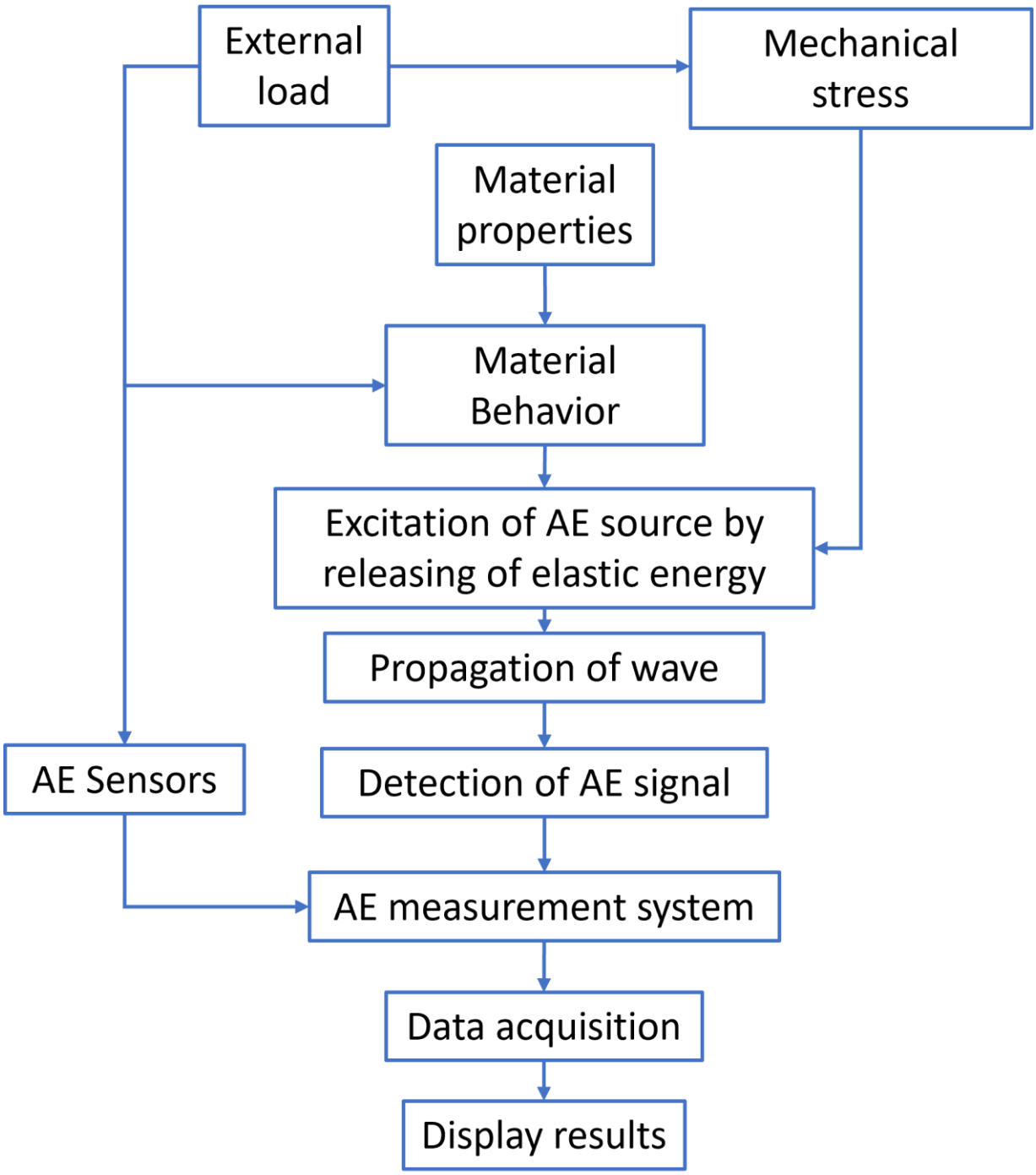

Figure 5-10: The AE process flow chart.

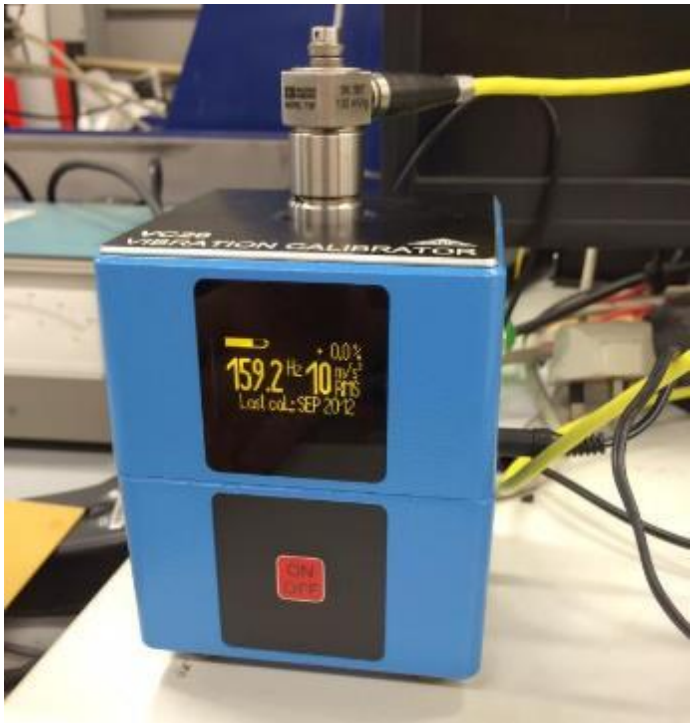

Figure 5-11: accelerometer Wilcoxon 712F and VC20 vibration calibrator.

The installation of vibration sensor was made by built-in magnets. Due to damping effects from the magnet, the top working frequency range is restricted to 5 kHz. Figure 5-11 illustrates accelerometer calibration.

5.2 Experiments

Trails on the excited signals have been done in order to identify the active frequency range that suits the resonance bandwidth of R50α sensor. The result from the bearing with defect when it is rotating at 400-500 RPM revealed the frequency range of 100-150 kHz. Therefore, the active frequency range in the actual experiment should cover that range without taking too much analysis time for the result.

Nyquist theory describes the relationship between the sampling rate and the result of frequency domain data. To be precise, the sampling rate will be halved at the frequency domain result. Therefore, the minimum of 500 kS/s sampling rate is required for any experiment in this study.

Considering a set of sampling rate containing 500 kS/s, 1 MS/s, and 2 MS/s would be useful to optimize the result in terms of the analysis time and the resolution. In general, the system would consume more analysis time when the high sampling rate is relatively high. Consequently, there is no peak for frequencies greater than 250 kHz, 500 kS/s sampling rate can be employed efficiently. Furthermore, reducing the sampling rate and data logging time as much as acceptable reduces the amount of data that must be processed and simplifies the processing power that must be deployed. Higher sample rates generally require a mighty computer processor as a larger amount of data is generated.

According to the manufacturing data, the resonance of R50α sensor is 170 kHz. In this experiment, a metal collision acts as a flaw to stimulate resonance frequencies. The minimum sampling rate of 500 kS/s is sufficient and suitable for the detection of mechanical noises. Moreover, significant peaks at the range above 250 kS/s are undetected during the test carried out by the manufacturer. As a result, 500 kS/s is the optimum sample rate for the whole experiment. Because of its resonance at 170 kHz, after evaluating several sample rates with other sensors, the R50 sensor was chosen for future investigation.

The distance between the AE sensor and the source should be considered as the signal amplitude would be affected. Higher amplitude signals can be expected from an AE source that is physically closer to the sensor because of less attenuation and scattering. Severe flaws, like a massive wheel flat, can cause high-amplitude AE events with each wheel revolution. The explements in this study measure the amplitude in the unit of Volt (V). Signal amplitude is proportional to source energy and amplification. The saturation of raw signals is related to the ability of signal analysis when the amplification was applied. To avoid saturated signals and to guarantee that relevant AE events associated to the existence of defects are detected, it is critical to set an adequate gain level at the amplification stages. The low signal strength is generated because of low gain levels of amplification. This low strength would make the signal analysis

challenging and time-consuming. Various experimental situations need different gains for optimal signal level.

A range of signal analysis provided in this study would be presented in the following sections. These include magnitude with time domain analysis and frequency analysis. However, some signal processing techniques might take high computing time when compared with fundamental magnitude analysis. Moreover, different file format types retrieved from the data acquisition would also alter the computation time.

5.2.1 Pencil lead break tests

The resonant type of AE sensor could unintentionally generate inevitably distorted signals because of its unique frequency response. As a result, the output spectrum could lose some essential waveforms generated from the defect. Therefore, as referred to the technical datasheet via the specially designed technique called a Hsu-Nielsen source or a pencil lead break test, the spectrum calibration could be done before the data collection starts (Hsu et al., 1977). A pencil lead break test that suppresses itself onto the samples applies the lead tip's braking to generate an impulse AE signal. Figure 5-12 displays the schematic diagram of Hsu-Nielsen source. As a result, the frequency of generated pulses could range from a few kHz to many MHz (Dukes & Culpan, 1984).

The pencil lead with 2H hardness could be either 0.5mm or 0.3mm in diameter with approximately 3mm and 0.5mm in length from its tip. The 2H hardness pencil lead is only certified as the others might not be able to generate a frequency range above 50 kHz. The mechanical noise that is unwanted generally sits below 50 kHz. The impulse signal emitted by pencil lead tip breaks is identical to that produced by a developing fracture in the sample (McLaskey & Glaser, 2012).

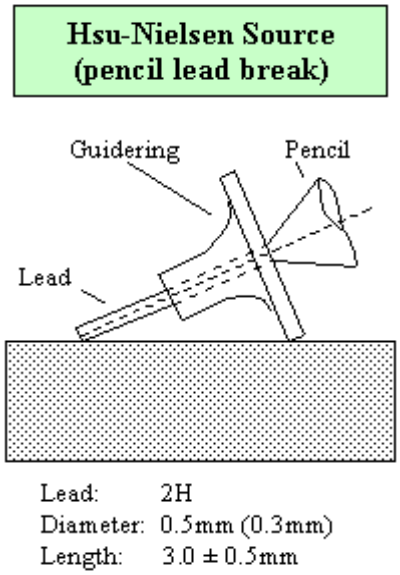

Figure 5-12: Hsu-Nielsen source (NDT Encyclopedia, 1996).

Fracture of brittle graphite lead in a fitting mimic an acoustic emission event. Two main goals of doing a pencil lead break test before conducting the main experiment are described (NDT Encyclopedia, 1996). The first is confirming the transducer's acoustic contact provided with the sample being monitored. The latter means investigating the system's accuracy based on the setup of the source location. This last goal entails establishing the observed item's real acoustic wave speed indirectly for the observed item.

Moreover, the benefits of a pencil lead break test could extend to other aspects, including confirmation of experiment configuration as following the standards, ensuring safety at work as referred to hazard and risk assessment, and understanding all AE signal characteristics as data acquisition output.

5.2.2 Amsler machine

The difficulty of diagnosing contact fatigue failure at the wheel-rail contacts leads to wheel and rail monitoring difficulties. To simplify the crack analysis, specific laboratory tests instead of field assessments. This test was created to concentrate on RCF fracture development. It also

allows more precise wheel-rail stress adjustment. Normal load, traction load, friction, lubrication, and other elements can impact wheel-rail contact. A well-known laboratory-based experiment for evaluating wheel-rail contact is the twin-disc model. Figure 5-13 shows the twin-disc model which contains a couple of two parallel cylinders.

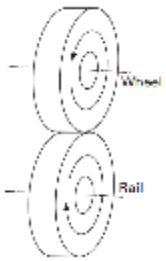

Figure 5-13: Twin-disc model (Lewis & Olofsson, 2009b).

While there are several twin-disc test machines, the Amsler machine which was revealed in 1922 was chosen for this study. Amsler created this equipment to analyse dry rolling-sliding wear conditions. Even though the machine is outdated, this well-known gadget is still in good operating order today. The major goal of creating this machine was to utilise it to inspect the steel wheel's wear. The rotational motion of the twin-disc type is generated by a single 3-phase, two-speed AC motor (Ichinose et al., 1978; Masumoto et al., 1978). Two discs of test material are rolled under pressure with a degree of sliding by the machine.

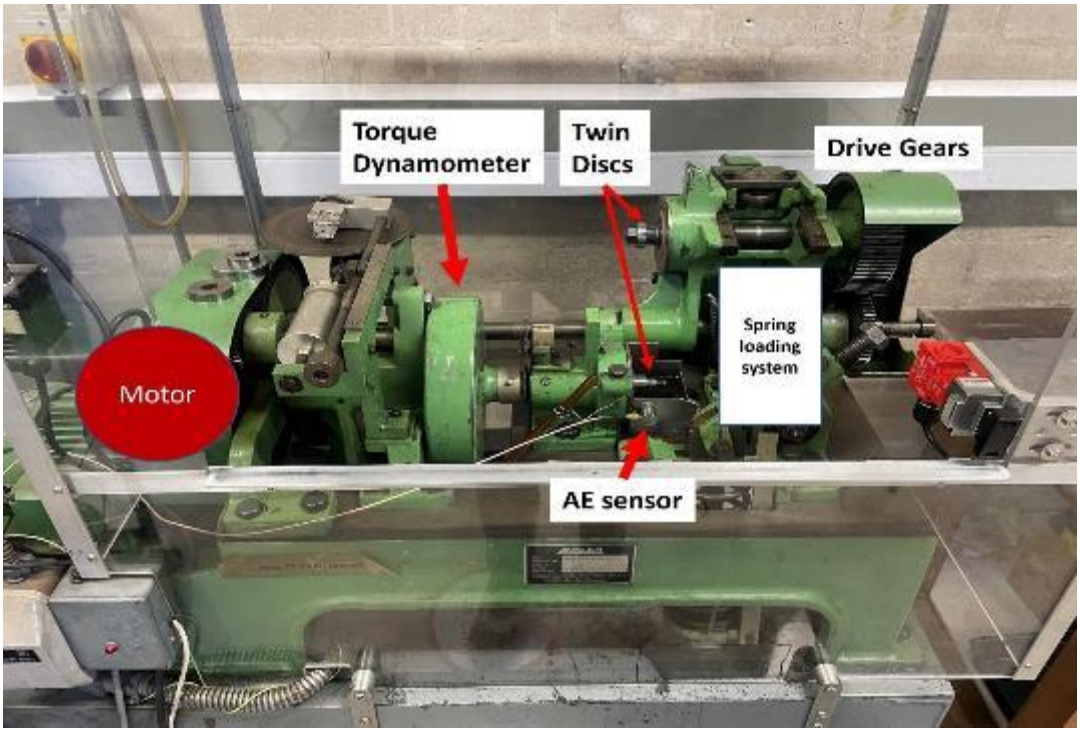

Figure 5-14: Amsler machine with opened cover and separated twin discs.

Figure 5-14 depicts an overview of the experiment. A solid green Amsler model A135 wear testing machine can be found. It was manufactured by Wolpert Werkstoffprüfmaschinen G.m.b.H. in 1973. Twin discs installed in the Amsler machine is displayed in Figure 5-15. The signal should be picked up by the AE sensor and shown on the PAC package programme named AEwin. R50α piezoelectric AE sensor was attached to the surface of the mounting plate using epoxy adhesive. Data acquisition and AEwin software were used to log and display all of the data as illustrated in Figure 5-16.

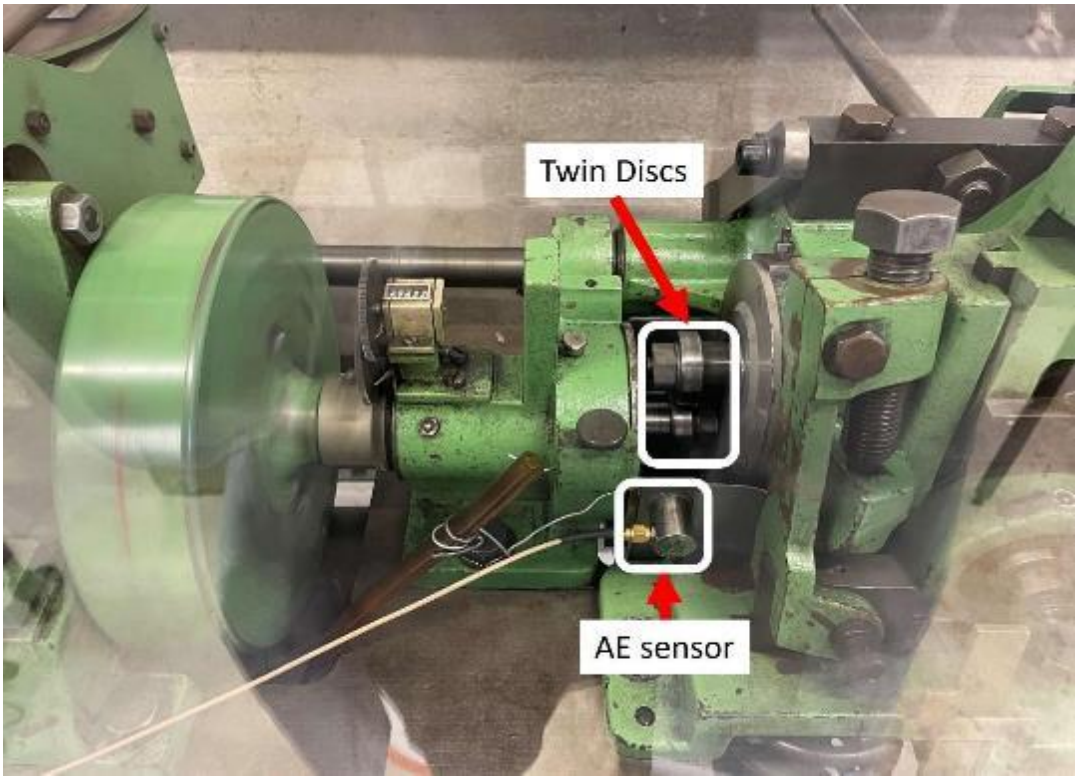

Figure 5-15: Detailed area of twin discs and an AE sensor.

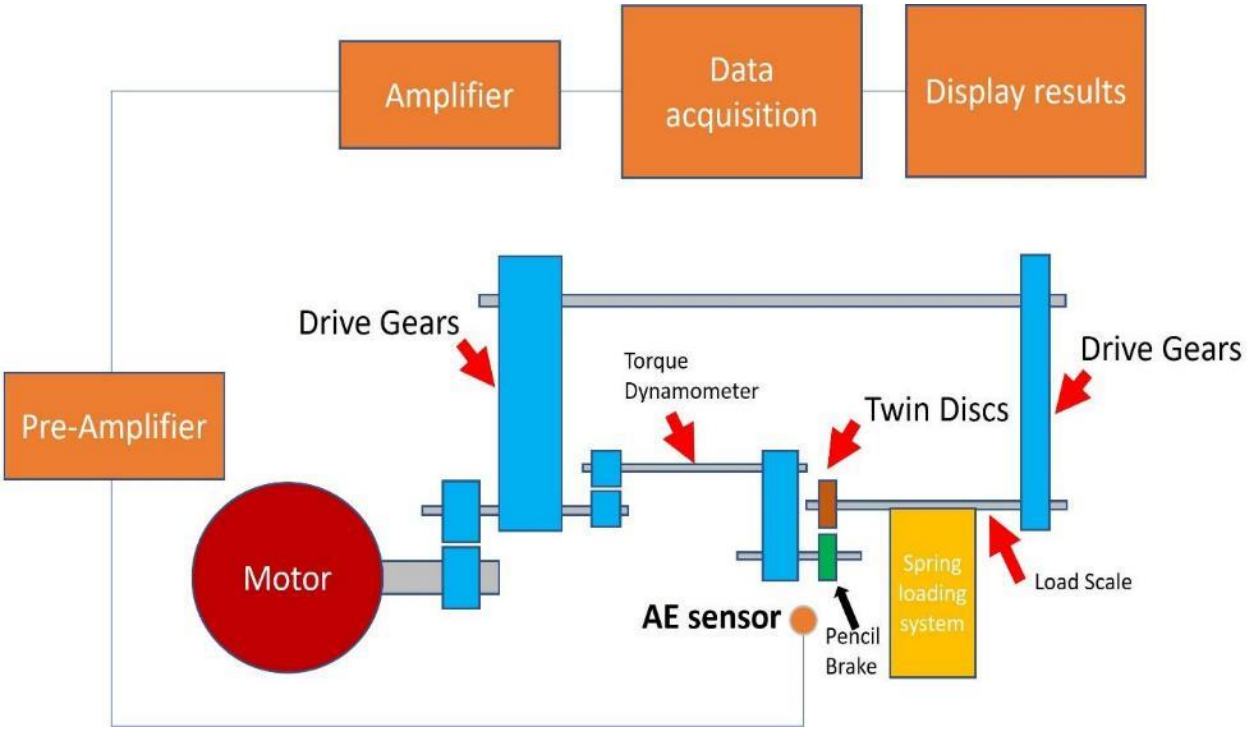

Figure 5-16: Schematic diagram of the Amsler machine.

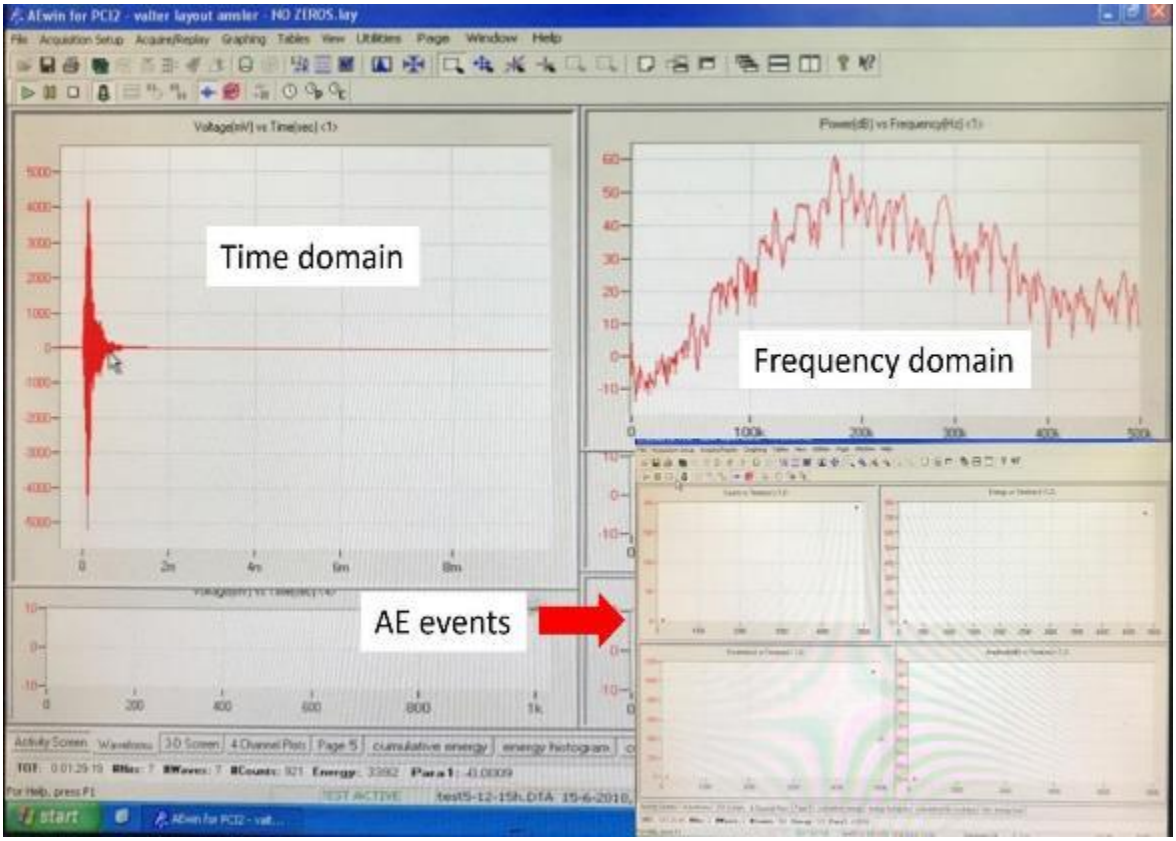

Figure 5-17: AEwin display of AE results.

The experiment start once the Amsler machine is powered, while twin discs of designated materials are placed. The AEwin application displays the event on every time domain parameter whenever the pencil lead tip contacted the machine. The experiment revealed that the pencil lead breaks at 4953 seconds according to hits that reach the threshold in Figure 5-18. Consequently, there are changes in various AE parameters on time domain retrieved from AEwin program as shown in Figure 5-17, including amplitude, count, duration, and energy. The similar trend was discovered on the parameters which were mentioned earlier. However, the rise time behave differently as it is fluctuated over time while the rest share related trend. Rise time does not endure the whole duration of the hit. As a result, it is dependent on the occurrence of the peak amplitude, which may occur at different times throughout each hit. The results of the test are as follows:

There are 6 hits discovered above the threshold (50 dB) as shown in Figure 5-18. Each hit had different value of parameters. Because of the longer detected signals, increasing the rise dramatically increases the number of counts and energy as illustrated in Figure 5-19.

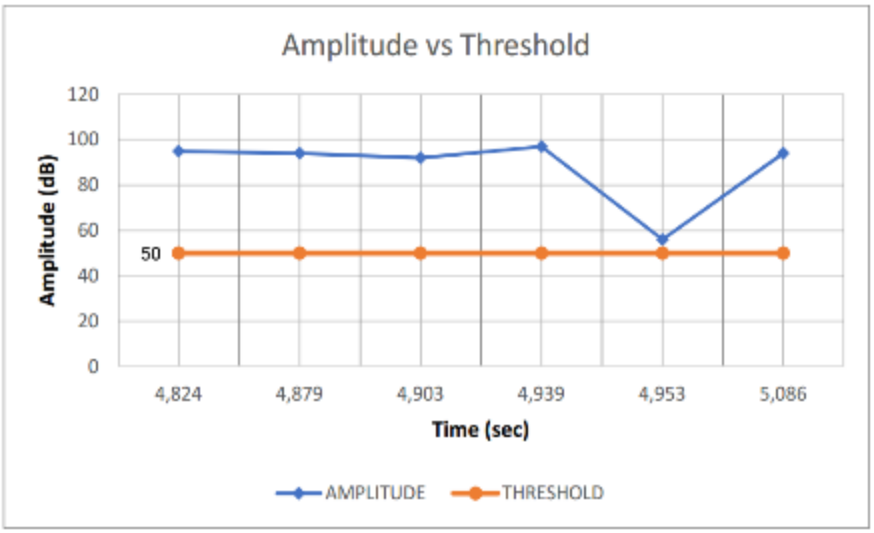

Figure 5-18: Total hits above the threshold.

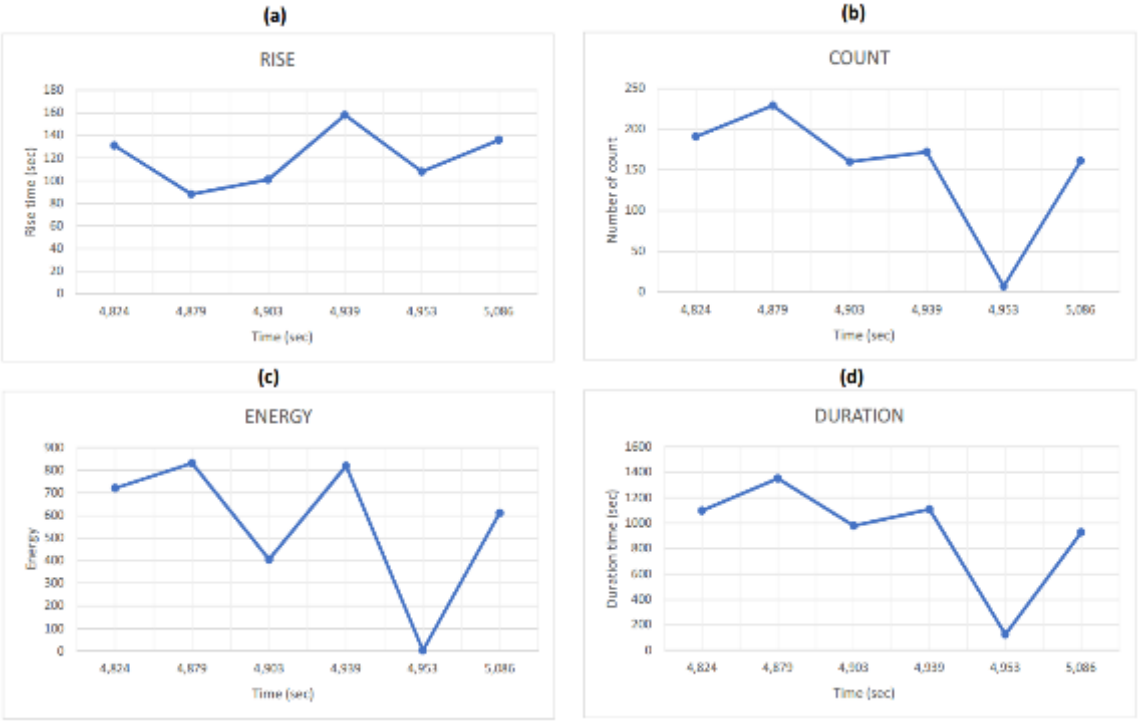

Figure 5-19: AE parameters of related hits.

5.2.3 Reduced scaled wheel trolley test

The goal of the preliminary experiment is how well the monitoring system generates AE signals from a manually powered trolley fitted with a reduced-scale train wheel that moves over a stretch of the test track. Attenuated AE signals came from a 0.16-m-diameter trolley wheel.

According to section 5.1.3, a preamplifier and amplifier amplified the output signals. The AE sensor was mounted on the rail using WD-40 and a magnetic connection. A 4-channel decoupling box sent the amplified signal to a 12-bit Agilent 2531A. Finally, using UOB-customized MATLAB software, the PC recorded the signals. An experimental condition is presented in Figure 5-20 which comprises a manually operated trolley equipped with either a healthy wheel or a faulty wheel, a section of rail track build in the laboratory, the AE sensor placed on the rail, a pre-amplifier and connecting wires. The experiment starts with the signal generated by the AE sensor which is later amplified by a pre-amplifier prior to the main amplifier. The data acquisition board consequently process the signal and send to the output display via a special application. The whole process of data acquisition is shown in Figure 5-21.

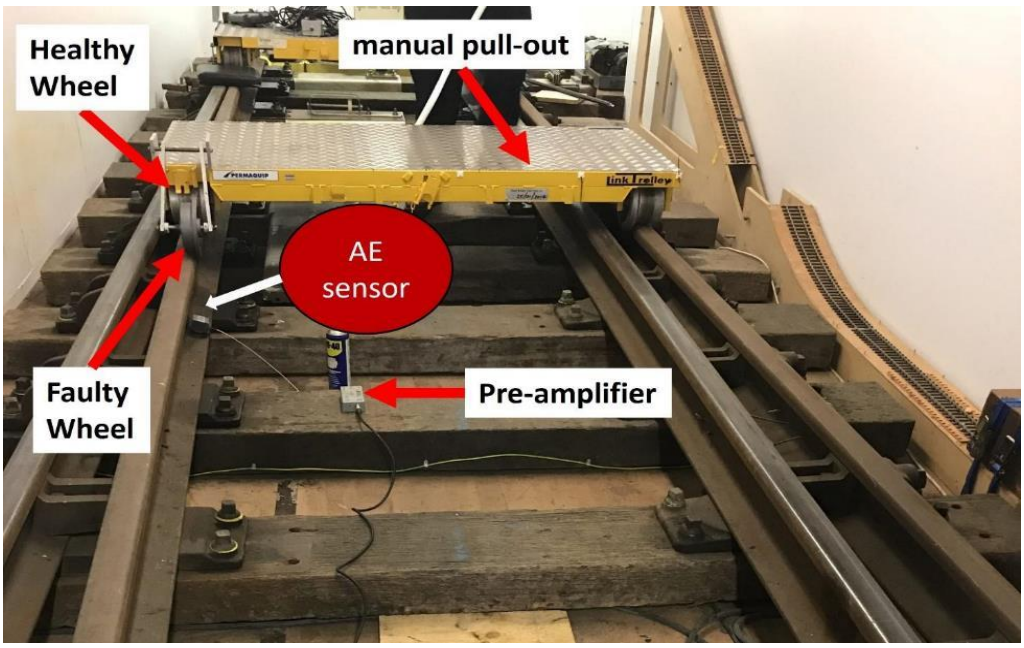

Figure 5-20: Wayside monitoring based on the healthy or faulty scaled single wheel.

The varied situations of railway wheels were represented by two similar railway wheels, the one representing the healthy wheel and the second representing the defective wheel. A metal build-up flaw on the wheel was performed to create the damaged wheel. As indicated in Chapter 2, the experiment replicates wheel failures involving spalling and shelling.

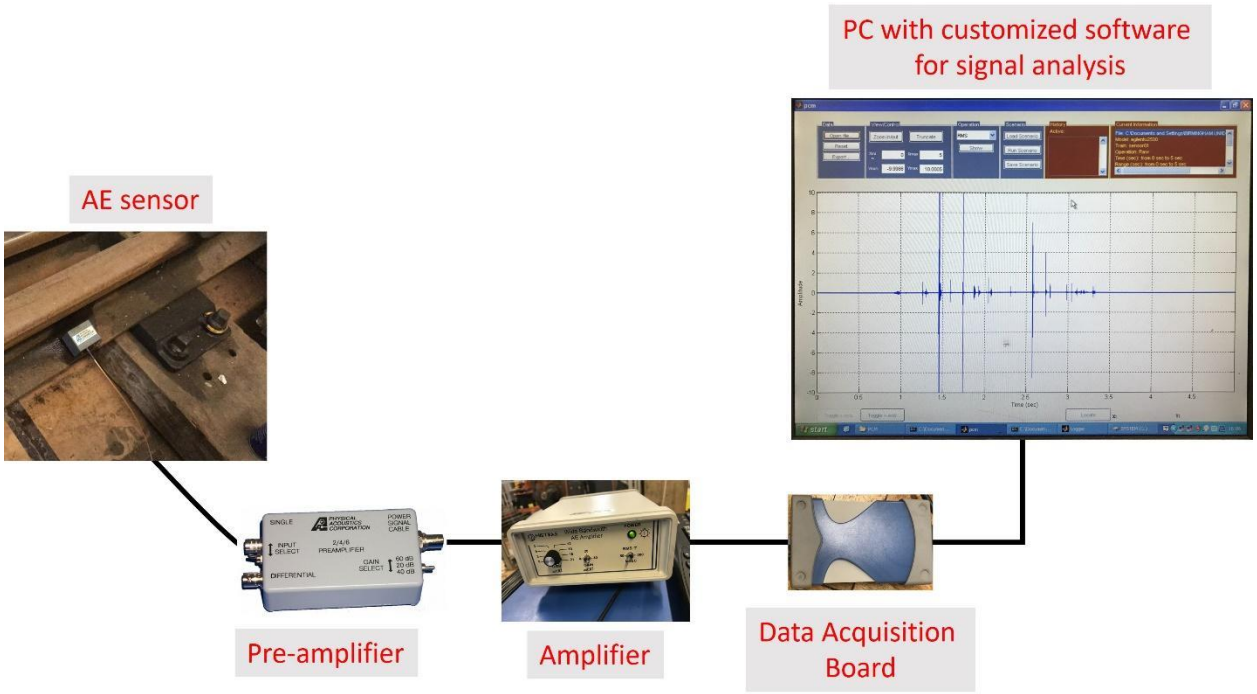

Figure 5-21: Experimental setup for a wayside monitoring of scaled wheel trolley.

The trolley was pulled by hand, allowing the wheels to rotate at 1m/s. AE signals were amplified with a 40-dB preamplifier and 18-dB amplifier. Figure 5-22 shows a piece of metal welded to a reduced scale wheel to simulate a wheel flat problem. A magnetically powered AE sensor was placed on the rail for the wayside inspection in Figure 5-23. The detailed picture represents a piece of magnetic adapter for the installation of the AE sensor is displayed in Figure 5-24.

The data collection logged the output signals and then given to the specifically created program. Digital filtering is generated, and raw signals are analysed using moving RMS and FFT. The moving RMS divides data into overlapping windows; each window generates better results

than the raw RMS analysis. The schematic diagram of the reduced scaled wheel trolley test is shown in Figure 5-25.

Figure 5-22: A faulty wheel used in the trolley.

Figure 5-23: AE sensor installed by a magnetic hold-down.

Figure 5-24: A magnetic adapter for the placement of AE sensor on the wayside measurement.

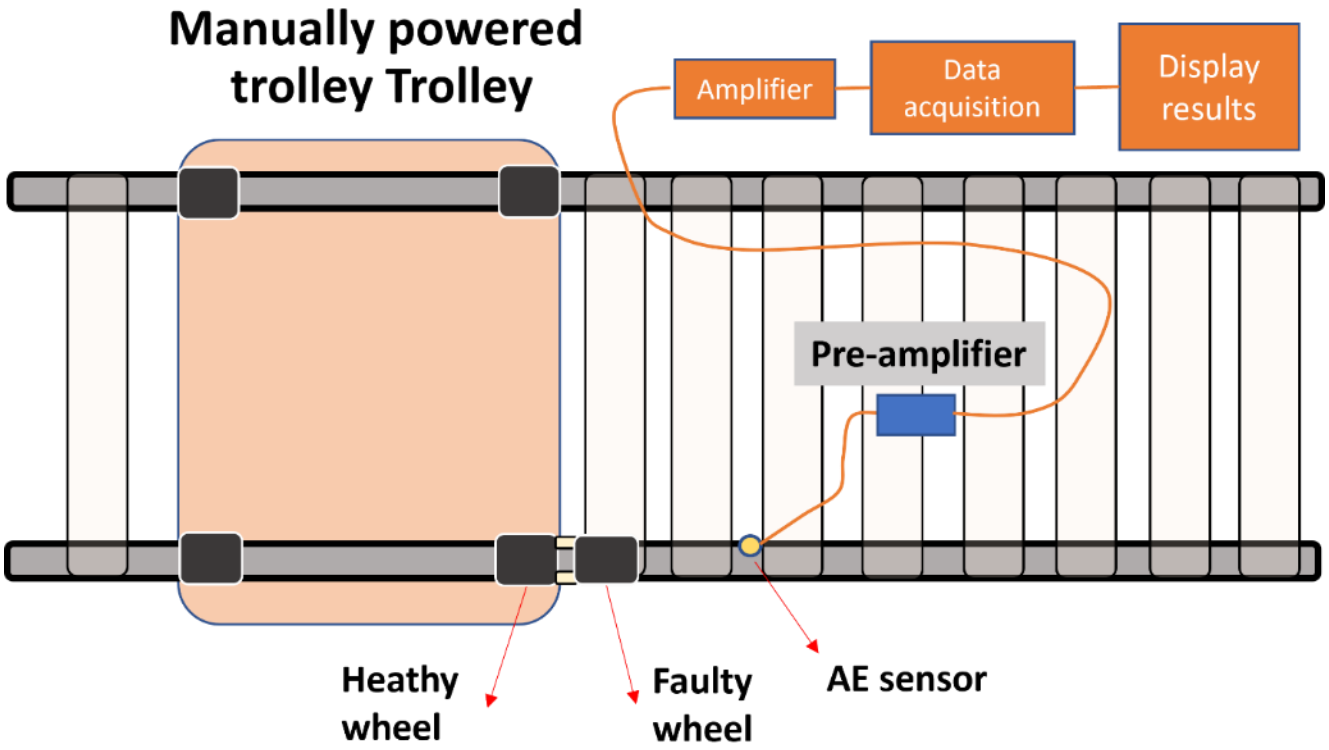

Figure 5-25: Schematic diagram of the Reduced scaled wheel trolley test.

5.2.4 Bearing test rig

In addition to the wheel and rail interface investigation, the experiment using a bearing test rig was designed to study how the bearing with range of conditions generate AE and vibration signals. Healthy bearings and bearings with several artificially induced defects were used for a series of experiments, which include different operating speed and loading conditions. Automotive wheel bearing samples were chosen as representatives of tapered roller bearings which are installed in the rolling stock wheelset. The bearing model PW29530037CSHD made by PFI has the dimensions of 29 x 53 x 37 mm. Figure 5-26 displays the bearing sample used in the laboratory rig test.

Figure 5-26: Bearing model PW29530037CSHD made by PFI.

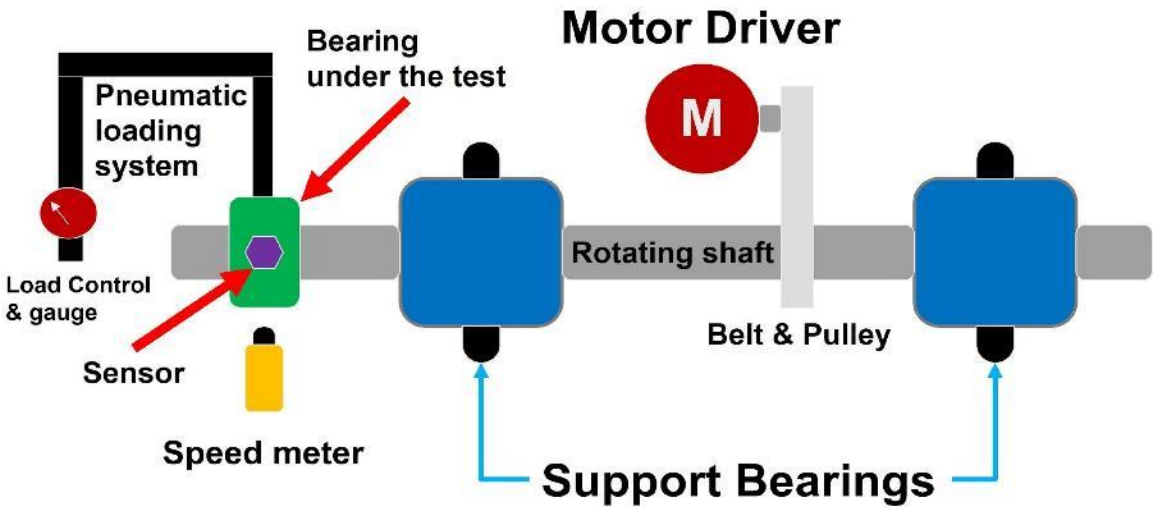

Figure 5-27: Laboratory test rig experiment.

The bearing test rig comprises of the main support bearings with motor driver connected via belt and pulley. Pneumatic loading system with variable pressure control is provided together with a speed sensor. Therefore, the experiment can experience a range of rotating speeds. Either an AE sensor or a vibration sensor was assigned to gain the signal from the bearing sample. Despite a small area on the bearing was provided, however, the installation of AE and vibration sensors did take only a handful of area. While the vibration sensor was able to be fitted using magnetic hold-down on the bearing, the AE sensor had to be wrapped and attached to the bearing using the duct tape as the magnetic scheme was not possible. Schematic of lab test rig is illustrated in Figure 5-27.

Heathy and damaged bearings which contain artificially induced roller defects and lubricant contamination were included as the samples for this laboratory experiment. The severity of roller damage was assessed through 10% and 50% fault size when compared with the circumference. Figure 5-28 displays the rollers with artificially induced defects. Disassembly of the test bearings allow the introduction of artificially induced defects before they are enclosed and installed on the test rig. Modified test rigs rotated bearings from 100 to 1000 RPM. In addition to speed variations, a range of loading conditions was added to the test.

Figure 5-28: Rollers with artificial defects.

Before testing, the calculation of fundamental frequencies of rolling element bearings that was mentioned earlier in section 4.4 would demonstrate the actual individual characteristic frequencies as refer to the speed parameters. Hence, four parameters including the FTF, BPFO,

BPFI and BSF were calculated using the provided equation in section 4.4 and listed in Table 5-1.

Table 5-1 Fundamental frequencies of bearing sample at different speed.

Speed (RPM)	Bearing frequency (Hz)			
	FTF	BPFI	BPFO	BSF
100	0.73	19.62	15.38	13.17
200	1.46	39.24	30.76	26.34
300	2.20	58.86	46.14	39.51
400	2.93	78.48	61.52	52.68
500	3.66	98.10	76.90	65.84
600	4.39	117.72	92.28	79.01
700	5.13	137.34	107.66	92.18

5.3 Results

5.3.1 Amsler machine

The first lab experiment used the Amsler machine to study the integration of AE sensors with a compact DAQ unit and other components (section 5.2). The DAQ unit from National instrument Co. Ltd. used in this experiment if 4-channel with the maximum sampling rate of 1 MS/s. A pair of samples made from EN24T steel was selected as refer to a twin discs model, which leading to the study of AE signals from material conditions. There are heathy and artificially damaged samples which are illustrated in Figure 5-29 and Figure 5-30 respectively.

Figure 5-29: A healthy EN24T sample.

Figure 5-30: A damaged EN24T sample.

EN24T (817M40T) is a nickel chromium molybdenum through hardening steel with a wide range of strengths that may be heat treated. EN24T is widely utilised in heavy-duty applications that need hardness, wear resistance, and tensile strength because to its hardenability characteristics. Based on nitriding or flame induction processes, its surface hardness would be extended to 60 RC.

Table 5-2 Chemical Composition (weight %) of EN24T.

EN24T	C	SI	MN	S	P	Cr	Mo	Ni
Min / Max	0.36 / 0.44	0.10 / 0.35	0.45 / 0.70	- / 0.040	- / 0.035	1.00 / 1.40	0.20 / 0.35	1.30 / 1.70

The Amsler machine has 2 speed variations including 180 RPM and 360 RPM. However, 360 RPM can provide more consistent speed during the experiment which was confirmed by the use of slow-motion videos. In that case, the fundamental frequency of the machine would be 360 RPM divided by 60 seconds, which is 6 Hz.

Test conditions contain the pre-amplifier value of 40dB gain and the main amplifier value of 23dB gain, which convert to 63dB gain in total. Sampling rate was chosen between 500 kS/s and 1 MS/s. The recording time was set to 20 seconds per each file with 10 seconds of saving time. The specially designed program for the data acquisition was made in-house by researchers in School of Metallurgy and Materials at the University of Birmingham. It can perform the whole experiment without any errors during the recording process, in fact, the program works seamlessly with other components in the measurement. Small but mighty NUC computer from Intel has done the job perfectly without any concerns. The main benefit is both DAQ unit and computer are very compact in size, which does require only an area of a half of A4 paper.

The setup of computer connected with a display monitor and DAQ unit joins a pair of amplifiers and a R50α piezoelectric AE sensor. The system diagram can refer to the Figure 5-16 as mentioned earlier.

Firstly, ensure the power connection of the data acquisition is provided separately from the Amsler machine in case there could be the power cut or other emergency event that would harm the acquisition board inside the DAQ unit. After that, confirm all connection harness and

wires between the AE sensor and other components. Lastly, everything shall conform to safety regulation before conducting the experiment since the machine operation is related to the rotation of heavy components with noisy generated environment. Therefore, a set of personal protective equipment must be provided.

Placing a pair of healthy discs onto the machine and start the revolution. Choosing speed level 2 of 360 RPM together with preparing the acquisition program for the recordings. The AE signal of two good samples coupled together with the recording time of 20 seconds.

Figure 5-31 shows the AE signal from a pair of good EN24T discs. Raw data could struggle with the identification of any sign stimulated by abnormalities of the components. To be illustrated, Figure 5-32 demonstrates the raw signal from a pair of healthy and damaged samples, that is failed to reveal the events related to the damage on the samples and the bearing of the Amsler machine. Further study using the FFT-based spectral analysis of the AE signal also fails to disclose the hidden events of damage on the samples and the bearing of the Amsler machine on the frequency domain as shown in Figure 5-29.

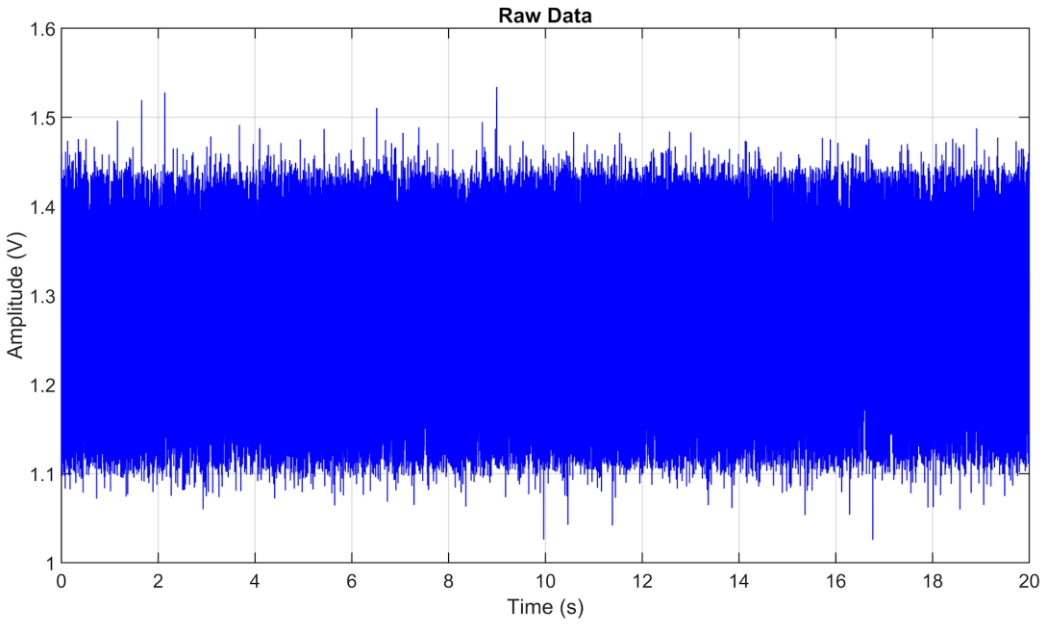

Figure 5-31: Raw data of a pair of good samples.

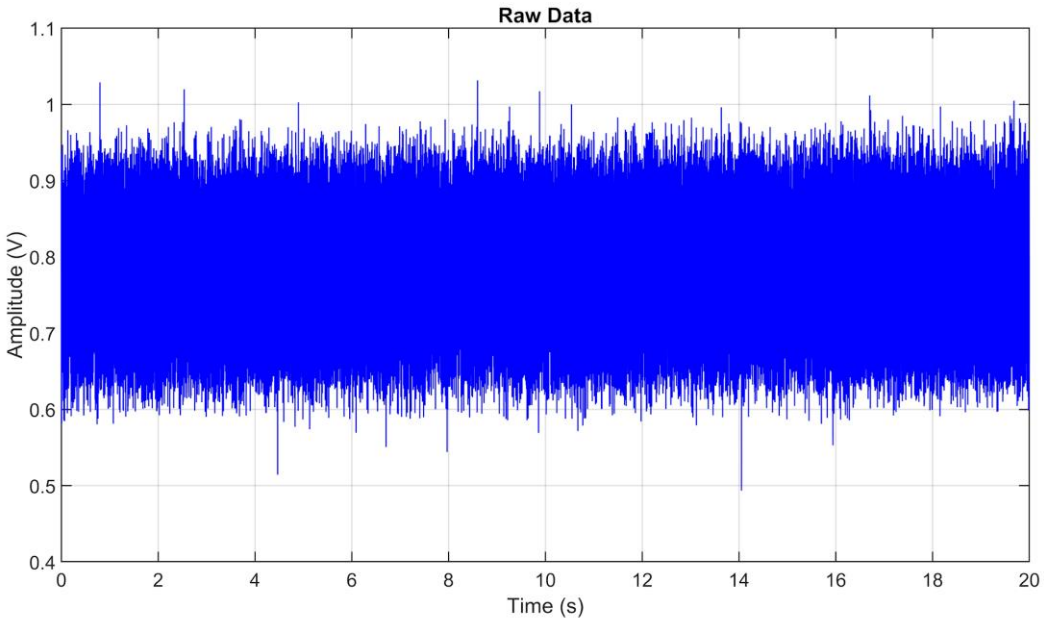

Figure 5-32: Raw data of healthy and damaged discs.

FFT provides the power spectrum of time-series data which would illustrate the power for each frequency contained in the input data. Therefore, there would be some peaks which mean the high power of that frequency, which generally define the events through the frequency domain.

However, analysis using FFT could be insufficient and challenging since it lacks the ability to identify the events on the frequency. Using FFT would require a lot of domain details to understand and interpret the output frequency domain data.

In case of Figure 5-33 and Figure 5-34, FFT does reveal some resonances generated by AE sensor as refer to the specification sheet. Peaks of 53kHz, 193 kHz and 198 kHz are dominant on both FFT results.

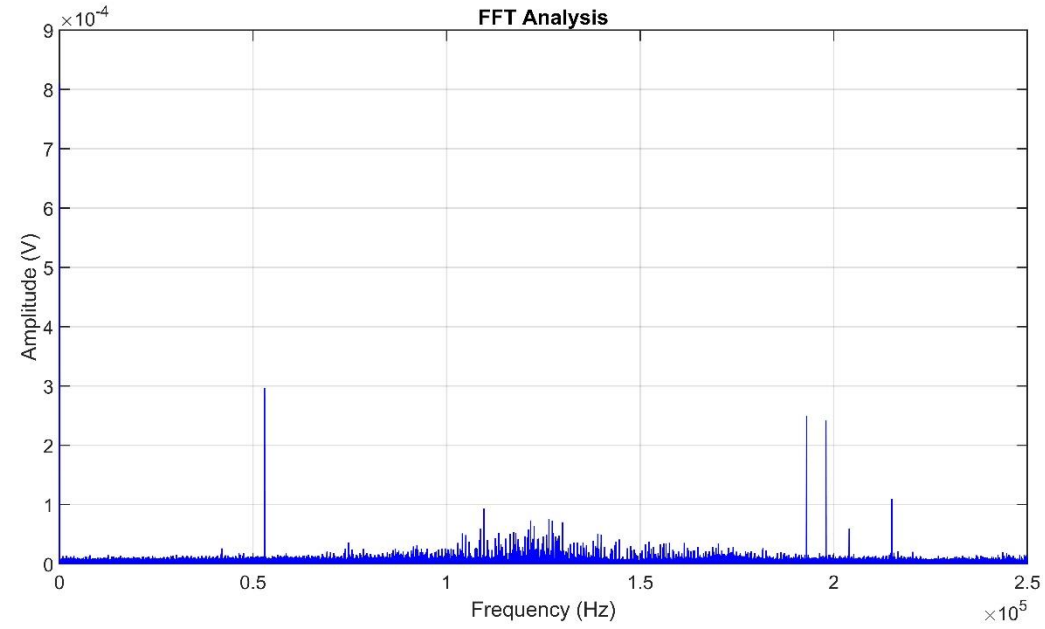

Figure 5-33: Power spectrum (FFT) of a pair of good samples.

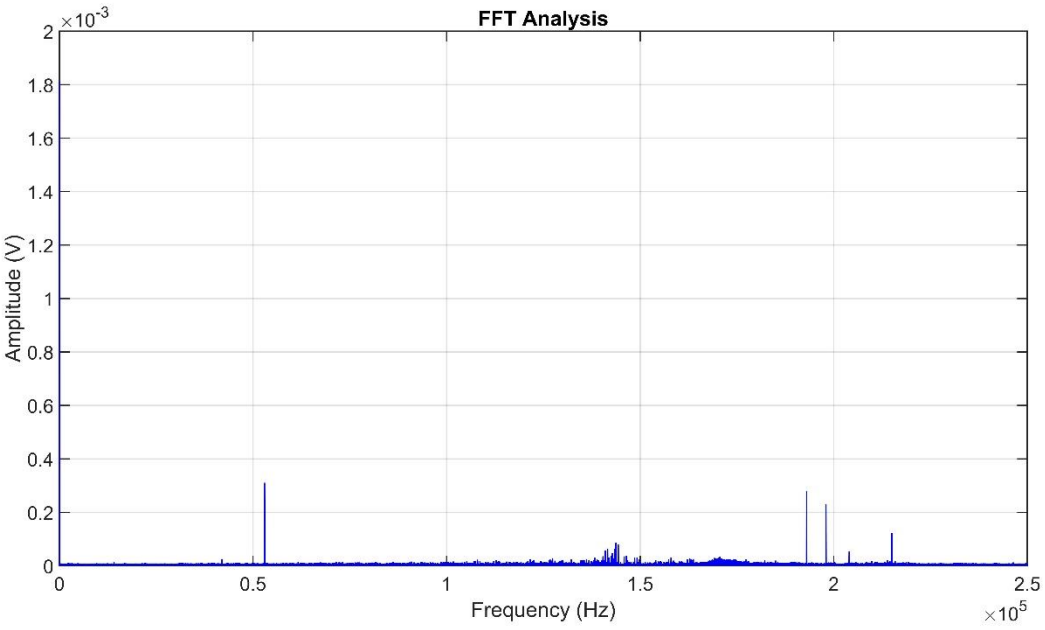

Figure 5-34: Power spectrum (FFT) of healthy and damaged discs.

On the other hand, spectral envelope analysis makes different results when compared with FFT analysis. The characteristic frequencies of bearing faults from the Amsler machine are detected in Figure 5-36. Since the Amsler machine speed is 360 RPM making a fundamental frequency

of 6 Hz, which is corresponded to the generated harmonics. The damage on one of the EN24T samples contributes to the presence of the bearing faults of the Amsler machine. In contrast, a pair of good samples as shown in Figure 5-35 is unable to reveal the harmonics from the bearing faults unless it reaches the satisfied level of vibration. Therefore, spectral envelope analysis of further records after few minutes of testing as shown in Figure 5-37 also reveals harmonics that are uniform to those detected in Figure 5-36.

Figure 5-37 illustrates the harmonics similar to those displayed in Figure 5-36 after the experiment was done by 8 minutes 30 seconds (18 samples). Since the bearing defect of the Amsler machine is dominant, the AE sensor will literally pick up those gain as the main harmonics despite the sample condition being healthy. In contrast, the normal Amsler machine would not harm the output signals, which are intended to reveal harmonics of the sample rather than the machine.

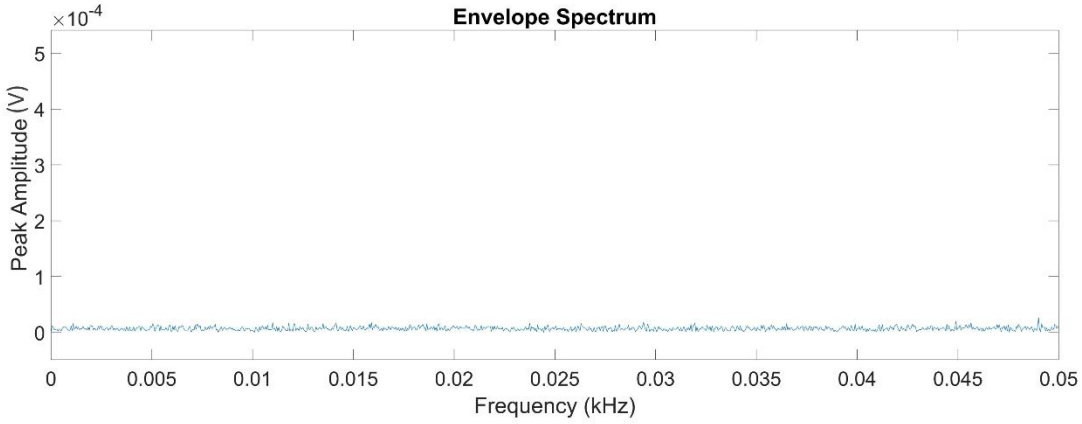

Figure 5-35: Spectral envelope analysis of a pair of good samples.

The analysis using one-dimensional wavelet decomposition which break the original signal into approximation coefficients and detail coefficients was also conducted in order to compare with the spectral envelope analysis. The number of detail coefficients relies on nth-level wavelet decomposition using the order 2 Daubechies wavelet.

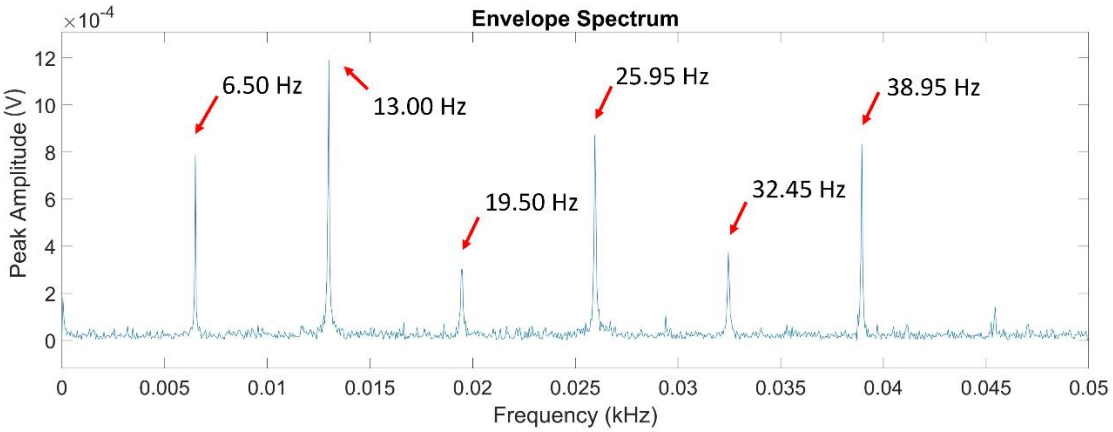

Figure 5-36: Spectral envelope analysis of a combination of healthy and damaged discs.

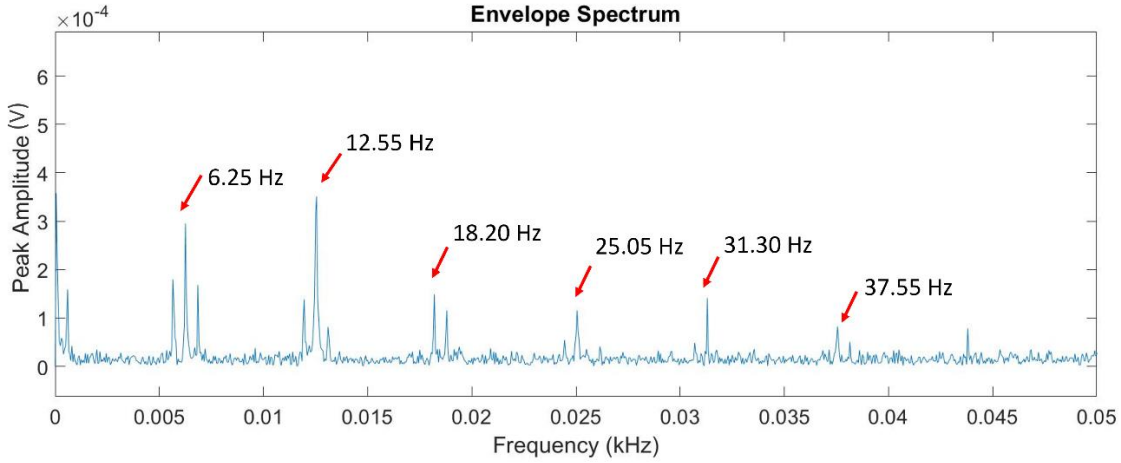

Figure 5-37: Spectral envelope analysis of a pair of good samples (with harmonics).

The 2nd-level wavelet decomposition using the order 2 Daubechies wavelet was chosen in this study. There are harmonics investigated in both level 1 and level 2 detail coefficients. Unfortunately, harmonics from both levels are not compatible with fundamental frequencies of Amsler machine at the speed of 360 RPM.

Figure 5-38 shows the spectral envelope analysis of level 1 detail coefficients of a pair of good samples which is correspond to the output from Figure 5-35. As a result, the data with no sign of defects generally reveal no harmonics when apply spectral envelope analysis.

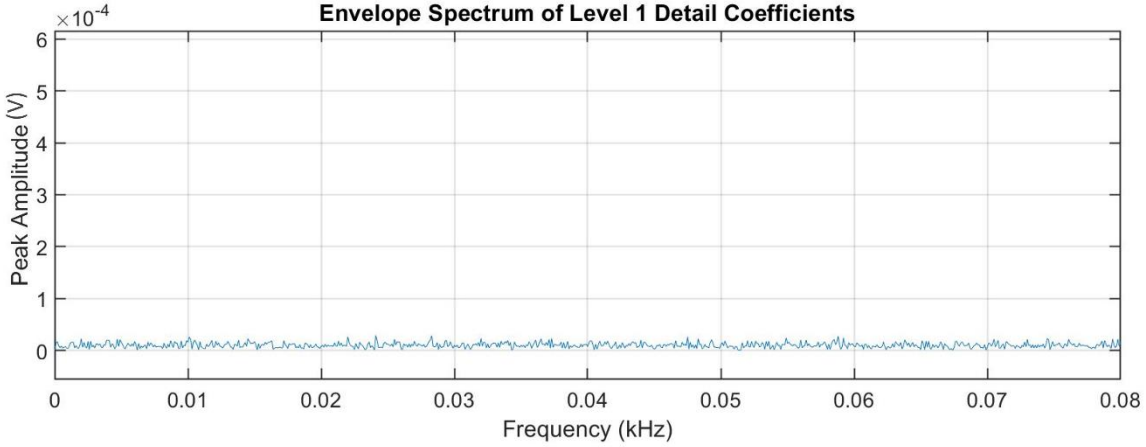

Figure 5-38: Envelope spectrum of level 1 detail coefficients of a pair of good samples.

To be concluded, One-dimensional wavelet decomposition could not help investigating harmonics of those data since the conventional method using spectral envelope analysis is more suitable for this case.

Level 1 detail coefficients from wavelet decomposition of healthy and damaged discs as shown in Figure 5-39. Harmonics detected in the spectral envelope analysis displayed in Figure 5-39 mismatch frequencies with those in Figure 5-36. Figure 5-40 also provide harmonics that are inconsistent with the original harmonics.

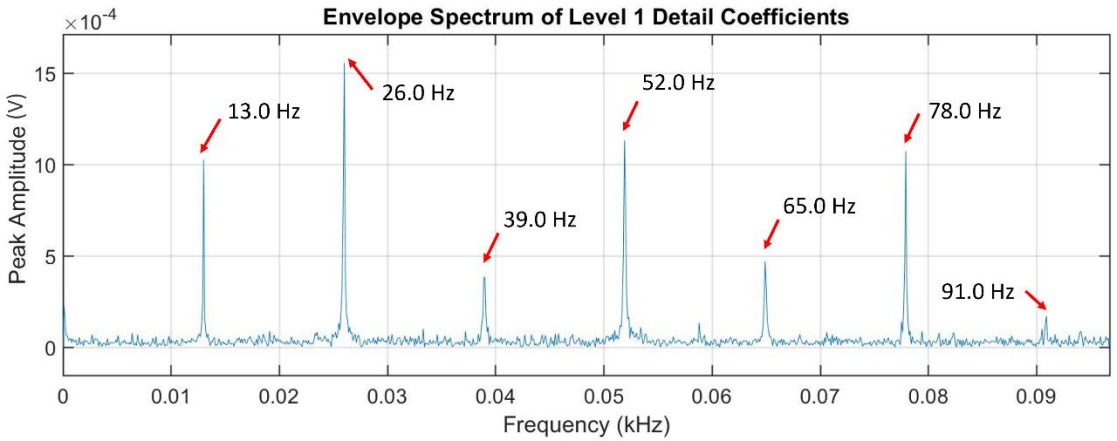

Figure 5-39: Envelope spectrum of level 1 detail coefficients of healthy and damaged discs.

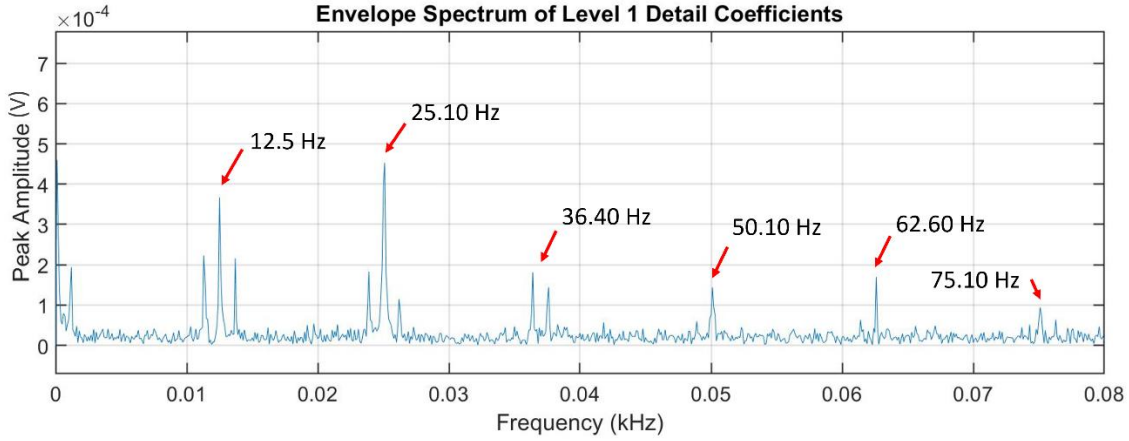

Figure 5-40: Envelope spectrum of level 1 detail coefficients of a pair of good samples (with harmonics).

5.3.2 Reduced scaled wheel trolley test

Normal and damaged wheel conditions were studied via a series of experiments using the test trolley equipped with reduced scale-sized railway wheel. The AE signal from individual condition as mentioned earlier in section 5.2.3 was retrieved from the analysis software based on MATLAB. The raw signal generated from a wheel with good health condition is illustrated in Figure 5-41. Overall, the raw signal shows no sign of defects as there is no significant bursts

on the time domain data. The low amplitude profile of the signal is generally provided when the signal is generated from the normal condition of the monitoring samples.

Figure 5-42 represents the raw AE signal received from a test performed with a single wheel with an artificial fault. Obviously, there are several bursts detected by the time domain analysis, which is significantly different from the previous data of the normal wheel. As a result, excited signals from metal-to-metal collision were detected by the AE sensor.

Based on the laboratory condition, the signal from damaged samples would help identifying the signs of defects as low noise from other components and environment is experienced.

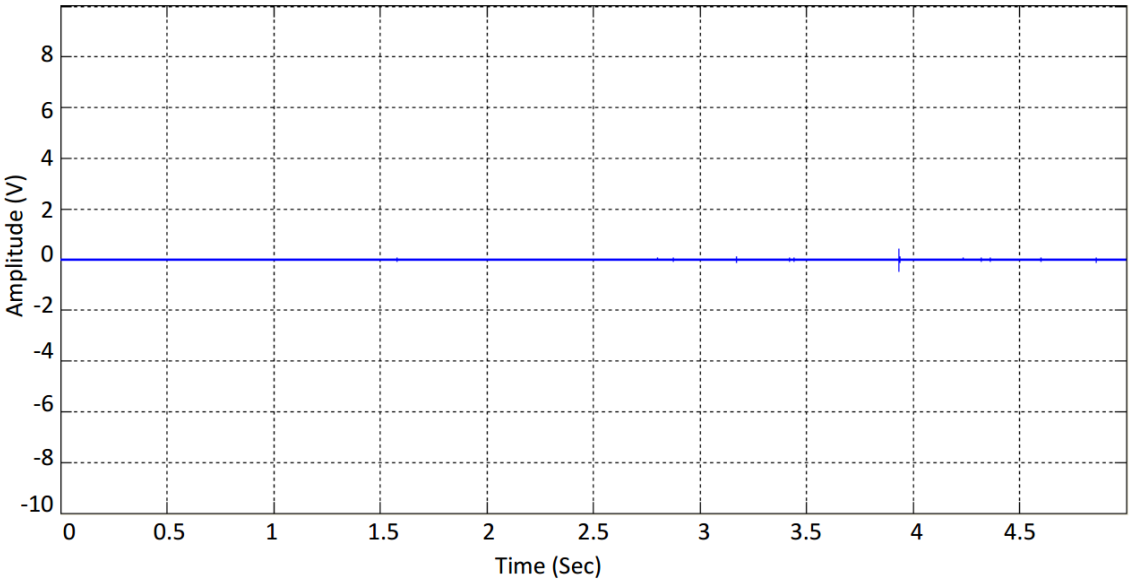

Figure 5-41: Raw signals from the normal wheel.

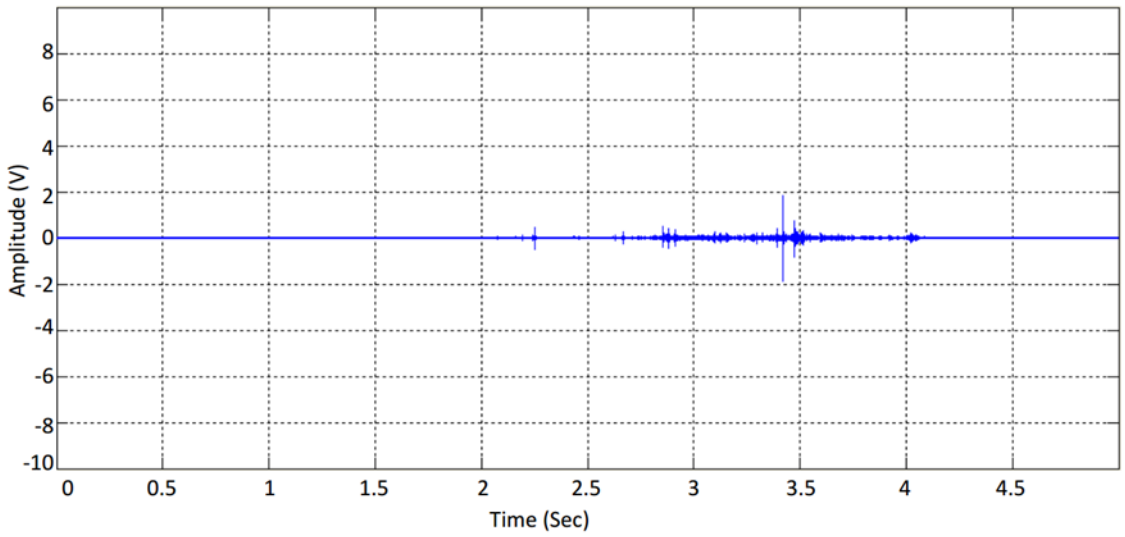

Figure 5-42: Raw signals from the faulty wheel.

Although raw data could demonstrate the different between the normal and the damaged wheel, it could be unclear in other situations. Reading the data using time domain analysis could be improved by the moving RMS. In order to optimize defect detection on time domain, the moving RMS algorithm has reduced some background noise. The moving RMS precisely defined data signals with a high peak. Background noise has no effect on the outcome when comparing the moving RMS to the raw signal.

The raw signal produced by a normal wheel is plotted as a moving RMS in Figure 5-43 In contrast, the wheel's converted signals with an artificial fault were plotted and displayed in Figure 5-44.

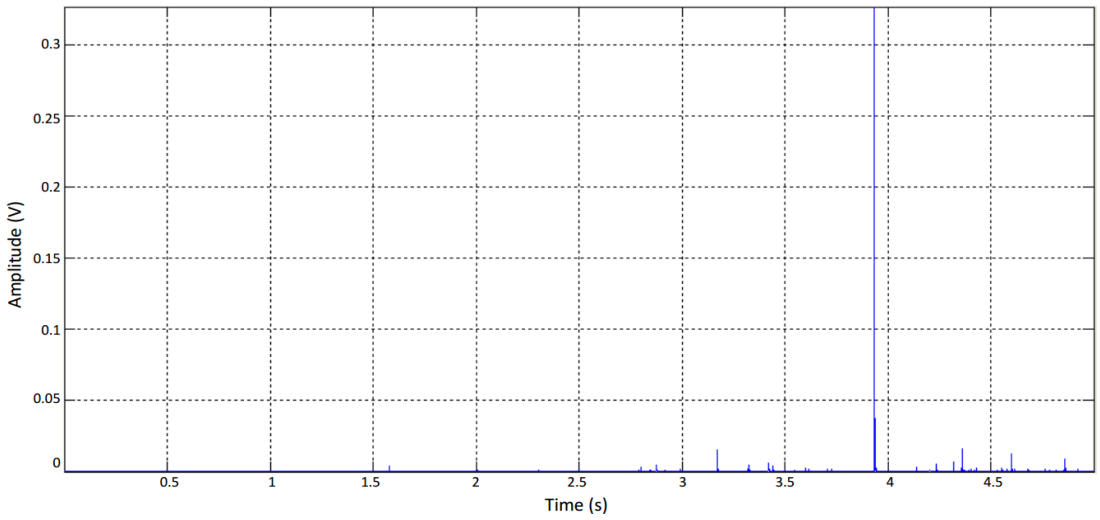

Figure 5-43: Moving RMS of the normal wheel.

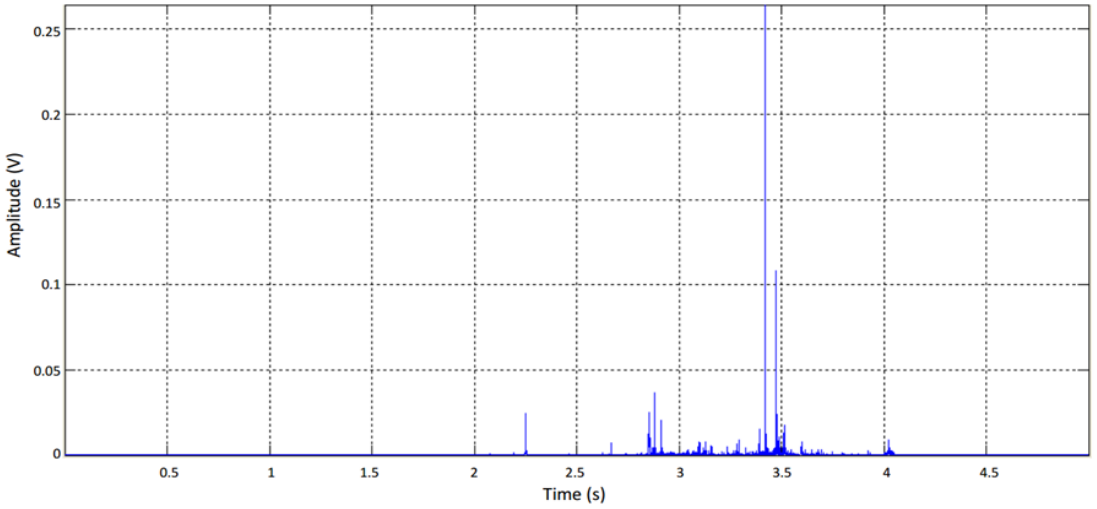

Figure 5-44: Moving RMS of the faulty wheel.

This experiment shows that normal wheels produce very little noise. In real-life inspections, friction between the wheel flange and rail and moving components might produce background noise.

5.3.3 Bearing test rig

The output signal gained from various bearing conditions are illustrated in following figures. There are three different conditions including a) healthy in Figure 5-45 b) 10% damage in

Figure 5-46 c) 50% damage in Figure 5-47. Judging the raw data is not possible for the complicated signals from rotating machines. Further analysis would help mitigate this problem as frequencies related to defects will be revealed. A range of time domain and frequency domain analysis as mentioned earlier in chapter 4 will be presented. Firstly, AE data from the bearing with roller defects (10%) is compared with the healthy bearing. Figure display the plot of raw data (a) and moving RMS (b) analysis of the healthy bearing in blue colour and the damaged bearing in red colour. The moving RMS plot for the damaged bearing shows the bearing defect peaks. Although the bearing with the roller fault has higher peak values, moving kurtosis analysis does not provide a clear conclusion. It calculates kurtosis value using the windowing function, therefore, the output from damaged bearing should display the kurtosis value higher than 3. Using only kurtosis value to interpret the data is not an effective method, moreover, the output signal could be sensitive to external noise sources.

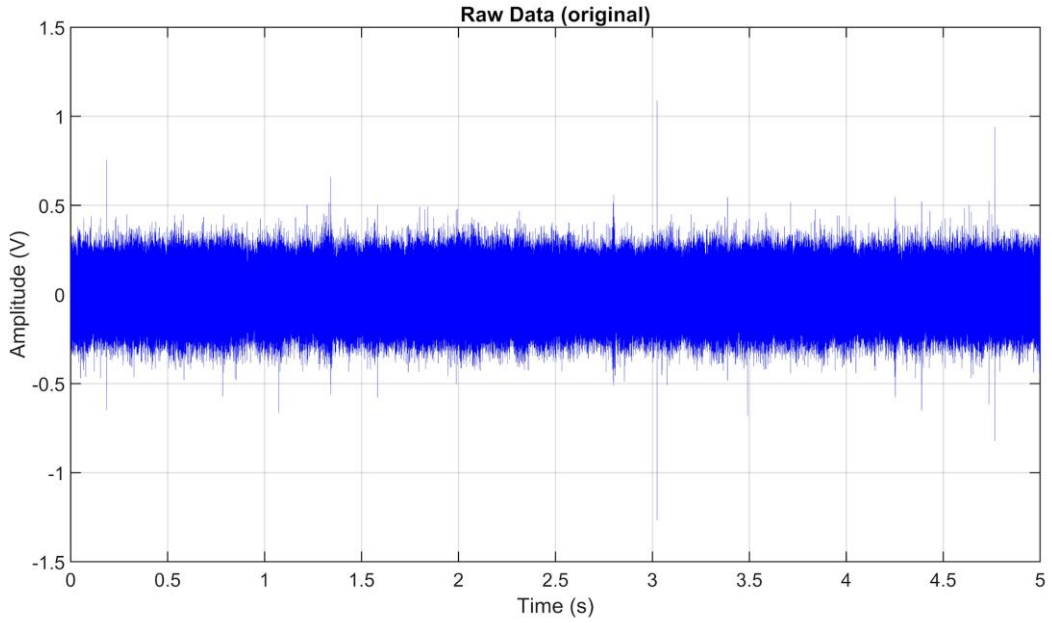

Figure 5-45: Raw data of healthy bearing.

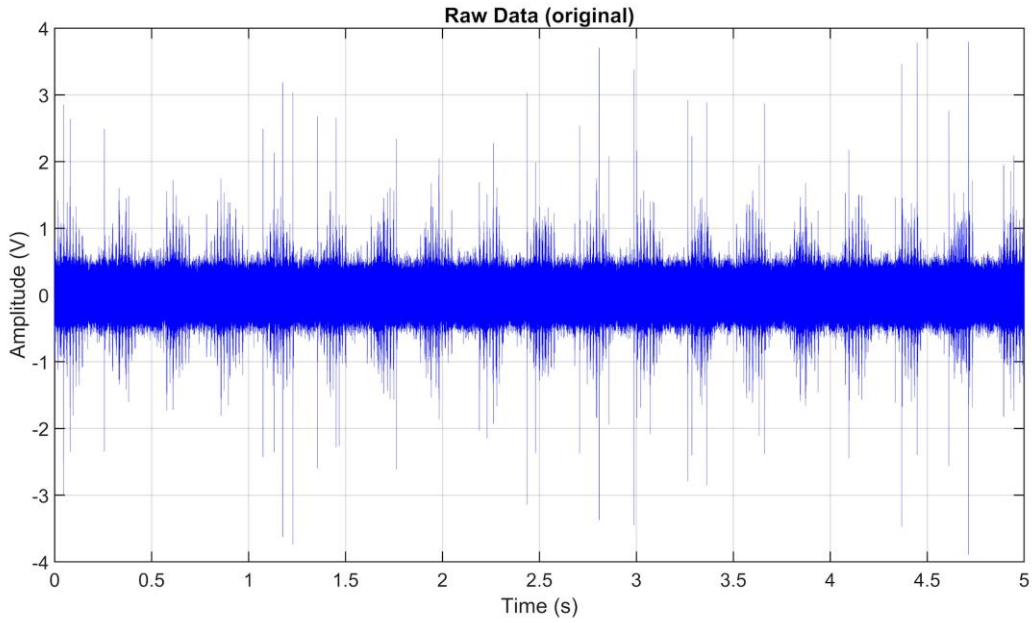

Figure 5-46: Raw data of 10% damage Faulty bearing @ load 5 & speed of 500 RPM.

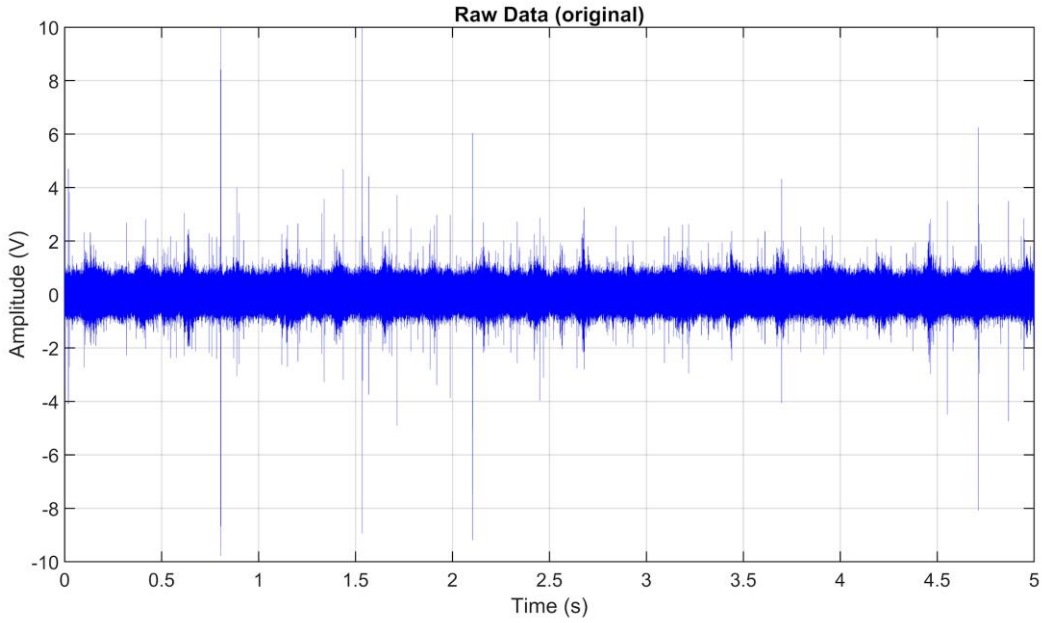

Figure 5-47: AE signal from damaged bearing (50%) @ load 5 & speed of 500 RPM.

Raw data of damaged bearing generally reveal amplitude modulation which could be generated by defects. However, raw data would not provide sufficient information of the damage condition either its type or severity. Such a vague analysis it is, thus, a predictive maintenance

of bearing cannot rely on the raw data interpretation. In addition, it is hard to set up the threshold of the damage level on the raw data, only the comparison of healthy and damaged data will initiate the detection of defects. Further analysis will reveal the detection of bearing faults based on the laboratory test rig experiment.

A series of comparisons between the two different conditions of bearing are presented in following sections. Initially, a pair of healthy and defective bearings from AE measurements with roller defect (10% damage) is displayed in Figure 5-48. Raw data on the time domain (a) could provide the different between the healthy and damaged bearing, however, moving RMS (b) significantly reveal the better different. Frequency domain (c) could struggle to clearly describe the amplitude between healthy and damaged bearing, which is the same case with Time Kurtosis (d).

However, vibration measurements (Figure 5-49) can clearly provide the different between healthy and damaged bearing via any parameters including time domain (a) Raw data and (b) Moving RMS, also frequency domain (c) FFT Analysis and (d) Time Kurtosis. Therefore, AE measurements require further signal analysis to enable the damage detection.

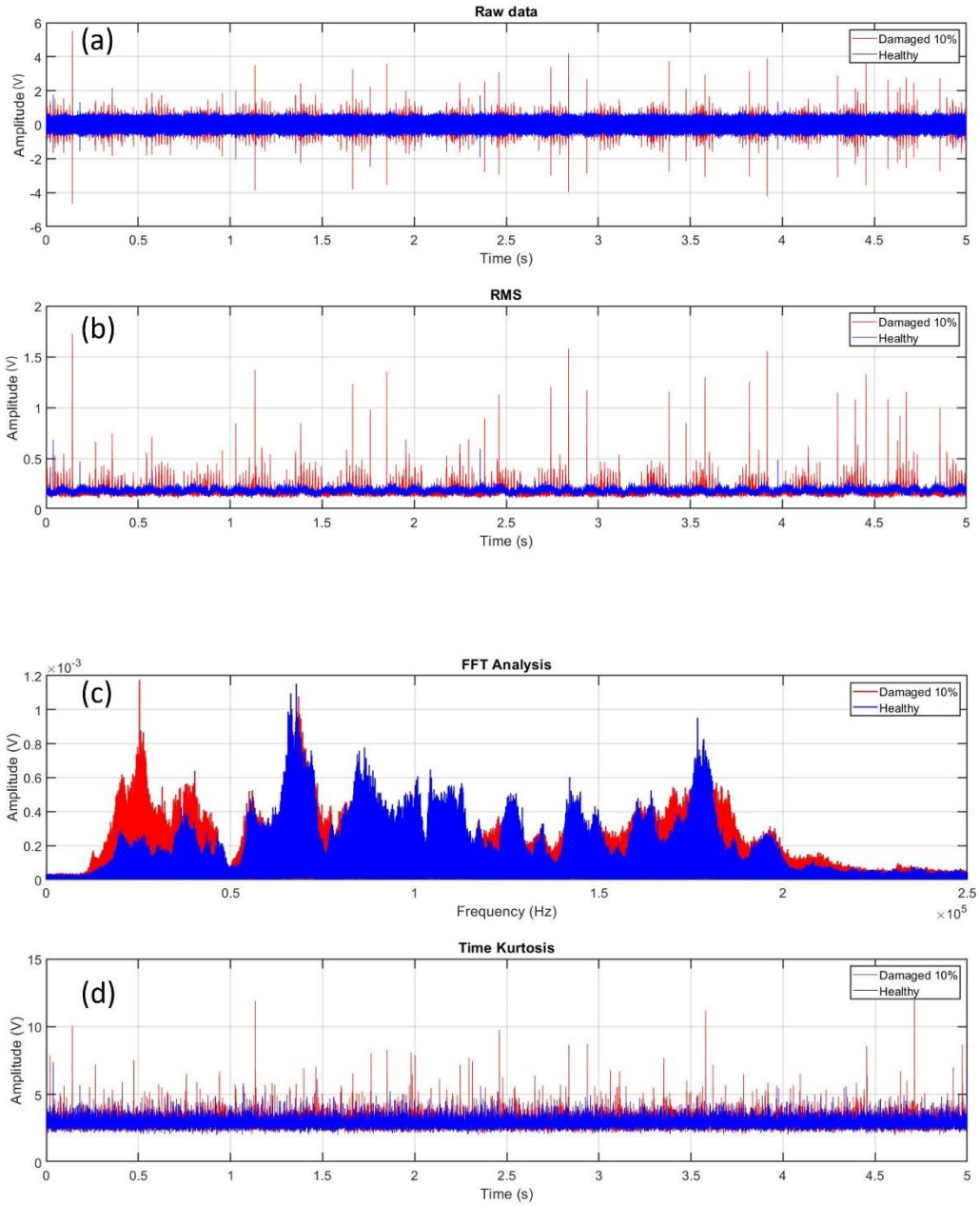

Figure 5-48: Comparisons between AE measurements from healthy and bearing with roller defect (10% damage) at load 5 bar and 500 RPM for (a) Raw data (b) Moving RMS (c) FFT Analysis (d) Time Kurtosis.

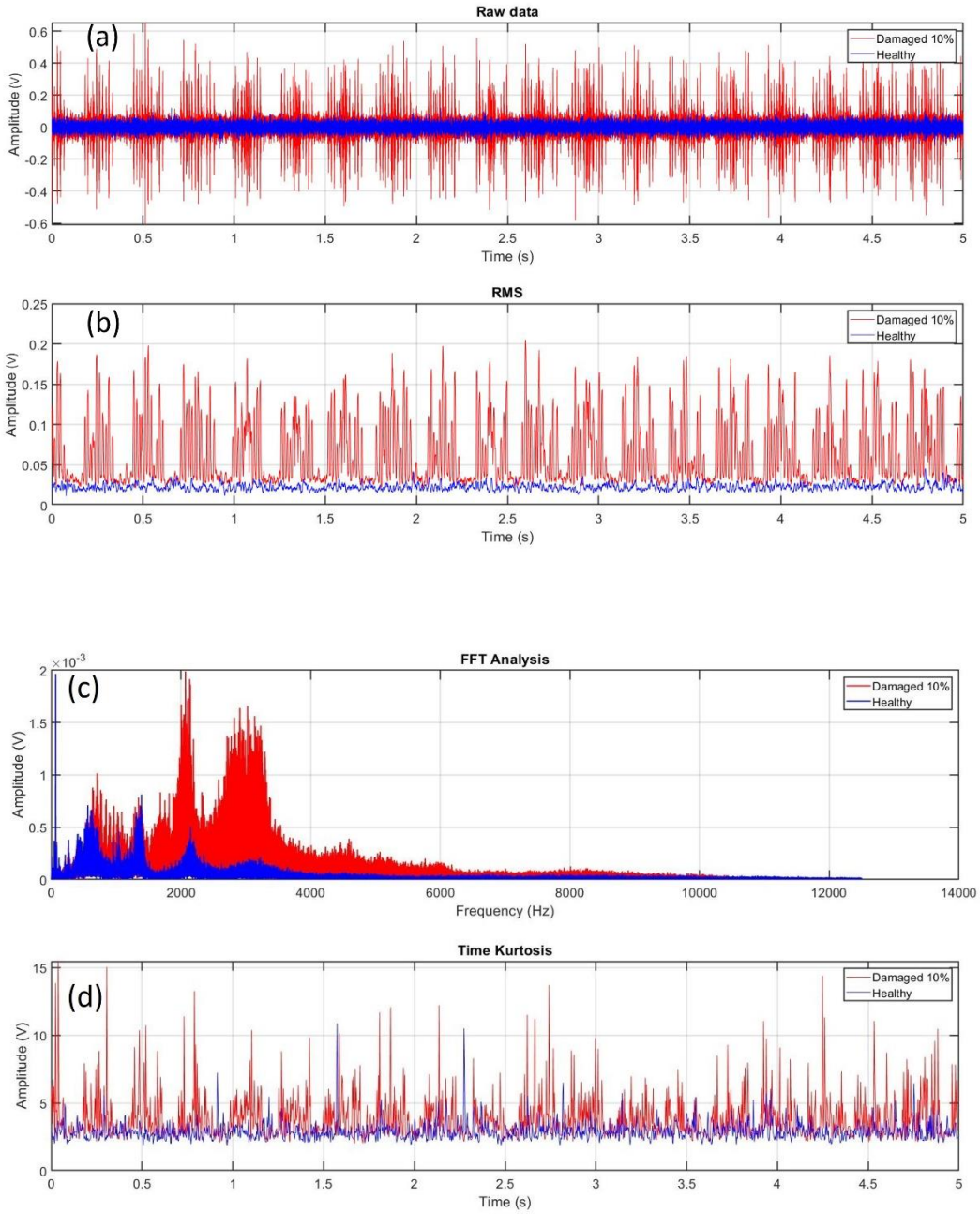

Figure 5-49: Comparisons between Vibration measurements from healthy and bearing with roller defect (10% damage) at load 5 bar and 500 RPM for (a) Raw data (b) Moving RMS (c) FFT Analysis (d) Time Kurtosis.

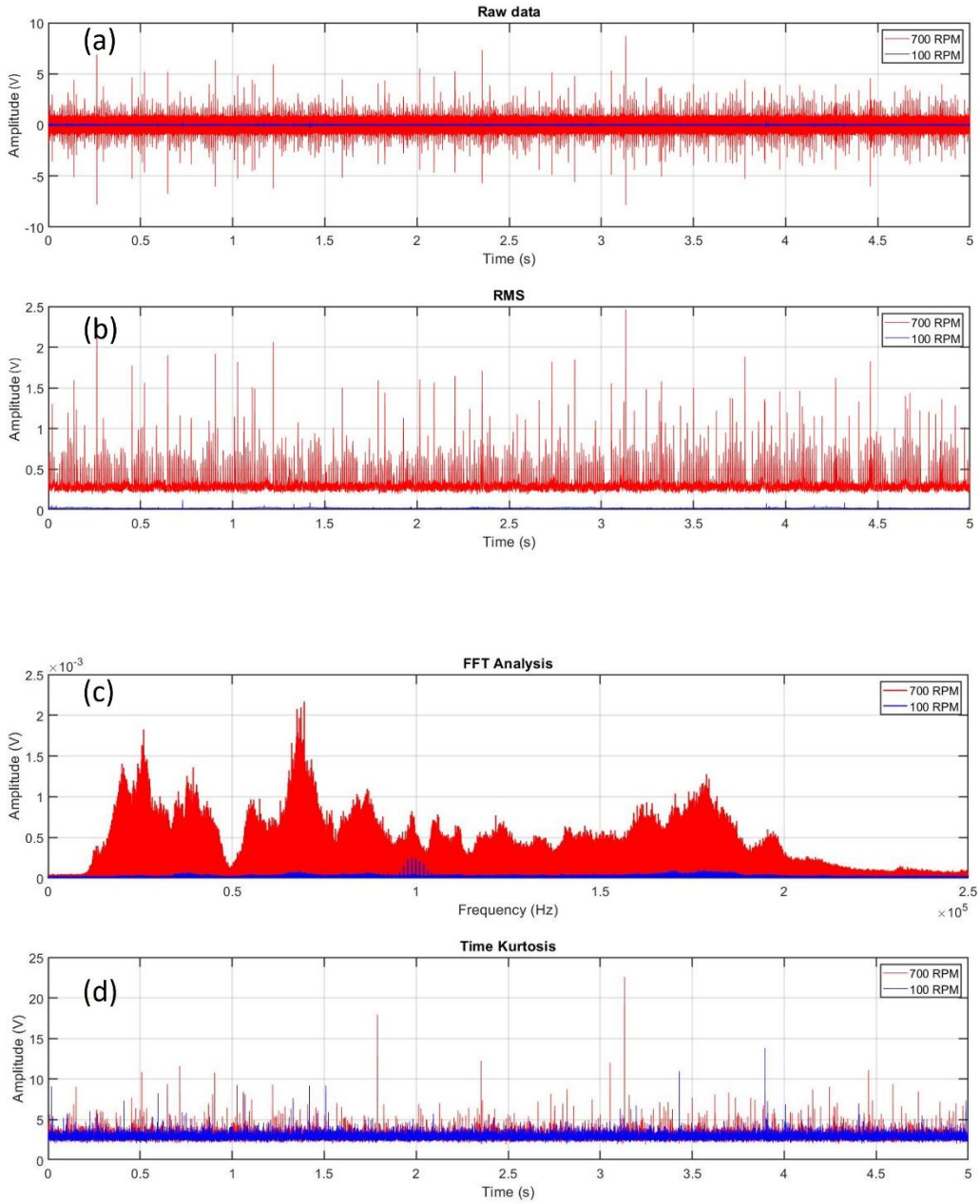

Figure 5-50: AE measurements from bearings with roller defect (10% damage) at speed 100 and 700 RPM and load 5 bar (a) Raw data (b) Moving RMS (c) FFT Analysis (d) Time Kurtosis.

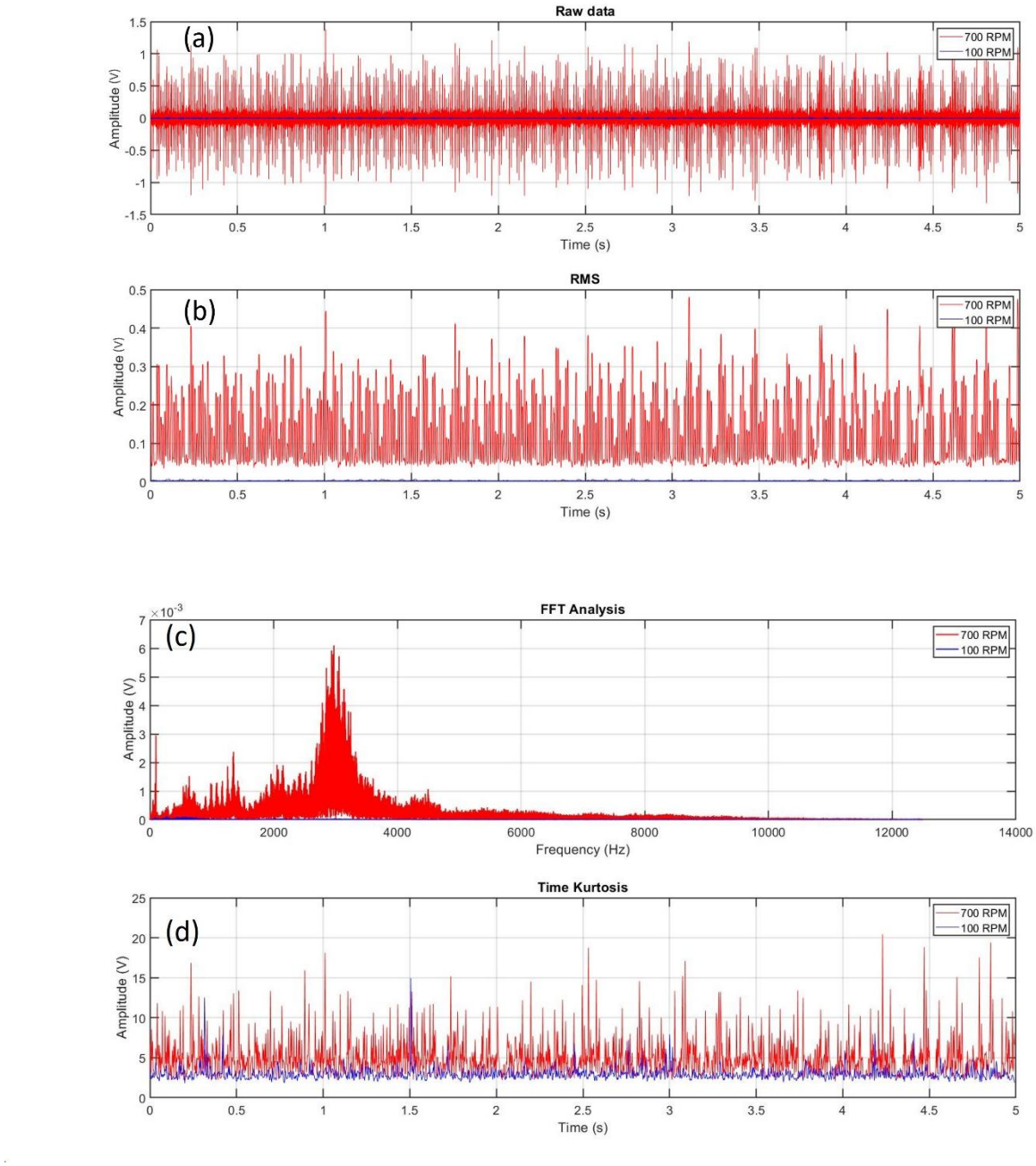

Figure 5-51: Vibration measurements from bearings with roller defect (10% damage) at speed 100 and 700 RPM and load 5 bar (a) Raw data (b) Moving RMS (c) FFT Analysis (d) Time Kurtosis.

Figure 5-50 and Figure 5-51 show how operation speed affects AE and vibration readings. The sufficient information could be retrieved via the appropriate speed of rotating machine. In time

and frequency domain analysis, lower speed means less amplitude. Since both signals arise from the same bearing situation, kurtosis remains the same.

Higher rotating speed would increase the amplitude of any raw data from both AE and vibration. However, RMS data of vibration data reveal significant difference in amplitude value between the higher RPM and lower RPM, while AE data is failed to. The intensive data from higher amplitude setting generally provide rich information for better quality of signal analysis.

Moreover, the effect on different loading conditions is investigated on AE and vibration measurements, which are shown in Figure 5-52 and Figure 5-53. Unlike the change in rotating speed, the loading condition will not differ any of parameters of the analysis on both AE and vibration measurements. All values are represented within the similar threshold.

Obviously, both AE and vibration RMS, FFT and Kurtosis values tended to increase over the running speed. While the more load input to the test did not present the effect on those values.

AE assessment identifies the degree of roller bearing faults by comparing 10% and 50% damaged bearings as seen in Figure 5-54. Frequency analysis in Figure 5-54 (c) demonstrate how to indicate the severity of bearing damage. However, the data from vibration measurement in Figure 5-55 is failed to reveal the amplitude different between 10% and 50% damage. Moreover, kurtosis value of AE data with 50% damage is significantly higher than another with 10% damage.

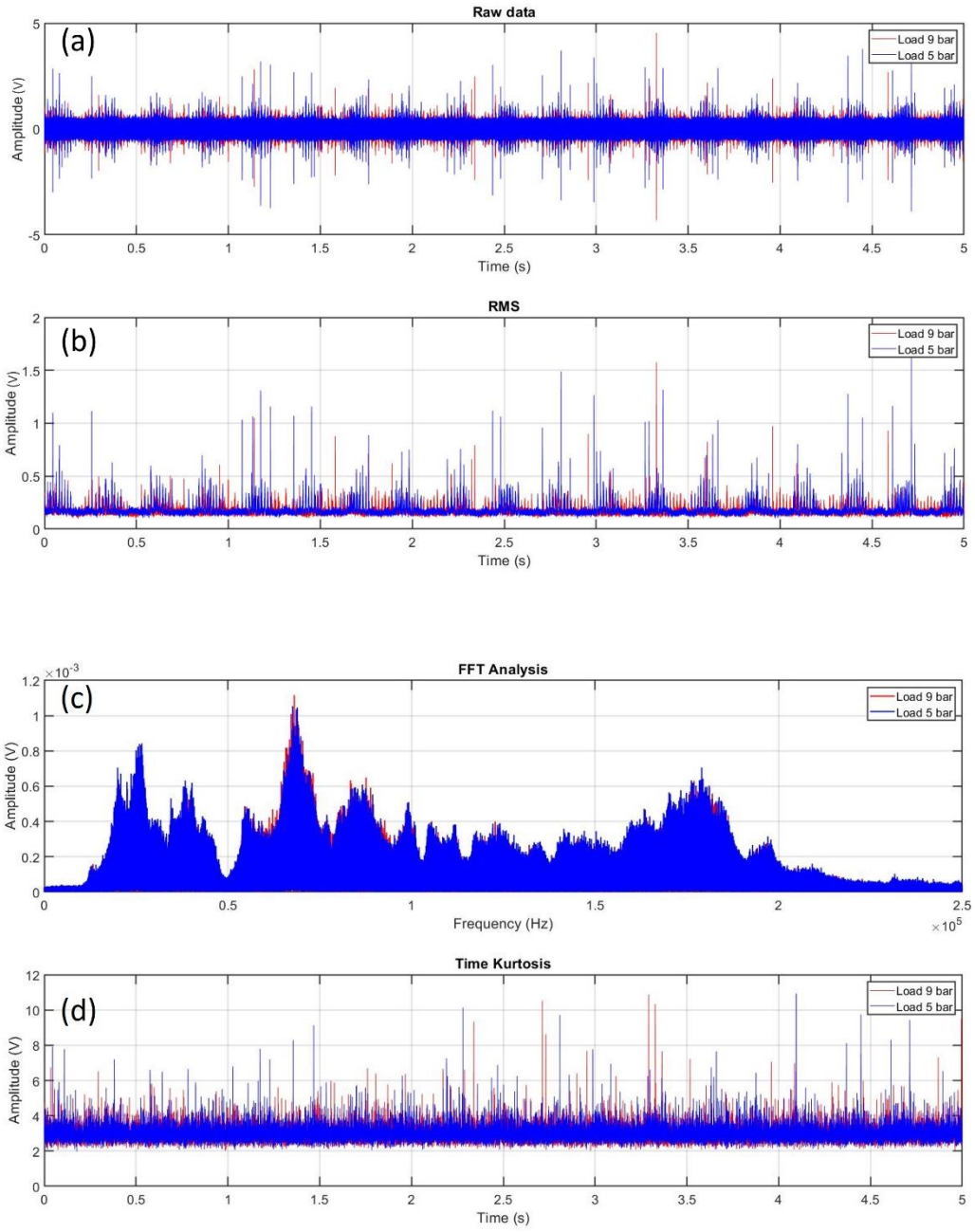

Figure 5-52: AE measurements from bearings with roller defect (10% damage) with load 5 bar and 9 bar at 500 RPM (a) Raw data (b) Moving RMS (c) FFT Analysis (d) Time Kurtosis.

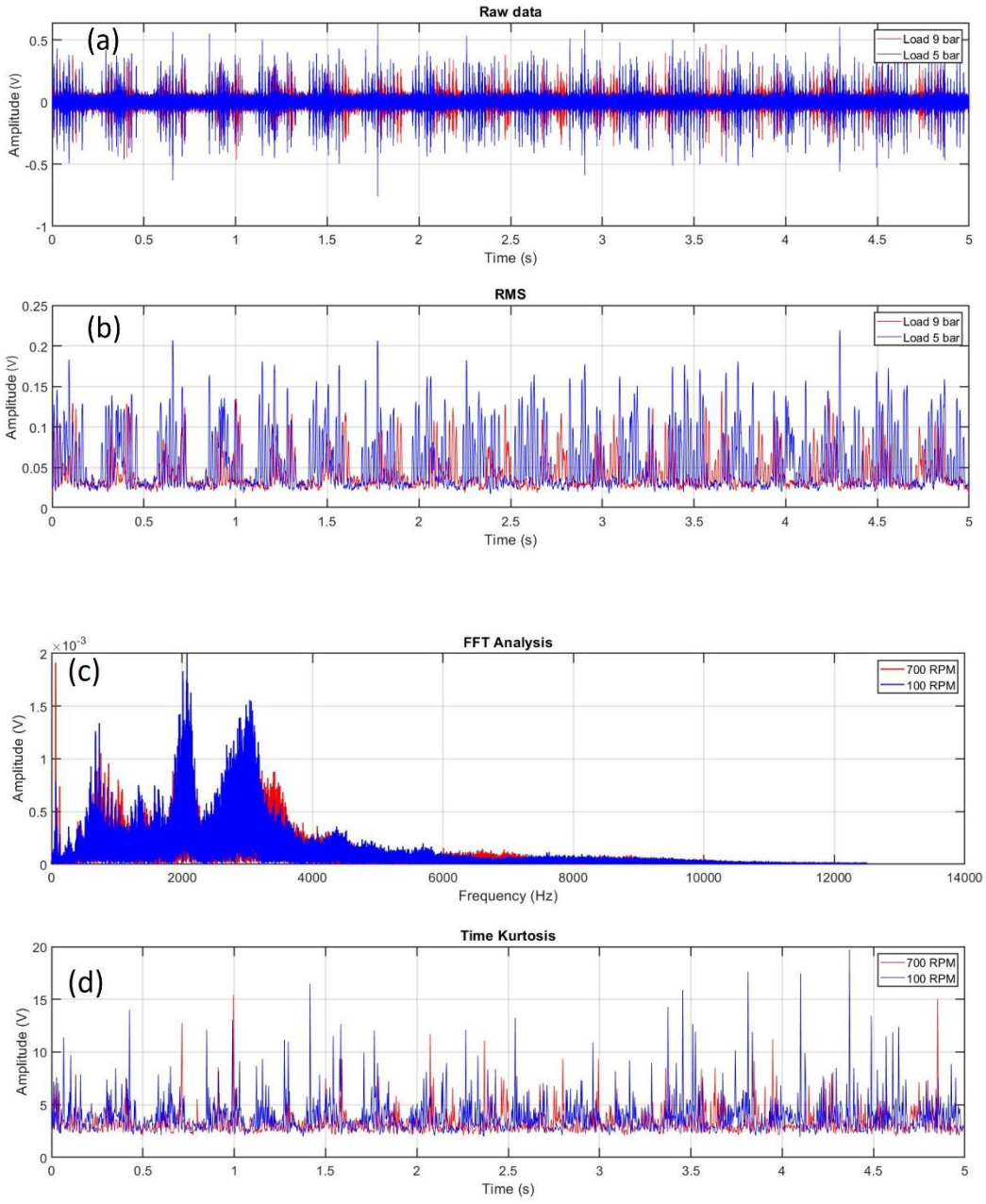

Figure 5-53: Vibration measurements from bearings with roller defect (10% damage) with load 5 bar and 9 bar at 500 RPM (a) Raw data (b) Moving RMS (c) FFT Analysis (d) Time Kurtosis.

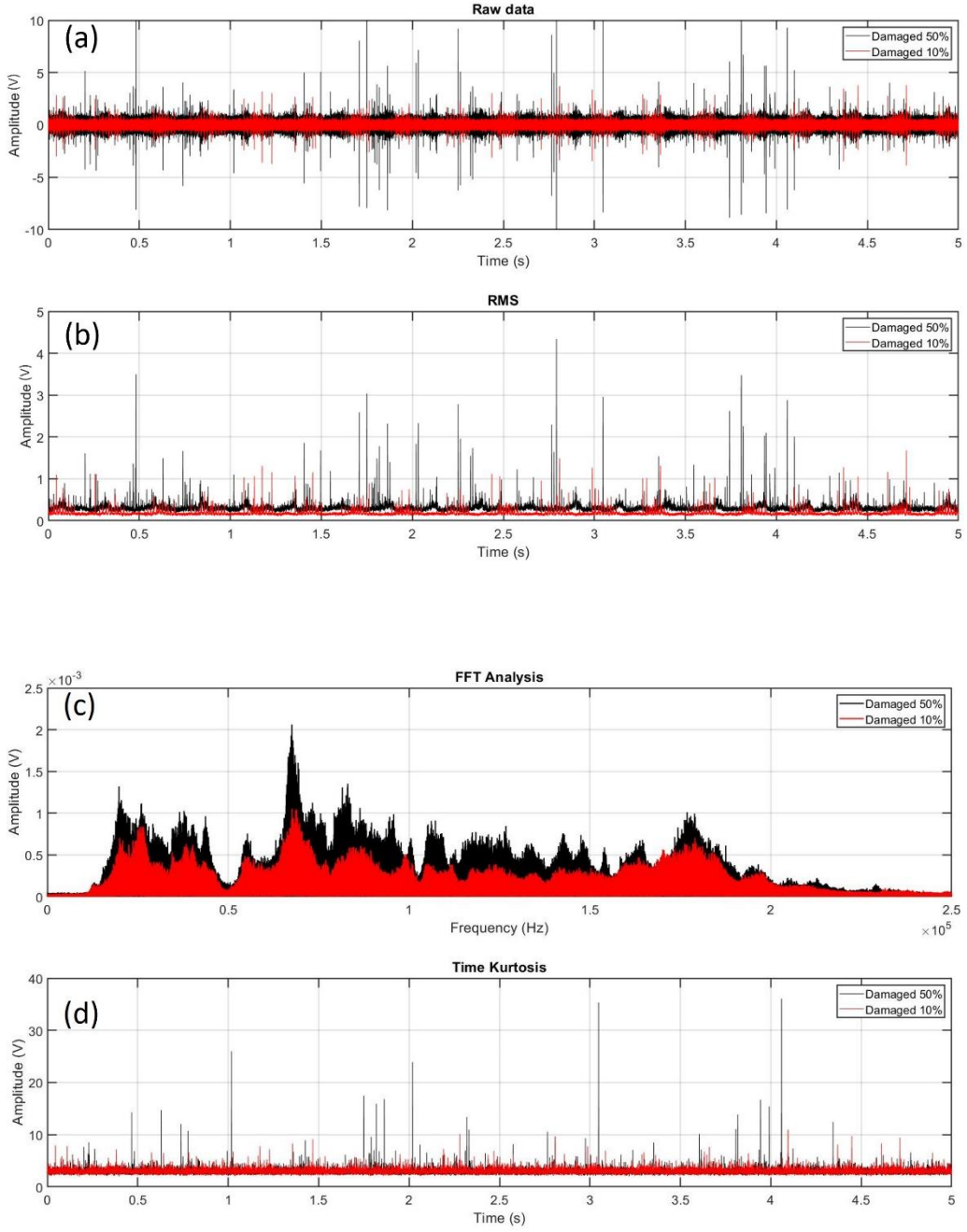

Figure 5-54: AE measurements from 10% and 50 % damaged bearings with roller defect at Load 5 bar and 500 RPM.

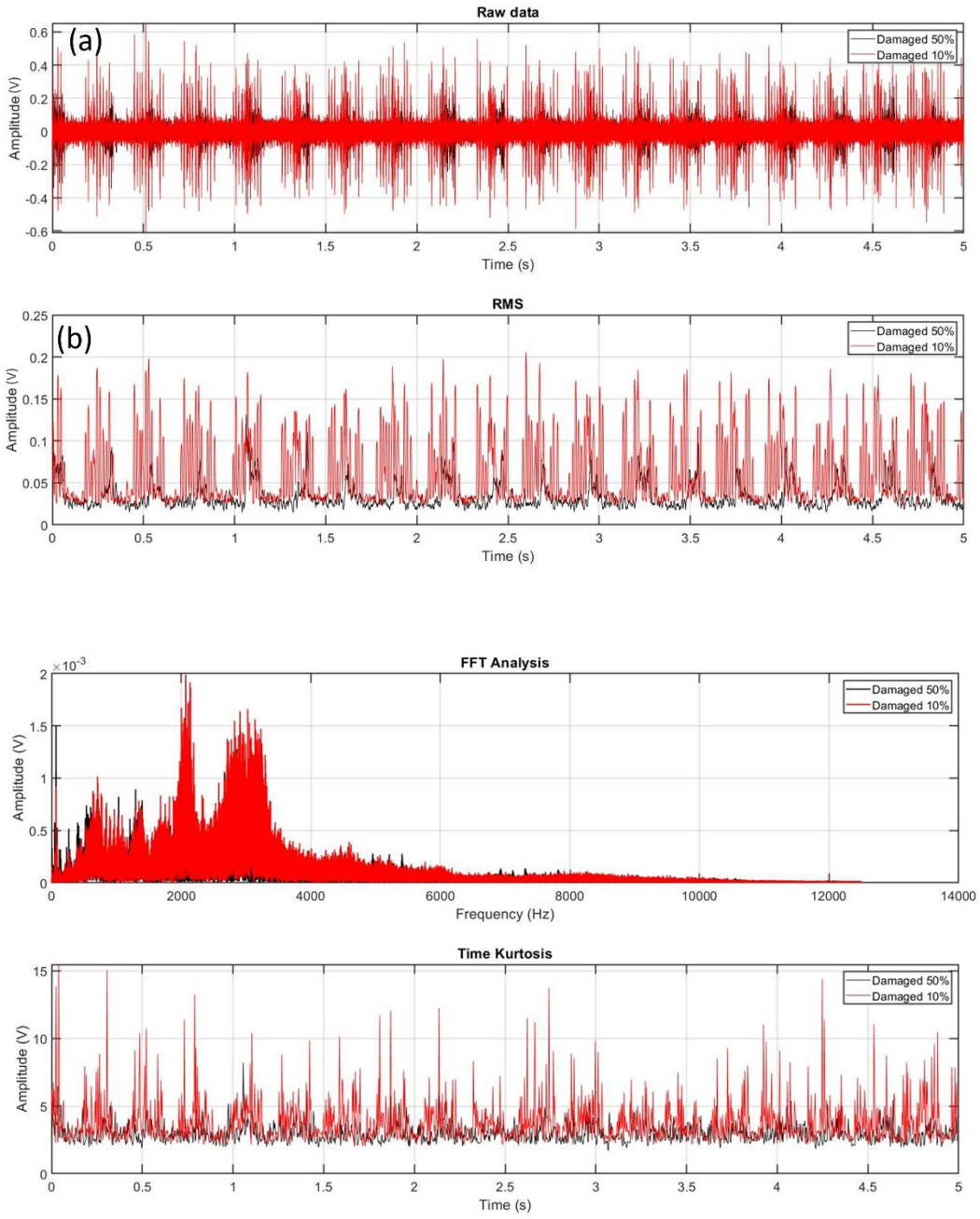

Figure 5-55: Vibration measurements from 10% and 50 % damaged bearings with roller defect at Load 5 bar and 500 RPM.

Spectral envelope analysis is required to reveal the characteristic frequencies of the bearing defect. In the bearing test rig experiment, there are AE and vibration data which were previously compared using time and frequency domain. However, there is no results that can indicate the defect type.

Figure 5-56 and Figure 5-57 displays the spectral envelope analysis of AE and vibration data on a healthy bearing condition respectively, which were tested in the test rig experiment. There is no evidence of a flaw in the analytical technique. However, the fundamental frequency and its harmonics will be triggered in the case of faulty bearing.

Figure 5-58 shows AE spectral envelope analysis for a bearing with a 10% roller defect. Consequently, 89.2 Hz and its harmonics are identified. Those peaks in the study confirm that roller faults were discovered since they correspond to the bearing's fundamental frequency at 700 RPM, as referred to Table 5-1. Figure 5-59 displays the same defective bearing as Figure 5-58 but with the vibration data. From the analysis, peaks of 62 Hz are detected which is also related to the characteristic frequency at the rotating speed of 500 RPM as referred to Table 5-1. Moreover, the vibration data of a 50% damaged bearing with roller defect at 500 RPM is shown in Figure 5-60. As a result, the different between 500 and 700 RPM is clearly seen by the harmonics detected by spectral envelope analysis. In addition, the amplitude of 50% damage is more than 10% damage.

The small gap between the calculated frequencies in Table 5-1 and the characteristic frequency retrieved by the analysis could be made by an unstable rotating speed change during the experiment.

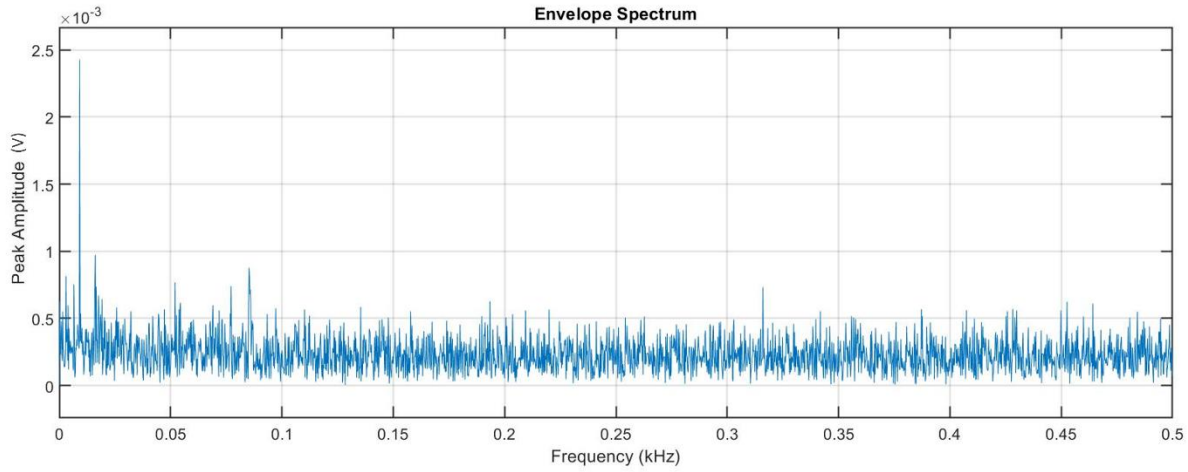

Figure 5-56 Spectral envelope analysis of AE signal for a healthy bearing at 500 RPM.

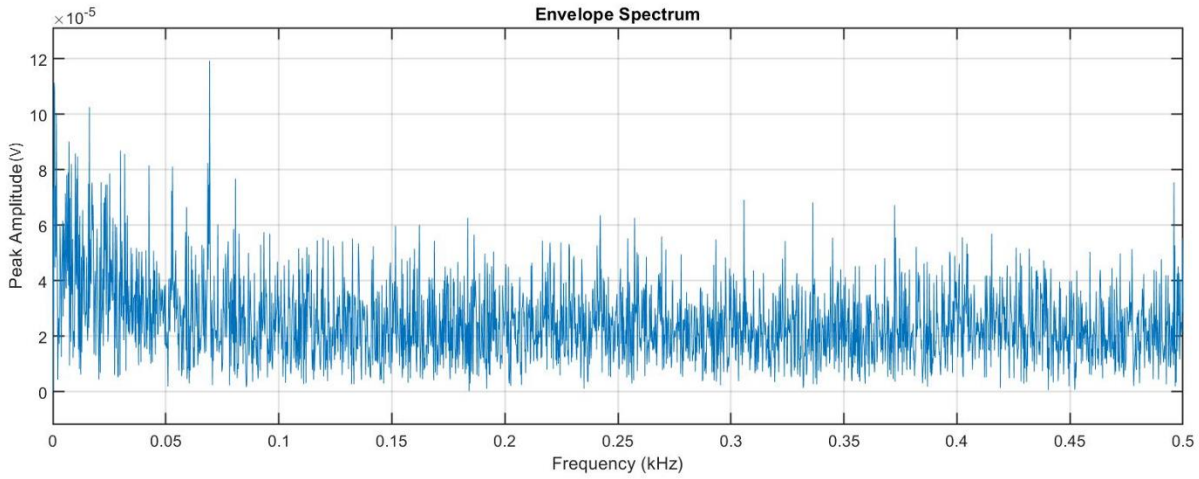

Figure 5-57 Spectral envelope analysis of vibration signal for a healthy bearing at 500 RPM.

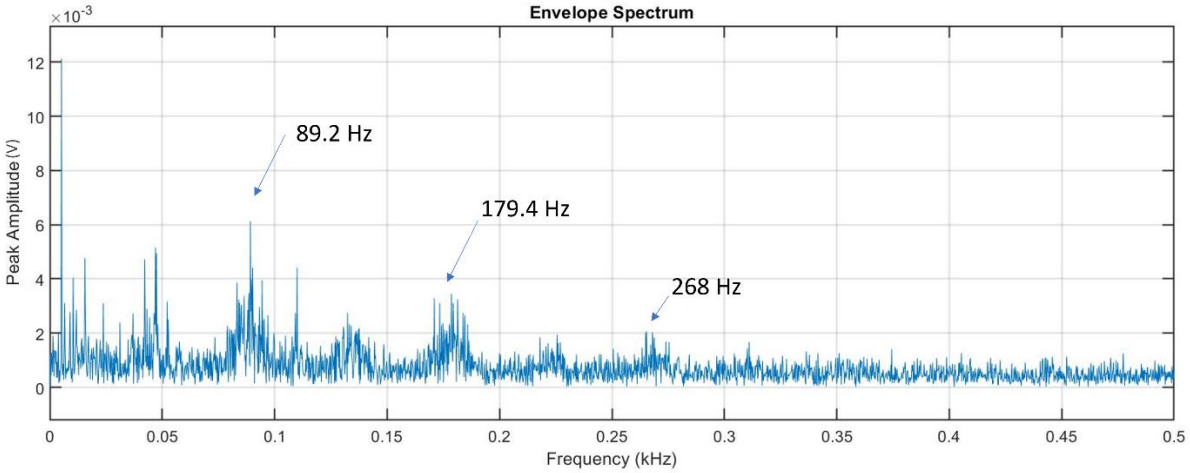

Figure 5-58 Spectral envelope analysis of AE signal for a 10% damaged bearing with roller defect at 700 RPM.

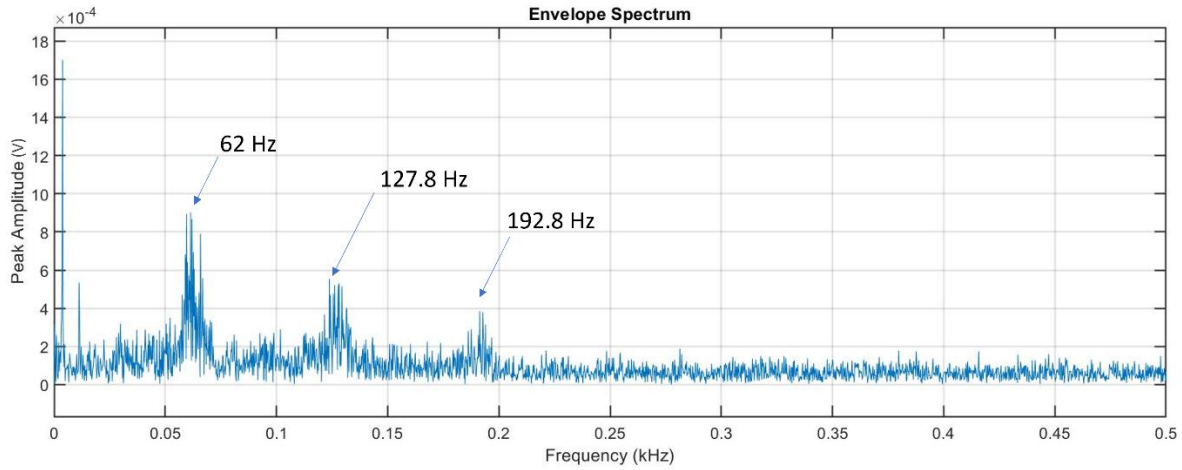

Figure 5-59 Spectral envelope analysis of vibration signal for a 10% damaged bearing with roller defect at 500 RPM.

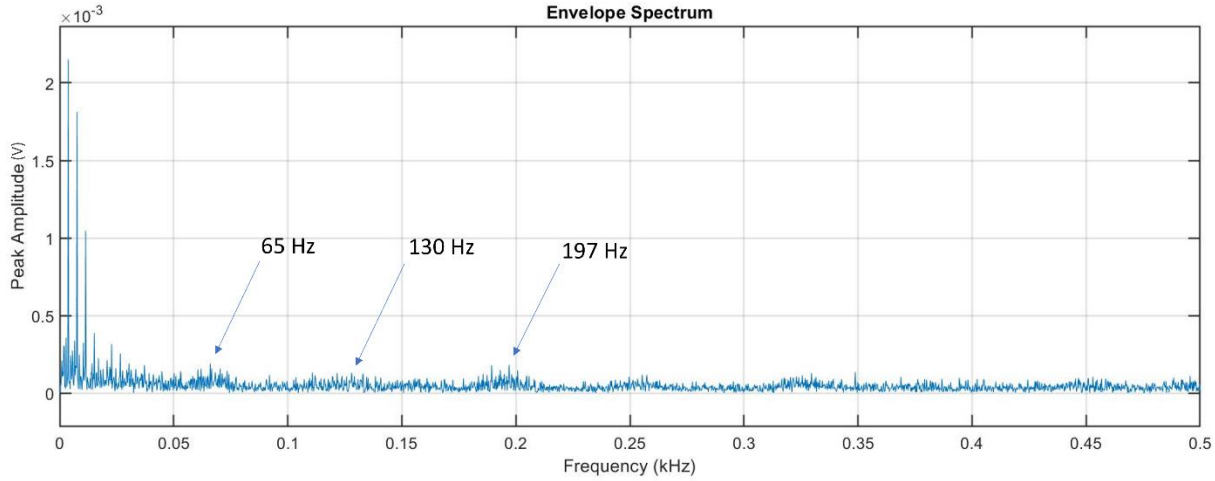

Figure 5-60 Spectral envelope analysis of vibration signal for a 50% damaged bearing with roller defect at 500 RPM.

Kurtogram helps find the ideal core frequency and bandwidth for a band-pass filter, boosting SNR. Optimal frequency band-pass for spectral envelope analysis increases the possibility of discovering fundamental frequencies buried in bearing data with noise. The frequency interval for the band-pass filter is gained when the kurtosis is at the maximum value. In order to improve the computational time, the fast kurtogram which was presented by (Antoni, 2007).

Figure 5-61 demonstrates the kurtogram of AE data of the bearing with 10% roller damage at a rotating speed of 700 RPM. The color bar indicates kurtosis value of the spectrum. The frequency and bandwidth at the highest kurtosis in this kurtogram would be used for the band-pass filter. Accordingly, at the maximum of kurtosis value, the centre frequency (Fc) is 27343 Hz and the bandwidth is 7812 Hz. Consequently, the AE signal was filtered using bandpass at the Fc with corresponded bandwidth. The results are compared between the original and filtered signal as seen in Figure 5-62. The red-coloured signal is the filtered signal together with the blue-coloured original signal. In order to see how the filtering can improve the SNR and generate the de-nosing process, the spectral envelope analysis was determined. Figure 5-58 indicates that the unfiltered signal's envelope analysis has higher noise than the filtered signals.

Improved signal quality makes it easy to detect the 90 Hz roller fault frequency and its harmonics.

Moreover, the vibration signal retrieved from the bearing with 50% roller damage at 500 RPM was analysed. Kurtogram as seen in Figure 5-64 also help improving SNR. Figure 5-65 illustrates the different between the original (blue) and filtered vibration (red) data. Finally, Figure 5-66 shows the spectral envelope analysis of the defective bearing. The defect frequency at 65 Hz with its harmonics, which were hardly to be detected in the unfiltered signal in Figure 5-60.

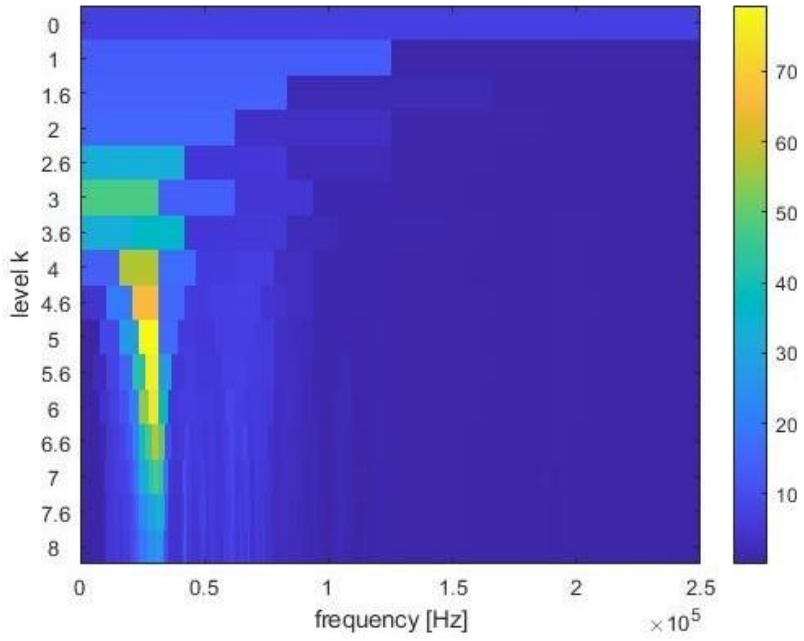

Figure 5-61 Kurtogram from AE data of the bearing with 10% roller damage at 700 RPM.

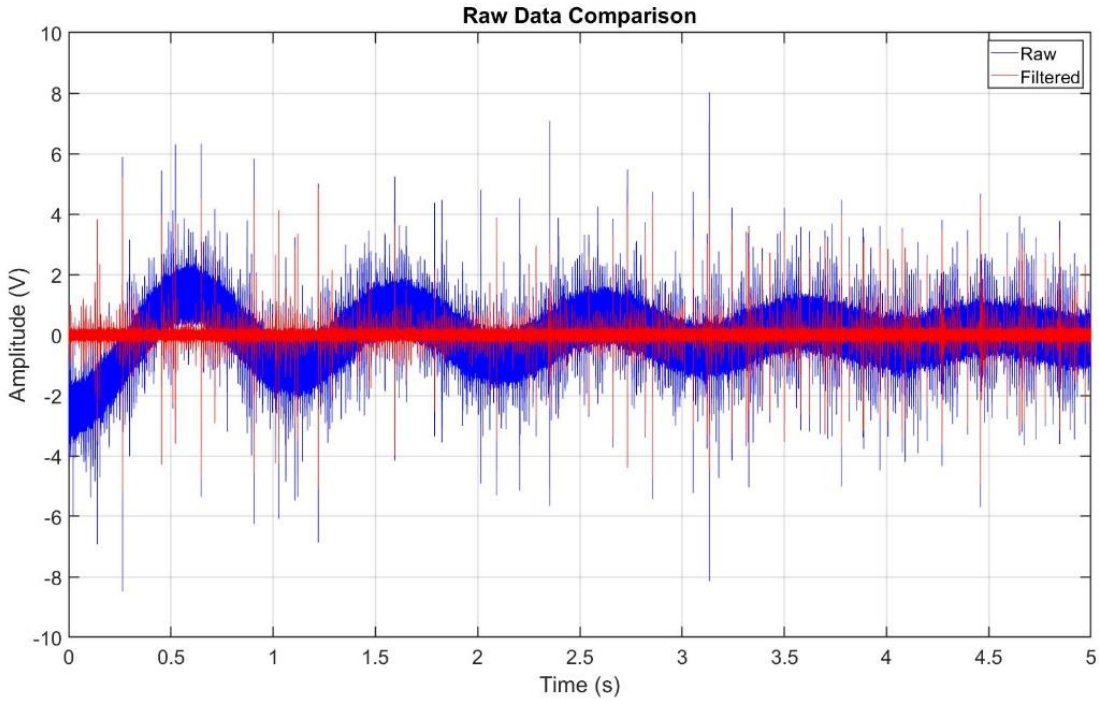

Figure 5-62 Comparison between original (blue colour) and filtered (red colour) AE data of the bearing with 10% roller damage at 700 RPM.

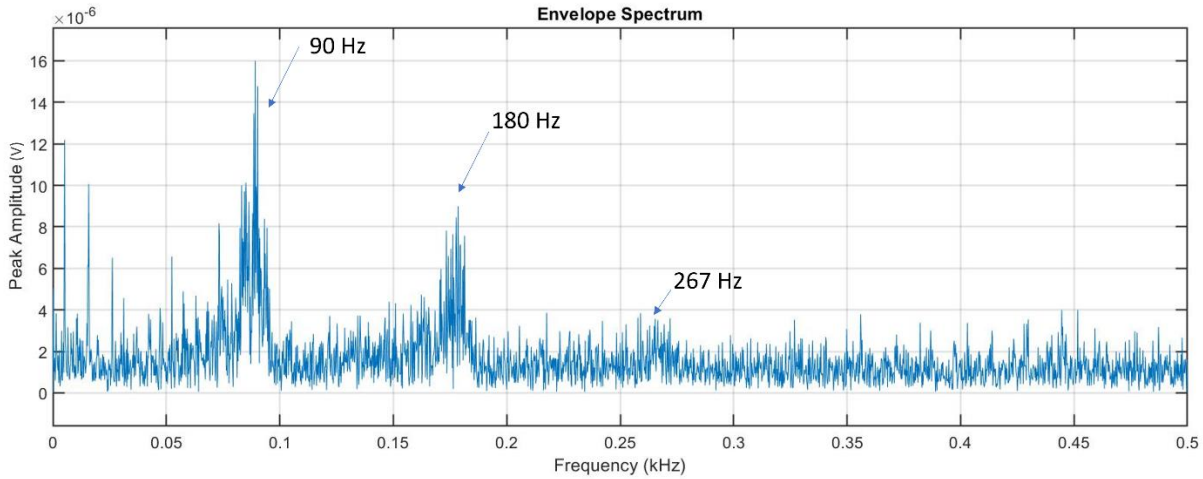

Figure 5-63 Spectral envelope analysis of filtered AE data of the bearing with 10% roller damage at of 700 RPM.

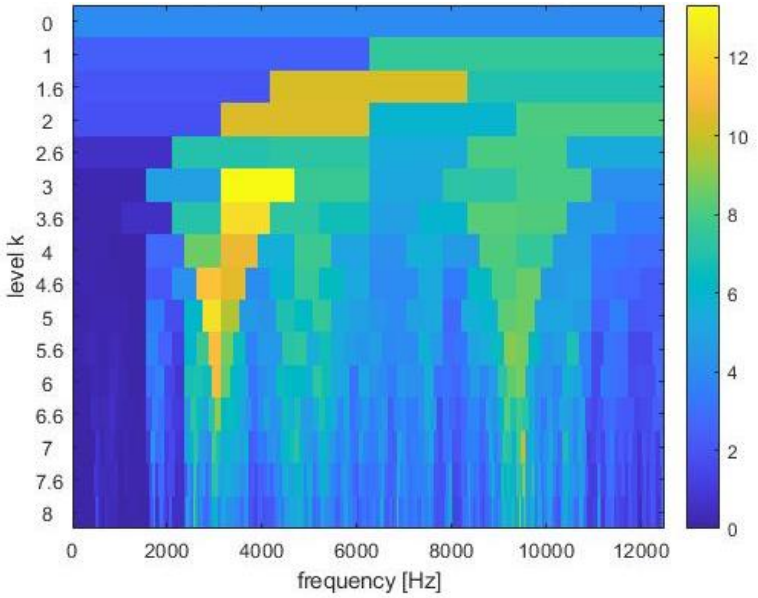

Figure 5-64: Kurtogram from vibration data of the bearing with 50% roller damage at 500 RPM.

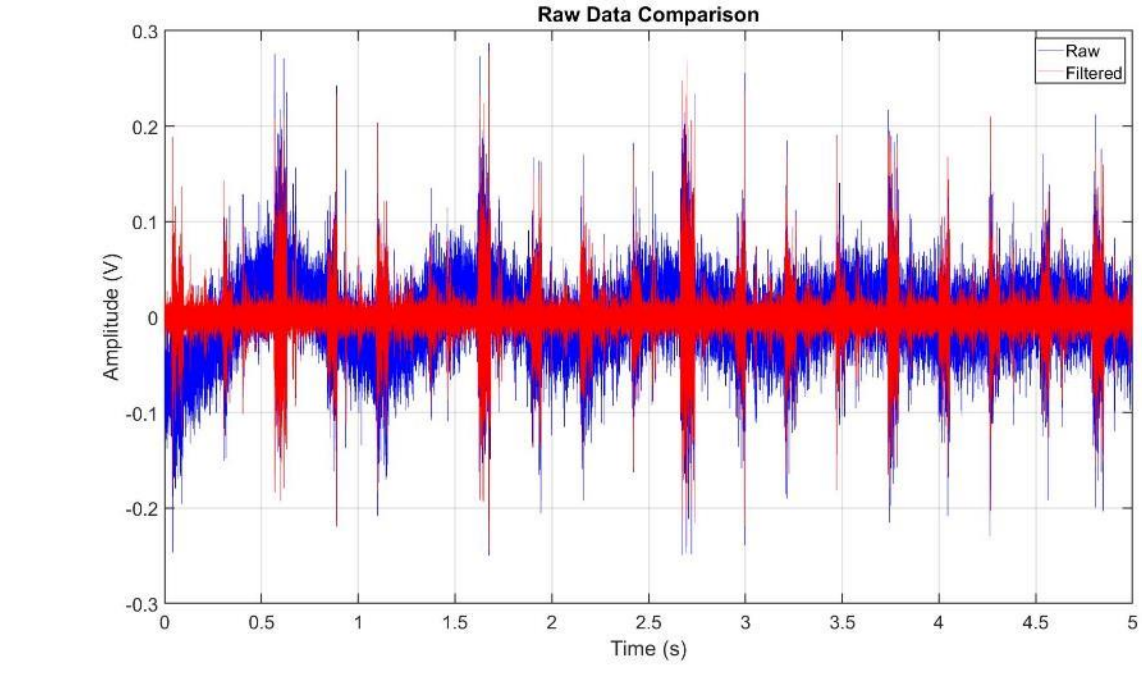

Figure 5-65: Comparison between original (blue colour) and filtered (red colour) vibration data of the bearing with 50% roller damage at 500 RPM.

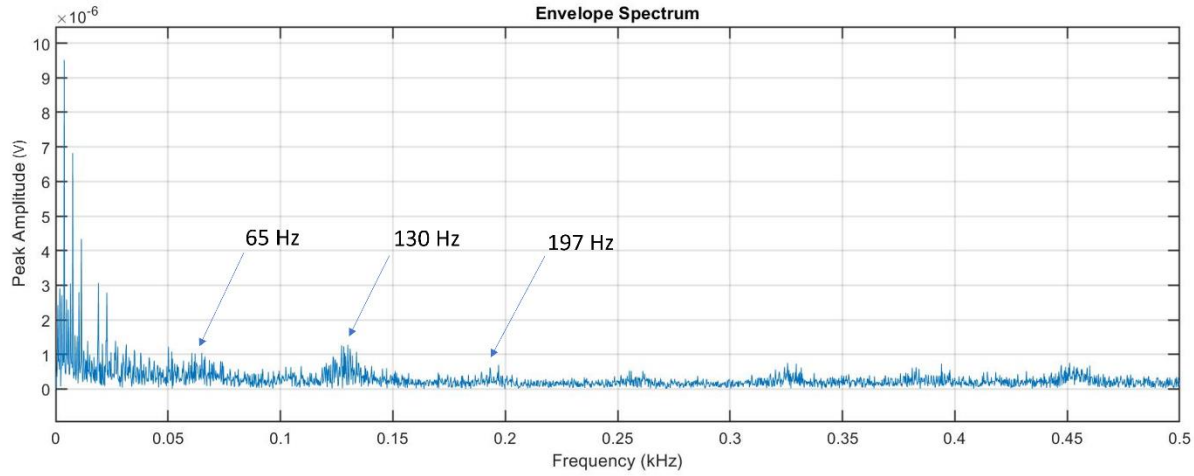

Figure 5-66: Spectral envelope analysis of filtered vibration data of the bearing with 50% roller damage at 500 RPM.

Cepstral analysis is also well-known for signal processing that relies on a nonlinear technique, especially for vibration signals. A methodology of cepstral analysis using Power cepstrum was described in Chapter 4 section 4.4.2. Cepstral analysis calculates the complex natural logarithm of the data's Fourier transform and the power spectrum's Inverse Fourier transform. The independent variable of a measure of time on the x-axis will be described as quefrency instead of frequency, which is measured in seconds.

Bearing test rig vibration data was analysed using cepstral analysis, which was spinning at 500 RPM. There are three different bearing conditions including healthy, roller defect with 10% damage, and roller defect with 50% damage. Obviously, the healthy bearing does not reveal any signs of harmonics on quefrency axis as shown in Figure 5-67.

However, cepstral analysis of the vibration measurement from the bearing with roller defect with 10% damage displayed in Figure 5-68 discovers a peak at 0.016 second of quefrency which means the rahmonics starting at 66.67 Hz (1/0.015). These rahmonics relate to the BSF fundamental frequency of 65.84 Hz as indicated in Table 5-1.

Moreover, cepstral analysis of the vibration measurement from the bearing with roller defect with 50% damage displayed in Figure 5-69 also reveals a peak at 0.015 second of quefrency which is related to the rahmonics starting at 66.67 Hz (1/0.015). They are very close to the BSF fundamental frequency of 65.84 Hz.

Based on the findings, it can be said that cepstral analysis can show the presence of the roller bearing defect with rahmonic at 0.015 s. Moreover, the amplitude of the cepstrum of the bearing with 10% roller damage is 0.02V, while for another bearing with 50% roller damage is 0.04V. Cepstral analysis identifies the bearing defect's harmonics. Larger roller fault bearings produce more significant results than smaller ones.

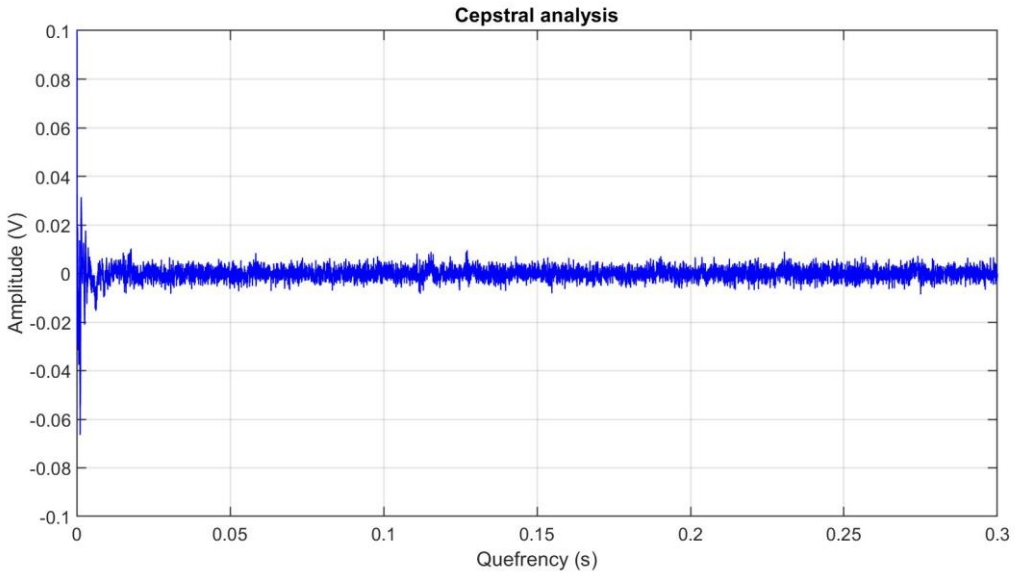

Figure 5-67: Cepstral analysis of the laboratory bearing test rig vibration measurement at 500 RPM with healthy condition.

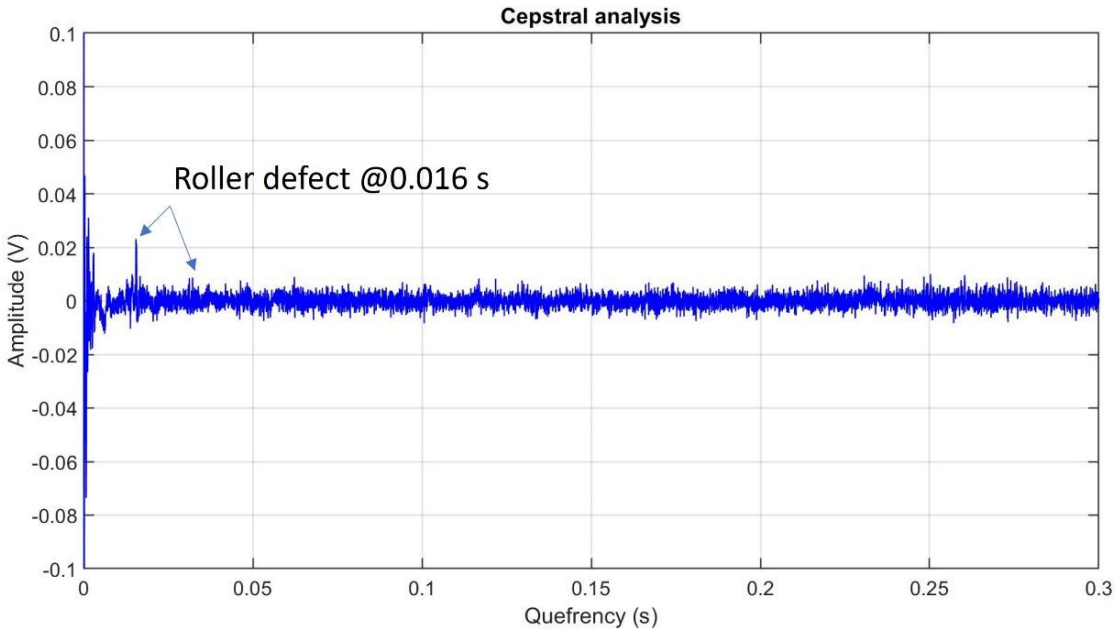

Figure 5-68: Cepstral analysis of the laboratory bearing test rig vibration measurement at 500 RPM with 10% roller damage.

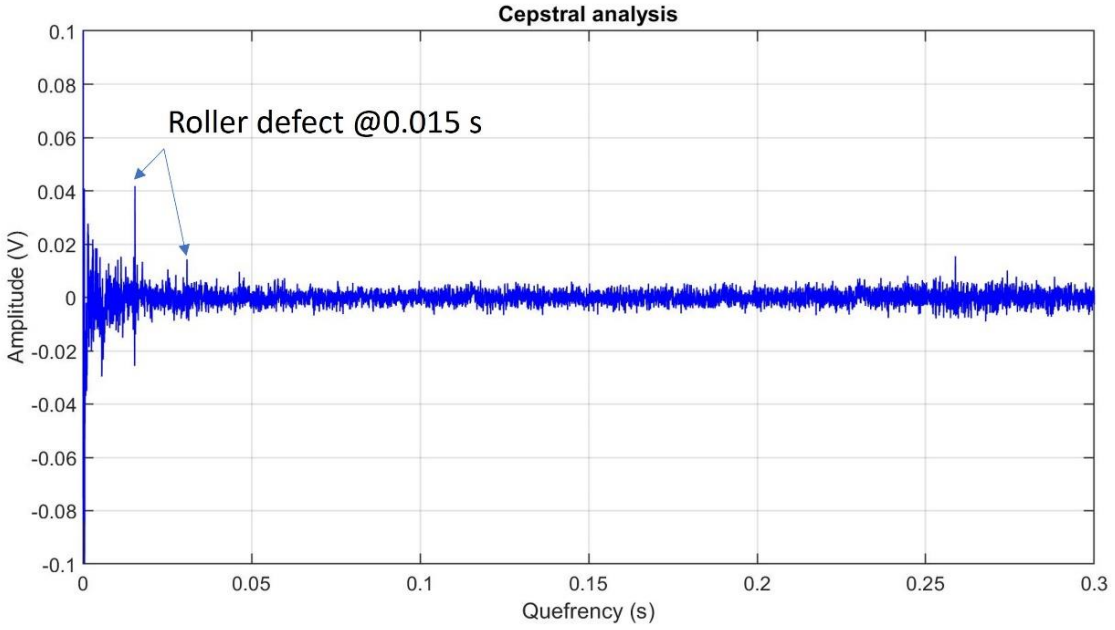

Figure 5-69: Cepstral analysis of the laboratory bearing test rig vibration measurement at 500 RPM with 50% roller damage.

Unfortunately, Cepstral analysis does not show the AE data containing bearing defects. Figure 5-70 shows the cepstral analysis of the laboratory bearing rig from AE measurement of the bearing with the 50% roller damage.

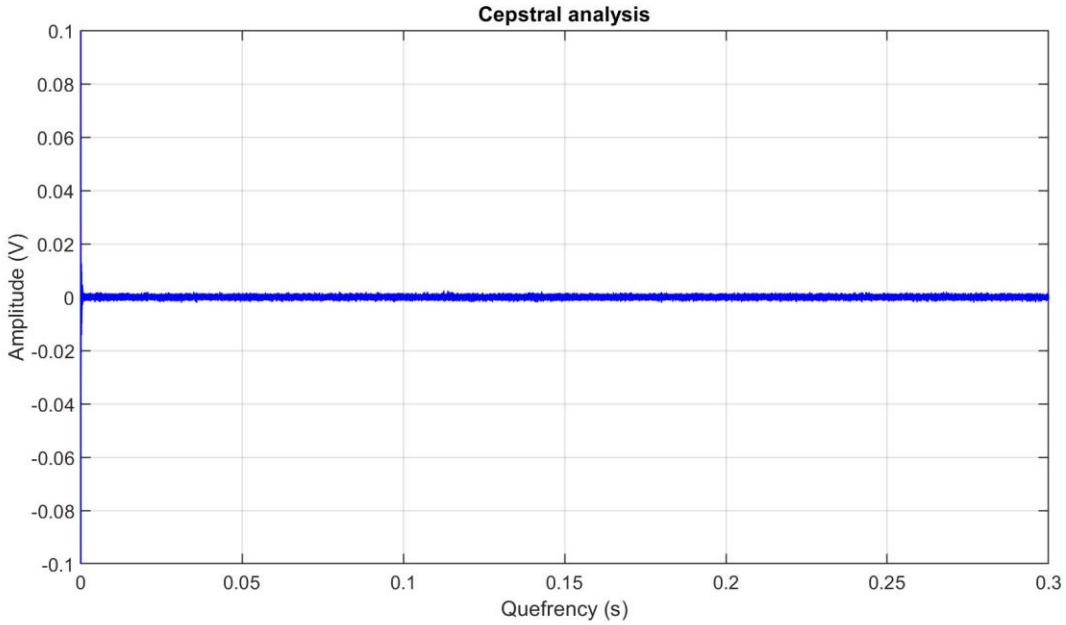

Figure 5-70: Cepstral analysis of the laboratory bearing test rig AE measurement at 500 RPM with 50% roller damage.

5.4 Summary

Various Laboratory experiments have been conducted and discussed in this chapter. Pencil lead break test provided AE sensor resonance frequencies with fundamental values related to the signal profile. Count, energy store, and rise time according to the threshold were presented.

Amsler machine provides the twin disk test, which proves that raw data and FFT analysis are not powerful enough to reveal defects. On the other hand, the spectral envelope can show the Amsler machine's bearing faults harmonics. Unfortunately, the one-dimensional wavelet decomposition cannot specifically reveal harmonics.

Reduced scaled wheel trolley test simulated wayside measurement setup while providing uninterrupted output signal by surrounding noises from the engine. Regarding the defective wheel, several bursts were detected by the time domain analysis. Moreover, moving RMS precisely defined data signals with a high peak. Background noise does not affect the outcome when comparing the moving RMS to the raw signal.

The bearing test rig provided the final statement that raw data is impossible for the complicated signals from rotating machines. Raw data of damaged bearings generally reveals amplitude modulation, which defects could generate. However, raw data would not provide sufficient information on the damage condition, whether its type or severity. Vibration measurements demonstrated the difference between healthy and damaged bearings. However, AE measurements required further signal analysis to enable damage detection. Both AE and vibration RMS, FFT, and Kurtosis values tended to increase over the running speed.

In comparison, the more load input to the test did not affect those values. Unfortunately, the data from vibration measurement failed to reveal the amplitude difference between 10% and 50% damage. The kurtosis value of AE data with 50% damage is significantly higher than 10% damage. AE spectral envelope analysis for a bearing with a 10% roller defect discovered 89.2 Hz and its harmonics. Kurtogram helps find the ideal core frequency and bandwidth for a band-pass filter. Fast Kurtogram can significantly reduce the computation time. As a result, the unfiltered signal's envelope analysis has higher noise than the filtered signals.

Cepstral analysis calculates the complex natural logarithm of the data's Fourier transform and the power spectrum's inverse Fourier transform. The results from cepstral analysis revealed that vibration measurement from the bearing with roller defect with 10% damage discovered a peak at 0.016 seconds of quefrency, meaning the rahmonics started at 66.67 Hz (1/0.015). These rahmonics relate to the BSF fundamental frequency of 65.84 Hz. Moreover, cepstral

analysis of the vibration measurement from the bearing with roller defect with 50% damage also revealed a peak at 0.015 seconds of quefrency, related to the rahmonics starting at 66.67 Hz (1/0.015). Additionally, the amplitude of the cepstral analysis of the bearing with 10% roller damage is 0.02V, while for another bearing with 50% roller damage is 0.04V. As a result, Cepstral analysis from vibration analysis can identify the bearing defect's harmonics. Larger roller fault bearings produce more significant results than smaller ones. Unfortunately, Cepstral analysis of AE data did not reveal bearing defects.

Chapter 6: Field experiments

This chapter demonstrates the field experiments conducted in this study. Several test sites include Bescot yard, Cropredy and Long Marston test track under different operating conditions. From the low speed below 20 km/h to 144 km/h, the RCM can handle and provide efficient data for the identification of the wheelset condition. VTG Rail, Motorail Logistics, Krestos Limited, and Network Rail made contributions to the Long Marston test track. Testing in Bescot yard and Cropredy was also supported by Network Rail.

6.1 Bescot Yard

The field test carried on the actual railway track in Bescot yard, which is located in Walsall in the West Midlands of England. The Bescot yard is also located next to a locomotive traction maintenance depot, operated by DB Cargo UK. A locomotive with unloaded wagons (Figure 6-1) was prepared for this experiment. The main objective of this trial is to demonstrate that the newly developed data acquisition application based on MATLAB works with AE monitoring system.

Figure 6-1: Locomotive used on the Bescot yard.

Figure 6-2: AE measurement system and the installation of two AE sensors

The freight wagons with a class 08 Number 08670 locomotive used in the experiments travelled along a straight track. Two AE sensors were installed on each side of the rails using Araldite A0002 Rapid Epoxy as mentioned earlier in Chapter 5. Both sensors link by flexible wires to a pre-amplifier and main amplifier before sending data to DAQ NI 9223. This experiment demonstrates how the wayside measurement works as a designed RCM of railway rolling stock wheelset which will be further described in detailed for both AE and vibration data. Figure 6-2 shows the location where two AE sensors are placed.

The 40 dB gain was set for the pre-amplifier together with 3 dB for the main amplifier. While the sampling rate was selected between 500 kS/s and 1 MS/s, the recording time was fixed at 30 seconds.

6.2 Cropredy

Another wayside measurement on the actual track was held at the Cropredy site near Banbury. The line is called Chiltern rail connecting London Marylebone with Birmingham Moor Street

station. The instrumented test site's main goal is to evaluate the RCM system's effectiveness and reliability at line speed. There were 2 channels of AE sensors placed on the track as the sensing unit. While other instruments were contained in the control room on the side of the track. The room contains data acquisition related equipment including PC, power supply for all sensors, pre-amplifier, main amplifier, and harness. With the sensing equipment and data collecting unit connected, remote wheelset CM begins.

The train service on this railway route is CrossCountry and Chiltern Railways with mixed traffic operation with freight services. Most passenger fleets are CrossCountry fleets, which typically include trainsets of three to five cars, while Chiltern Railways operates this line with 2-car class 172 fleet. The freight train has up to 25 carriages for its vehicles. The route is not electrified, and the installation segment has no rail junctions. The maximum speed allowed for the track is 100 MPH (160 km/h). At the track section which the measurement was taken, it is a straight section that allow trains travelling at operating speed. Since the rails are continuously welded, there are no places where impact noise can arise.

This test site on the mainline is a collaboration between the University of Birmingham and Network Rail providing the CM of the rail traffic. Figure 6-3 displays the schematic diagram of the proposed wayside CM system. Figure 6-4 shows the equipment inside the control room situated on the trackside.

The specialised program, which was developed by the University of Birmingham using LabVIEW ® and MATLAB®, was used to acquire all data of this experiment. Live traffic nformation was used to timing the monitoring system's trigger activation.

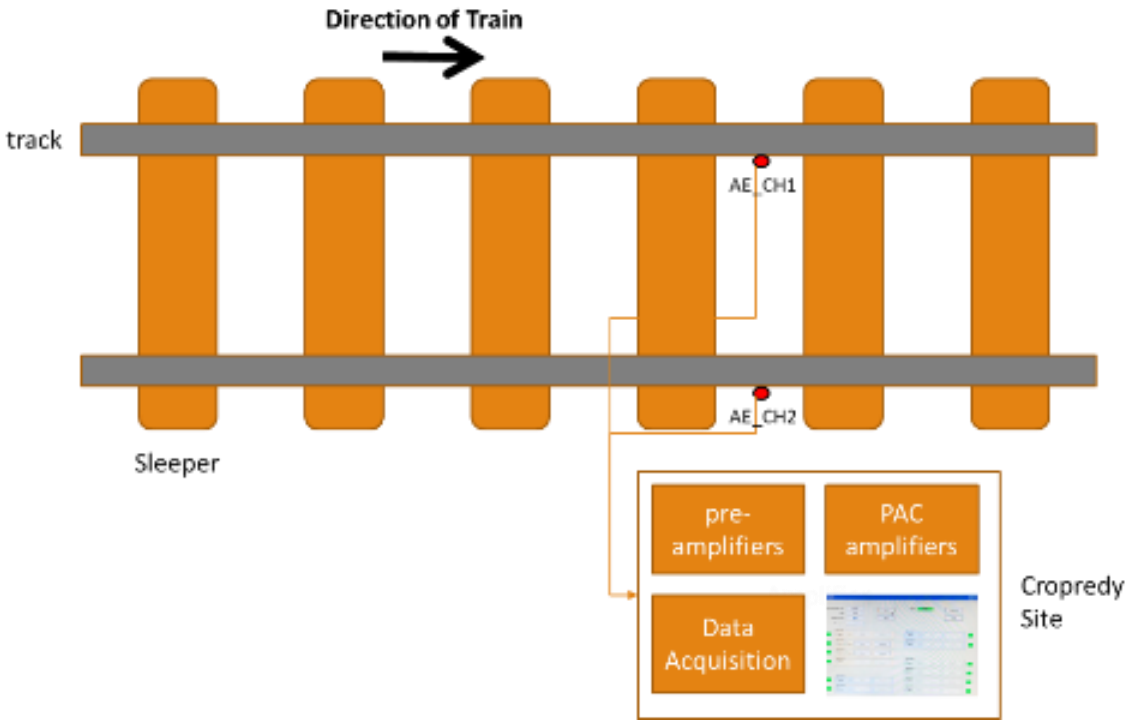

Figure 6-3: The installation layout of two AE sensors in conjunction with the control unit.

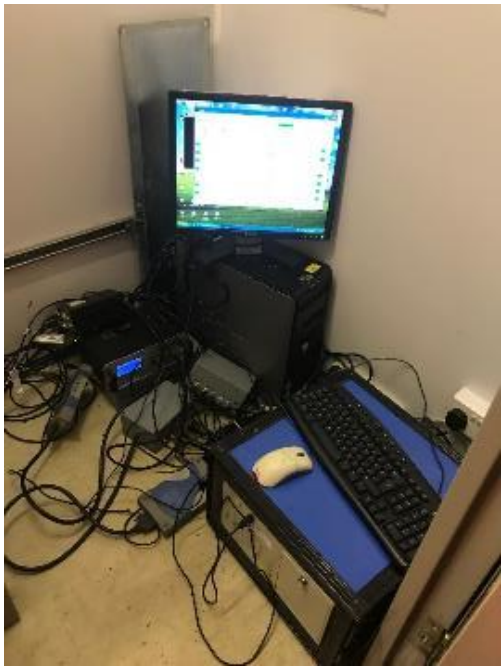

Figure 6-4: The data acquisition with the customized software for RCM.

Figure 6-5 shows the screenshot of the customised program which was used for the data collection. Figure 6-6 shows one of the track's AE sensors.

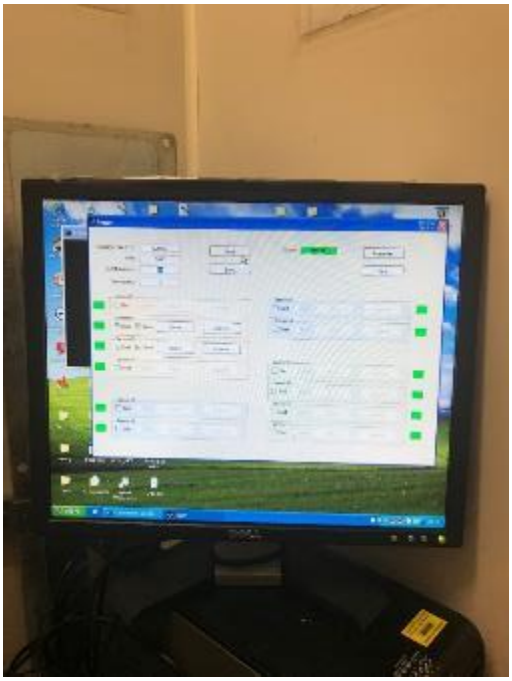

Figure 6-5: The special program used for the remote condition monitoring.

Figure 6-6: An AE sensor installed on one side of the rails.

Cropredy site triggle in trials used a Type 59 Cautor electromechanical treadle. The actuating arm of the treadle, which is forced down by the first wheel's flange as the train passes by the instrumented site, detects the presence of a train and activates the treadle.

Once the actuating arm is lowered, the treadle relay sends a signal. Consequently, the signal will be transmitted to the DAQ unit enabling the trigger system to start the acquisition of the data. At the end of the process, the actuating arm will get back to the default position preparing for another trainset. As a result, the treadle would generate only one signal for each trainset.

This is a robust system which is not only reliable but also resistant to the electromagnetic interference effects. Unlike the transmitter receiver IR optical sensors in Long Marston, it can't detect each wheelset's location or compute the train's speed.

6.3 Long Marston

The experiment at Long Marston site was appointed to assess the ability of the specially designed RCM using acoustic emission and vibration techniques in detecting several defects on the wheelset. These faults include wheel and axle bearing problems of varying severity. RCM measures onboard and wayside

The objectives of this field trail mainly involve the evaluation of detectability and reliability of the RCM system. VTG Rail provided freight tanker waggons for Long Marston tests. Moreover, Motorail Logistics supplied a locomotive with healthy wheelset condition which was used as the prime mover for the test wagons during this field trials.

Testing conditions include forward and backward directions with a fixed speed of 48 km/h (30 MPH) and 32 km/h (20 MPH) respectively. It should be noted that the test in forward direction faced the engine at the front and vice versa. The test wagons were pulled over a straight track section with instruments installed for few hundred metres. The continuously welded track eliminated wheel impact sounds at rail joints. In addition, the train was assigned to coast and remain the constant speed to produce the minimum interference from the wheel sliding and braking.

Wheelset defects were split into wheel flat and bearing defects with different sizes in the Long Marston trials. VTG Rail introduced both defects manually. The bearing defects were studied in both roller and race defects using freight wagons. Different sizes of 2, 4 and 8 mm were introduced for roller defects. The bearing lubricant contamination was further added to the test. All faults were on one side of the wheelsets; the other was healthy.

The sampling rates applied for this field trail were 500 kSa/s for acoustic emission and 25 kSa/s for vibration measurement. Consequently, the FFT analysis would be halved to 250 kHz and 12 kHz respectively. The recording time for onboard measurement was 10 seconds, while the wayside measurement utilised 12-24 seconds. The wayside measurement relied on different sizes of trainset, the shorter one could save the data size by reducing the duration of the acquisition.

6.3.1 Onboard measurement for axle bearing defects

Onboard measurement is generally applied when the early identification of developing defects takes place. Since the sensor is closer to the signal source, a series of measurements may handle continuous axle bearing revolution records.

Since wayside measurement can only be used in passing trains along the test site, which is the limitation on a number of recorded data. Moreover, the wayside measurement is subjected to noise from the passage of the train being considered which is significantly reduced for the onboard measurement.

Another advantage of onboard measurement against wayside is the possibility to run an alarm system of a detectable damage soon. Before installing onboard systems, any train fleet would need useful wayside measurements. Moreover, the number of sensors required for any onboard measurement could be expensive to operate and maintain. It should be noted that the power source of the onboard measurement could make the monitoring system more complicated. In

case the passenger train is being monitored, the power source is more convenient than the freight train.

Figure 6-7: Onboard measurements of axle bearings with roller defects on the wagon tanker.

Figure 6-7 shows onboard axle measuring setup. The sensor was placed near the bearing's loaded zone. The sensor's adhesive performance can affect signal transmission.

6.3.2 Onboard measurement for contamination of axle bearings caused by lubrication

The evaluation of wheel defects was expanded to the contamination of lubricants with water and sand. AE sensor and accelerometer were carried over as the sensing techniques. The results could provide a different overview of the signals retrieved from axle bearing with roller defects.

6.3.3 Wayside measurement for axle bearing defects

The installation of AE sensors and accelerometers was conducted on the rail using magnetic couple as shown in Figure 6-9. The pre-treatment of rail surface at the sensor location was done by grounding to provide the better contact. The sensor position should be less impacted by rail movements. AE sensors and accelerometers were mounted above sleepers to reduce rail noise

caused by rolling stock. Figure 6-8 shows four R50 AE sensors and two Wilcoxon 712F accelerometers. Separately linked AE sensors and accelerometers to Agilent DAQ. While AE sensors require the pre-amplifier for the acquired signals, accelerometers do not need to.

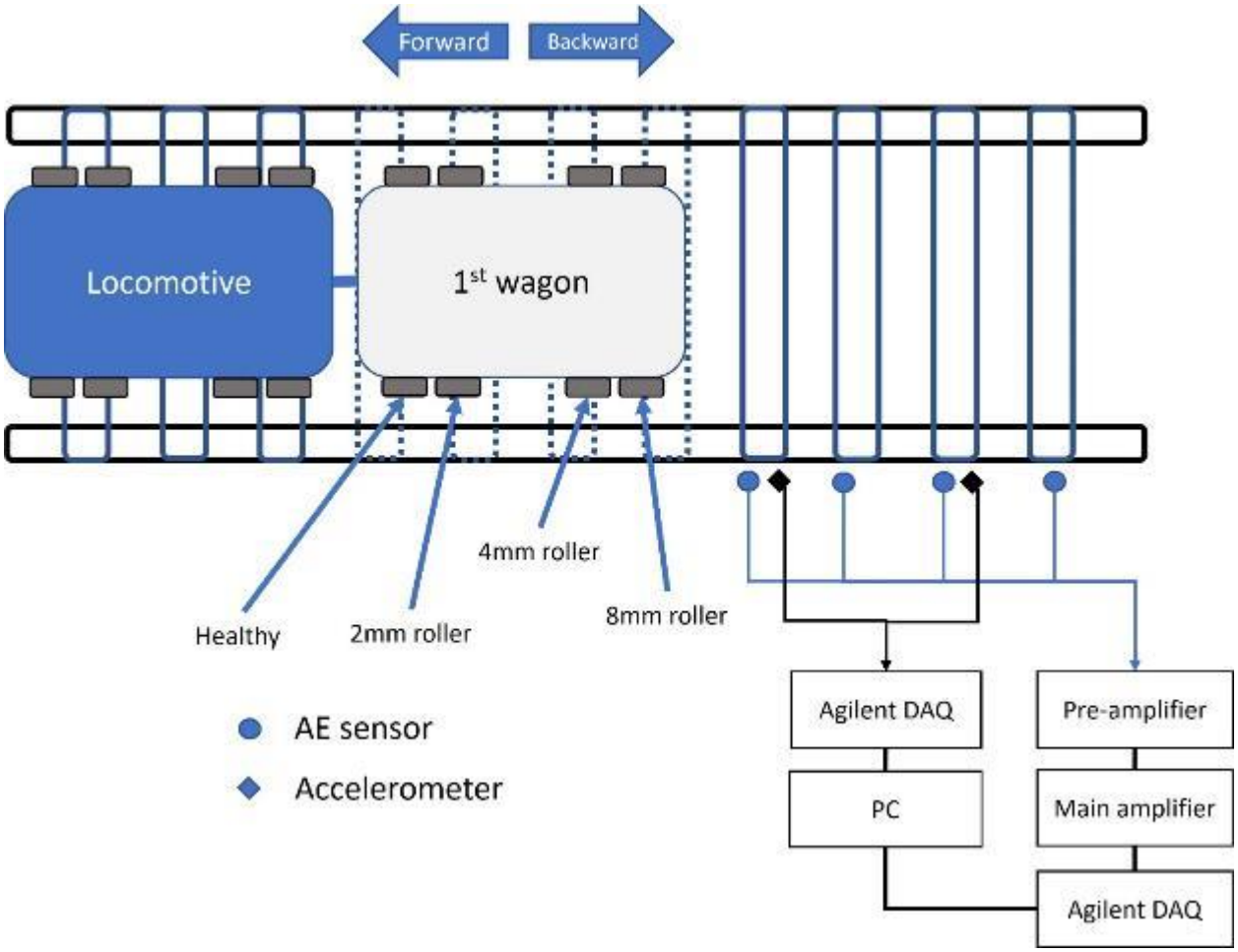

Figure 6-8: Diagram of the installation of the wayside RCM system with AE sensors and accelerometers at Long Marston.

All of the bad bearings on the first wagon were on the same side, which had four different wheel sets. The output signals were recorded in both forward and backward directions with different speed conditions.

Wayside measurements require the trigger system to initiate the recording of signals. The trigger system should be carefully designed to deal with the entire passage of any trainset on the line. Thanks to the controlled environment on the Long Marston test track which enhance

an uninterrupted operation during the experiment. A semi-permanent trigger system has two sets of IR optical sensors.

Figure 6-9: Wayside accelerometers and AE sensors.

When the train is passing at each set of transmitter receiver, each train's wheel will suspend the transmission of IR beam resulting the rise of electric pulse. The trigger is turn on when the IR system's electric pulse is detected. Consequently, the DAQ unit will start the recording of the signal. Each wheelset that passes across the detecting zone records the train's AE and vibration.

The number of axles could be retrieved by counting the number of transmitted IR blockages by passing wheelsets. The known distance between each pair of transmitter receivers makes the speed measurement of the passing train available for the data analysis process. Moreover, the position of each wheel can be noted in order to help data analysis. AE and vibration data can be truncated when each wheelset passes through the detection zone and above each sensor. The RCM flowchart is shown in Figure 6-10.

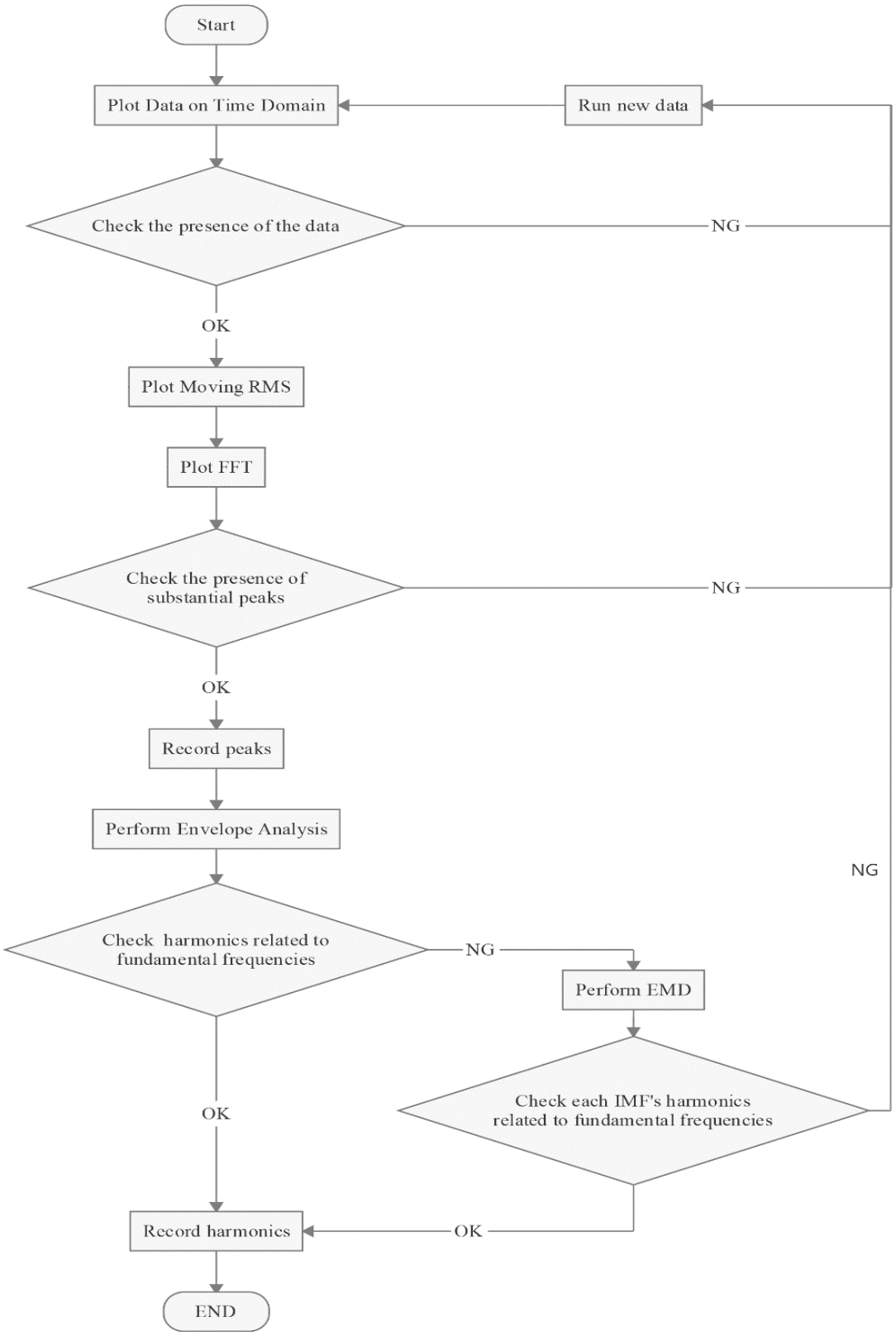

Figure 6-10: RCM flowchart.

6.4 Results

6.4.1 Bescot Yard

Wayside measurements on a freight train containing one locomotive at one side and a number of wagons were conducted on the side loop of railway track at Bescot yard. There are two AE sensors placed on each side of the rails as mentioned earlier. The results here would provide the overview of how AE signal retrieved from the wayside measurement looks like. The recording time was set at 30 seconds which is related to the speed of the trainset. Moreover, the saving time is also assigned to 30 seconds in order to reassure the recoding is written properly. It is always a case that the longer recording time for the output, the more saving time the system requires.

Two sets of raw data of AE signals from the wayside measurement while a locomotive with wagons was moving at the low speed with 1MS/s sampling rate are shown in Figure 6-11 and Figure 6-12. They include the sign of locomotive and wagon movement.

Another sample providing the signal without locomotive movement is shown in Figure 6-13. The signal amplitude is lower than the previous two samples. Moreover, the signal profile is in the flat shape instead of the peaks contained in the data that include the signal from the trainset. However, none of these raw data can indicate the faults of the rolling stock.

Raw data of AE signal could not provide the useful information for the detection of the rolling stock during the measurement. The signal profile is not uniform, thus, unable to be sorted. The maximum amplitude of each raw data might be used as the reference when compare with other records. As refer to this experiment, the maximum observed amplitude is 10. Therefore, the analysis of any record which displays the amplitude of 10 would be able to see the presence of the locomotive with wagons. Since the AE signal is sensitive to other noises existed in the environment, the raw data normally packs these noises during the recordings. However, AE

signal contains defect detection information that requires further signal analysis.

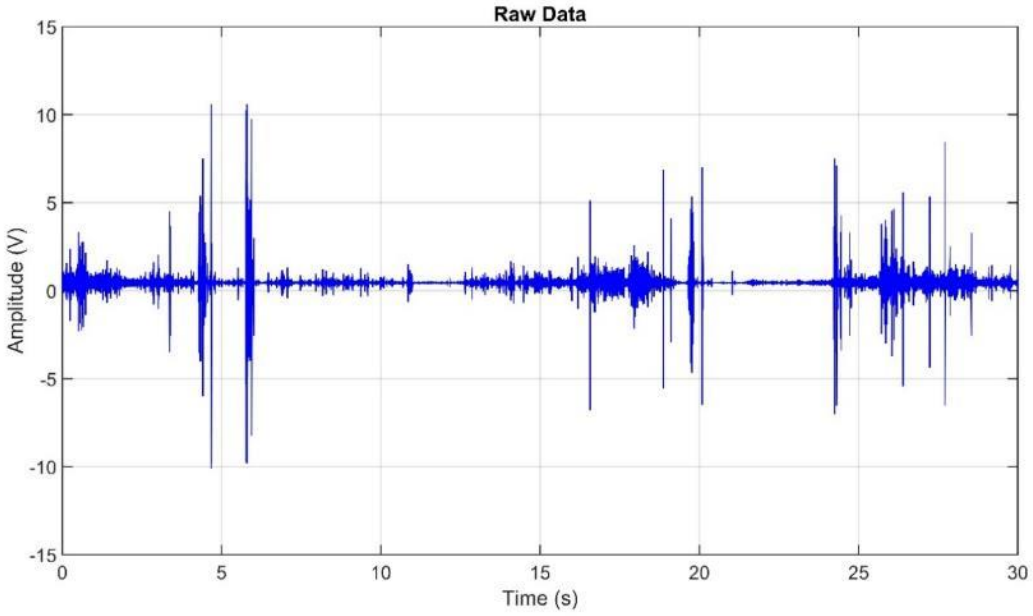

Figure 6-11: Raw data of sample 1 with 1 MS/s sampling rate.

The first and fundamental magnitude analysis relies on the time-domain is RMS which was mentioned earlier in chapter 4. Generally, RMS effectively improve data interpretation of time-series signals by focusing on energy content rather than the whole sinusoidal waves. RMS value of a data is calculated using the equation 4-6. It breaks down the raw data into cleaner signal providing major peaks related to the acquired signal.

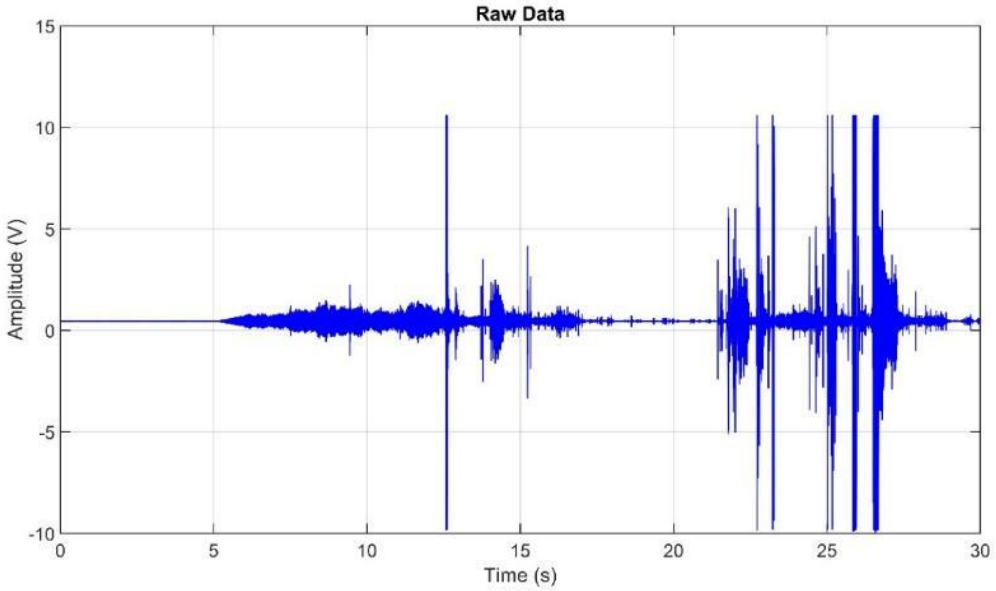

Figure 6-12: Raw data of sample 2 with 1 MS/s sampling rate.

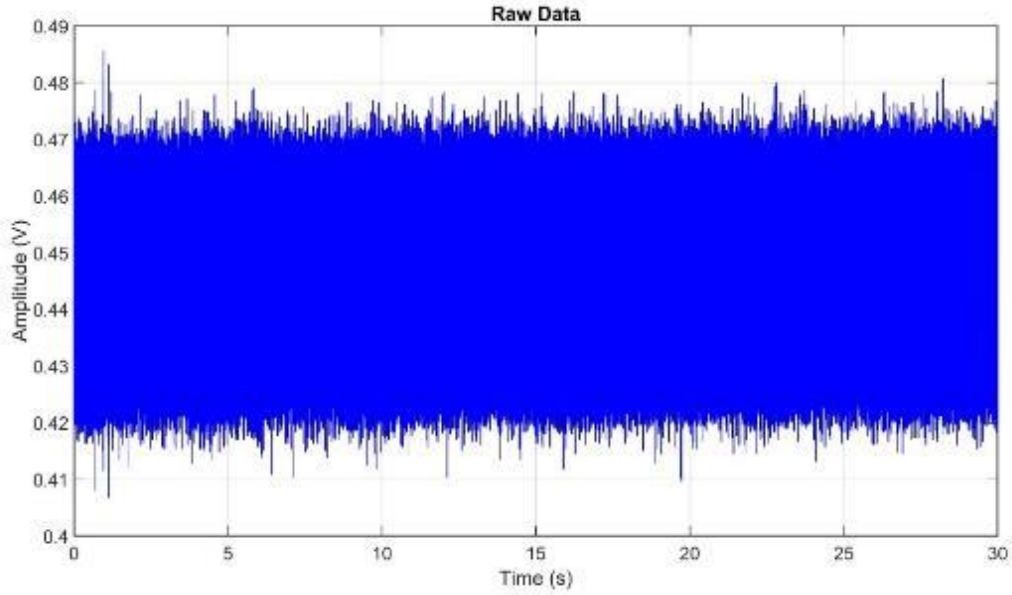

Figure 6-13: Raw data of sample 3 with 1 MS/s sampling rate.

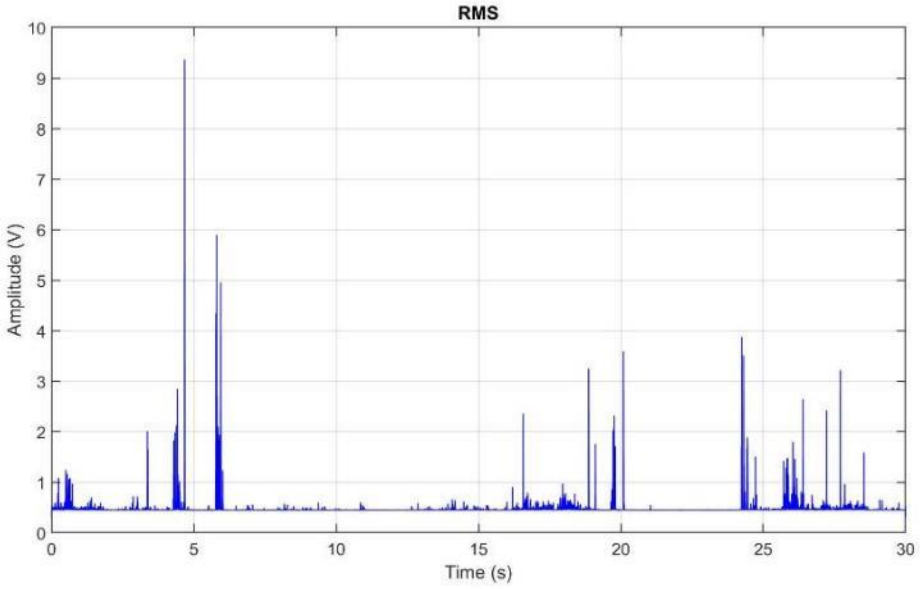

Figure 6-14: RMS analysis of sample 1 with 1 MS/s sampling rate.

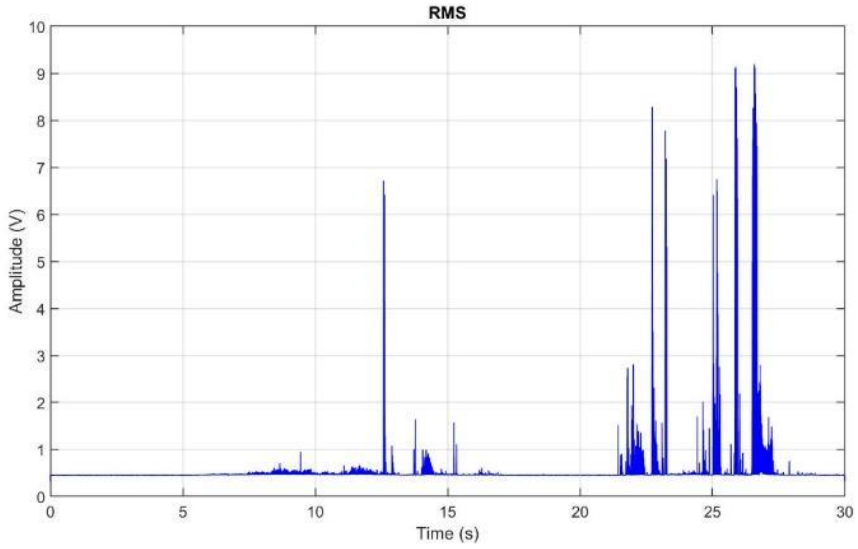

Figure 6-15: RMS analysis of sample 2 with 1 MS/s sampling rate.

In general, the output of RMS analysis will not make a big step of data analysis since it still relies on the time domain which is unable to identify the event in conjunction with rotating machine's parameters. Peaks from RMS would be compared among signals from different conditions, particularly healthy and unhealthy. RMS of vibration data might show low and high-speed amplitude differences. Therefore, AE data generally require more sophisticated

signal analysis in order to differentiate the signal when compared to the data retrieved from accelerometers.

Figure 6-14 and Figure 6-15 revealed that RMS data provide better clarification for the AE signal. The amplitude of those two signals is clearly identified. Moreover, Figure 6-16 also shows the flat amplitude which is identified as no appearance of rolling stock. Correspondingly, the RMS would also be insufficient for further analysis of damage identification of rolling stock wheelset. Since the threshold could make an error on data reading which could be normally occur for any measurement.

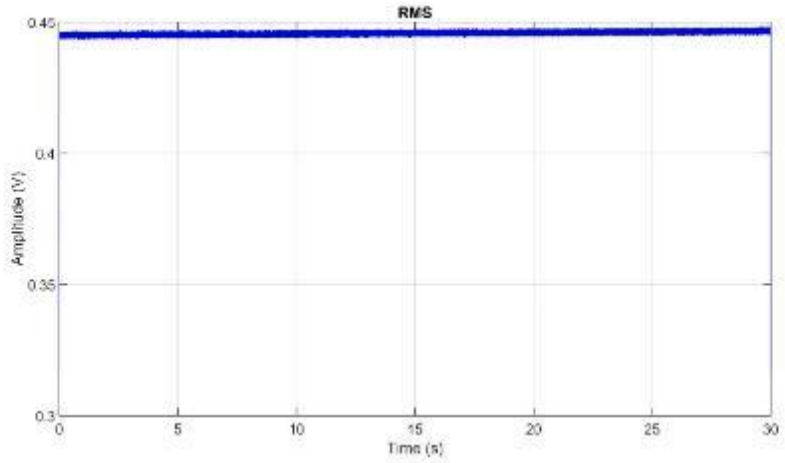

Figure 6-16: RMS analysis of sample 3 with 1 MS/s sampling rate.

Frequency domain analysis would improve the signal interpretation as it may help identify behaviour of each component within the rotating machine. In the application of field measurements, FFT is one of the well-known solutions for revealing something happening in the data. Figure 6-17 shows AE data from sample 1 with FFT analysis. There are consequences of peaks describing the related resonance frequencies to the locomotive with wagons movement. All peaks shown in the output data include 53 kHz, 165 kHz, 170 kHz, 198 kHz, 234 kHz, 287 kHz, 307 kHz and 347 kHz. Figure 6-18 displays FFT analysis of another sample which reveal less peaks than the previous sample. Those peaks contain 53 kHz, 170 kHz, 198

kHz and 307 kHz. According to information of R50α AE sensor in chapter 5, They are related to resonant frequencies. Therefore, this sample does not contain information related to the train passage.

FFT would not be powerful enough to reveal useful events on the frequency domain. FFT generally struggle with the identification of the event type or the defects. In some cases, it would not notify the peaks from events even there are some existed on the time domain.

In this real-world situation, the resonance frequencies are key points to the interpretation of the signal. When a defect exists, short-duration pulses excite resonances at the characteristic frequency. These resonances require signal demodulation to determine the component's health. As the data acquired from the field contain overwhelming information, the excessive data should be filtered out before doing further analysis. Therefore, a band-pass filter would remove the excessive vibration signals from the environment and unwanted sources. The signal is filtered at one of the major resonance frequencies. Removing undesirable signals increases the SNR.

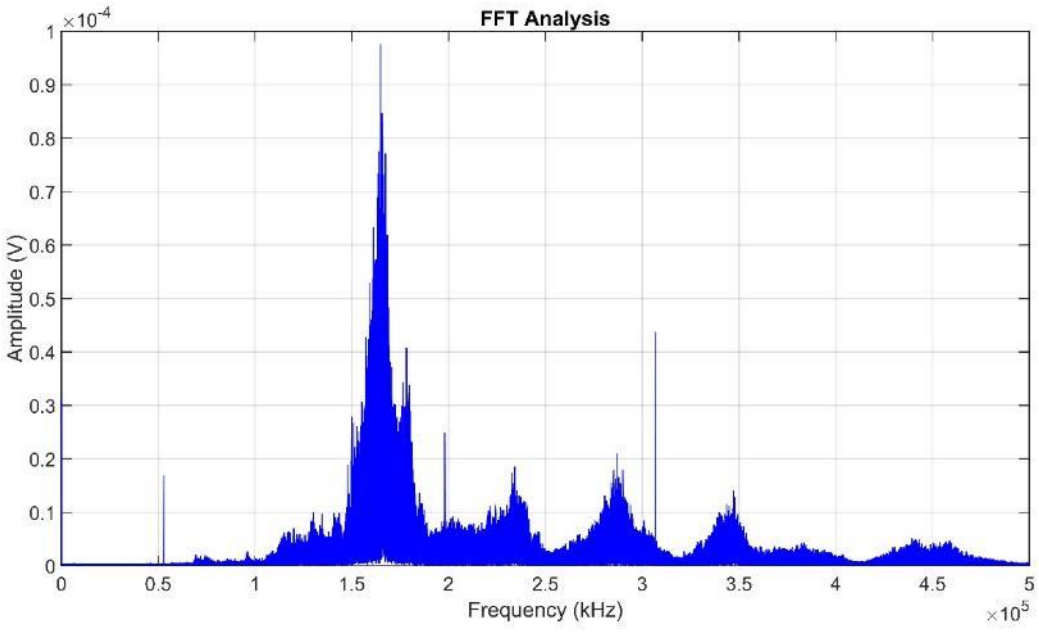

Figure 6-17: FFT analysis of sample with 1 MS/s sampling rate (contains train passage).

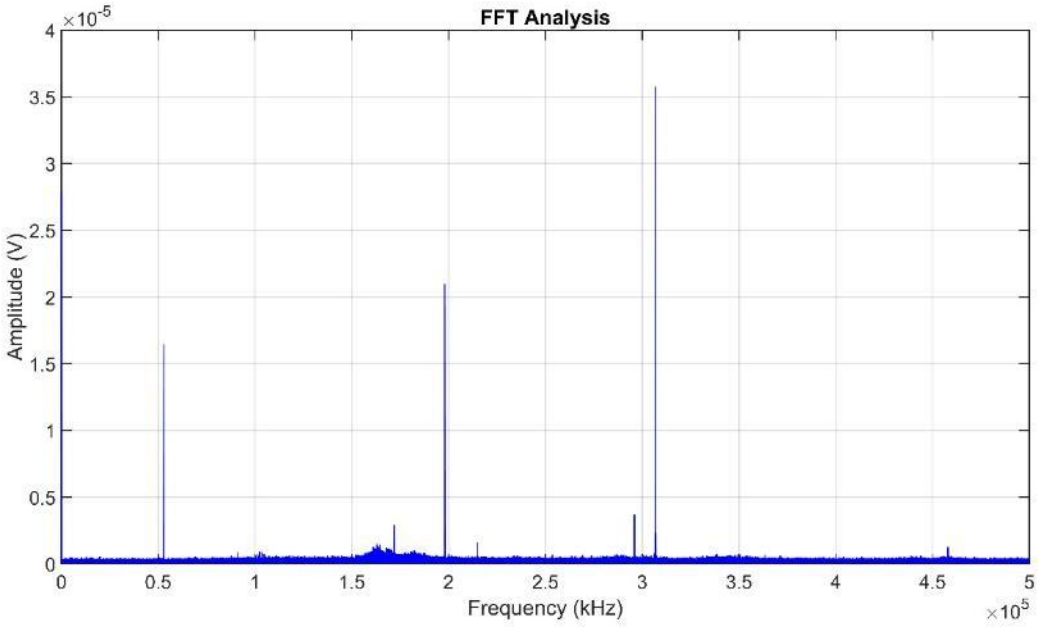

Figure 6-18: FFT analysis of sample with 1 MS/s sampling rate (no train passage).

Kurtogram band-pass filter algorithm was introduced by (Antoni, 2007). Data was processed using the Kurtogram's highest frequency and band-pass window. An optimum frequency band to be used for the band-pass filter can be retrieved by the extraction of the most impulsive signal stored in the raw data. The output of kurtogram will be the Fc and bandwidth which will be selected as the input of the band-pass filter. An output filtered signal will be more impulsive in characteristics which would help reveal the useful information related to the health condition of rotating component when dealing with spectral envelope analysis.

With the help of the fast Kurtogram presented by Antoni, the computation time of Kurtogram is significantly reduced. As a result, Fast Kurtogram reduce the computation time in less than a half. The fast Kurtogram utilise the ½ binary tree kurtogram estimator for the algorithm.

Comparing the result from normal Kurtogram with fast kurtogram as display in Figure 6-19 and Figure 6-20 respectively. There are no significant different despite the computation time is reduced more than a half. Since the Fc of Kurtogram is 334.96 kHz with bandwidth (Bw) of 1.953 kHz, which is identical to those retrieved from Fast Kurtogram.

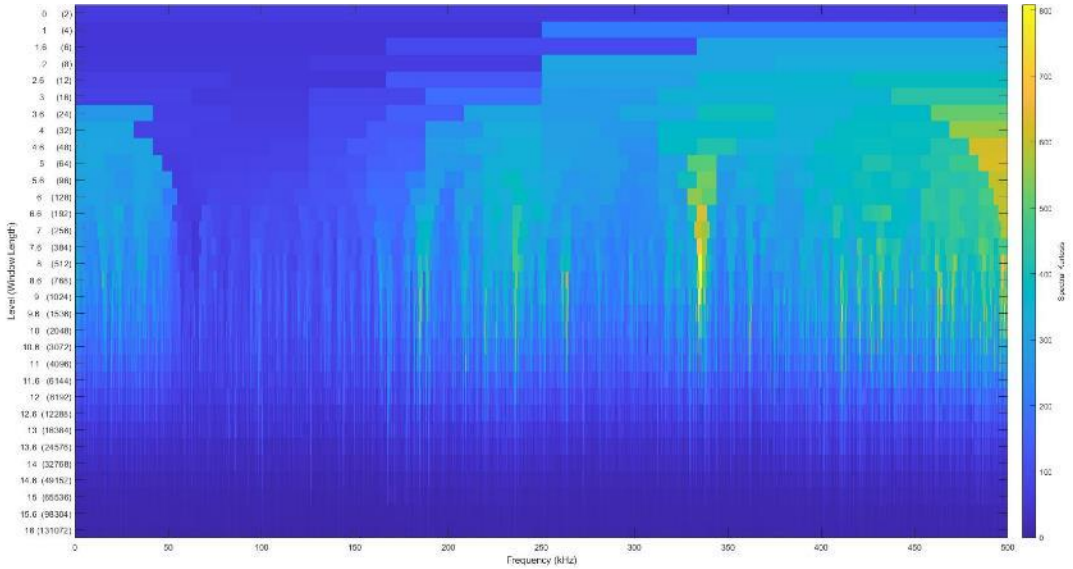

Figure 6-19: Kurtogram of sample with 1 MS/s sampling rate.

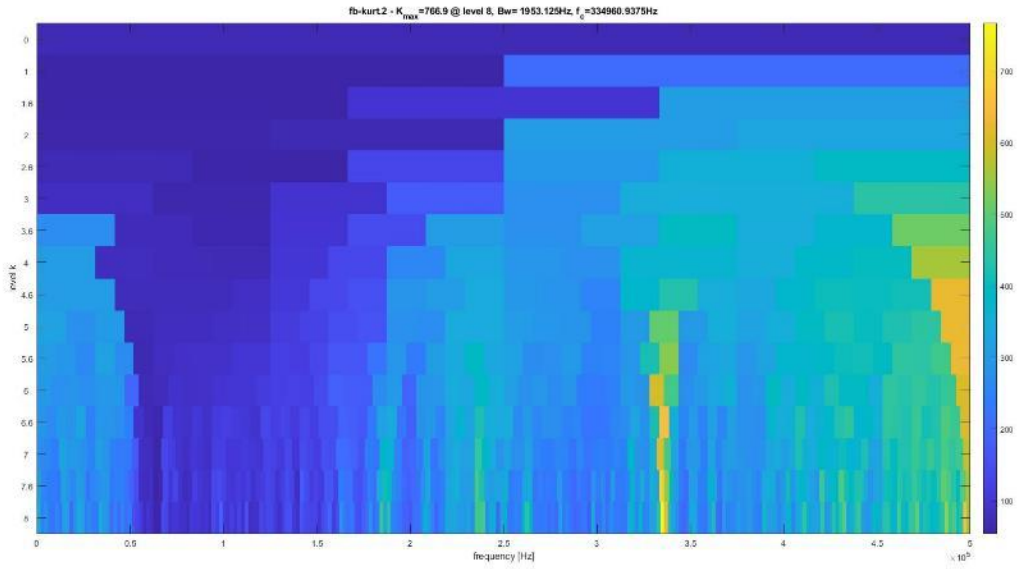

Figure 6-20: Fast Kurtogram of sample with 1 MS/s sampling rate.

An example of the analysis using Fast Kurtogram of AE data from the Bescot yard (sample 1) is presented in Figure 6-21. The signal was band-pass filtered at 414062 Hz with 15625 Hz Bw based on highest kurtosis. The filtered signal in red colour compared with the original signal in blue colour as displayed in Figure 6-22.

Obviously, the filtered signal contains less noises than the original signal. The potential of using Kurtogram approach for de-nosing the AE data could be assessed by calculating the parameters related to magnitude of original signal and filtered signal. Kurtosis value and crest factor can help investigate how signal is improved by filtering process.

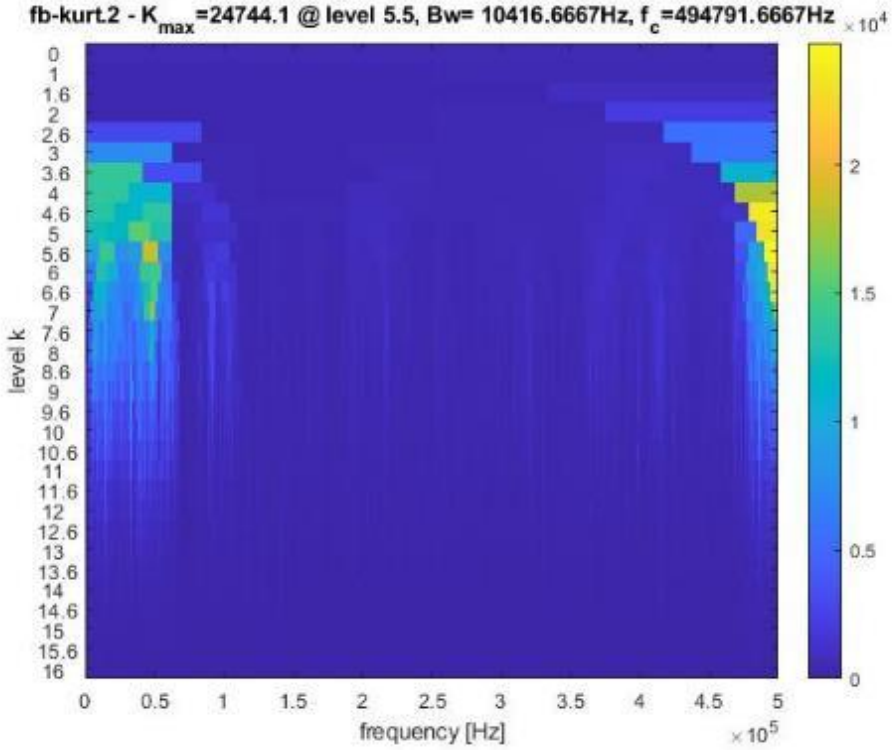

Figure 6-21: Kurtogram from AE data of sample 1 with 1 MS/s sampling rate.

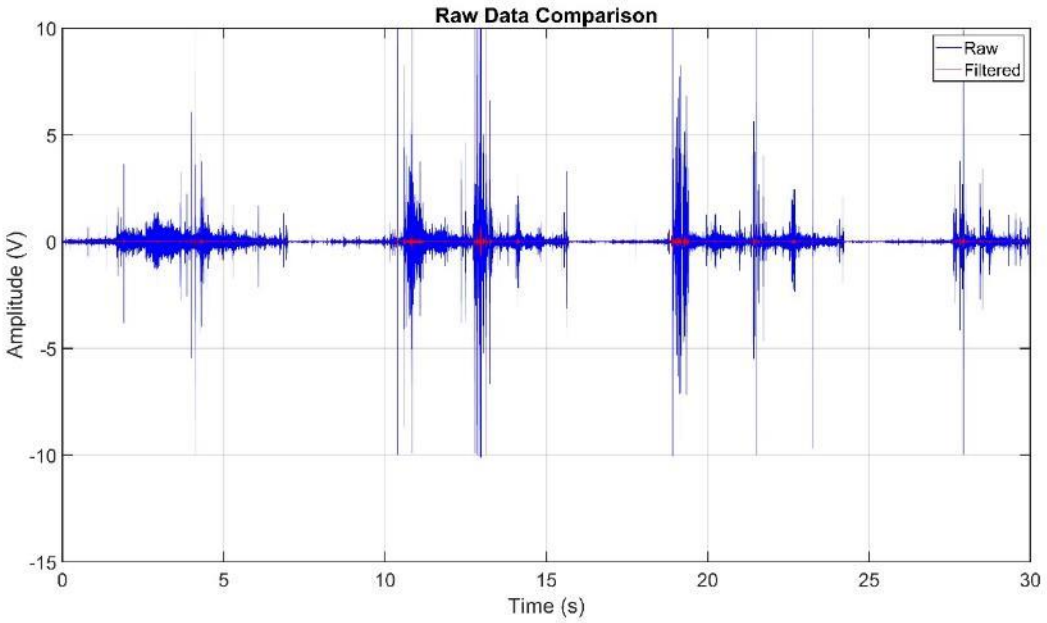

Figure 6-22: Raw data Filter vs unfiltered.

6.4.2 Cropredy

The results of field trials at the Cropredy site were collected in March 2019. Since the operational speed is over 120 km/h, recording time can be reduced to 8 seconds to minimise the output data size. The sampling rate was 500 kS/s.

The response of R50α is illustrated in Figure 6-23 as pulses generated by the impact test using pencil lead break. Each pulse is spaced equally in time domain different. FFT analysis of this test is displayed in Figure 6-24. There are 4 main resonances which related to AE sensor including 53 kHz, 162 kHz, 193 kHz, 198 kHz and 215 kHz.

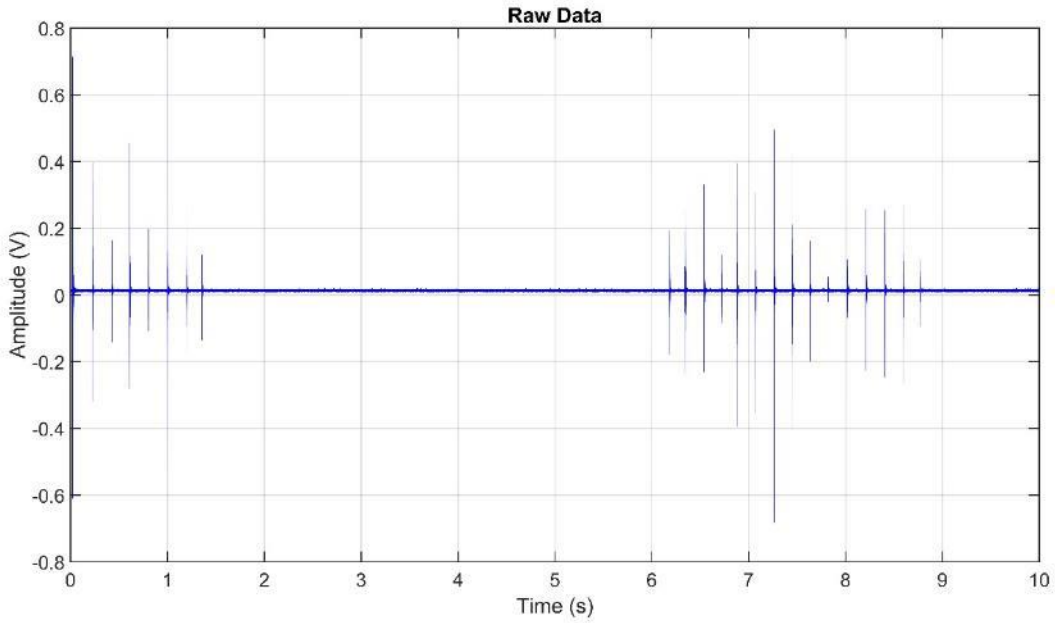

Figure 6-23: AE sensor testing.

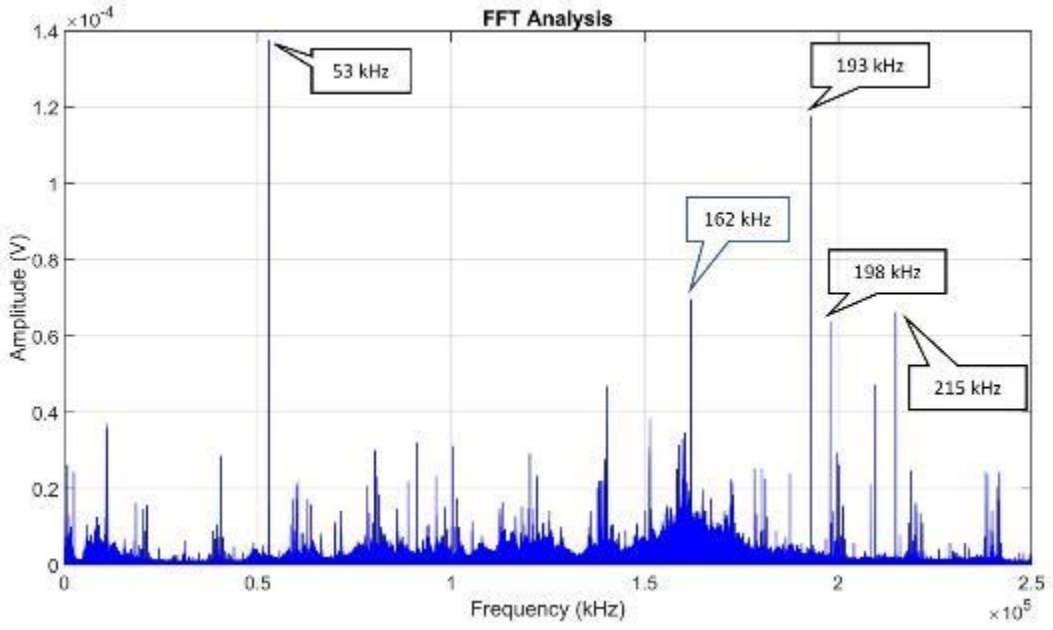

Figure 6-24: FFT analysis of AE sensor testing.

Figure 6-25 shows the first 3 seconds of the signal presents the passenger train passage. Raw data might show peaks related to the location of each wheelset. On the other hand, moving RMS data was retrieved in Figure 6-26. Peaks with low amplitude can present the wheelset

condition. In order to locate each bogie and carriage, the moving RMS allows for a good vision of the rolling stock. Low-amplitude peaks from each axle indicate the gained energy. Therefore, this trainset's wheelset contains no defects.

Considering the raw data, there are several parameters related to the output signal as shown in Figure 6-25, which can generate lots of information including the dynamics of the rolling stock, the power transmitted to any powered wheelset, and the load imbalance on the wheelset. However, these data are normally hidden in the time domain and require further analysis to reveal. In that case, FFT and spectral envelope analysis together with proper signal filtering could help uncover those hidden details in the output signals.

Measurements on passenger trains and freight trains rely on different operating conditions, especially the train's length and the traction systems. Since the freight trains always use the locomotive as a powered car at the front, the passage of the signal could display the engine signal at the very first seconds of the record. In this experiment condition, passenger fleets passing the Cropredy site are diesel multiple units (DMUs) which each car is powered by its own engine installed underneath the body.

Different train lengths effect the duration of the recording for the whole passage of the trainset. Moreover, different fleet type will not generate matched maximum amplitude in the data. The varying weights and traction systems of each fleet type is responsible for this.

Parameters related to train preferences are required for the design of the appropriate threshold for AE and vibration measurements. The trains' speed can be obtained via the sensor installed on the trackside.

Figure 6-26 shows the raw data analysis using Moving RMS to identify the whole train passage. In this case, there are 3 cars within EMU fleet of passenger train service. Each bogie can generate peak on time domain which can help identify the location within the data for further

analysis. Moreover, FFT analysis is also displayed in Figure 6-27 and confirm that there are no significant peaks apart from AE sensor's resonances.

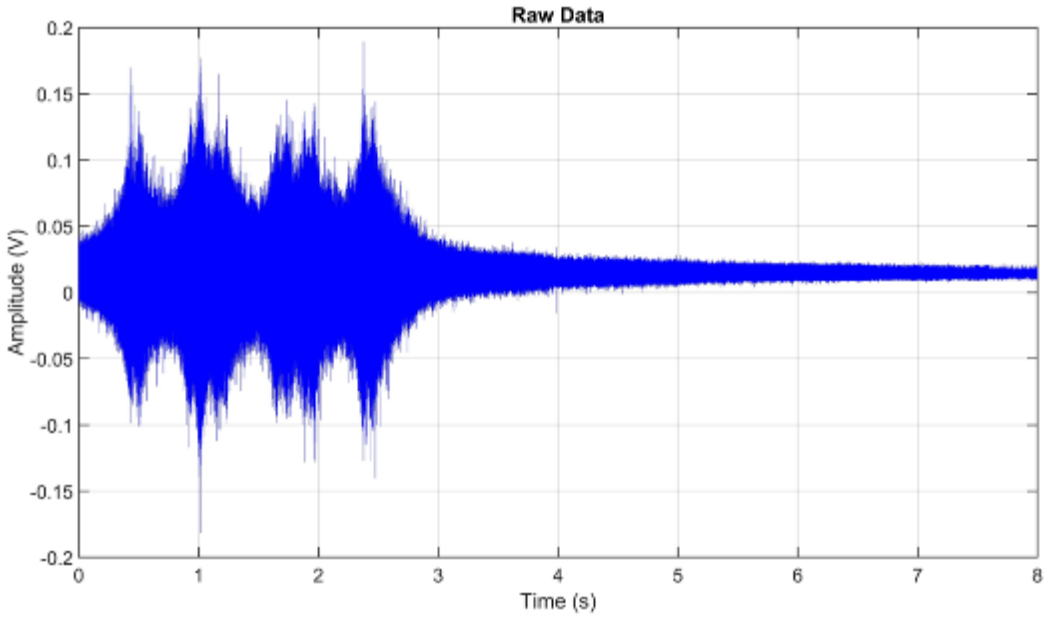

Figure 6-25: Raw signal from a passenger train.

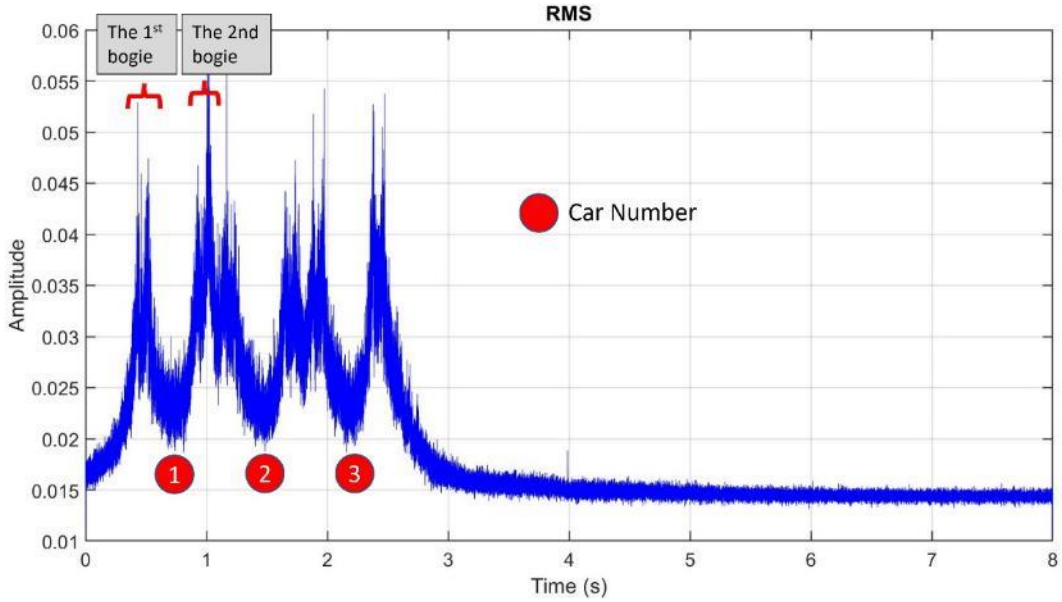

Figure 6-26: Moving RMS signal from a passenger train.

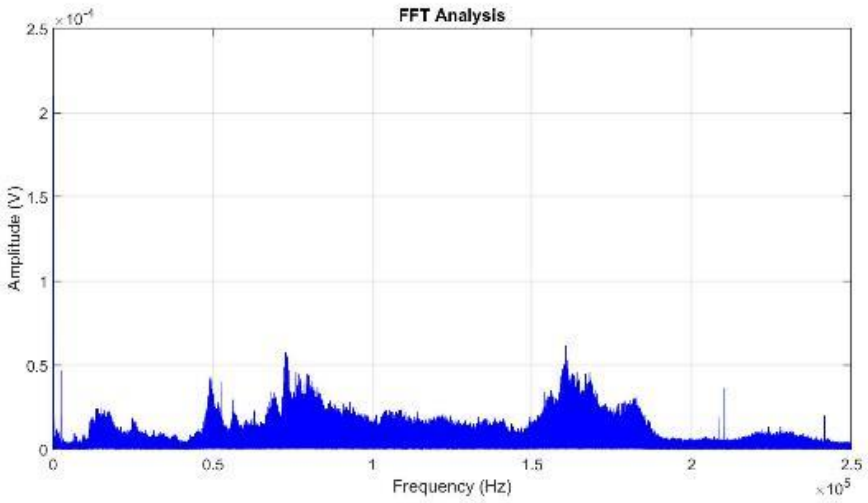

Figure 6-27: FFT Analysis of a signal from a passenger train.

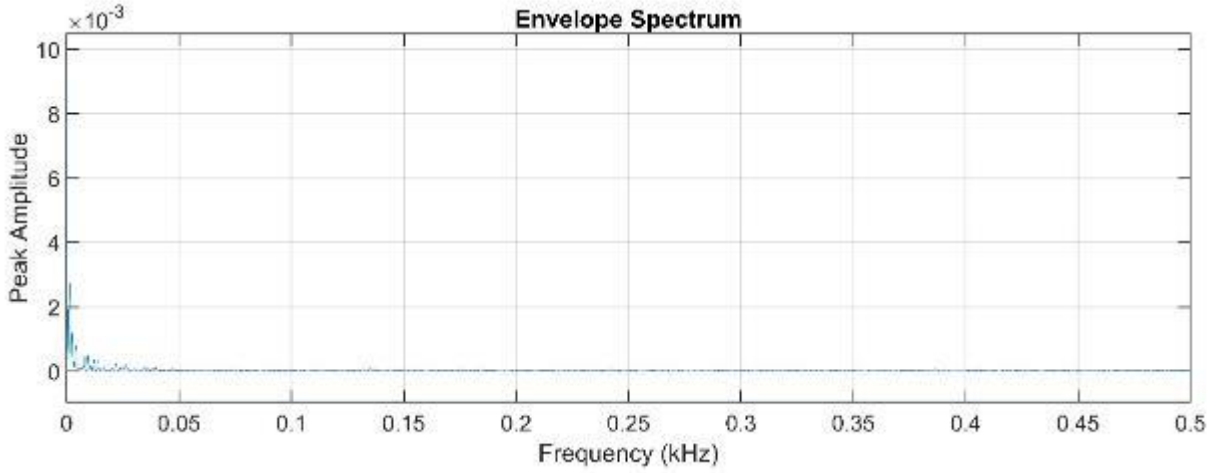

Figure 6-28: Spectral envelope analysis of a signal from a passenger train.

The same data was further analysed by spectral envelope analysis. The result is shown in Figure 6-28. Obviously, there are no harmonics observed on the frequency domain. Therefore, wheelset failures are not detected in the data from the passenger train on the mainline.

6.4.3 Long Marston

Onboard and wayside measurements were held in Long Marston test track. Roller defects in the axle bearing with different defect sizes and lubrication contamination were included as interested parameters. All details related to the filed experiments were described in chapter 6.3.

6.4.3.1 Onboard measurement for axle bearing defects

Vibration and AE measurements were carried out onboard the axle bearing of the wagon tanker as shown in section 6.3. The result of vibration analysis compared between the healthy and damaged bearing with 2mm defect is presented in Figure 6-29. Figure 6-30 shows the result of the same comparison with the AE. Despite the lower amplitude on damaged bearing, the impact on 2mm roller defect can be identified.

Figure 6-31 and Figure 6-32 illustrate the spectral envelope analysis comparing a healthy bearing to one with a 2mm roller flaw respectively. However, the fundamental frequency and its harmonics were not discovered in 2mm roller defect.

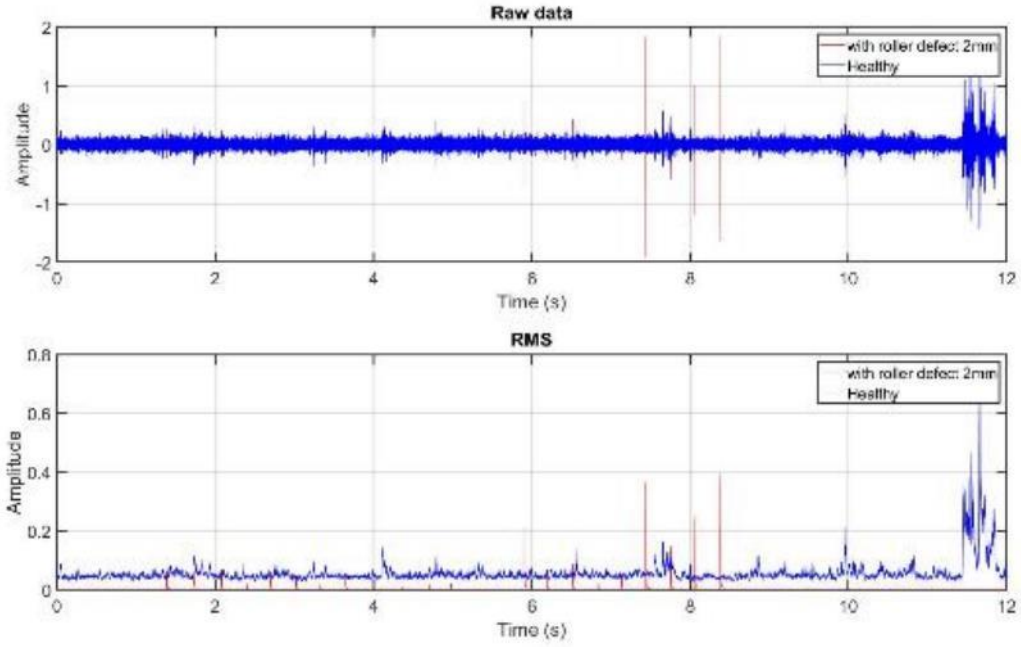

Figure 6-29: Raw data and moving RMS of vibration signal in comparison between healthy bearing and with roller defect 2mm using onboard measurement.

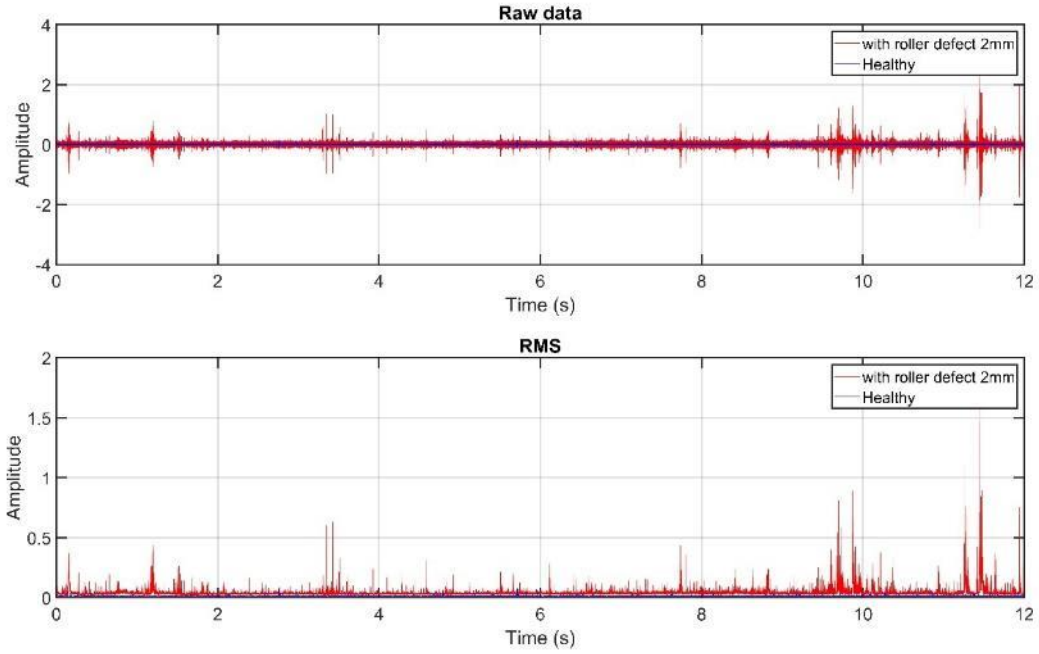

Figure 6-30: Raw data and moving RMS of AE signal in comparison between healthy bearing and with roller defect 2mm using onboard measurement.

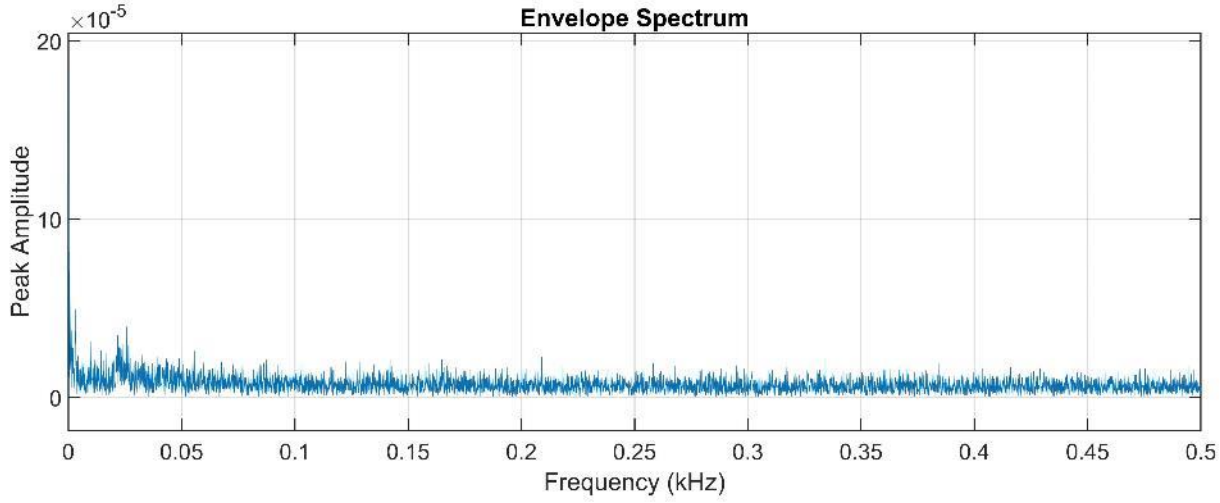

Figure 6-31: Spectral envelope analysis of AE signal from healthy bearing using onboard measurement.

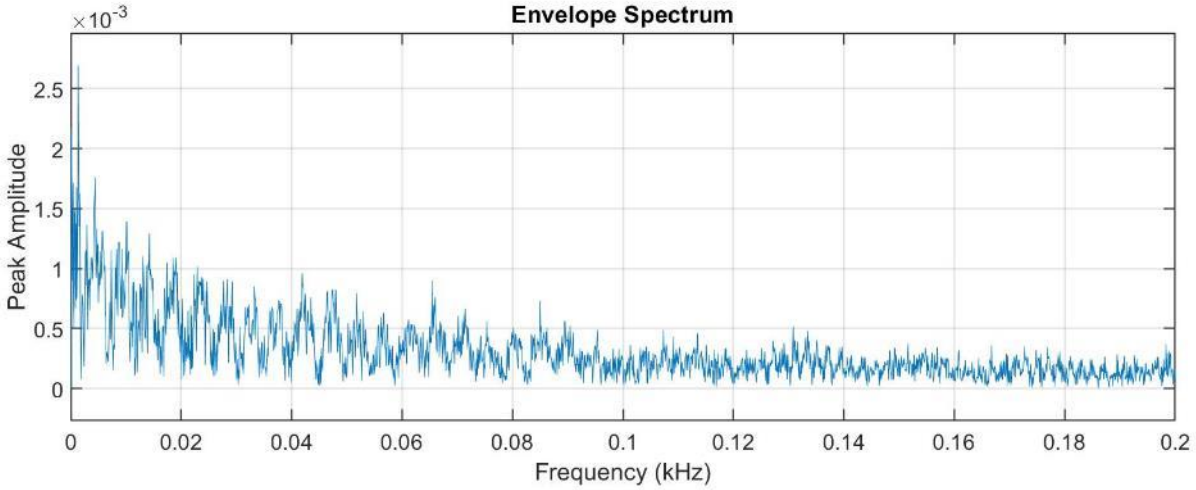

Figure 6-32: Spectral envelope analysis of AE signal from bearing with 2mm roller defect using onboard measurement.

Raw data of bearing with 8mm roller defect is shown in Figure 6-33. The higher amplitude on time domain is more significant when compare with the data from 2mm defect size. In addition, the comparison of raw data between healthy bearing and with roller defect 8mm is shown in Figure 6-34. Spectral envelope analysis of bearing with roller defect 8mm reveal harmonics but not related to fundamental frequency, as shown in Figure 6-35.

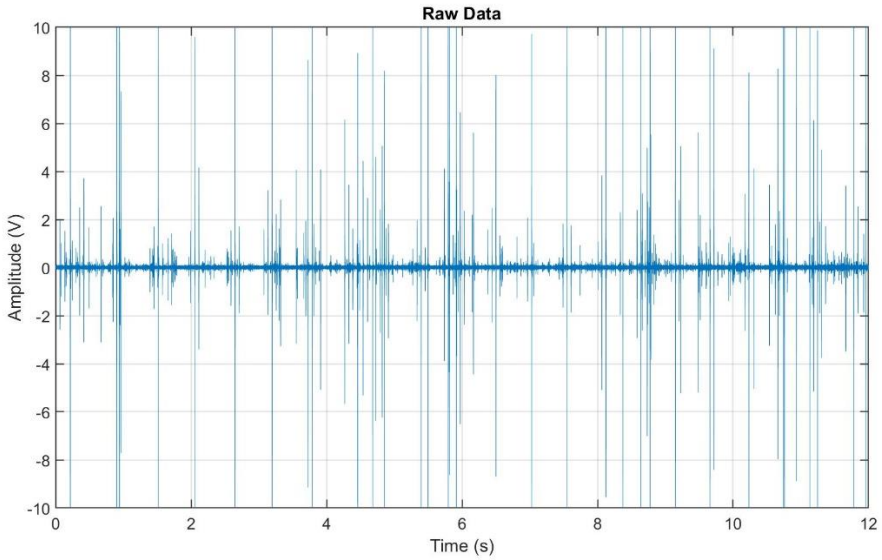

Figure 6-33 Raw data of bearing with 8mm roller defect.

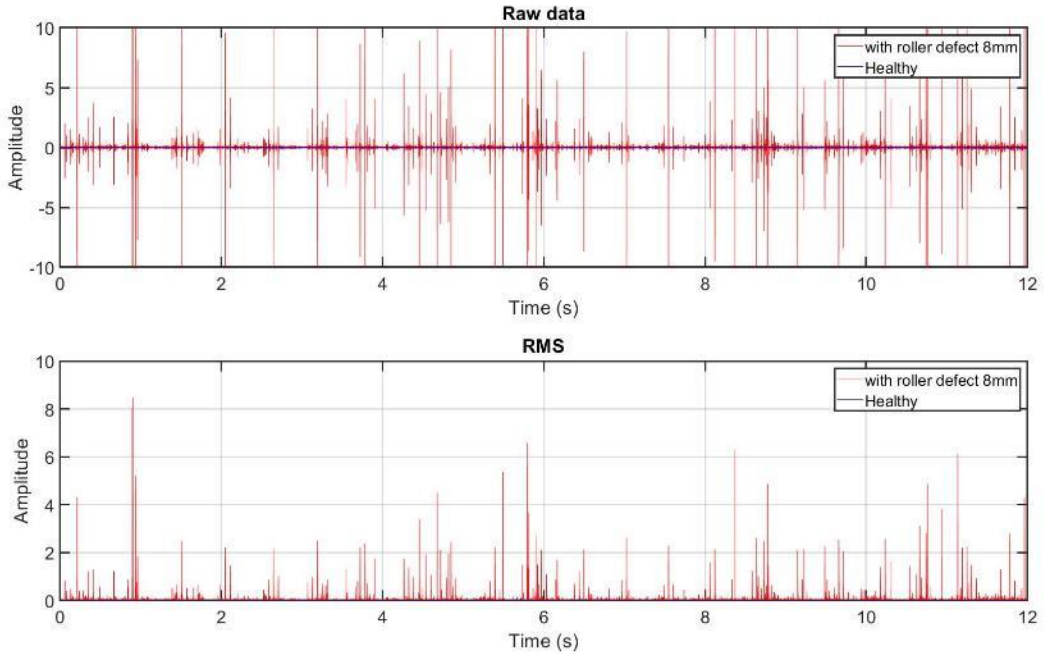

Figure 6-34: Raw data and moving RMS of AE signal in comparison between healthy bearing and with roller defect 8mm using onboard measurement.

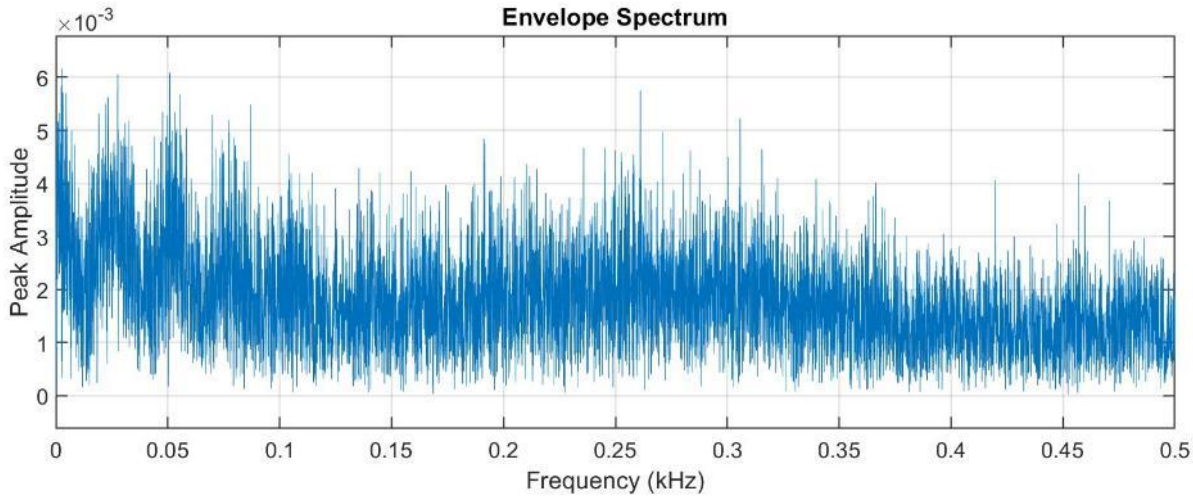

Figure 6-35: Spectral envelope analysis of AE signal from bearing with 8mm roller defect using onboard measurement.

Since the spectral envelope analysis cannot reveal correct fundamental frequency with its harmonics starting at around 17.6 Hz. The decomposition using EMD method as stated in

Chapter 4. Multiple IMFs and the residue were extracted from the original signal. The analysis discovered that the IMF 4 of bearing with 8mm roller defect as shown in Figure 6-36 can improve the defect detection over the original signal by providing the higher kurtosis value.

As a result, the spectral envelope analysis of IMF 4 in Figure 6-37 can reveal related harmonics to fundamental frequency of 17.6 Hz, 34.50 Hz, 51.42 Hz, 67.33 Hz, and 83.83 Hz.

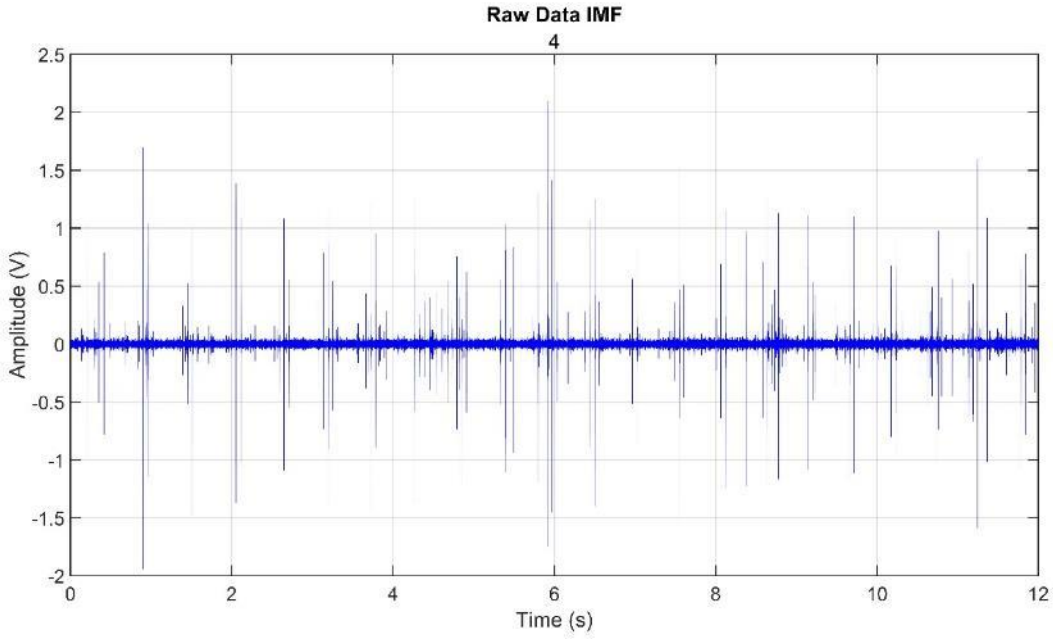

Figure 6-36: Raw data of bearing with 8mm roller defect (IMF 4).

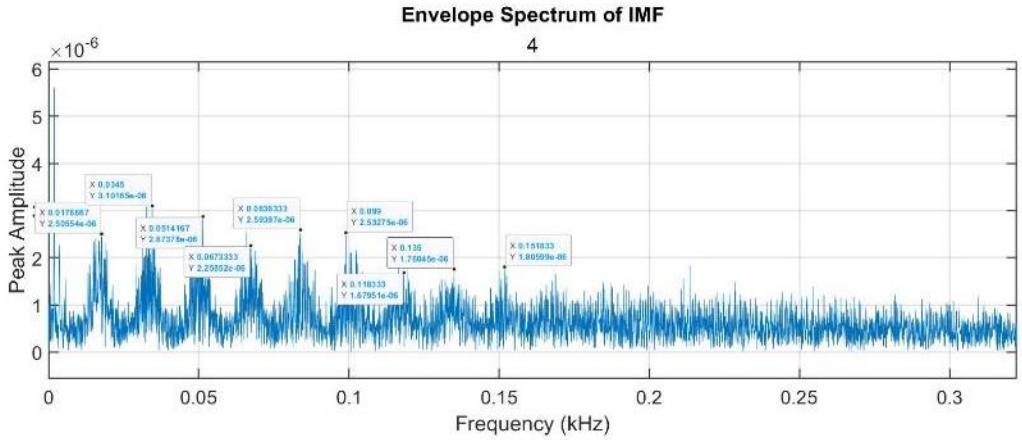

Figure 6-37 Spectral envelope analysis of 8 mm roller defect.

6.4.3.2 Wayside measurement

Wayside measurement demonstrates the use of RCM in the actual railway network, which contains noises from the environment. As refer to the field trials in Long Marston test track, the engine noise generates the highest amplitude in the retrieved data. The result obtained from the trackside compared the healthy bearing with the damaged bearing (2mm roller defect) using AE and vibration techniques are shown in Figure 6-38 and Figure 6-39 respectively.

AE measurement can reveal higher amplitude of acoustic waves while the rolling stock passing above the sensor. However, vibration technique is not appropriate for wayside measurements of roller bearing defect since both healthy and damaged raw data cannot indicate the different among each other.

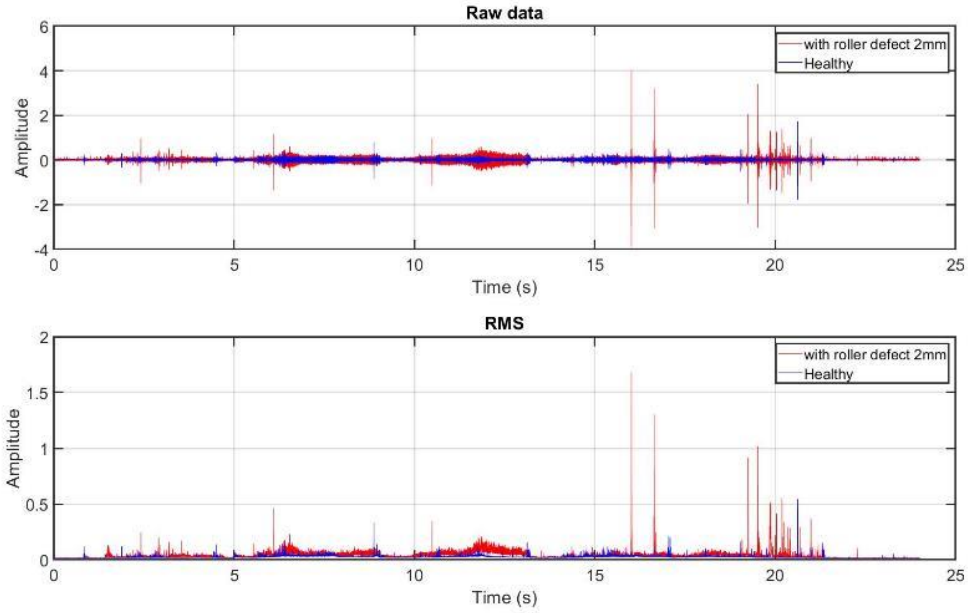

Figure 6-38: Raw data and moving RMS of AE signal in comparison between healthy bearing and with roller defect 2mm using wayside measurement.

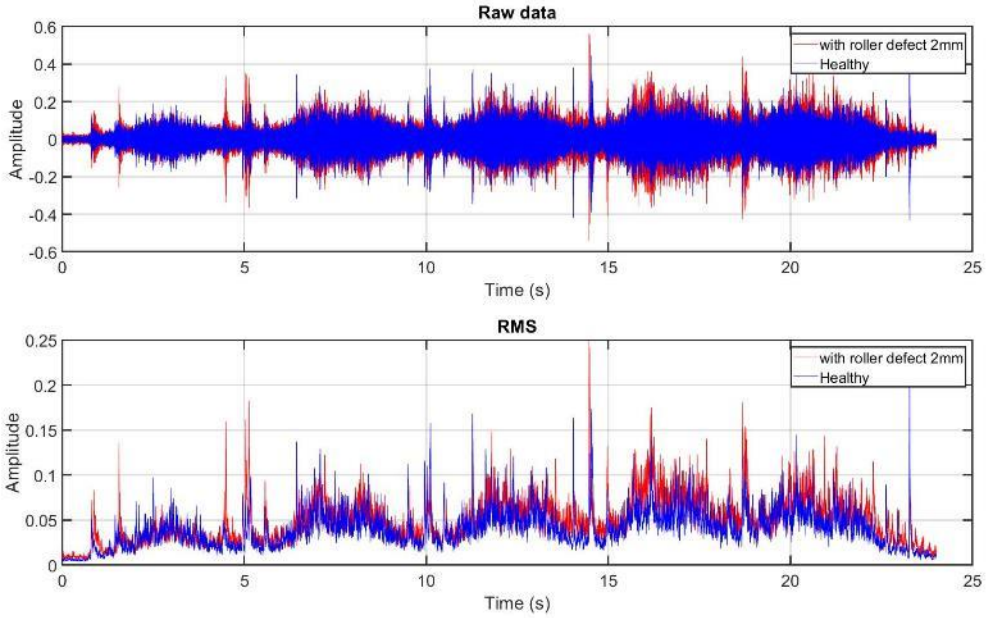

Figure 6-39: Raw data and moving RMS of vibration signal in comparison between healthy bearing and with roller defect 2mm using wayside measurement.

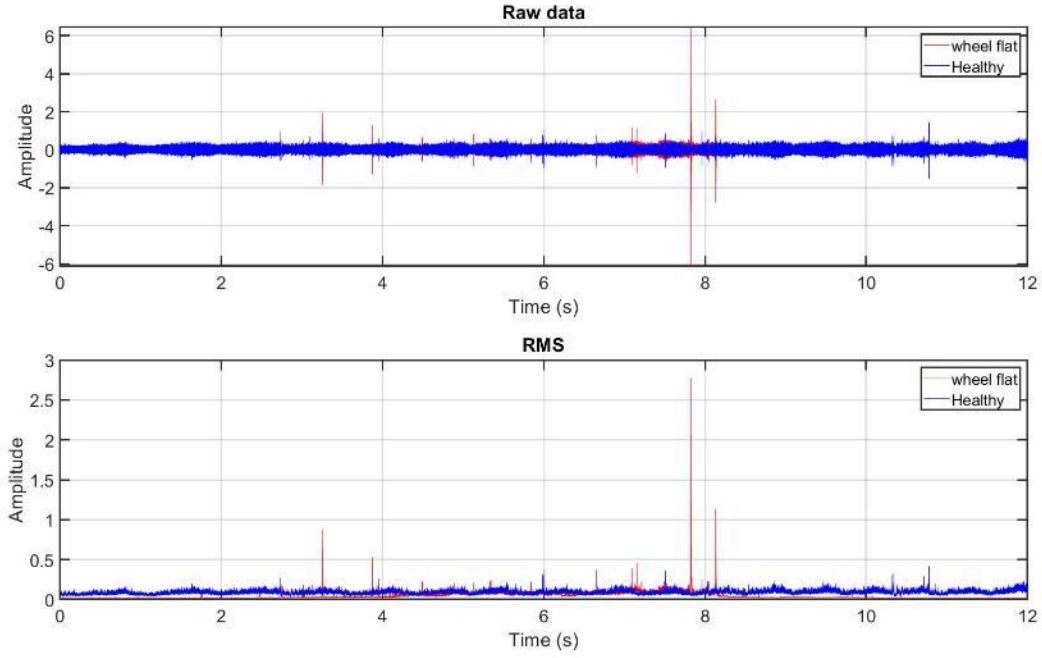

Figure 6-40: Raw data and moving RMS of AE signal in comparison between healthy wheelset and with the wheel flat using wayside measurement.

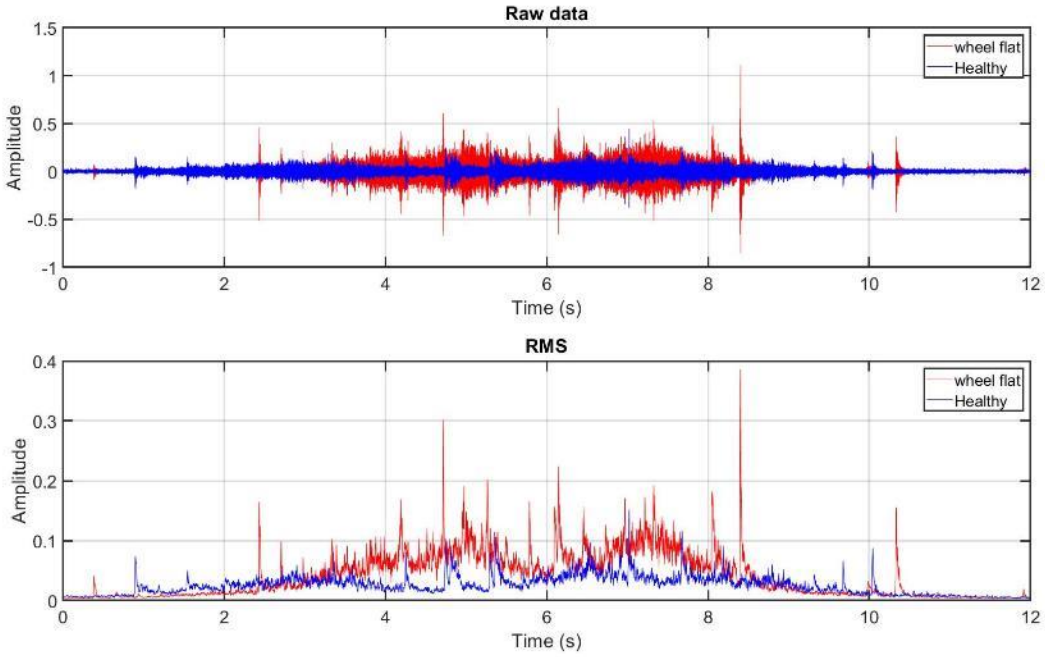

Figure 6-41: Raw data and moving RMS of vibration signal in comparison between healthy wheelset and with the wheel flat using wayside measurement.

The wheel flat monitoring must be held on the trackside as the normal RCM works. The raw data of AE and vibration techniques on the wheel flat monitoring are shown in Figure 6-40 and Figure 6-41 respectively.

The result indicates that vibration technique can overcome the advance AE measurement on the ability to reveal the difference on time domain analysis.

6.4.3.3 Onboard measurement of lubrication bearing defect

Another bearing failure which was generated by the contamination of the lubricant with water and sand provided the evaluation of AE and vibration measurement through different defects. Onboard measurements were carried out to reveal the signals retrieved from the axle bearing lubricant contamination.

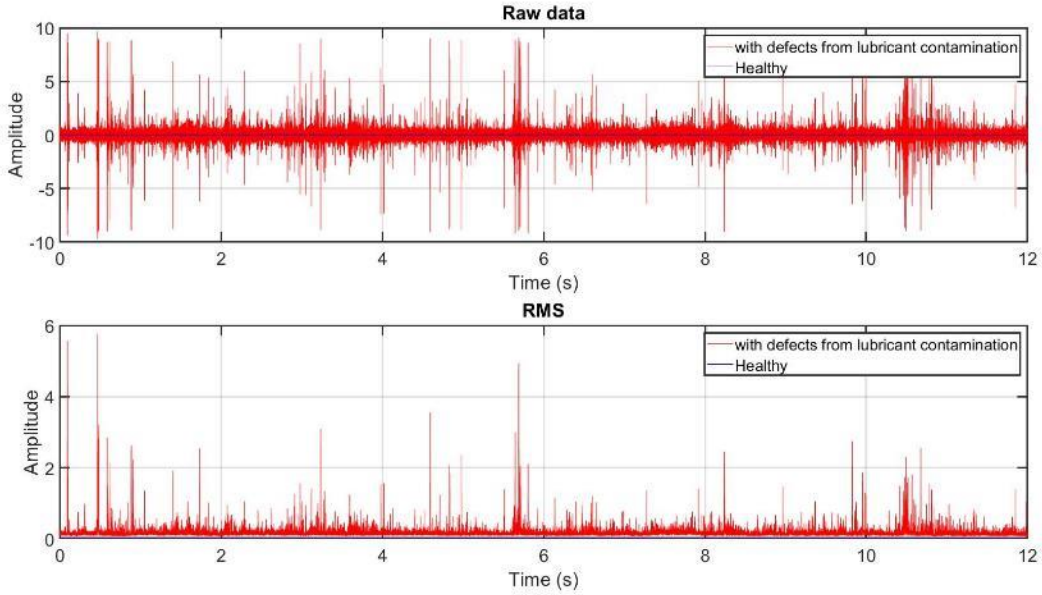

Figure 6-42: AE measurement of lubricant-contaminated and healthy bearings.

Figure 6-42 shows a comparison between the bearing with lubricant contamination and healthy condition. Both raw data and RMS of AE data can reveal the marginal different between damaged and healthy bearing.

However, FFT analysis was also carried out to investigate the lubrication fault on frequency domain as shown in Figure 6-43.

Lubrication won't make any harmonics since the damage is very severe and the raw data could literally make the detection of defects.

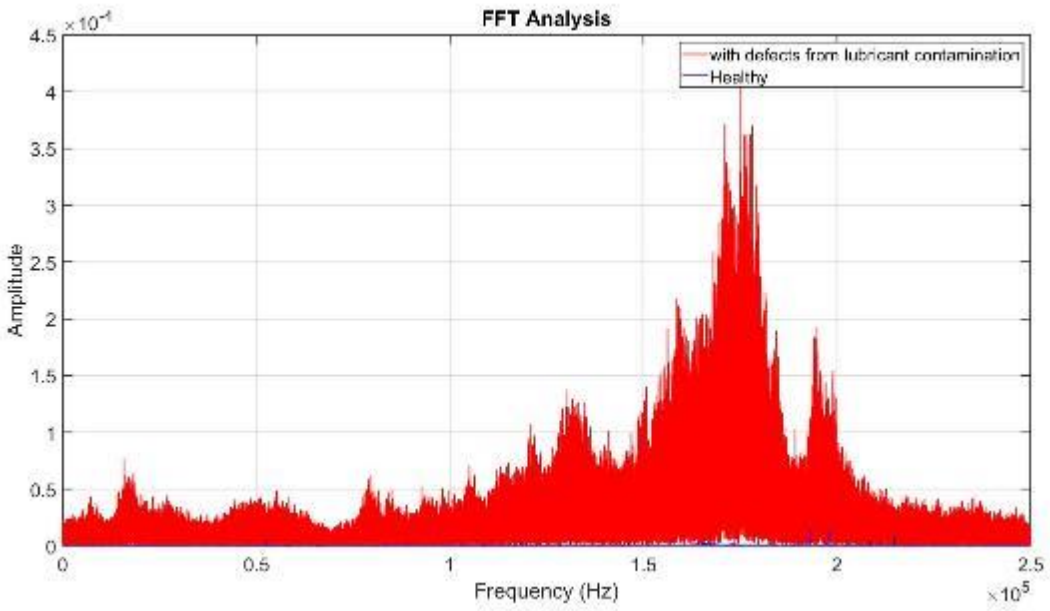

Figure 6-43: FFT analysis of the measurement of lubricant-contaminated and healthy bearings.

When testing for axle bearing lubricant contamination, the signals detected have a different form compared with the testing for roller or race defects. The main difference of output signal between roller defects and the bad lubrication is the signal peaks. While roller defects generally reveal peaks related to bearing revolution, metal interactions between sand and water with the bearing cause random peaks in both AE and vibration signals for lubrication defects.

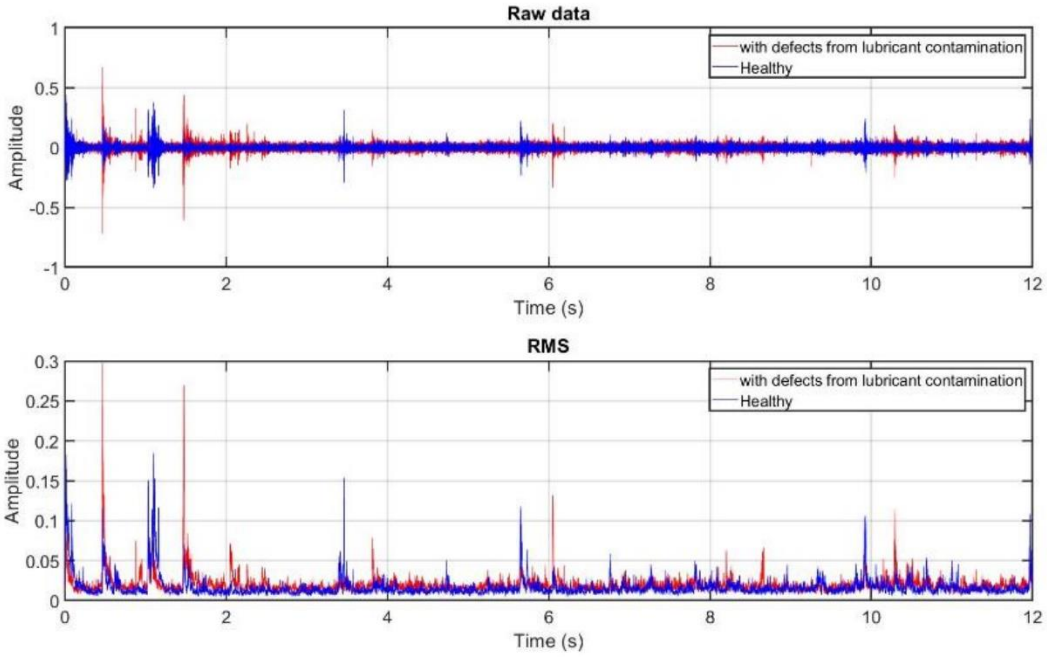

Figure 6-44: Vibration measurement of the measurement of lubricant-contaminated and healthy bearings.

However, vibration technique is failed to distinguish between the two bearing conditions. Figure 6-44 shows only a minimal difference visible on the vibration data.

Moreover, the parameters including Kurtosis, crest factor and pk-pk values of AE data with lubrication contamination increase significantly over values from the healthy bearing, while those values of vibration data did not make a marginal gap between a healthy and a faulty bearing.

6.5 Summary

Several field experiments were conducted throughout the study. The demonstration of wayside measurement using the newly developed data acquisition application based on MATLAB works with an AE monitoring system was carried out at Bescot yard. Two AE sensors were placed on the straight track section. The output data revealed no signs that could indicate the fault of the wheelset. Frequency domain analysis has been used to improve signal interpretation

as it may help identify the behaviour of each component. Moreover, A band-pass filter using a kurtogram would remove the excessive vibration signals from the environment and unwanted sources. As a result, the filtered signal with a higher signal-to-noise ratio contains less noise than the original signal.

Another field experiment was conducted at the Cropredy site on the actual operating railway line. The moving RMS has been used to find the location of each bogie and carriage. FFT, spectral envelope analysis, and proper signal filtering could help uncover hidden details in the output signals. FFT analysis can confirm no significant peaks apart from the AE sensor's resonances. Therefore, wheelset failures are not detected in the data from the passenger train on the mainline.

Long Marston test track was the main site for onboard and wayside measurements with different stimulated defects on the wheelset. Roller defects in the axle bearing with different defect sizes and lubrication contamination were included as interesting parameters. The analysis of AE onboard measurement using spectral envelope analysis and the decomposition using EMD effectively revealed 2mm and 8mm roller defects according to bearing fundamental frequency. Unfortunately, vibration data from the same experiment had no amplitude modulation, which failed to reveal the defects.

Wayside measurements were carried out to demonstrate the use of RCM in the existing railway network, which contains environmental noises and a damaged bearing with a 2mm roller defect. AE measurement can reveal a higher amplitude of acoustic waves while the rolling stock passes above the sensor. Results from the wayside setup confirmed that AE measurement effectively revealed the roller defect of the wheelset bearing while vibration measurement failed to. In contrast, vibration measurement has the capability of wheel flat detection.

Lastly, AE and vibration were evaluated to detect lubricant-contaminated bearings based on the onboard measurement. Raw data and RMS of AE measurement revealed the difference between damaged and healthy bearings. Metal interactions between sand and water with the bearing cause random peaks in AE and vibration signals for lubrication defects. However, the vibration technique failed to distinguish between the two bearing conditions.

Chapter 7: Conclusions and Recommendations for future work

7.1 Conclusions

As global demand for rail transport overgrows with increasing operational speed, the downtime of railway operations is more limited. Rolling stock inspection and maintenance is crucial for persons' and products' safety. There is an excellent opportunity for remote CM to participate in advanced and minimised inspection and maintenance campaigns. Current infrastructure and rolling stock management must be controlled by updated innovations that allow operational RAMS. Consequently, the railway systems are needed to work with an effective RCM and related tools to ensure the highest level of safety for both rail infrastructure and rolling stock.

Fundamental knowledge of wheelset defect detection has been studied through laboratory and field experiments that have presented a practical, reliable, compact, and economical approach to identifying faults in rolling stock wheelsets. Defects in axle bearings effectively increase the peaks in the raw data and generate amplitude modulation. AE and vibration data require further signal analysis since the raw data is inefficient for defect detection. The kurtosis filtering technique was carried out to improve the signal-to-noise ratio over the study.

A laboratory experiment using the Amsler machine proves that the capability of using spectral envelope analysis can reveal fault-related harmonics. Reduced scaled wheel trolley test also demonstrates a wayside measurement setup. The output signal contained less background noise indicating artificial defect detection. As a result, moving RMS accurately identified high-peak data signals. Bearing test rig experiment also proves that raw data is impossible for the complicated signals from rotating machines. AE and vibration signals were evaluated through further signal analysis to provide damage severity detection. Accordingly, AE revealed an amplitude difference between 10% and 50% damage.

Moreover, the kurtosis value of AE data with 50% damage is significantly higher than another with 10% damage. Kurtogram determines band-pass filter core frequency and bandwidth. Unfiltered signals' envelope analysis has more noise. Fast Kurtogram lowered computation time without affecting signal quality. Cepstral analysis calculates power spectrum inverse Fourier transform. Vibration analysis' cepstral study finds the bearing defect's harmonics. Larger roller fault bearings generate better outcomes.

A field experiment at Bescot yard confirmed the possibility of using an advanced yet compact CM module using a newly developed application that works with AE measurement. Two AE sensors were installed on each side of the rails, providing the raw data indicating the presence of the locomotive and wagon. The trial confirms the lack of ability to reveal helpful information on the frequency domain when using FFT. Thus, a band-pass filter removes excessive contents from the environment. As a result, Kurtugram proves it can be utilised for de-nosing the AE data.

Another experiment at the Cropredy site confirmed that wayside measurement using AE sensors on the railway track is possible. The raw data has been processed using FFT analysis. It can ensure that there is no indication of wheelset damage.

The last field experiment was conducted at the Long Marston test track, providing sufficient facilities for evaluating AE and vibration measurements. Onboard measurement for axle bearing defects compares AE and vibration measurements. The result claimed that with the help of EMD analysis, AE could reveal roller defects of bearing with different sizes. Unfortunately, vibration failed to complete the same purpose since there was no amplitude modulation. However, the wayside measurement based on vibration signal provided wheel flat detection. AE can overcome vibration on roller defect detection. Finally, the onboard measurement of lubrication bearing defect has been evaluated between AE and vibration. The

result from vibration data could not provide the difference between healthy and damaged conditions.

Onboard and wayside CM systems were also studied. Utilising AE and vibration techniques in rolling stock wheelset CM, together with creating signal processing procedures, revealed information from AE and vibration data. The results of AE and vibration techniques are summarised below:

- Acoustic emission and vibration analysis can effectively monitor railway wheelsets' online CM. However, both did a different range of detection. Therefore, one cannot replace another.
- AE can detect frequency-sensitive components, i.e. crack propagation, because this happens on high frequency while vibration has operational performance at a lower frequency.
- The installation can be carried out rapidly and is non-intrusive since magnets and Araldite are used to fix the sensors on the rail
- The equipment cost is low, and therefore, multiple sites can be readily instrumented
- No particular line intervention is required

The acquired results from laboratory and field tests have indicated that the approach developed within this study can be applied to advance and effective RCM of rolling stock wheelset defects. Axle bearing and wheel defects were effectively captured by the selected technique, which depends on operational circumstances. Therefore, applying AE and vibration techniques can help each other to provide reliable diagnoses of wheelset failures.

7.2 Recommendations for future work

The utilisation of the decomposition method, including the wavelet and empirical mode decomposition based on multiple sensors, including AE and accelerometers, needs to be further evaluated with field tests on the existing railway network in Thailand. There are still a lot of available scenarios on the field test that would improve the performance of onboard and wayside RCM systems from the advanced hardware of the small but mighty DAQ unit. The compact size and small energy consumption would make any test possible.

Moreover, supervised machine learning for damage severity of time-series data would also help identify bearing damages using AE and vibration techniques. The input of such a system could be a time sequence including Recurrent Neural Network, long short-term memory, and Gated Recurrent Units. The insufficient data volume should be mitigated by using available data augmentation techniques.

References

Abernethy, R. B., Benedict, R. P., & Dowdell, R. B. (1985). *ASME measurement uncertainty*.

Adams, R. D., Cawley, P., Pye, C. J., & Stone, B. J. (1978). A vibration technique for non-destructively assessing the integrity of structures. *Journal of Mechanical Engineering Science*, *20*(2), 93–100.

Alatefi, M., Ahmad, S., & Alkahtani, M. (2019). Performance evaluation using multivariate non-normal process capability. *Processes*, *7*(11), 833.

Al-Dossary, S., Hamzah, R. I. R., & Mba, D. (2009). Observations of changes in acoustic emission waveform for varying seeded defect sizes in a rolling element bearing. *Applied Acoustics*, *70*(1), 58–81.

Al-Dossary, S., Raja Hamzah, R. I., & Mba, D. (2006). Acoustic emission waveform changes for varying seeded defect sizes. *Advanced Materials Research*, *13*, 427–432.

Alegranzi, S. B., Gonçalves, J. F., & Gomes, H. M. (2012). Ball bearing vibration monitoring for fault detection by the envelope technique. *Proceedings of the 10th World Congress on Computer Mechanics, São Paulo, Brazil*, 8–13.

Al-Ghamd, A. M., & Mba, D. (2006). A comparative experimental study on the use of acoustic emission and vibration analysis for bearing defect identification and estimation of defect size. *Mechanical Systems and Signal Processing*, *20*(7), 1537–1571.

Al-Ghamdi, A. M., Zhechkov, D., & Mba, D. (2004). The use of Acoustic Emission for bearing defect identification and estimation of defect size. *The 26th European Conference on Acoustic Emission Testing, EWGAE, Sep*, 15–17.

Amini, A. (2016a). *Online condition monitoring of railway wheelsets*. University of Birmingham.

Amini, A. (2016b). *Online condition monitoring of railway wheelsets*. University of Birmingham.

Amini, A., Entezami, M., Huang, Z., Rowshandel, H., & Papaelias, M. (2016). Wayside detection of faults in railway axle bearings using time spectral kurtosis analysis on high-frequency acoustic emission signals. *Advances in Mechanical Engineering*, *8*(11), 1687814016676000.

Amini, A., Entezami, M., & Papaelias, M. (2016a). Onboard detection of railway axle bearing defects using envelope analysis of high frequency acoustic emission signals. *Case Studies in Nondestructive Testing and Evaluation*, *6*, 8–16.

Amini, A., Entezami, M., & Papaelias, M. (2016b). Onboard detection of railway axle bearing defects using envelope analysis of high frequency acoustic emission signals. *Case Studies in Nondestructive Testing and Evaluation*, *6*, 8–16.

Amini, A., Huang, Z., Entezami, M., & Papaelias, M. (2017). Evaluation of the effect of speed and defect size on high-frequency acoustic emission and vibration condition monitoring of railway axle bearings. *Insight-Non-Destructive Testing and Condition Monitoring*, *59*(4), 184–188.

Amsted Rail. (2019, September). *BOGIES*. https://www.amstedrail.com/products/bogies/

Anastasopoulos, A., Bollas, K., Papasalouros, D., & Kourousis, D. (2010). Acoustic emission on-line inspection of rail wheels. *Proc. 29th Eur. Conf. Acoust. Emission Testing*, 1–8.

Anderson, D. R. (2006). Detecting flat wheels with a fiber-optic sensor. *Proceedings of the 2006 IEEE/ASME Joint Rail Conference*, 25–30.

Andréason, S. (1973). Load distribution in a taper roller bearing arrangement considering misalignment. *Tribology*, *6*(3), 84–92.

Antoni, J. (2006). The spectral kurtosis: a useful tool for characterising non-stationary signals. *Mechanical Systems and Signal Processing*, *20*(2), 282–307.

Antoni, J. (2007). Fast computation of the kurtogram for the detection of transient faults. *Mechanical Systems and Signal Processing*, *21*(1), 108–124.

Antoni, J., & Randall, R. B. (2006). The spectral kurtosis: application to the vibratory surveillance and diagnostics of rotating machines. *Mechanical Systems and Signal Processing*, *20*(2), 308–331.

Australian Transport Safety Bureau. (2016). *Derailment of freight train MB520*. www.atsb.gov.au

Azovtsev, A., & Barkov, A. (1970). Automatic computer systems for roller bearings diagnostics. *WIT Transactions on The Built Environment*, *21*.

Baasch, B., Heusel, J., Roth, M., & Neumann, T. (2021). Train wheel condition monitoring via cepstral analysis of axle box accelerations. *Applied Sciences*, *11*(4), 1432.

Barkan, C. P., Dick, C. T., & Anderson, R. (2003). Railroad Derailment Factors Affecting Hazardous Materials Transportation Risk. *Transportation Reasearch Record*, *1825*(1), 64–74.

Barke, D., & Chiu, W. K. (2005a). Structural health monitoring in the railway industry: a review. *Structural Health Monitoring*, *4*(1), 81–93.

Barke, D., & Chiu, W. K. (2005b). Structural health monitoring in the railway industry: a review. *Structural Health Monitoring*, *4*(1), 81–93.

Beattie, A. (1997). Acoustic emission monitoring of a wind turbine blade during a fatigue test. *35th Aerospace Sciences Meeting and Exhibit*, 958.

Belotti, V., Crenna, F., Michelini, R. C., & Rossi, G. B. (2003). Wavelet signal processing applied to railway wheelflat detection. *Proc. XVII IMEKO World Congress Metrology in the Third Millennium, Dubrovnik, Croatia*, 22–27.

Belotti, V., Crenna, F., Michelini, R. C., & Rossi, G. B. (2006). Wheel-flat diagnostic tool via wavelet transform. *Mechanical Systems and Signal Processing*, *20*(8), 1953–1966.

Bendjama, H., Bouhouche, S., & Boucherit, M. S. (2012). Application of wavelet transform for fault diagnosis in rotating machinery. *International Journal of Machine Learning and Computing*, *2*(1), 82–87.

Bernal, E., Spiryagin, M., & Cole, C. (2018). Onboard condition monitoring sensors, systems and techniques for freight railway vehicles: a review. *IEEE Sensors Journal*, *19*(1), 4–24.

Bladon, K., Rennison, D., Izbinsky, G., Tracy, R., & Bladon, T. (2004). Predictive condition monitoring of railway rolling stock. In *CORE 2004: New Horizons for Rail* (pp. 21–22). Railway Technical Society of Australasia Darwin, NT.

Bollas, K., Papasalouros, D., Kourousis, D., & Anastasopoulos, A. (2013). Acoustic emission monitoring of wheel sets on moving trains. *Construction and Building Materials*, *48*, 1266–1272.

Bondarenko, V. v, Skurikhin, D. I., Vizniak, R. I., Ravlyuk, V. H., & Skurikhin, V. I. (2019). EXPERIMENTAL STUDY OF THE METHOD AND DEVICE FOR WHEEL-SETS ACOUSTIC MONITORING OF RAILWAY CARS IN MOTION. *Scientific Bulletin of National Mining University*, *4*.

Bonnardot, F., Randall, R. B., Antoni, J., & Guillet, F. (2004). Enhanced unsupervised noise cancellation using angular resampling for planetary bearing fault diagnosis. *International Journal of Acoustics and Vibration*, *9*(2), 51–60.

Bracciali, A. (2016a). Railway Wheelsets: History, Research and Developments. *International Journal of Railway Technology*, *5*, 23–52. https://doi.org/10.4203/ijrt.5.1.2

Bracciali, A. (2016b). Railway Wheelsets: History, Research and Developments. *International Journal of Railway Technology*, *5*, 23–52. https://doi.org/10.4203/ijrt.5.1.2

British Standards Institution. (2020a). *Railway applications — Wheelsets and bogies — Wheelsets — Product requirements*.

British Standards Institution. (2020b). *Railway applications — Wheelsets and bogies — Wheelsets — Tread profile*. https://standards.iteh.ai/catalog/standards/sist/61a6a9e6-9c8a-4c53-9627-41c93f624c7d/sist-en-13715-2020

Brizuela, J., Fritsch, C., & Ibáñez, A. (2011a). Railway wheel-flat detection and measurement by ultrasound. *Transportation Research Part C: Emerging Technologies*, *19*(6), 975–984.

Brizuela, J., Fritsch, C., & Ibáñez, A. (2011b). Railway wheel-flat detection and measurement by ultrasound. *Transportation Research Part C: Emerging Technologies*, *19*(6), 975–984.

Brizuela, J., Ibañez, A., & Fritsch, C. (2009). Railway wheel tread inspection by ultrasonic techniques. *2009 IEEE International Ultrasonics Symposium*, 1–4.

Brizuela, J., Ibañez, A., & Fritsch, C. (2010). NDE system for railway wheel inspection in a standard FPGA. *Journal of Systems Architecture*, *56*(11), 616–622.

Brizuela, J., Ibañez, A., Nevado, P., & Fritsch, C. (2010). Railway wheels flat detector using Doppler effect. *Physics Procedia*, *3*(1), 811–817.

Brommundt, E. (1997). A simple mechanism for the polygonalization of railway wheels by wear. *Mechanics Research Communications*, *24*(4), 435–442.

Brundisch, V. (2018). *Axle Bearings and condition monitoring for railway vehicles*. Global Railway Review. https://www.globalrailwayreview.com/article/74369/axle-bearing-point-bombardier/

Catlin, J. B. (1983). The use of ultrasonic diagnostic technique to detect rolling element bearing defects. *Proceeding of Machinery and Vibration Monitoring and Analysis Meeting*, 123–130.

Cavuto, A., Martarelli, M., Pandarese, G., Revel, G. M., & Tomasini, E. P. (2016). Train wheel diagnostics by laser ultrasonics. *Measurement*, *80*, 99–107.

Cavuto, A., Martarelli, M., Pandarese, G., Revel, G. M., & Tomasini, E. P. (2018). Experimental investigation by Laser Ultrasonics for train wheelset flaw detection. *Journal of Physics: Conference Series*, *1149*(1), 012015.

Chang, W., Xu, H., Zhang, X., Xing, Y., Meng, W., Li, H., & Li, X. (2020). Impact of journal bending on the failure of axle bearings in railroad passenger cars. *Proceedings of the Institution of Mechanical Engineers, Part J: Journal of Engineering Tribology*, *234*(8), 1296–1309.

Chen, B., Yan, Z., & Chen, W. (2014). Defect detection for wheel-bearings with time-spectral kurtosis and entropy. *Entropy*, *16*(1), 607–626.

Chong, S. Y., Lee, J.-R., & Shin, H.-J. (2010). A review of health and operation monitoring technologies for trains. *Smart Structures and Systems*, *6*(9), 1079–1105.

Cline, J. E., Bilodeau, J. R., & Smith, R. L. (1998). Acoustic wayside identification of freight car roller bearing defects. *Proceedings of the 1998 ASME/IEEE Joint Railroad Conference*, 79–83.

Concari, C., Franceschini, G., & Tassoni, C. (2008). Differential diagnosis based on multivariable monitoring to assess induction machine rotor conditions. *IEEE Transactions on Industrial Electronics*, *55*(12), 4156–4166.

Cuanang, J., Tarawneh, C., Amaro Jr, M., Lima, J., & Foltz, H. (2020). Optimization of railroad bearing health monitoring system for wireless utilization. *ASME/IEEE Joint Rail Conference*, *83587*, V001T03A007.

Daniel, R. V., Siddhappa, S. A., Gajanan, S. B., Philip, S. V., & Paul, P. S. (2017). Effect of bearings on vibration in rotating machinery. *IOP Conference Series: Materials Science and Engineering*, *225*(1), 012264.

Darlow, M. S., Badgley, R. H., & Hogg, G. W. (1974). *Application of high-frequency resonance techniques for bearing diagnostics in helicopter gearboxes*. Mechanical Technology Inc Latham NY.

de Almeida Costa, M., Braga, J. P. de A. P., & Andrade, A. R. (2020). Assessing the performance of different devices in railway wheelset inspection. *Measurement*, *165*, 108145.

de la Rosa, J. J. G., Moreno, A., Gallego, A., Piotrkowski, R., Castro, E., & Vico, J. (2008). A Virtual Instrument For Acoustic Termite Detection Based In The Spectral Kurtosis. *12th IMEKO TC1 & TC7 Joint Symposium on Man Science & Measurement*.

de Los Santos, N., Jones, R., Tarawneh, C. M., Fuentes, A., & Villarreal, A. (2017). Development of prognostic techniques for surface defect growth in railroad bearing rolling elements. *ASME/IEEE Joint Rail Conference*, *50718*, V001T02A009.

Dukes, R., & Culpan, E. A. (1984). Acoustic emission: its techniques and applications. *IEE Proceedings A (Physical Science, Measurement and Instrumentation, Management and Education, Reviews)*, *131*(4), 241–251.

Dukkipati, R. v, & Dong, R. (1999a). Impact loads due to wheel flats and shells. *Vehicle System Dynamics*, *31*(1), 1–22.

Dukkipati, R. v, & Dong, R. (1999b). Impact loads due to wheel flats and shells. *Vehicle System Dynamics*, *31*(1), 1–22.

Dunegan, H., & Harris, D. (1969). Acoustic emission-a new nondestructive testing tool. *Ultrasonics*, *7*(3), 160–166.

Dunegan, H. L., Harris, D. O., & Tatro, C. A. (1968). Fracture analysis by use of acoustic emission. *Engineering Fracture Mechanics*, *1*(1), 105–122.

Dwyer, R. (1983). Detection of non-Gaussian signals by frequency domain kurtosis estimation. *ICASSP'83. IEEE International Conference on Acoustics, Speech, and Signal Processing*, *8*, 607–610.

Dybała, J., & Zimroz, R. (2012). Application of Empirical Mode Decomposition for impulsive signal extraction to detect bearing damage–industrial case study. In *Condition Monitoring of Machinery in Non-Stationary Operations* (pp. 257–266). Springer.

Dyer, D., & Stewart, R. M. (1978). *Detection of rolling element bearing damage by statistical vibration analysis.*

Engineering Manager Schaeffler UK. (2008). *An Overview of Bearing Vibration Analysis*.

Entezami, M., Roberts, C., Weston, P., Stewart, E., Amini, A., & Papaelias, M. (2020a). Perspectives on railway axle bearing condition monitoring. *Proceedings of the Institution of Mechanical Engineers, Part F: Journal of Rail and Rapid Transit*, *234*(1), 17–31.

Entezami, M., Roberts, C., Weston, P., Stewart, E., Amini, A., & Papaelias, M. (2020b). Perspectives on railway axle bearing condition monitoring. *Proceedings of the Institution of Mechanical Engineers, Part F: Journal of Rail and Rapid Transit*, *234*(1), 17–31.

Entezami, M., Stewart, E., Roberts, C., Kono, T., Bayram, S., Morley, S., & Hayward, M. (2016). Wayside acoustic monitoring techniques for railway axlebox bearing on high-speed lines. *11 Th World Congress on Railway Research, Milan*, 5–29.

Entezami, M., Stewart, E., Tutcher, J., Driscoll, W., Ellis, R., Yeo, G., Zhang, Z., Roberts, C., Kono, T., & Bayram, S. (2014). *Acoustic analysis techniques for condition monitoring of roller bearings*.

Erhard, A., Bertus, N., Montag, H.-J., Schenk, G., & Hintze, H. (2003). Ultrasonic Phased Array System for Railroad Axle Examination. *Journal of Nondestructive Testing*, *8*(3), 1–6.

Éric, F., & Reinhard, C. (2020). *Rolling Stock in the Railway System* (Vol. 2). PMC Media House GmbH.

Ferrando, A., & Mulier, K. (2015). Firms' Financing Constraints: Do Perceptions Match the Actual Situation? *Economic and Social Review*, *46*(1), 87–117. https://doi.org/10.2139/ssrn.2305940

Ferrando Chacon, J. L. (2015). *Fault Detection in Rotating Machinery Using Acoustic Emission*. https://doi.org/10.13140/RG.2.1.2369.5444

Filograno, M. L., Corredera, P., Rodriguez-Plaza, M., Andres-Alguacil, A., & Gonzalez-Herraez, M. (2013). Wheel flat detection in high-speed railway systems using fiber Bragg gratings. *IEEE Sensors Journal*, *13*(12), 4808–4816.

FRA (Federal Railroad Administration). (2011). *FRA guide for preparing accident/incident reports*. USDOT Washington, DC.

Gao, R., He, Q., & Feng, Q. (2019). Railway wheel flat detection system based on a parallelogram mechanism. *Sensors*, *19*(16), 3614.

Gao, Y., Feng, Q., & Cui, J. (2014). A simple method for dynamically measuring the diameters of train wheels using a one-dimensional laser displacement transducer. *Optics and Lasers in Engineering*, *53*, 158–163.

Gegner, J. (2011). Tribological aspects of rolling bearing failures. *Tribology-Lubricants and Lubrication*, 33–94.

Gerdun, V., Sedmak, T., Šinkovec, V., Kovše, I., & Cene, B. (2007). Failures of bearings and axles in railway freight wagons. *Engineering Failure Analysis*, *14*(5), 884–894.

Getmanova, M. E., Ilyukhin, D. S., Nikulin, A. N., & Filippov, G. A. (2017). Composition and properties of steel in cast and forged railroad wheels. *Steel in Translation*, *47*(1), 70–77.

Gohar, R. (2001). *Elastohydrodynamics*. World Scientific.

Gomez, E., Giménez, J. G., & Alonso, A. (2011). Method for the reduction of measurement errors associated to the wheel rotation in railway dynamometric wheelsets. *Mechanical Systems and Signal Processing*, *25*(8), 3062–3077.

Grabulov, A. (2010). *Fundamentals of rolling contact fatigue*.

Graney, B. P., & Starry, K. (2012). Rolling element bearing analysis. *Materials Evaluation*, *70*(1), 78.

Grosse, C. U., & Ohtsu, M. (2008). *Acoustic emission testing*. Springer Science & Business Media.

Guo, W., Cao, H., Zi, Y., & He, Z. (2018). Material analysis of the fatigue mechanism of rollers in tapered roller bearings. *Science China Technological Sciences*, *61*(7), 1003–1011.

Gupta, K. K., & Gupta, R. (2007). Despeckle and geographical feature extraction in SAR images by wavelet transform. *ISPRS Journal of Photogrammetry and Remote Sensing*, *62*(6), 473–484.

Gupta, P., & Pradhan, M. K. (2017). Fault detection analysis in rolling element bearing: A review. *Materials Today: Proceedings*, *4*(2), 2085–2094.

Gurumoorthy, K., & Ghosh, A. (2013). Failure investigation of a taper roller bearing: A case study. *Case Studies in Engineering Failure Analysis*, *2*(1), 110–114.

Hackenberger, D. E., & Lonsdale, C. P. (1998). An initial feasibility study to develop a wayside cracked railroad wheel detector. *Proceedings of the 1998 ASME/IEEE Joint Railroad Conference*, 65–77.

Hashizume, H., Yamada, Y., Miya, K., Toda, S., Morimoto, K., Araki, Y., Satake, K., & Shimizu, N. (1992). Numerical and experimental analysis of eddy current testing for a tube with cracks. *IEEE Transactions on Magnetics*, *28*(2), 1469–1472.

Hawman, M. W., & Galinaitis, W. S. (1988). Acoustic emission monitoring of rolling element bearings. *IEEE 1988 Ultrasonics Symposium Proceedings.*, 885–889.

He, D., Li, R., Zade, M., & Zhu, J. (2011). Development and evaluation of AE based condition indicators for full ceramic bearing fault diagnosis. *2011 IEEE Conference on Prognostics and Health Management*, 1–7.

Heirich, O., Steingass, A., Lehner, A., & Strang, T. (2013). Velocity and location information from onboard vibration measurements of rail vehicles. *Proceedings of the 16th International Conference on Information Fusion*, 1835–1840.

Hemmati, F., Orfali, W., & Gadala, M. S. (2016). Roller bearing acoustic signature extraction by wavelet packet transform, applications in fault detection and size estimation. *Applied Acoustics*, *104*, 101–118.

Hillmansen, S., & Smith, R. A. (2004). The management of fatigue crack growth in railway axles. *Proceedings of the Institution of Mechanical Engineers, Part F: Journal of Rail and Rapid Transit*, *218*(4), 327–336.

Hirakawa, K., Toyama, K., & Kubota, M. (1998). The analysis and prevention of failure in railway axles. *International Journal of Fatigue*, *20*(2), 135–144.

Hiremath, N., & Reddy, D. M. (2014). Bearing fault detection using acoustic emission signals analyzed by empirical mode decomposition. *International Journal of Research in Engineering and Technology*, *3*(3).

Hoskins, W. (2017). *Reliability, Availability and Maintainability*.

Hsu, N. N., Simmons, J., & Hardy, S. C. (1977). An approach to acoustic emission signal analysis--theory and experiment. *Materials Evaluation*, *35*(10), 100–106.

Huang, N. E., Shen, Z., Long, S. R., Wu, M. C., Shih, H. H., Zheng, Q., Yen, N.-C., Tung, C. C., & Liu, H. H. (1998). The empirical mode decomposition and the Hilbert spectrum for nonlinear and non-stationary time series analysis. *Proceedings of the Royal Society of London. Series A: Mathematical, Physical and Engineering Sciences*, *454*(1971), 903–995.

Huang, N. E., & Wu, Z. (2008). A review on Hilbert-Huang transform: Method and its applications to geophysical studies. *Reviews of Geophysics*, *46*(2).

Huang, Z. (2017). *Integrated Railway Remote Condition Monitoring*. University of Birmingham.

Hutton, P. H. (1970). *ACOUSTIC EMISSION APPLIED TO DETERMINATION OF STRUCTURAL INTEGRITY.* Battelle-Northwest, Richland, Wash. Pacific Northwest Lab.

Ichinose, H., Takehara, J., Iwasaki, N., & Ueda, M. (1978). An investigation on contact fatigue and wear resistance behaviour in rail steels. *Heavy Haul Railways Conference Held September 18-22, 1978, Perth, Western Australia. Sponsored by Cliffs Robe River Iron Associates, Goldsworthy Mining Limited, Hamersley Iron Proprietary Limited, Mt. Newman Mining Company Proprietary Limited and Westrai, Session 307 Pap I. 3 Conf Paper*.

Iele, A., Lopez, V., Laudati, A., Mazzino, N., Bocchetti, G., Cutolo, A., & Cusano, A. (2016). Fiber optic sensing system for weighing in motion (WIM) and wheel flat detection (WFD) in railways assets: the TWBCS system. *Proceedings of the 8th European Workshop On Structural Health Monitoring (EWSHM 2016), Bilbao, Spain*, 5–8.

Jacobs, G., & Plogmann, M. (2014). Rolling Bearing: Types and Features. In T. Mang (Ed.), *Encyclopedia of Lubricants and Lubrication* (pp. 1633–1655). Springer Berlin Heidelberg. https://doi.org/10.1007/978-3-642-22647-2_295

Janousek, L., Capova, K., Yusa, N., & Miya, K. (2008). Multiprobe inspection for enhancing sizing ability in eddy current nondestructive testing. *IEEE Transactions on Magnetics*, *44*(6), 1618–1621.

Jergéus, J. (1998). Martensite formation and residual stresses around railway wheel flats. *Proceedings of the Institution of Mechanical Engineers, Part C: Journal of Mechanical Engineering Science*, *212*(1), 69–79.

Jergéus, J., Odenmarck, C., Lunden, R., Sotkovszki, P., Karlsson, B., & Gullers, P. (1999). Full-scale railway wheel flat experiments. *Proceedings of the Institution of Mechanical Engineers, Part F: Journal of Rail and Rapid Transit*, *213*(1), 1–13.

Jin, X. (2020). Evaluation and analysis approach of wheel–rail contact force measurements through a high-speed instrumented wheelset and related considerations. *Vehicle System Dynamics*, *58*(8), 1189–1211.

Joosse, P. A., Blanch, M. J., Dutton, A. G., Kouroussis, D. A., Philippidis, T. P., & Vionis, P. S. (2002). Acoustic emission monitoring of small wind turbine blades. *J. Sol. Energy Eng.*, *124*(4), 446–454.

Juna, A. P. (2017). *On the characterisation and detection of rolling contact fatigue (RCF) type cracks in railway vehicle wheels using an alternating current field measurement (ACFM) technique*.

Kannan, V., Li, H., & Dao, D. V. (2019). Demodulation band optimization in envelope analysis for fault diagnosis of rolling element bearings using a real-coded genetic algorithm. *IEEE Access*, *7*, 168828–168838.

Kappes, W., Rockstroh, B., Bahr, W., Kroning, M., Rodner, C., Goetz, J., & Nemec, D. (2007). Application of new front-end electronics for non-destructive testing of railroad wheel sets. *Insight-Northampton-Including European Issues*, *49*(6), 345–349.

Karunakaran, S., & Snyder, T. W. (2007). Bearing temperature performance in freight cars. *Proceedings of the Bearing Research Symposium Sponsored by the AAR Research Program in Conjunction with the ASME RTD 2007 Fall Technical Conference*, 11–12.

Kenderian, S., Cerniglia, D., Boro Djordjevic, B., & Green Jr, R. E. (2005). Laser-generated acoustic signal interaction with surface flaws on rail wheels. *Research in Nondestructive Evaluation*, *16*(4), 195–207.

Kenderian, S., Cerniglia, D., Djordjevic, B. B., & Garcia, G. (2005). Laser-air hybrid ultrasonic technique for dynamic railroad inspection applications. *Insight-Non-Destructive Testing and Condition Monitoring*, *47*(6), 336–340.

KEYSIGHT Technology. (2019). *U2500A Series Data SHeet*. https://www.keysight.com/us/en/assets/7018-03521/data-sheets/5991-0651.pdf

Khanam, S., Tandon, N., & Dutt, J. K. (2014). Fault size estimation in the outer race of ball bearing using discrete wavelet transform of the vibration signal. *Procedia Technology*, *14*, 12–19.

Konstantin-Hansen, H., & Herlufsen, H. (2010). Envelope and cepstrum analyses for machinery fault identification. *Sound & Vibration*, *44*(5), 10–12.

Kouroussis, G., Caucheteur, C., Kinet, D., Alexandrou, G., Verlinden, O., & Moeyaert, V. (2015). Review of trackside monitoring solutions: from strain gages to optical fibre sensors. *Sensors*, *15*(8), 20115–20139.

Kouroussis, G., Kinet, D., Mendoza, E., Dupuy, J., Moeyaert, V., & Caucheteur, C. (2016). Edge-filter technique and dominant frequency analysis for high-speed railway monitoring with fiber Bragg gratings. *Smart Materials and Structures*, *25*(7), 075029.

Krusuansombat, P. (2018). *Quantifying the damage of in-service rolling stock wheelsets using remote condition monitoring*. University of Birmingham.

Kulkarni, P. G., & Sahasrabudhe, A. D. (2013). Application of wavelet transform for fault diagnosisof rolling element bearings. *Int J Sci Technol Res*, *2*(4), 138–148.

Kulkarni, S., & Wadkar, S. B. (2012). Investigation for Distributed defects in Ball bearing using Vibration Signature Analysis- A Review. *International Journal of Scientific Research*, *2*, 157–160. https://doi.org/10.15373/22778179/DEC2013/51

Laing O'Rourke. (2020a). *E17H RAIL WHEEL INSPECTION*.

Laing O'Rourke. (2020b). *E17H RAIL WHEEL INSPECTION*.

Lamari, A. C. (2008). *Rolling stock bearing condition monitoring systems*.

Lanzagorta, J. L., Decitre, J. M., Nozais, F., Aizpurua, I., Hidalgo-Gato, R., Castro, I., & Lasa, L. (2018). New inspection approaches for railway based on Eddy Current. *12th European Conference on Non-Destructive Testing*, *7*.

Law, L.-S., Kim, J. H., Liew, W. Y. H., & Lee, S.-K. (2012). An approach based on wavelet packet decomposition and Hilbert–Huang transform (WPD–HHT) for spindle bearings condition monitoring. *Mechanical Systems and Signal Processing*, *33*, 197–211.

Lawson H.I.S. Ltd. (2022). *ARALDITE ARL400005 RAPID TUBES*. https://www.lawson-his.co.uk/araldite-arl400005-rapid-tubes-2-x-15ml-p148267

Lebold, M., McClintic, K., Campbell, R., Byington, C., & Maynard, K. (2000). Review of vibration analysis methods for gearbox diagnostics and prognostics. *Proceedings of the 54th Meeting of the Society for Machinery Failure Prevention Technology*, *634*, 16.

Lei, Y., He, Z., & Zi, Y. (2009). Application of the EEMD method to rotor fault diagnosis of rotating machinery. *Mechanical Systems and Signal Processing*, *23*(4), 1327–1338.

Lei, Y., Lin, J., He, Z., & Zuo, M. J. (2013). A review on empirical mode decomposition in fault diagnosis of rotating machinery. *Mechanical Systems and Signal Processing*, *35*(1–2), 108–126.

Lewis, R., Dwyer-Joyce, R. S., Olofsson, U., Pombo, J., Ambrosio, J., Pereira, M., Ariaudo, C., & Kuka, N. (2010). Mapping railway wheel material wear mechanisms and transitions. *Proceedings of the Institution of Mechanical Engineers, Part F: Journal of Rail and Rapid Transit*, *224*(3), 125–137.

Lewis, R., Dwyer-Joyce, R. S., & Yao, C. (2008). Feasibility study for an ultrasonic sensor for monitoring wheel flange contact. *ASME/IEEE Joint Rail Conference*, *48124*, 119–124.

Lewis, R., & Olofsson, U. (2009a). Basic tribology of the wheel–rail contact. In *Wheel–rail interface handbook* (pp. 34–57). Elsevier.

Lewis, R., & Olofsson, U. (2009b). Basic tribology of the wheel–rail contact. In *Wheel–rail interface handbook* (pp. 34–57). Elsevier.

Lewisa, R., & Dwyer-Joyce, R. S. (2004). Wear mechanisms and transitions in railway wheel steels. *Proceedings of the Institution of Mechanical Engineers, Part J: Journal of Engineering Tribology*, *218*(6), 467–478.

Li, C. J., & Li, S. Y. (1995). Acoustic emission analysis for bearing condition monitoring. *Wear*, *185*(1–2), 67–74.

Li, Y., Liang, X., Lin, J., Chen, Y., & Liu, J. (2018). Train axle bearing fault detection using a feature selection scheme based multi-scale morphological filter. *Mechanical Systems and Signal Processing*, *101*, 435–448. https://doi.org/10.1016/j.ymssp.2017.09.007

Li, Y., Liu, J., & Wang, Y. (2016). Railway wheel flat detection based on improved empirical mode decomposition. *Shock and Vibration*, *2016*.

Liu, H., Wang, L., & Li, Y. (2019). Simulation of rail wheel axle bearing vibration due to local damages on outer races. *Proceedings of the Institution of Mechanical Engineers, Part K: Journal of Multi-Body Dynamics*, *233*(2), 429–440.

Liu, X. (2015). Statistical Temporal Analysis of Freight Train Derailment Rates in the United States. *Transportation Research Record*, *2476*(1), 119–125.

Liu, X. (2017). Statistical causal analysis of freight-train derailments in the United States. *Journal of Transportation Engineering*, *143*(2). https://doi.org/10.1061/jtepbs.0000014

Liu, X., Barkan, C. P. L., & Saat, M. R. (2011). Analysis of derailments by accident cause: Evaluating railroad track upgrades to reduce transportation risk. *Transportation Research Record, 2261*, 178–185. https://doi.org/10.3141/2261-21

Liu, X., Ni, Y., & Zhou, L. (2018). Condition-based maintenance of high-speed train wheels through trackside monitoring. *Proc. 2nd Int. Workshop Struct. Health Monit. Railway Syst.(IWSHM-RS)*, 1–12.

Liu, X., Saat, M. R., & Barkan, C. P. L. (2012). Analysis of causes of major train derailment and their effect on accident rates. *Transportation Research Record*, *2289*, 154–163. https://doi.org/10.3141/2289-20

Liu, X.-Z., & Ni, Y.-Q. (2017). Wheel tread defect detection for high-speed trains using wheel impact load detector. *Proceedings Advances in Structural Engineering and Mechanics*, 1–12.

Loutas, T. H., Sotiriades, G., Kalaitzoglou, I., & Kostopoulos, V. (2009). Condition monitoring of a single-stage gearbox with artificially induced gear cracks utilizing on-line vibration and acoustic emission measurements. *Applied Acoustics*, *70*(9), 1148–1159.

Lugg, M., & Topp, D. A. (2006). *Recent Developments and Applications of the ACFM Inspection Method and ACSM Stress Measurement Method*.

Machine design. (2002, November). *Bearing materials* . https://www.machinedesign.com/mechanical-motion-systems/bearings/article/21812845/bearing-materials

Mädler, K., & Bannasch, M. (2006). *Materials used for rolling stock wheels - Alternatives and limits*. *130*, 428–435.

Maglio, M., Vernersson, T., Nielsen, J. C. O., Pieringer, A., Söderström, P., Regazzi, D., & Cervello, S. (2022). Railway wheel tread damage and axle bending stress–Instrumented wheelset measurements and numerical simulations. *International Journal of Rail Transportation*, *10*(3), 275–297.

Malla, C., & Panigrahi, I. (2019). Review of condition monitoring of rolling element bearing using vibration analysis and other techniques. *Journal of Vibration Engineering & Technologies*, *7*(4), 407–414.

Mancini, G., Corbizi, A., Lombardo, F., & Cervello, S. (2006). Design of railway axle in compliance with the European Norms: high strength alloyed steels compared to standard steels. *Proceedings of WCRR*.

Masumoto, H., Sugino, K., Nisida, S., & Kurihara, R. (1978). Some Features and Metallurgical. *Rail Steels, Developments, Processing, and Use: A Symposium Sponsored by ASTM Committee A-1 on Steel, Stainless Steel, and Related Alloys, American Society for Testing and Materials, Denver, Colo., 17-18 Nov. 1976*, *644*, 233.

Matsumoto, K., & Tanimoto, M. (2018). Condition monitoring for the management of running safety in commercial line. *2018 International Conference on Intelligent Rail Transportation (ICIRT)*, 1–4.

Mba, D., & Rao, R. (2006). Development of acoustic emission technology for condition monitoring and diagnosis of rotating machines: bearings, pumps, gearboxes, engines, and rotating structures. *Shock and Vibration Digest*, *38*(1), 3–18.

McFadden, P. D., & Smith, J. D. (1984a). Acoustic emission transducers for the vibration monitoring of bearings at low speeds. *Proceedings of the Institution of Mechanical Engineers, Part C: Journal of Mechanical Engineering Science*, *198*(2), 127–130.

McFadden, P. D., & Smith, J. D. (1984b). Model for the vibration produced by a single point defect in a rolling element bearing. *Journal of Sound and Vibration*, *96*(1), 69–82.

McFadden, P. D., & Smith, J. D. (1984c). Vibration monitoring of rolling element bearings by the high-frequency resonance technique—a review. *Tribology International*, *17*(1), 3–10.

McLaskey, G. C., & Glaser, S. D. (2012). Acoustic emission sensor calibration for absolute source measurements. *Journal of Nondestructive Evaluation*, *31*(2), 157–168.

Mealer, A., Tarawneh, C., & Crown, S. (2017). Radiative heat transfer analysis of railroad bearings for wayside hot-box detector optimization. *ASME/IEEE Joint Rail Conference*, *50718*, V001T02A008.

Meixedo, A., Gonçalves, A., Calçada, R., Gabriel, J., Fonseca, H., & Martins, R. (2015). On-line monitoring system for tracks. *2015 3rd Experiment International Conference (Exp. at'15)*, 133–134.

Meywerk, M. (1999). Polygonalization of railway wheels. *Archive of Applied Mechanics*, *69*(2), 105–120.

Miettinen, J., & Pataniitty, P. (1999). Acoustic emission in monitoring extremely slowly rotating rolling bearing. *Proceedings of COMADEM*, *99*, 289–297.

MISTRAS. (2011a). *2/4/6 Preamplifier Product Data Sheet*. https://www.physicalacoustics.com/by-product/2-4-6/

MISTRAS. (2011b). *R50α Sensor Product Data Sheet*. https://www.physicalacoustics.com/content/literature/sensors/Model_R50a.pdf

Mistry, P. J., & Johnson, M. S. (2020). Lightweighting of railway axles for the reduction of unsprung mass and track access charges. *Proceedings of the Institution of Mechanical Engineers, Part F: Journal of Rail and Rapid Transit*, *234*(9), 958–968.

Molyneux-Berry, P., Davis, C., & Bevan, A. (2014). The influence of wheel/rail contact conditions on the microstructure and hardness of railway wheels. *The Scientific World Journal*, *2014*.

Montinaro, N., Epasto, G., Cerniglia, D., & Guglielmino, E. (2019). Laser ultrasonics inspection for defect evaluation on train wheel. *NDT & E International*, *107*, 102145.

Montinaro, N., Epasto, G., Cerniglia, D., & Guglielmino, E. (2020). Laser ultrasonics for defect evaluation on coated railway axles. *NDT & E International*, *116*, 102321.

Mosleh, A., Montenegro, P., Alves Costa, P., & Calçada, R. (2021). An approach for wheel flat detection of railway train wheels using envelope spectrum analysis. *Structure and Infrastructure Engineering*, *17*(12), 1710–1729.

Moyar, G. J., & Stone, D. H. (1991). An analysis of the thermal contributions to railway wheel shelling. *Wear*, *144*(1–2), 117–138.

Náhlík, L., Pokorný, P., Ševčík, M., Fajkoš, R., Matušek, P., & Hutař, P. (2017). Fatigue lifetime estimation of railway axles. *Engineering Failure Analysis*, *73*, 139–157.

NATIONAL INSTRUMENTS. (2016). *NI 9223 Datasheet*.

NDT Encyclopedia. (1996). *Acoustic Emission (AE): Hsu-Nielsen source*. https://www.ndt.net/article/az/ae/hsunielsensource.htm

Nerella, M. J., Ratnam, C., & Rao, V. v. (2017). Study of Detection of Defects in Rolling Element Bearings Using Acoustic Measurement Methods-A Review. *SSRG International Journal of Mechanical Engineering (SSRG-IJME)*, *5*, 110–116.

Nicholson, G. L., & Davis, C. L. (2012). Modelling of the response of an ACFM sensor to rail and rail wheel RCF cracks. *Ndt & E International*, *46*, 107–114.

Nicholson, G. L., Rowshandel, H., Hao, X. J., & Davis, C. L. (2013). Measurement and modelling of ACFM response to multiple RCF cracks in rail and wheels. *Ironmaking & Steelmaking*, *40*(2), 87–91.

Nielsen, J. C. O., & Johansson, A. (2000a). Out-of-round railway wheels-a literature survey. *Proceedings of the Institution of Mechanical Engineers, Part F: Journal of Rail and Rapid Transit*, *214*(2), 79–91.

Nielsen, J. C. O., & Johansson, A. (2000b). *Out-of-round railway wheelsÐa literature survey*.

Nielsen, J. C. O., Lundén, R., Johansson, A., & Vernersson, T. (2003). Train-track interaction and mechanisms of irregular wear on wheel and rail surfaces. *Vehicle System Dynamics*, *40*(1–3), 3–54.

Nikas, D. (2016). *Effect of Temperature on Mechanical Properties of Railway Wheel Steels*.

Norton, M. P., & Karczub, D. G. (2003a). *Fundamentals of noise and vibration analysis for engineers*. Cambridge university press.

Norton, M. P., & Karczub, D. G. (2003b). *Fundamentals of noise and vibration analysis for engineers*. Cambridge university press.

Novosad, M., Fajkoš, R., Řeha, B., & Řezníček, R. (2010). Fatigue tests of railway axles. *Procedia Engineering*, *2*(1), 2259–2268.

NSK. (2010). *BEARINGS FOR RAILWAY ROLLING STOCK*.

NTN. (2020). *Ball and Roller Bearings*.

Okagata, Y. (2013a). Design technologies for railway wheels and future prospects. *Nippon Steel & Sumitomo Metal Technical Report*, *105*(105), 26–33.

Okagata, Y. (2013b). Design technologies for railway wheels and future prospects. *Nippon Steel & Sumitomo Metal Technical Report*, *105*(105), 26–33.

Olver, A. v. (2005). The mechanism of rolling contact fatigue: an update. *Proceedings of the Institution of Mechanical Engineers, Part J: Journal of Engineering Tribology*, *219*(5), 313–330.

Otai Special Steel. (2021). *ASTM 52100 Bearing Steel | 1.3505 | 100Cr6 | SUJ2 | EN31*. http://www.astmsteel.com/product/52100-bearing-steel-aisi/

Ouyang, Y., Li, X., Barkan, C. P. L., Kawprasert, A., & Lai, Y. (2009). Optimal locations of railroad wayside defect detection installations. *Computer-Aided Civil and Infrastructure Engineering*, *24*(5), 309–319.

PAC. (2004). *AE2A & AE5A Amplifier Systems Product Bulletin*. http://www.physicalacoustics.com/content/literature/small_systems/AE2A_AE5A_Product_Bulletin.pdf

Pao, Y., Gajewski, R. R., & Ceranoglu, A. N. (1979). Acoustic emission and transient waves in an elastic plate. *The Journal of the Acoustical Society of America*, *65*(1), 96–105.

Papaelias, M., Amini, A., Huang, Z., Vallely, P., Dias, D. C., & Kerkyras, S. (2016a). Online condition monitoring of rolling stock wheels and axle bearings. *Proceedings of the Institution of Mechanical Engineers, Part F: Journal of Rail and Rapid Transit*, *230*(3), 709–723.

Papaelias, M., Amini, A., Huang, Z., Vallely, P., Dias, D. C., & Kerkyras, S. (2016b). Online condition monitoring of rolling stock wheels and axle bearings. *Proceedings of the Institution of Mechanical Engineers, Part F: Journal of Rail and Rapid Transit*, *230*(3), 709–723.

Papaelias, M., Amini, A., Huang, Z., Vallely, P., Dias, D. C., & Kerkyras, S. (2016c). Online condition monitoring of rolling stock wheels and axle bearings. *Proceedings of the Institution of Mechanical Engineers, Part F: Journal of Rail and Rapid Transit*, *230*(3), 709–723.

Papaelias, M., Huang, Z., Amini, A., Vallely, P., Day, N., Sharma, R., Kerkyras, Y., & Kerkyras, S. (2014). Advanced wayside condition monitoring of rolling stock wheelsets. *Proceedings of the 11th ECNDT, Prague, Czech*, 6–10.

Papaelias, M. P., Roberts, C., Davis, C. L., Lugg, M., & Smith, M. (2008). Detection and quantification of rail contact fatigue cracks in rails using ACFM technology. *Insight-Non-Destructive Testing and Condition Monitoring*, *50*(7), 364–368.

Partington, W. (1993). Wheel impact load monitoring. *Proceedings of the Institution of Civil Engineers-Transport*, *100*(4), 243–245.

Patidar, H., & Mandloi, R. K. (2015). Study of detection of defects in rolling element bearings using vibration and acoustic measurement methods-A Review. *International Journal of Mechanical Engineering Research & Technology*, *1*(1), 1–15.

Peng, J., Li, W., Yu, Z., Xiaorong, G., Zeyong, W., Quanke, Z., Chaoyong, P., & Kai, Y. (2012). *The Design and Application of Lateral Phased Array Probe for Railway Wheel Rim Ultrasonic Detection System*.

Peng, J., Wang, L., Zhang, Y., Gao, X., Wang, Z., & Peng, C. (2014). Study on the ultrasonic inspection method using the full matrix capture for the in service railway wheel. *AIP Conference Proceedings*, *1581*(1), 42–48.

Pieringer, A., Kropp, W., & Nielsen, J. C. O. (2014). The influence of contact modelling on simulated wheel/rail interaction due to wheel flats. *Wear*, *314*(1–2), 273–281.

Pimentel-Junior, G. L. S., Oliveira, F. B., & Faria, M. T. C. (2016). On the bump tests of cracked shafts using acoustic emission techniques. *Engineering*, *8*(09), 572.

Pohl, R., Erhard, A., Montag, H.-J., Thomas, H.-M., & Wüstenberg, H. (2004). NDT techniques for railroad wheel and gauge corner inspection. *NDT & e International*, *37*(2), 89–94.

Pollock, A. A. (1969). Stress-wave emission in ndt. *Non-Destructive Testing*, *2*(3), 178–182.

PRC Rail Consulting Ltd. (2019). *Bogies*. http://www.railway-technical.com/trains/rolling-stock-index-l/bogies.html

Raad, A., Zhang, F., & Sidahmed, M. (2004). Acoustic Emission for gear fault detection: A promising tool. *Surveillance 5 Cetim Senlis*.

Rafsanjani, A., Abbasion, S., Farshidianfar, A., & Moeenfard, H. (2009). Nonlinear dynamic modeling of surface defects in rolling element bearing systems. *Journal of Sound and Vibration*, *319*(3–5), 1150–1174.

Rail Accident Investigation Branch. (2006). *Freight train derailment at Hatherley, near Cheltenham Spa 18 October 2005*.

Rail Accident Investigation Branch. (2019a). *Derailment of a rail head treatment train near Dunkeld & Birnam, 29 October 2018*.

Rail Accident Investigation Branch. (2019b). *Derailment of a rail head treatment train near Dunkeld & Birnam, 29 October 2018*.

Rail Accident Investigation Branch. (2020). *Passenger train collision with a derailed locomotive at Bromsgrove 23 March 2020*. www.gov.uk/raib.

Rail Safety and Standards Board. (2019). *Railway Wheelsets*. www.rssb.co.uk/railway-group-standards.

Rajaee, T., & Shahabi, A. (2016). Evaluation of wavelet-GEP and wavelet-ANN hybrid models for prediction of total nitrogen concentration in coastal marine waters. *Arabian Journal of Geosciences*, *9*(3), 1–15.

Randall, R. B. (2004). State of the art in monitoring rotating machinery-part 1. *Sound and Vibration*, *38*(3), 14–21.

Randall, R. B., & Antoni, J. (2011). Rolling element bearing diagnostics—A tutorial. *Mechanical Systems and Signal Processing*, *25*(2), 485–520.

Remennikov, A. M., & Kaewunruen, S. (2008). A review of loading conditions for railway track structures due to train and track vertical interaction. *Structural Control and Health Monitoring: The Official Journal of the International Association for Structural Control and Monitoring and of the European Association for the Control of Structures*, *15*(2), 207–234.

Ren, Y., & Chen, J. (2019). A new method for wheel–rail contact force continuous measurement using instrumented wheelset. *Vehicle System Dynamics*, *57*(2), 269–285.

Robinson, N. P. M., Scott, P., Lafaix, B., Kozyr, G., Zarembski, A., Gordana, N., Francis, V., Gilmartin, F. ben, Schoebel, A., & Ripke, B. (2012). *Development of the Future Rail Freight System to Reduce the Occurrences and Impact of Derailment Summary report and database of derailments incidents Duration: 36 months Organisation name of lead contractor for this deliverable: UNEW*.

Roger, L. M. (1979a). The application of vibration analysis and acoustic emission source location to on-line condition monitoring of anti-friction bearings. *Tribology International*, *12*(2), 51–58.

Roger, L. M. (1979b). The application of vibration analysis and acoustic emission source location to on-line condition monitoring of anti-friction bearings. *Tribology International*, *12*(2), 51–58.

Sandström, J., & Ekberg, A. (2009). Predicting crack growth and risks of rail breaks due to wheel flat impacts in heavy haul operations. *Proceedings of the Institution of Mechanical Engineers, Part F: Journal of Rail and Rapid Transit*, *223*(2), 153–161.

Saruhan, H., Saridemir, S., Qicek, A., & Uygur, I. (2014). Vibration analysis of rolling element bearings defects. *Journal of Applied Research and Technology*, *12*(3), 384–395.

Savaskan, T., & Veinot, D. E. (1987). On the wear and failure of high speed roller bearings. *Wear*, *116*(3), 361–380.

Sawalhi, N., & Randall, R. B. (2004). The application of spectral kurtosis to bearing diagnostics. *Proceedings of ACOUSTICS*, 3–5.

Schaeffler Technologies. (2019). *Materials for Rolling Bearing Technology.*

Schmid, F. (2017). *Introduction: What is a Railway System?*

Scott, D. (1973). Bearing failures diagnosis and investigation. *Wear*, *25*(2), 199–213.

Sejdić, E., Djurović, I., & Jiang, J. (2009). Time–frequency feature representation using energy concentration: An overview of recent advances. *Digital Signal Processing*, *19*(1), 153–183.

Sharan, P., Singh, M., & Kaur, I. (2021). *Smart Monitoring of Flat Wheel in Railway Using Optical Sensors*.

Shi, X., Yan, Q., Zhang, X., Diao, G., Zhang, C., Hong, Z., Wen, Z., & Jin, X. (2019). Hardness matching of rail/wheel steels for high-speed-train based on wear rate and rolling contact fatigue performance. *Materials Research Express*, *6*(6), 066501.

Shiroishi, J., Li, Y., Liang, S., Kurfess, T., & Danyluk, S. (1997a). Bearing condition diagnostics via vibration and acoustic emission measurements. *Mechanical Systems and Signal Processing*, *11*(5), 693–705.

Shiroishi, J., Li, Y., Liang, S., Kurfess, T., & Danyluk, S. (1997b). Bearing condition diagnostics via vibration and acoustic emission measurements. *Mechanical Systems and Signal Processing*, *11*(5), 693–705.

Singh, A., Houser, D. R., & Vijayakar, S. (1996). Early detection of gear pitting. *Power Transmission and Gearing Conference, ASME*, 673–678.

SKF Group. (2011). *Railway technical handbook Vol.1*.

SKF Group. (2012). *Railway technical handbook* (Vol. 2).

SKF Group. (2017). *Bearing damage and failure analysis*. https://www.skf.com/binaries/pub12/Images/0901d1968064c148-Bearing-failures---14219_2-EN_tcm_12-297619.pdf

SKF Group. (2018). *Rolling bearings*.

SKF USA. (2018). *SKF bearings and mounted products*.

Smith, D. J. (2017). *Reliability, maintainability and risk: practical methods for engineers*. Butterworth-Heinemann.

Smith, J. D. (1982). Vibration monitoring of bearings at low speeds. *Tribology International*, *15*(3), 139–144.

Smith, R. A., & Hillmansen, S. (2004). A brief historical overview of the fatigue of railway axles. *Proceedings of the Institution of Mechanical Engineers, Part F: Journal of Rail and Rapid Transit*, *218*(4), 267–277.

Sneed, W. H., & Smith, R. L. (1998). On-board real-time railroad bearing defect detection and monitoring. *Proceedings of the 1998 ASME/IEEE Joint Railroad Conference*, 149–153.

Soares, H., Zucarelli, T., Vieira, M., Freitas, M., & Reis, L. (2016). Experimental characterization of the mechanical properties of railway wheels manufactured using class B material. *Procedia Structural Integrity*, *1*, 265–272.

Soua, S., van Lieshout, P., Perera, A., Gan, T.-H., & Bridge, B. (2013). Determination of the combined vibrational and acoustic emission signature of a wind turbine gearbox and generator shaft in service as a pre-requisite for effective condition monitoring. *Renewable Energy*, *51*, 175–181.

Spiroiu, M.-A., & Nicolescu, M. (2018). Failure modes analysis of railway wheel. *MATEC Web of Conferences*, *178*, 06005.

Steets, P. G., & Tse, Y. H. (1998). Conrail's integrated automated wayside inspection. *Proceedings of the 1998 ASME/IEEE Joint Railroad Conference*, 113–125.

Stratman, B., Liu, Y., & Mahadevan, S. (2007). Structural health monitoring of railroad wheels using wheel impact load detectors. *Journal of Failure Analysis and Prevention*, *7*(3), 218–225.

Strážovec, P., Suchánek, A., Šťastniak, P., & Harušinec, J. (2019). Detection of residual stress in a railway wheel. *Transportation Research Procedia*, *40*, 898–905.

Sturm, A., & Uhlemann, D.-I. S. (1985). Diagnosis of plain bearings by acoustic emission analysis. *Measurement*, *3*(4), 185–191.

Sunnersjö, C. S. (1978). Varying compliance vibrations of rolling bearings. *Journal of Sound and Vibration*, *58*(3), 363–373.

Sutherland, H., Beattie, A., Hansche, B., Musial, W., Allread, J., Johnson, J., & Summers, M. (1994). *The application of non-destructive techniques to the testing of a wind turbine blade*. Sandia National Labs., Albuquerque, NM (United States).

Tandon, N., & Choudhury, A. (1999a). A review of vibration and acoustic measurement methods for the detection of defects in rolling element bearings. *Tribology International*, *32*(8), 469–480.

Tandon, N., & Choudhury, A. (1999b). A review of vibration and acoustic measurement methods for the detection of defects in rolling element bearings. *Tribology International*, *32*(8), 469–480.

Tandon, N., & Nakra, B. C. (1992a). Comparison of vibration and acoustic measurement techniques for the condition monitoring of rolling element bearings. *Tribology International*, *25*(3), 205–212.

Tandon, N., & Nakra, B. C. (1992b). Comparison of vibration and acoustic measurement techniques for the condition monitoring of rolling element bearings. *Tribology International*, *25*(3), 205–212.

Tao, G., Wen, Z., Jin, X., & Yang, X. (2020). Polygonisation of railway wheels: a critical review. *Railway Engineering Science*, *28*(4), 317–345.

Tarawneh, C., Aranda, J. A., Hernandez, V. v, & Ramirez, C. J. (2018). An analysis of the efficacy of wayside hot-box detector data. *ASME/IEEE Joint Rail Conference*, *50978*, V001T02A012.

Tarawneh, C., Lima, J. D., Santos, N. D. L., & Jones, R. E. (2019). Prognostics models for railroad tapered roller bearings with spall defects on inner or outer rings. *Tribology Transactions*, *62*(5), 897–906.

Tarawneh, C. M., Sotelo, L., Villarreal, A. A., de los Santos, N., Lechtenberg, R. L., & Jones, R. (2016). Temperature profiles of railroad tapered roller bearings with defective inner and outer rings. *ASME/IEEE Joint Rail Conference*, *49675*, V001T06A018.

Tarawneh, C., Montalvo, J., & Wilson, B. (2021). Defect detection in freight railcar tapered-roller bearings using vibration techniques. *Railway Engineering Science*, *29*(1), 42–58.

Tedrail. (2015a). *RAILWAY AXLE*. RAILWAY AXLE

Tedrail. (2015b). *TIRED WHEEL AND COMPONENTS*. http://www.tedrail.com/products/classify/Tired%20Wheel%20And%20Components

Thakkar, N. A., Steel, J. A., & Reuben, R. L. (2010). Rail–wheel interaction monitoring using Acoustic Emission: A laboratory study of normal rolling signals with natural rail defects. *Mechanical Systems and Signal Processing*, *24*(1), 256–266.

Thakkar, N. A., Steel, J. A., & Reuben, R. L. (2012). Rail–wheel contact stress assessment using acoustic emission: a laboratory study of the effects of wheel flats. *Proceedings of the Institution of Mechanical Engineers, Part F: Journal of Rail and Rapid Transit*, *226*(1), 3–13.

The SKF Evolution Team. (2010a, December 7). *THE EVOLUTION OF RAILWAY AXLEBOX TECHNOLOGY*. Evolution Technology Magazine from SKF. https://evolution.skf.com/the-evolution-of-railway-axlebox-technology/

The SKF Evolution Team. (2010b, December 7). *THE EVOLUTION OF RAILWAY AXLEBOX TECHNOLOGY*. Evolution Technology Magazine from SKF.

The SKF Evolution Team. (2017, January). *CONTRACT EXTENSION WITH RUSSIAN RAIL COMPANY*.

Topp, D., & Smith, M. (2005). Application of the ACFM inspection method to rail and rail vehicles. *Insight-Non-Destructive Testing and Condition Monitoring*, *47*(6), 354–357.

Transportation Safety Board of Canada. (2015). *Railway Investigation Report R14M0002*.

Turabimana, P., & Nkundineza, C. (2020). Development of an on-board measurement system for railway vehicle wheel flange wear. *Sensors*, *20*(1), 303.

Tyagi, S., & Panigrahi, S. K. (2017). An improved envelope detection method using particle swarm optimisation for rolling element bearing fault diagnosis. *Journal of Computational Design and Engineering*, *4*(4), 305–317.

Upadhyay, R. K., Kumaraswamidhas, L. A., & Azam, M. S. (2013). Rolling element bearing failure analysis: A case study. *Case Studies in Engineering Failure Analysis*, *1*(1), 15–17.

Vale, C. (2021). Wheel Flats in the Dynamic Behavior of Ballasted and Slab Railway Tracks. *Applied Sciences*, *11*(15), 7127.

Vale, C., Bonifácio, C., Seabra, J., Calçada, R., Mazzino, N., Elisa, M., Terribile, S., Anguita, D., Fumeo, E., & Saborido, C. (2016). Novel efficient technologies in Europe for axle bearing condition monitoring–the MAXBE project. *Transportation Research Procedia*, *14*, 635–644.

Vallen, H. (2002a). AE testing fundamentals, equipment, applications. *Journal of Nondestructive Testing(Germany)*, *7*(9), 1–30.

Vallen, H. (2002b). AE testing fundamentals, equipment, applications. *Journal of Nondestructive Testing(Germany)*, *7*(9), 1–30.

Vallen-Systeme GmbH. (2011). *AE Testing (AT). Fundamentals - Equipment – Data Analysis. (Overview)*. http://www.schallemission.de/zdownload/pdf/sea204E.pdf

van Dyk, B. J., Dersch, M. S., Edwards, J. R., Ruppert Jr, C., & Barkan, C. P. L. (2013). Quantifying shared corridor wheel loading variation using wheel impact load detectors. *ASME/IEEE Joint Rail Conference*, *55300*, V001T01A002.

van Dyk, B. J., Edwards, J. R., Dersch, M. S., Ruppert Jr, C. J., & Barkan, C. P. L. (2017). Evaluation of dynamic and impact wheel load factors and their application in design processes. *Proceedings of the Institution of Mechanical Engineers, Part F: Journal of Rail and Rapid Transit*, *231*(1), 33–43.

Wang, H., Conry, T. F., & Cusano, C. (1996). *Effects of cone/axle rubbing due to roller bearing seizure on the thermomechanical behavior of a railroad Axle*.

Wang, J., He, Q., & Kong, F. (2014). A new synthetic detection technique for trackside acoustic identification of railroad roller bearing defects. *Applied Acoustics*, *85*, 69–81.

Wang, J., Li, D., Qu, S., & Zhang, D. (2021). A Nondestructive Instrumented Wheelset System for Contact Forces Measurements. *Engineering*, *13*(7), 361–371.

Wang, K., Hao, Q., Zhang, X., Tang, Z., Wang, Y., & Shen, Y. (2020). Blind source extraction of acoustic emission signals for rail cracks based on ensemble empirical mode decomposition and constrained independent component analysis. *Measurement*, *157*, 107653.

Wang, W., Guo, J., & Liu, Q. (2013). Experimental study on wear and spalling behaviors of railway wheel. *Chinese Journal of Mechanical Engineering*, *26*(6), 1243–1249.

Wang, W. J., Guo, J., Liu, Q. Y., & Zhou, Z. R. (2008). An analysis of wear and spalling characteristics of the wheel steel under rolling—sliding conditions. *Proceedings of the Institution of Mechanical Engineers, Part J: Journal of Engineering Tribology*, *222*(2), 81–86.

Wang, Y. W., Ni, Y. Q., & Wang, X. (2020). Real-time defect detection of high-speed train wheels by using Bayesian forecasting and dynamic model. *Mechanical Systems and Signal Processing*, *139*, 106654.

Wang, Y.-F., & Kootsookos, P. J. (1998). Modeling of low shaft speed bearing faults for condition monitoring. *Mechanical Systems and Signal Processing*, *12*(3), 415–426.

Wei, C., Xin, Q., Chung, W. H., Liu, S., Tam, H., & Ho, S. L. (2011). Real-time train wheel condition monitoring by fiber Bragg grating sensors. *International Journal of Distributed Sensor Networks*, *8*(1), 409048.

Wu, Z., & Huang, N. E. (2009). Ensemble empirical mode decomposition: a noise-assisted data analysis method. *Advances in Adaptive Data Analysis*, *1*(01), 1–41.

Wüstenberg, H., Erhard, A., Bertus, N., Hintze, H., & Schüssler, M. (2001). Recent advances in ultrasonic inspection of railway axles and wheels. *Insight*, *43*(3), 180–182.

Yasniy, O., Lapusta, Y., Pyndus, Y., Sorochak, A., & Yasniy, V. (2013). Assessment of lifetime of railway axle. *International Journal of Fatigue*, *50*, 40–46.

Yi, C., Wang, D., Fan, W., Tsui, K.-L., & Lin, J. (2018). EEMD-based steady-state indexes and their applications to condition monitoring and fault diagnosis of railway axle bearings. *Sensors*, *18*(3), 704.

Yüksel, K., Kinet, D., Moeyaert, V., Kouroussis, G., & Caucheteur, C. (2018). Railway monitoring system using optical fiber grating accelerometers. *Smart Materials and Structures*, *27*(10), 105033.

Zakharov, S. M., & Goryacheva, I. G. (2005). Rolling contact fatigue defects in freight car wheels. *Wear*, *258*(7–8), 1142–1147.

Zhang, D., Entezami, M., Stewart, E., Roberts, C., & Yu, D. (2018). Adaptive fault feature extraction from wayside acoustic signals from train bearings. *Journal of Sound and Vibration*, *425*, 221–238.

Zheng, F., Zhang, B., Gao, R., & Feng, Q. (2019). A high-precision method for dynamically measuring train wheel diameter using three laser displacement transducers. *Sensors*, *19*(19), 4148.

Zhu, Y., Yang, Y., Mu, X., Wang, W., Yao, Z., & Yang, H. (2019). Study on wear and RCF performance of repaired damage railway wheels: Assessing laser cladding to repair local defects on wheels. *Wear*, *430*, 126–136.